JOHANNES GUTENBERG UNIVERSITÄT MAINZ

JG|U

Interplay of Structure and Dynamics in Metallo–Supramolecular Polymer Networks

Dissertation zur Erlangung des akademischen Grades

„Doktor der Naturwissenschaften“ (Dr. rer. nat.)

im Promotionsfach Chemie

am Fachbereich 09 Chemie, Pharmazie und Geowissenschaften

der Johannes Gutenberg–Universität Mainz

M. Sc. Martha Franziska Koziol

geboren in Mainz

Mainz, 2022

Die vorliegende Arbeit wurde unter der Leitung von [redacted] im Zeitraum von März 2018 bis Dezember 2021 am Department für Chemie angefertigt.

1. Gutachter: [redacted]

2. Gutachter: [redacted]

Tag der mündlichen Prüfung:

Eidesstattliche Erklärung

Hiermit versichere ich, Martha Franziska Koziol, gemäß § 10 Abs. 3d der Promotionsordnung vom 24.07.2007:
Ich habe die jetzt als Dissertation vorgelegte Arbeit selbst angefertigt und alle benutzten Hilfsmittel (Literatur, Apparaturen, Material) in der Arbeit angegeben. Ich hatte weder die jetzt als Dissertation vorgelegte Arbeit noch Teile davon bei einer anderen Fakultät bzw. einem anderen Fachbereich als Dissertation eingereicht.

Datum Unterschrift

_____ _____

Acknowledgements

Mein besonderer Dank gilt [redacted] für die Bereitstellung des interessanten und lehrreichen Themas, die Betreuung während der gesamten Promotion sowie den Freiraum, auch eigene Projekte entwickeln und umsetzen zu können. Desweiteren möchte ich mich vor allem für die wundervolle Möglichkeit bedanken, ein halbes Jahr in den USA zu verbringen und dort an einem spannenden Projekt zu arbeiten. Diese Zeit mit all ihren Erfahrungen wird mir immer in Erinnerung bleiben. Danken möchte ich auch [redacted] für die Übernahme des Zweitgutachtens und viele nützliche und wertvolle Anstöße bezüglich der Lichtstreu-Experimente. Ich danke auch [redacted] und allen Mitgliedern seiner Arbeitsgruppe am MIT für die herzliche Aufnahme und die hervorragende Zusammenarbeit.

Ich möchte mich bei allen aktuellen und ehemaligen Mitgliedern des Arbeitskreises [redacted] bedanken, für die hervorragende nicht nur fachliche, sondern vor allem auch freundschaftliche Atmosphäre und für die vielen gemeinsamen Aktivitäten. Besonders hervorheben möchte ich [redacted] und [redacted], die von Anfang an Wegbegleiterinnen waren.
Vielen Dank auch an [redacted] und [redacted] für die Fürsorge und Herzlichkeit, für euer offenes Ohr, jede nächtliche Stunde an der Lichtstreuung und jeden Ausflug, jede Weihnachtsfeier oder jedes AK-Grillen, das ihr so liebevoll organisiert habt. [redacted] und ihrer Nachfolgerin [redacted] danke ich für die kompetente und schnelle Unterstützung in allen administrativen Fragen.
Ich danke [redacted] für unzählige Kaffeepausen, ein Jahr voller Mittwoche, eine besondere Playlist und den Halt in den letzten Wochen und Monaten.
[redacted] danke ich von Herzen für die konstante Unterstützung, für jeden (nicht nur wissenschaftlichen) Rat und jede Hilfe, die ich sehr zu schätzen weiß.
Allen Korrekturleser*innen dieser Arbeit möchte ich herzlich für ihre investierte Zeit und Arbeit danken. Meinen Bachelorand*innen und Modulant*innen [redacted], [redacted], [redacted], [redacted], [redacted], [redacted], [redacted], [redacted], und [redacted] für die geleistete Arbeit und die lehrreiche Zeit.

Der Deutschen Forschungsgemeinschaft (DFG) danke ich für finanzielle Unterstützung.

Ich danke allen meinen Freunden und Wegbegleitern, zu nennen sind hier vor allem [redacted], [redacted], [redacted] und [redacted] für jedes motivierende und aufbauende Wort, vor allem in schwierigen Zeiten.

Meinen Eltern und meinem Bruder, schlichtweg meiner gesamten Familie gilt großer Dank für Eure unendliche und vielfältige Unterstützung, Liebe und Geduld mit mir während dieser doch sehr langen Strecke. Ohne Euch wäre diese Arbeit nicht möglich gewesen.

Man sagte uns, man bekomme nie etwas umsonst – nie etwas für nichts.
Aber heute, nach einem Leben in der Forschung, bin ich der Meinung,
dass man ein ganzes Universum ganz umsonst haben kann.
(Stephen Hawking, aus „Kurze Antworten auf große Fragen“)

Abstract

The present thesis focuses on the interplay of structure, mechanical response, and dynamics in model-type supramolecular polymer networks. Reversible networks formed by star-shaped monodisperse macromolecules that are interlinked via metal-ligand interactions (dative transition metal–terpyridine bonds), serve as material basis to establish structure–property–relationships. To fully unravel the dynamics in such transient networks, contributions from all network-forming components (e. g. polymer chain physics or chemistry of sticky motifs) and their mutual dependences have to be considered.

The first part of this thesis addresses the characterization of poly(ethylene glycol) (PEG) solutions in the semi-dilute concentration regime. A low-frequency plateau in the storage modulus as indicated by rheology, leads to the assumption of a weak energy-storing substructure. However, static and dynamic light scattering results demonstrate no aggregate or cluster formation in the polymer solutions if special care is taken during sample purification and preparation. The frequency range accessible by rheology experiments is extended to higher frequencies by several decades using coated spherical gold nanoparticles as microprobes. The results underline the urgent necessity of a thorough sample purification by means of filtration if artefact-free light scattering autocorrelation functions are targeted.

In a second study, the scattering behavior of transiently connected supramolecular polymer networks is investigated. The combination of static and dynamic light scattering simultaneously provides information about the network structure (static inhomogeneities), as well as the underlying relaxation processes and their length scale-dependence. A delayed gel preparation procedure is implemented that allows for externally tunable gelation times and a facilitated preparation of the mandatory dust-free gels for light scattering experiments. This new method opens up the opportunity to monitor the scattering intensity and evolving of relaxation modes in real-time during gelation, and enables the postulation of a molecular gelation mechanism. A targeted control of network relaxation times is achieved through the use of either cadmium, zinc, or nickel cations as their metal-terpyridine dissociation constants differ by several orders of magnitude.

The combination of multiple characterization techniques (rheology, DLS, SLS, FRS, UV-Vis) is required to scan a length scale and timescale range of five, respective 15 decades, and to gain knowledge on the complex hierarchy of relaxation processes in the networks. The macroscopic terminal relaxation times measured by rheology and the relaxation modes obtained by dynamic light scattering are examined, as well as the self-diffusivities of fluorescently labelled four-arm macromolecules measured by

forced Rayleigh scattering. These kinetically controlled relaxation times are related to the complex dissociation of an isolated zinc-terpyridine bond and the resulting activation energies are compared. Static inhomogeneities in the range of several tens of nanometers are detected by static light scattering thereby unravelling a direct impact of the local structure on the viscoelastic intensity autocorrelation modes.

A further approach towards desired structure control in transient networks is presented in the last part of this thesis. The above introduced star-PEG network structures are modified by systematically incorporating connectivity defects to independently investigate the influence of connectivity mismatches on the mechanical properties and self-diffusivities. Despite a constant overall sticker concentration, an increasing defect fraction leads to a decrease in the elastic response. In addition to that, the microscopic structural irregularities further impact the center-of-mass diffusion of entire macromolecules within the network. The increased number of intramolecular loops coming along with an apparent dilution effect, leads to an accelerated diffusion. These fundamental relations have an enormous importance especially in the field of smart material design of self-healing materials with intrinsic transport properties.

Zusammenfassung

In der vorliegenden Arbeit wird das Zusammenspiel zwischen Struktur, mechanischen Eigenschaften und Dynamik in supramolekularen Modellnetzwerken untersucht. Monodisperse stern-förmige Polymermoleküle, die durch Metall-Ligand-Wechselwirkungen (dative Übergangsmetall-Terpyridin-Bindungen) reversibel miteinander zu Netzwerken verknüpft werden, bilden die Materialbasis, um Struktur–Eigenschafts–Beziehungen aufstellen zu können. Um die komplexe Dynamik in solchen Netzwerken vollständig verstehen zu können, werden zunächst die Einzelbeiträge der netzwerkbildenden Komponenten (Polymerphysik der Ketten oder Assoziationschemie der Verknüpfungseinheiten) und ihre gegenseitigen Wechselwirkungen genauer untersucht.

Im ersten Teil der Arbeit liegt der Fokus auf der Charakterisierung halbverdünnter Poly(ethylenglykol)-Lösungen. Statische und dynamische Lichtstreuung zeigen, dass diese Polymerlösungen nach sorgfältiger Aufbereitung und Reinigung keine Aggregate oder Cluster aufweisen, die einem niederfrequenten Plateau im Speichermodul der Rheologie zugeordnet werden könnten. Beschichtete Goldnanopartikel werden verwendet, um als Mikrosonden den Frequenzbereich der makroskopisch zugänglichen elastischen Module um mehrere Dekaden zu erweitern. Die Ergebnisse zeigen deutlich, dass eine gründliche Probenvorbereitung / -filtrierung erfolgen muss, um artefaktfreie Korrelationsfunktionen in der Lichtstreuung erhalten zu können.

In einem weiteren Projekt wird das Lichtstreuverhalten von transienten Modellnetzwerken untersucht. Die Kombination aus statischer und dynamischer Lichtstreuung liefert zeitgleich Informationen über die Struktur solcher Netzwerke (statische Inhomogenitäten), als auch über vorliegende Relaxationsprozesse und ihre q-Abhängigkeit. Um homogene Gele zu erhalten, wird die Herstellungsweise der Gele modifiziert, sodass eine Gelierung erst nach einer vorher einstellbaren Gelierzeit einsetzt und eine staubfreie Präparation möglich wird. Mithilfe dieser neuen Methode ergibt sich die Möglichkeit, die Streuintensität und das Auftreten von Relaxationsmoden in Echtzeit während der Gelierung aufzunehmen und darauf basierend einen Gelierungsmechanismus aufzustellen.

Cadmium-, Zink- und Nickelkationen werden als vernetzende Metallionen eingesetzt, um durch die unterschiedlichen kinetischen Metall-Terpyridin-Dissoziationskonstanten die Netzwerkrelaxation gezielt steuern zu können.

Zur weiterführenden Charakterisierung des Zusammenspiels von Struktur und Dynamik wird mithilfe mehrerer komplementären Methoden (UV-Vis, Rheologie, DLS, SLS, FRS) ein weiter Längen-,

aber auch Zeitskalenbereich von fünf, beziehungsweise 15 Dekaden erforscht, um die komplexe Hierarchie der auftretenden Relaxationsprozesse besser verstehen zu können. Neben der terminalen Relaxationszeit des Gesamtnetzwerkes wird auch auf die diffusiven und viskoelastischen Moden aus der Lichtstreuung, sowie die Selbstdiffusion fluoreszenzmarkierter Vierarm-Makromoleküle eingegangen. Alle kinetisch bedingten Prozesse werden mit der Dissoziationskonstante der isolierten Zink-Terpyridin-Bindung in Relation gebracht und die in temperaturabhängigen Messungen erhaltenen Aktivierungsenergien verglichen. Statische Lichtstreuung detektiert Heterogenitäten im Bereich von einigen zehn Nanometern und diese bewirken eine ungewöhnlich breite gelpositionsabhängige Verteilung von Relaxationszeiten der langsamen viskoelastischen Autokorrelationsmode.

Im letzten Teil der Arbeit werden gezielt Strukturmodifikationen in Form von Konnektivitätsdefekten an den transienten Stern–PEG–Netzwerken vorgenommen, um den Einfluss auf die mechanischen Eigenschaften und die Diffusivität zu erforschen. Dafür werden systematisch jeweils zwei Äquivalente von Vierarm-Molekülen durch ein Äquivalent von Achtarm-Molekülen ausgetauscht, um den Grad der Konnektivität zu beeinflussen. Eine erhöhte Defektfraktion mit steigendem Achtarm-Anteil führt zu einem Absinken des elastischen Moduls trotz gleichbleibender Terpyridin-Konzentration in den Netzwerken. Diese mikroskopische Strukturänderung wirkt sich zudem direkt auf die Selbstdiffusion der Polymere innerhalb des Netzwerkes aus. Durch die vermehrte Schlaufenbildung tritt ein scheinbarer Verdünnungseffekt auf, der eine beschleunigte Diffusion einzelner Makromoleküle zur Folge hat. Vor allem in der Materialentwicklung von selbstheilenden Materialien mit intrinsischen Transporteigenschaften sind die aufgestellten fundamentalen Zusammenhänge von enormer Bedeutung.

Content

Anmerkungen zur Gliederung

Zu Beginn erfolgt eine zusammenfassende Darstellung aktueller Forschungsarbeiten, um in das Thema der vorliegenden Dissertation einzuführen. Dabei wird auf die für die Arbeit relevantesten Eigenschaften supramolekularer Polymernetzwerke näher eingegangen, um eine thematische Einordnung zu generieren. Anschließend daran werden im zweiten Kapitel die Ziele der Arbeit motiviert.
Den Hauptteil bilden drei bereits veröffentlichte Publikationen und ein fertiges Manuskript, welches zum Zeitpunkt der Abgabe noch nicht akzeptiert, allerdings bereits in einer überarbeiteten Fassung erneut eingereicht wurde.

1) Koziol, M.; [redacted]. Origin of the low-frequency plateau and the light-scattering slow mode in semidilute poly(ethylene glycol) solutions. *Soft Matter* **2019**, *15*, 2666–2676. (DOI: 10.1039/C8SM02263A)

2) Koziol, M. F.; [redacted] Structural and Gelation Characteristics of Metallo-Supramolecular Polymer Model-Network Hydrogels Probed by Static and Dynamic Light Scattering. *Macromolecules* **2021**, *54*, 4375–4386. (DOI: 10.1021/acs.macromol.1c00036)

3) Koziol, M. F.; [redacted] Hierarchy of Relaxation Times in Supramolecular Polymer Model Networks (revised submission to *Physical Chemistry Chemical Physics*, 21.12.2021)

4) [redacted].;* Koziol, M. F.;* [redacted] Defect-controlled softness, diffusive permeability, and mesh-topology of metallo-supramolecular hydrogels. *Soft Matter* **2022**. (DOI: 10.1039/D1SM01456K)

Vor jedem Manuskript wird die erbrachte Eigenleistung detailliert beschrieben sowie eine kurze zusammenfassende Einordnung in den Gesamtkontext der Arbeit gegeben. Abschließend erfolgt eine Gesamtzusammenfassung der Ergebnisse und ein Ausblick.

List of Abbreviations and Symbols

α	Stretch exponent
Γ	Gamma function
γ_0	Deformation amplitude
η	Viscosity
$[\eta]$	Intrinsic viscosity
θ	Scattering angle
λ	Wavelength
μ	Number of elastically active cross-links
ν	Number of elastically active chains
Ξ	Static correlation length
ξ	Hydrodynamic correlation length
σ^2	Amplitude of the intensity correlation function
τ	Correlation time
τ_b	Bond lifetime
τ_b^*	Renormalized bond lifetime
τ_{fast}	Fast relaxation time
τ_R	Relaxation time
τ_{slow}	Slow relaxation time
τ_{Zimm}	Zimm chain relaxation time
ϕ	Polymer weight fraction
ω	Frequency

---

a	Particle radius
A	Associated state
A_2	Second virial coefficient
B_0	Magnetic field
c	Concentration
c^*	Chain overlap concentration
cw	Continuous wave
d	Holographic grid spacing

$\delta c(q,t)$	Total concentration fluctuations
$\delta c_F(q,t)$	Thermodynamic concentration fluctuations
$\delta c_C(q,t)$	Frozen concentration inhomogeneities
D	Diffusion coefficient
D_A	Apparent collective gel diffusion coefficient
DCM	Dicholormethane
D_{HT}	Heterodyne diffusion coefficient
DLS	Dynamic light scattering
DMF	*N,N*-Dimethylformamide
DMSO	Dimethylsulfoxide
DNA	Deoxyribonucleic acid
DOPA	L-3,4-dihydroxyphenylalanine
$\langle \Delta r(t)^2 \rangle$	Mean squared displacement
D_S	Self-diffusion coefficient
E_A	Activation energy
EDTA	Ethylenediamintetraacetic acid
$E_F(q,t)$	Fluctuating electric field
$E_F^*(q,t)$	Complex conjugate of the fluctuating electric field
f	Functionality
FRAP	Fluorescence recovery after photobleaching
FRS	Forced rayleigh scattering
F_τ	Force
γK_{eq}	Anomaly constant
$g^{(1)}(q,t)$	Field correlation function
$g^{(2)}(q,t)$	Intensity correlation function
$G^*(\omega)$	Complex shear modulus
$G'(\omega)$	Storage modulus
$G''(\omega)$	Loss modulus
GDL	D-glucono-1,5-lactone
G_P	Plateau modulus
H	Heaviside function

HRD	Histidine rich domains
HV	High vacuum
I_C	Time-independent static intensity
$I_{DQ}(t_{DQ})$	Double quantum build-up function
$\langle I \rangle_E$	Ensemble-averaged intensity
$\langle I \rangle_{Excess}$	Excess intensity
$\langle I_F \rangle_T$	Time-averaged fluidic intensity
$I_{ref}(t_{DQ})$	Reference function
$\langle I \rangle_T$	Time-averaged intensity
$J(t)$	Creep compliance
K	Optical constant
k_B	Boltzmann constant
k_d	Bond dissociation rate constant
K_{eq}	Equilibrium constant
KOH	Potassium hydroxide
KWW	Kohlrausch-Williams-Watts
LS	Light scattering
LVE	Linear viscoelastic regime
M	Molecular state
MLCT	Metal ligand charge transfer
M_n	Number average molecular weight
MQ-NMR	Multiple quantum nuclear magnetic resonance
MSD	Mean squared displacement
M_w	Weight average molecular weight
n	Refractive index
N_A	Avogadro number
NBD	(*S*)-(+)-4-(3-amino-pyrrolidino)-7-nitrobenzofurazan
NDS	Network disassembly spectroscopy
NHS	*N*-hydroxysuccinimide
NSE	Neutron spin echo
P	Probability

PEG	Poly(ethylene glycol)
PDI	Polydispersity index
pK_a	Acid dissociation constant
pNIPAAm	Poly(*N*-isopropylacrylamide)
Ppy	Polypyrrole
PVA	Poly(vinyl alcohol)
q	Scattering vector
R	Universal gas constant
RDC	Residual dipolar coupling
RENT	Real elastic network theory
R_g	Radius of gyration
R_H	Hydrodynamic radius
RI	Refractive index
RR	Rayleigh ratio
SANS	Small angle neutron scattering
SAXS	Small angle X-ray scattering
SEC	Size exclusion chromatography
$S_{Guinier}$	Structure factor
SI	Supporting information
SLS	Static light scattering
t	Time
T	Temperature
T_1	Longitudinal relaxation time
tan(δ)	Loss factor
t_{DQ}	Double quantum evolution time
TEA	Triethylamine
THF	Tetrahydrofuran
T_{min}	Minimum torque
tpy	Terpyridine
X_p	Homodyne scattering contribution
Y	Ratio of ensemble and time average intensity

1 INTRODUCTION

1.1 Supramolecular Polymer Networks

1.1.1 Definition

Since Hermann Staudingers discovery and postulation of the term "macromolecule" in 1920,[1] an extensive and impactful further development of his first concept is represented by supramolecular polymer networks. According to the IUPAC definition, a network is *"A highly ramified macromolecule in which essentially each constitutional unit is connected to each other constitutional unit and to the macroscopic phase boundary by many permanent paths through the macromolecule, the number of such paths increasing with the average number of intervening bonds; the paths must on the average be co-extensive with the macromolecule.*

1. Usually, and in all systems that exhibit rubber elasticity, the number of distinct paths is very high, but, in most cases, some constitutional units exist which are connected by a single path only.

2. If the permanent paths through the structure of a network are all formed by covalent bonds, the term covalent network may be used.

3. The term physical network may be used if the permanent paths through the structure of a network are not all formed by covalent bonds but, at least in part, by physical interactions, such that removal of the interactions leaves individual macromolecules or a macromolecule that is not a network." [2]

Connection of functionalized macromolecules through either covalent bonds or physical interchain interactions (such as hydrogen bonding, π-π stacking, or metal-ligand complexation)[3] leads to infinite three-dimensional entities that are spanned throughout a given volume. An important property of these percolated network structures is the ability to form gels if swollen in various solvents (such as water or organic solvents), as a large quantity of solvent molecules is entrapped within the polymer matrix. Supramolecular polymer networks belong to the class of soft matter and can be categorized as in-between pure solids and pure liquids thereby combining properties of both: rigid structure elements and elasticity as well as dynamic flow and mobility.[4,5]

Over the past decades, several types of material bases for network and gel formation have been investigated including natural as well as synthetic polymers.[4] Natural polymers, e. g. alginate, cellulose or several peptides / proteins,[4] entail excellent biocompatibility, low cytotoxicity and sustainability. Well established synthesis routes also allow the use of a broad spectrum of synthetic polymers including

amphiphiles, block-copolymers, ionomers, and dendritic or multi-arm polymers. The immense multitude of suitable polymeric materials consisting of flexible or rigid sub-segments, incorporated functional monomers, or branched architectures in combination with various kinds of crosslinking chemistries opens a huge playground for the design of highly tunable and responsive materials.

The most pronounced features of supramolecular polymer networks, e. g. their dynamics, structure, self-diffusion properties, and applications are reviewed in the following sections, including a special focus on metal-ligand coordination-based networks and star-polymer systems.

1.1.2 Structure

Polymer networks are amorphous or semi-crystalline constructs with characteristic structural features that span a wide range of length scales between one and several hundreds of nanometers. From a very simple perspective, *ideal* networks are specified by uniformly distributed unentangled polymer strand lengths that unrestrictedly obey Gaussian conformations in combination with identical crosslinker functionalities. Overall homogeneity and regularity is achieved on all length scales (microscopic and macroscopic perspectives).[6,7] In strong contrast to that, the existence of inherent spatial confinement and a hindered mass transport during crosslinking reactions offer optimum pre-conditions for the most essential property of supramolecular networks: the occurrence of structural inhomogeneities that can be refined as any deviations from the aforementioned requirements for ideal networks.
Those inhomogeneities can further be classified into three types:[8,9] *Spatial inhomogeneities* are random variations of the crosslinking or polymer strand density in the range of 10–100 nm whereas *topological inhomogeneities* manifest themselves in loops, dangling chains or physical entanglements (**Figure 1-1**). A third category of *connectivity inhomogeneities* (1–10 nm) represents misconnectivities and cluster formation. The existing classifications of network heterogeneities are widely ambiguous and recent studies use a more general terminology thereby only differentiating between global heterogeneities (that resemble the former spatial inhomogeneities) and topologically local defects that include all types of misconnectivities, loops or dangling strands on length scales of a network mesh.[10,11] To uncover this richness in structures, a variety of experimental techniques that complementary covers a broad range of length scales is required. Network formation can be partly dictated using pre-programmed macromolecular precursors with distinct branching functionalities or other structural features that come along with their chemical composition.[12] However, full control over network topology

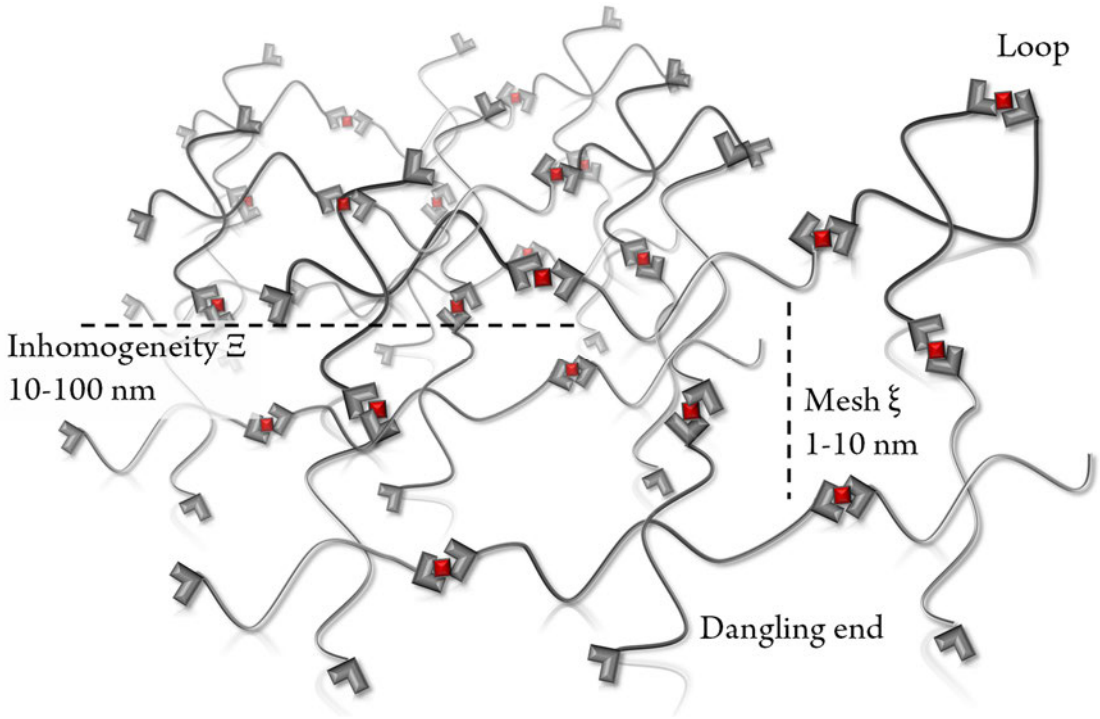

Figure 1-1. Schematic representation of a supramolecular polymer network with inhomogeneities on length scales of 10–100 nm, regular mesh sizes (1–10 nm) and network defects (loops, dangling ends).

remains challenging as it has to be achieved on both, global as well as local length scales. Another challenge coming along with structure control is linked to the difficulty of experimentally quantifying local network defects such as dangling chains or loops. Conventional scattering techniques (e.g. small angle neutron scattering (SANS), X-ray scattering (SAXS), or light scattering) lack in distinguishing between regular and defective connected network strands and therefore, less prevalent characterization techniques such as multiple-quantum nuclear magnetic resonance (MQ-NMR) or network disassembly spectroscopy (NDS) have to be considered.[10,13–15] Few approaches exist that successfully detect and reduce the formation of loops thereby enhancing the materials elastic modulus.[16–18] These studies show that even the implemented rather complex semi-batch synthesis strategies are not able to fully prevent loop formation. Even the prominent end-linking tetra-PEG gels by Shibayama and co-workers are found to exhibit microstructural topological defects,[13] such that the appearance of local defects can be considered as an intrinsic structural feature of polymer networks regardless of their chemical composition. Furthermore, a complex interplay between microstructural defects and spatial inhomogeneities can be assumed. The gained knowledge on the extent of elastically ineffective loops allows for a correction of the existing theories of predicting the elastic network modulus, as the classic phantom or affine network theories are based on defect-free ideal networks. Zhong *et al.* combined rheology and NDS to establish the relationship between number of loops and elastic plateau, thereby developing the 'real elastic network theory' (RENT).[18] They achieved good agreement between their predictions that

include a concentration-dependent elastically ineffective loop fraction and the measured bulk elasticities whereas phantom and affine network theories overestimated the modulus by far.

Regarding transient supramolecular networks or other self-assembling systems, the incorporation of sticky motifs into the polymer backbone often comes on cost of another structural and temporal irregularity: the formation of junction clusters. Sticker association often entails a drastic decrease in solubility followed by agglomeration and final formation of either ordered or irregular microphase separated domains. Such hierarchical assemblies are mainly found in biological systems with peptide-based structures, but also exist in synthetic networks constituted by hydrogen bonds or metal-ligand coordination.[19] Higher-ordered clusters and superstructures significantly influence the mechanical properties as well as the relaxation dynamics. Not only single sticker dissociation but also subsequent disintegration of clusters are required before complete chain relaxation can occur, resulting in decelerated terminal relaxation times.[20] Researchers can exploit cluster formation to design new materials with enhanced toughness as these multi-assembled structures provide a great number of additional attractive forces to strengthen the soft polymeric networks.

Until today, the goal of comprehensively understanding the interplay between structural defects or irregularities and final material properties, as well as the field of inhomogeneity control in soft matter is still a cause of great interest. Many macroscopic network properties such as the swelling capacity, optical clarity, elastic response, or transport characteristics are strongly influenced by the type and degree of heterogeneity. A recent review by Jangizehi *et al.* introduces the term 'defect engineering in soft matter' and demonstrates how controlled incorporation of heterogeneities and defects in soft matter materials can be used for rational material design.[11]

Topological defects do not only influence the elasticity of a network, but also strongly affect the dynamics if transient gels are regarded. A major influence on the network topology and concurrent relaxation dynamics is exerted by the distribution of sticky groups along the polymer backbone.[21] It has been found that multiple clustered binding sites can equally enhance the network toughness but also weaken it, depending on the material. A recent comparison between linear chains with either uniformly distributed sticky histidine groups or multiple histidine groups at each chain end revealed a decreased plateau modulus and higher relaxation activation energies for the clustered gels, as the clustered junctions act as one strong link.[22] Complementary self-diffusion measurements proved the formation of superloops with a high number of intrachain bonds that facilitate diffusion on large distances (several times of R_g).

1.1.3 Dynamics

Supramolecular soft matter materials generally exhibit a rich variety of dynamics evoked by several underlying microscopic stress relaxation mechanisms. The relaxation dynamics of *transiently* connected polymer networks are mainly governed by two contributions: the polymer segmental relaxation and sticker assembly / disassembly. The former depends on polymer-related parameters such as the backbone architecture, monomer-solvent interactions or chain lengths whereas the latter is impacted by the type of associative units and their kinetics, especially their dissociation (e.g. metal-ligand coordination, hydrogen bonding).[19,23] Due to the bond reversibility, a permanent dynamic structural rearrangement with even center-of-mass diffusion of single network components is possible. As the supramolecular sticker motifs are connected to the polymer chains, a sophisticated interplay opens up with additional influences originating from the structural complexity of the network. A large timescale is spanned if all relaxation times are considered and several scaling laws describing the effects of concentration, molar mass, or number of stickers are found.[12] Apart from those large timescales, also broad length scales including macroscopic, mesoscopic, and microscopic perspectives are required if the full dynamic spectrum is explored. On small length scales, chain motion manifests itself in sticky Rouse relaxation modes.[24] Unlike polymer chain motion in melts or semi-dilute solutions through reptation or Rouse dynamics, chain diffusion is significantly decelerated by several orders of magnitude, if sticky groups are incorporated.[25] In unentangled associative polymer networks, a sticker needs several attempts of opening and re-closing with the former partner before it releases stress due to an exchange with a new partner (bond renormalization). Rubinstein *et al.*[26] implemented an effective bond lifetime τ_b^* that accounts for the abovementioned scenario and is a multiple of the single bond lifetime that is programmed by the chemistry of the transient junction ($\tau_b^* >> \tau_b$). The isolated single bond lifetime τ_b is inverse to the junction dissociation rate constant k_d ($k_d = \tau_b^{-1}$). τ_b^* and τ_b exhibit a complex interplay depending on many parameters such as the chain architecture, the number of stickers per chain, and their position (end group vs. side group). This bond renormalization model has been expanded also for entangled networks (sticky reptation or living reptation)[27–29] where the association with a new partner is strictly limited to an area confined by the hypothetic confining tube, and an increasing number of intrachain bonds occurs at high concentrations. On time scales smaller than the bond lifetime τ_b, chains are considered as uninfluenced by the sticker units and exhibit segmental Rouse-type dynamics, like chain relaxation in permanent connected networks. Numerous models are established to theoretically describe and predict the dynamics of various network types, including molecular simulations

of linear chains with incorporated sticky monomers or telechelic multi-arm polymers,[30–33] interconnected associative micellar networks,[34] or diffusion-mediated mechanisms of self-healing.[35]

These concepts have been verified by a multitude of experimental studies.[36,37] For example, Tang *et al.*[38] investigated a broad hierarchy of relaxation times in transient networks of linear polymer chains connected through reversible nickel-histidine bonds (sidechain stickers). As the sticker exchange times (rheology) and the single metal exchange kinetics (UV-Vis, dilute conditions) significantly deviate due to the different chemical crowded environment of a gel compared to a solution, they implemented 'sticker dissociation and diffusion spectrometry' (SDDS) to measure the sticker dissociation kinetics directly within a gel. This time τ_{off} is concentration-independent and marks the lowest possible dissociation time in the gel state. A recent experimental study by Rao *et al.*[39] used neutron spin echo (NSE) to reveal unaffected Zimm dynamics ($\tau_{Zimm} \sim q^{-3}$) in an associative protein network on timescales much shorter than sticker dissociation. On large length scales, self-diffusivities D of entire protein molecules correlate with the sticky Rouse model predictions with a concentration dependence of $D \sim \phi^{-5.19}$.[26] A complex transition from segmental chain relaxation dynamics to mesoscopic self-diffusion including several molecular relaxation modes and a caging regime becomes evident. Additional structural influences of cluster formation on the mobility of small sticky tracer molecules indicate that relaxation can occur due to cluster diffusion with a high proportion of bound stickers within the clusters.

These works demonstrate that a plethora of experimental characterization techniques is required in order to examine the full relaxation spectrum of transiently connected networks, as the dynamics cover a broad length as well as time scale. The aforementioned models provide a multitude of dynamic parameter relationships, manifesting themselves in scaling law-interdependencies of concentration, polymer molecular weight, terminal relaxation time, diffusivities, or zero-shear viscosities. However, it remains challenging to generalize and adapt these models as their applicability is often restricted to the specifically described system they are developed from. As a result, the predicted dependences mostly deviate if minor changes in the system occur. Since the majority of transiently connected networks is responsive to external stimuli such as pH, light, or temperature, the network dynamics are also influenced by these external parameters. Often, this impact cannot adequately be captured by generalized models, albeit the prediction of dynamic parameters and timescales plays a key role in designing new smart materials with tailored properties.[40] Marco-Dufort *et al.*[41] used a broad library of star-shaped dynamic covalent networks with boronic ester groups as transient network junctions to independently decouple thermodynamic from kinetic parameters. The underlying junction chemistry and preferred

association / dissociation mechanisms (if more than one pathway leads to stable addition products) clearly dictate the macroscopic network properties, such as the plateau modulus G_P obtained by rheology. It is even possible to map microscopic reaction pathways if a series of macroscopic network stabilities (G_P) depending on varying thermodynamic parameters is known.

The temperature-dependence of junction rate constants is described by Arrhenius or Eyring equations that allow for quantification of the underlying activation energies, and enthalpic as well as entropic contributions.[41]

1.1.4 Self-Diffusion

On timescales larger than the bond lifetime τ_b, detachment of polymer building blocks and hindered diffusion through the network becomes relevant. Besides understanding the relaxation dynamics of transient networks, knowledge of diffusion properties with related self-healing mechanisms, transport processes or permeabilities is of crucial importance in the field of material engineering.[42–44]

Suitable methods to quantify (self-)diffusivities are Fluorescence Recovery after Photobleaching (FRAP) and Forced Rayleigh Scattering (FRS). Both techniques monitor the diffusion of fluorescently dye-labelled moieties into a beforehand bleached area either by analysis of time-dependent confocal microscope images (FRAP) or by Bragg diffraction of a reading laser beam (FRS), thereby covering length scales of several hundred nanometer to micrometers.

In a series of studies,[22,25,39,45,46] Olsen and co-workers discovered unexpected anomalous superdiffusion in associative protein gels and later also in tetra-arm PEG-terpyridine metallo-gels. Although sticky groups cause additional friction to the chains and therefore decelerate their motion, apparent superdiffusion with a mean squared displacement (MSD) $<r^2(t)> = t^\alpha$ with $\alpha > 1$ is found at length scales of $0.05 - 50\ \mu m^2$.[25] On length scales either smaller or larger than this regime, Fickian diffusion is observed. A two-state model based on the phenomenological description of that superdiffusive behavior has been implemented,[25] capturing well the experimental results. In a simplistic view, the diffusing chains are assigned to two molecular states: an associated state with a low mobility (most stickers are closed) and a diffusive state with high mobility (most stickers are open). It was stated that superdiffusion arises from the interconversion between both states. Even though this model provides effective diffusivities, anomaly constants and interconversion rate constants, their physical meaning remains doubtful as realistically, more than those two molecular states are imaginable.

To overcome this shortage, Ramírez *et al.*[47] used Brownian dynamics simulations to introduce three types of molecular motion in a network composed of sticky four-arm polymers: walking diffusion, hindered diffusion, and molecular hopping, with the latter being responsible for superdiffusion. More precise, hopping molecules can completely disengage from the network and travel distances much larger than their R_g. Conversely, walking describes chain motion with a stepwise dissociation and re-association of junctions thereby at no time being completely disengaged from the network. The model (**Figure 1-2**) predicts Fickian diffusion with a slope of 1 at small length scales, a caging regime in the length scale magnitude of R_g followed by superdiffusion at intermediate length scales and again, Fickian diffusion at large length scales with an effective diffusivity D_{eff} entailing additive contributions from walking and hopping.

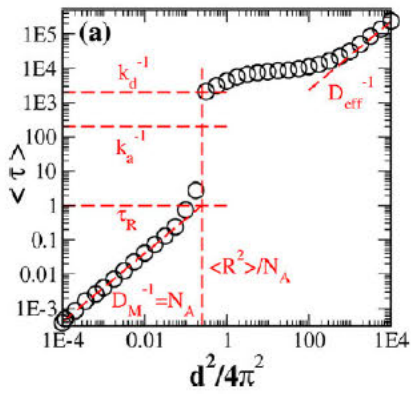

Figure 1-2. Simulated FRS relaxation times <τ> vs. grid spacing d^2 of a diffusing tetra-arm molecule. Four regimes with distinct diffusivities are visible. Reprinted with permission from *Macromolecules* **2018**, *51*, 2517–2525. Copyright 2018, American Chemical Society.

Comparison of the model with experimental results of self-diffusion of star-shaped polymers[46] showed good agreement in capturing the curve shapes of the superdiffusive regime. Although real molecular parameters are provided by the model, overestimated values for R_g and τ are obtained revealing the need for further refinements.

A combined FRS, NSE, and SANS study on protein-based associative networks by Rao *et al.*[39] revealed the existence of more than one superdiffusive regime and therefore concludes the consequent coexistence of more than the earlier described diffusive modes on different length scales. Comparison of the experimental results with the above-introduced model that postulates only one superdiffusive regime demonstrated obvious discrepancies. Very recently, this model has been improved and adapted to linear chains with regularly spaced stickers.[48] In agreement to the experimental findings, the hybrid Brownian dynamics / Monte Carlo simulations predict at least two distinct superdiffusive regimes with different molecular origins.

Rapp *et al.*[49] used a linear telechelic protein-based system with two sticky groups per chain to develop a reaction-diffusion three state model: next to the associated (both stickers bound) and the diffusive state (both stickers unbound), a third state describing the situation with one sticker bound and the other one dangling is implemented. Their predictions and measured diffusivities showed discrepancies that were hypothesized to be originated by an asymmetric binding. In a follow-up work, [50] the same authors demonstrated that molecular hopping can be the dominating diffusion mode in associative

networks due to an effective decreased equilibrium constant for binding. Each equilibrium constant of a sticky group in multi-arm polymers exhibits the same magnitude as preset by its chemistry. However, binding of one arm to the network results in a strong entropic penalty for all other arms of the same molecule as the number of possible chain conformations is drastically decreased. Consequently, the binding constants of stickers will continuously decrease the more arms are attached to the network and an enhanced fraction of hopping chains is obtained. The authors implemented a thermodynamic model that is able to describe the junction density and chain length dependences of their experimental diffusivity measurements.

Since the first discovery of superdiffusion in such associative networks, much work has been performed to elucidate the impacts of several parameters such as the sticker density, fixed sticker spacing, or sticker position on the superdiffusive regime. For example, Rasid *et al.*[45] investigated the effects of an increased sticker density (up to 15 sticky groups per linear chain) in transient poly(*N,N*-dimethylacrylamide)-histidine-nickel gels. With molecular hopping as the origin for superdiffusion, the increase in number of stickers was expected to suppress hopping, as the probability of simultaneously releasing all stickers from the network is significantly decreased. In contrast to this assumption, superdiffusion was found in all studied gels. It is hypothesized that an increased fraction of intrachain bonds is the reason for the occurrence of molecular hopping even though they are not predicted by the sticky Rouse model. Another work by the same authors researched the effect of clustered sticky end groups vs. evenly distributed stickers along the backbone on the diffusive properties.[22] Their combined study relates structure characteristics measured by small angle neutron scattering (SANS) to cooperative sticker effects resulting from clustered stickers at the ends of each linear chain.

The investigation of diffusion properties in such model type networks also enables to transfer the postulated concepts and knowledge to various kinds of permeable materials where transport processes play a crucial role like in biological membranes.

1.1.5 Applications

One of the unique and outstanding properties of supramolecular polymer networks is their inherent dynamicity introduced by reversible bonds. A common feature of these transient bonds is the responsiveness to several external stimuli such as pH, light, ultrasound, redox-potential, or temperature (or arbitrary combinations among them).[51] Consequently, mechanical response, optical properties, or self-healing abilities can be tailored more easily compared to their permanently connected counterparts.

Dissolution of these assembled structures in suitable solvents leads to the formation of gels, a material class with broad application opportunities. Facilitated by their 3D network structure, gels are able to retain additionally incorporated smaller molecules, diffusants or particles (magnetic nanoparticles, clay, microorganisms, pharmaceutical therapeutics) thereby opening the possibility to design composite materials with highly specific properties and enhanced elastic response. Christoff-Tempesta *et al.*[52] subdivide into four reasonable main application categories: optoelectronics, energy, biomedicine, and biology. An additional fifth unspecified category includes catalysis and environmental remediation. However, the latter mentioned might be the most emergent field, also impacting all other categories, with the urgent challenge of developing strategies to address the global climate change, for example with drinking water or wastewater treatment. High swelling capacities and the ability to repeatedly take up large amounts of contaminated water with the subsequent adsorption of salts,[53,54] heavy metal ions, petrochemicals,[55,56] or toxic ionic dyes,[57,58] render gels suitable and often biocompatible candidates to fight water scarcity and pollution.

In general, the most versatile application field for supramolecular polymer networks / hydrogels is represented in the biomedical section. Numerous examples exist for hydrogels in tissue engineering,[59–62] as artificial cartilage,[63] wound dressings,[64] or drug deliverers,[65–67] only to highlight a small selection. Networks consisting of biocompatible and biodegradable natural or synthetic polymers such as poly(lactic acid), poly(caprolactone), cellulose, or chitosan provide scaffolds for cell growth and proliferation.[68,69]

One decisive advantage of the dynamic networks is their softness and shear-thinning behavior, therefore being capable to adapt form and shape of the extracellular matrix (ECM) of native tissue and even spontaneously recover from damage. Due to their pronounced viscoelasticity, hydrogels loaded with active substances (e. g. non-steroidal anti-inflammatory drugs[70], anti-tumor drugs,[71] etc.) act as medical mini depots that can be sprayed, injected, or locally applied to the site of interest thereby minimizing the need for large surgical procedures.[72] Hydrogels are pre-programmed to achieve controlled drug release only in the targeted local environment of the human body regulated by a specific pH-value or redox-potential, and consequently, the need for repeatedly high-dosed drug injections with often unintended side-effects is drastically reduced. In addition to the injection of hydrogels via syringe, desired shapes can be produced by 3D printing. [73]

Besides the abovementioned pharmaceutical active substances, a large number of hydrogels with incorporated inorganic minerals is investigated as biomedical smart materials. Hybrid composites are synthesized either by in situ preparation of nanoparticles during gel formation or by introducing pre-

prepared nanoparticles into the final gels.[74,75] Bisphosphonates,[76] hydroxyapatite nanoparticles,[77,78] or vaterite nanoparticles[59] delivered to infectious or diseased bones are appropriate composite materials for bone regeneration. Antimicrobial properties that are required for improved wound healing are obtained if silver ions or nanoparticles are integrated into the networks.[74,79]

Myriad other applications for supramolecular hydrogels are found in the field of optoelectronics[80] or soft electronics.[81] Conducting or luminescing properties in many gels mainly arise from the incorporation of metal ions or lanthanoids. The emitted wavelengths can be intensified or tuned by various parameters such as the metal-ligand-ratio or mixtures of different lanthanoid ions.[82,83] Further, electronic conductivity is achieved using conducting polymer building blocks such as poly(para-phenylene), poly(thiophene), or poly(pyrrole).[74] Again, the flexibility and self-healing abilities of the supramolecular networks are main advantages over permanently connected rigid systems, making them suitable candidates for soft robotics with shape memory effects.[84]

The implementation of ionic conductivity into the networks leads to applications in the sector of energy storage / energy conversion. To avoid leakage or volatilization of highly toxic substances, electrolyte liquids in battery materials, capacitors or dye-sensitized solar cells can be replaced by ionic liquid-based supramolecular gels.[85,86] The solid-like 3D network structure swollen in a large amount of liquid combines fast ionic diffusivity with a stable but yet dynamic framework. High elastic stretchability and the ability to re-shape after iterated deformation without loss in the conductivity performance are main challenges facing the development soft electronic materials. [87] The emerging field of flexible and wearable electronics is realized through the use of ionic hydrogels, for example stretchable sodium-ion batteries,[88] ionic touch panels,[89] soft actuators,[90] or bio-sensing.[91]

The abovementioned examples demonstrate that the use of supramolecular networks is by no means restricted to a certain application area but is rather extended to all kinds of fields where material engineering becomes relevant, further including life sciences, food industry, personal and home care, catalysis, and development of technical devices. Through infinite combinations of desired material properties, supramolecular polymer networks are multiply deployable like almost no other material class.

1.2 Metal-coordination in supramolecular polymer networks

Many properties such as repeatable self-healing[92] of a material can be achieved by incorporation of metal-ligand coordination bonds into the polymer network.[51] Inspired by numerous smart and ingenious material functionalities in biological systems that are caused by metal-ligand coordination, many efforts have been made to mimic these qualities and transfer them to controlled material engineering.[93–96] A prominent and well explored example are zinc(II)-histidine and iron(III)-L-3,4-dihydroxyphenylalanine (DOPA) interactions in marine mussel byssal threads, giving this material unusual toughness and adhesive strength.[97,98] In many cases, metal-ligand bonds are thermodynamically stable while kinetically labile: a desired combination leading to high mechanical network strengths as well as fast ligand exchange under ambient temperature conditions. Depending on the chosen ligands and metal ions, a broad range of bond strengths between 2–350 kJ mol^{-1} is covered[99] and additional metal-related characteristics such as catalytic activity[100] or dielectricity[101] are implied.

Stress loading on reversible network junction points with characteristic coordination bond lifetimes τ_b results in a permanent restoring of the network structure.[93] Ligand-induced crystal field splitting of the metal ion d-orbitals allows for electronic transitions coming along with luminescence or photo-responsiveness.[82,102,103] Additionally, incomplete occupied orbitals with unpaired electrons are the origin of magnetic properties.[104] Another advantage of metal-ligand coordination chemistry is the simple change in coordination number that can be achieved by variation of the type of ligand or metal ion

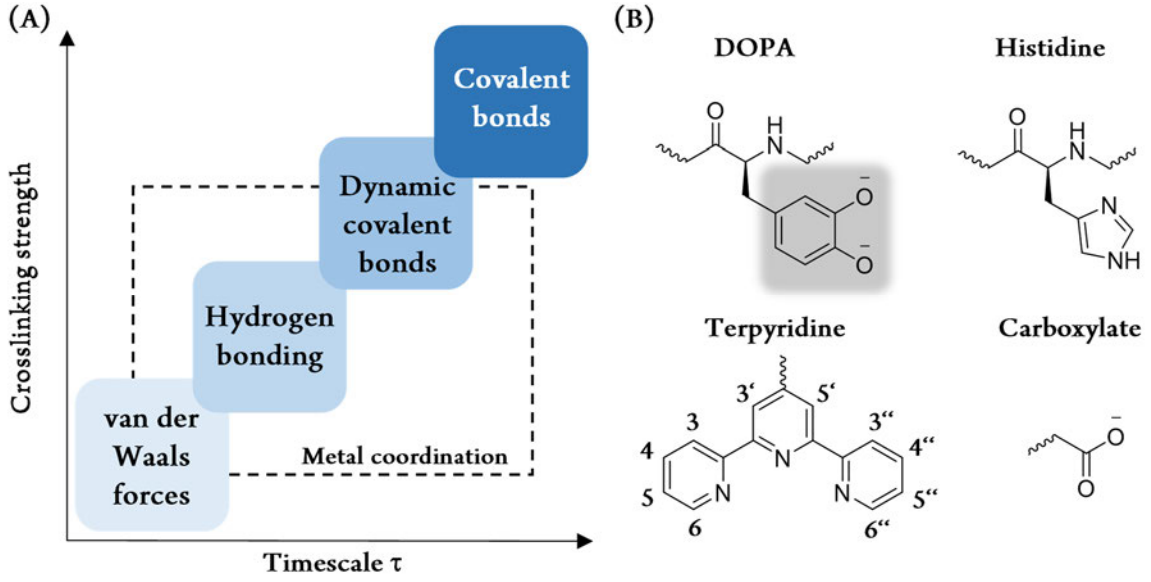

Figure 1-3. (A) Metal coordination bond strengths and bond lifetimes compared to van der Waals forces, hydrogen bonding, dynamic covalent bonds, and covalent bonds. Adapted with permission from Khare, E.; Holten-Andersen, N.; Buehler, M. J. *Nat Rev Mater* **2021**, *6*, 421–436. Copyright 2021, Springer Nature Limited. (B) Prominent examples for ligands used as coordinative binding motifs in metal-mediated supramolecular polymer or protein materials. The catechol-unit in DOPA is highlighted in grey.

valency. Using this complexation-based strategy offers the possibility to create model systems wherein characteristic network parameters like the number or functionality of junctions can independently be tuned. This is in strong contrast to many chemically connected networks, where a modulation of the mechanic response is often only possible through modification of the polymer precursor characteristics, such as molecular weight or polymer architecture. Highlighted examples as suitable ligands for metal complexation are catechols (as aforementioned in DOPA), histidines, pyridinyl-derivatives, or carboxylates (**Figure 1-3(B)**). Catechol coordination chemistry with ferric ions (Fe^{2+} and Fe^{3+}) is strongly pH-dependent: mono-metal-complexes are dominant at low pH-values whereas bis- and tris-complexes are formed with an increase in pH. These materials exhibit exceptional adhesive power even in aqueous environments; an outstanding property that is aimed to be imitated for the construction of wet surface adhesives.[105,106] Recent works in the field of bio-inspired soft matter are focused on the design and fabrication of tunable materials that are simultaneously responsive to several external stimuli. Advincula *et al.*[107] synthesized a multi-functional composite hydrogel by incorporating poly(pyrrole) (Ppy) nanoparticles into a catechol-modified chitosan and poly(*N*-isopropylacrylamide) Fe(III) network, thereby uniting near infrared light-, thermo-, and pH-responsive properties.

Another well investigated class of bio-inspired metal-ligand interactions is formed by metal-histidine (imidazole) complexation.[108] Commonly found in ragworm jaws, spider fangs, and insect mandibles, these type of complexes ensure extraordinary toughness and hardening. Histidine-based protein domains in combination with Zn^{2+}-, Cu^{2+}-, or Ni^{2+}-ions build the base for the enhanced mechanical properties. The active metal-binding site is an imidazole ring whose deprotonated N-atoms can pH-dependently donate lone pair electrons into the metal d-orbitals thereby achieving a variation in several coordination geometries.[109,110] Mozhdehi *et al.*[111] used monodentate imidazole ligands to achieve coordination numbers ranging from 4 (Zn^{2+} and Cu^{2+}), through 5 (Cu^{2+}), up to 6 (Co^{2+}) by sole variation of the metal ion. In addition to that, they showed that not only the crosslinker functionality, but also the concentration of free imidazole ligands can exhibit an influence on the mechanic responses in such weakly coordinated systems. Less unbound ligands entail a drastic reduction of the kinetic network exchange rates; a property that might be utilized for controlled material engineering with tailored dynamics. Further, Sanoja *et al.*[112] incorporated imidazole groups into a PEG-based statistical copolymer to investigate the interplay between ion conductivity, polymer strand relaxation and mechanical network response. They found a significant trade-off between elastic response, ion concentration and ion-mobility upon gradual addition of nickel(II) bis(trifluoromethylsulfonyl)imide with a maximum ion conductivity at the gel percolation threshold.

The most prominent example in the category of pyridyl-ligands is the chelating *N,N',N''*-tridentate ligand 2,2':6',2''-terpyridine (terpyridine, tpy, see **Figure 1-3 (B)**), that has been synthesized for the first time in 1931.[113,114] Since that time, mainly two effective synthetic routes have been developed to access terpyridine and a variety of multifunctional symmetrically and asymmetrically substituted derivatives in large scales.[115] Addition of suitable metal cations in a 1 : 2 ratio (metal ion : terpyridine) leads to the formation of stable and directed pseudo-octahedral achiral complexes with distinct and well-investigated kinetic and thermodynamic properties. The row of kinetic stabilities has been investigated to be $Ru^{2+} > Os^{2+} > Fe^{2+} > Zn^{2+} > Cd^{2+}$.[116,117] Due to the sufficient synthetic availability,[118,119] terpyridine ligands (and their derivatives) attached to polymers or proteins are a manifold utilized linkage unit for the controlled supramolecular 2D and 3D self-assembling into structures with numerous architectures[120] such as giant networks, Sierpińsky triangles,[121] or metallocages.[122] Besides end group functionalization, linear chains with terpyridine side groups are accessible by polymerization of suitable terpyridine-containing monomers such as norbornenes via ring-opening metathesis polymerization (ROMP).[123] The three heteronuclear aromatic rings with σ-donor and π-acceptor abilities provide excellent electron conjugation during complex formation and therefore stabilize metal ions with low valencies. The energetically low LUMO of the pyridyl-rings allows for electron transfer from the metal center to the π-system (metal ligand charge transfer), thereby creating the basis for a multitude of electron-mediated photophysical, catalytic and redox-chemical properties. For example, Sato *et al.*[124] prepared fluorescent supramolecular polymer films with high quantum yields based on terpyridine-zinc complexes. Depending on the nature of substituent (electron-withdrawing or electron-donating) at position 6 of the terpyridine unit, a distinct shift in the emission wavelength is achieved. Besides d-metal ions, terpyridines are also able to form stable and fluorescing complexes with rare earth metals such as europium (Eu^{3+}) or lanthanum (La^{3+}). White light emission of a self-assembled four-arm PEG system with Eu and Tb terpyridine complexes was obtained by Chen and co-workers.[82] In this work, a wavelength shift was induced by varying the stoichiometric ratio of both used ions. These properties can be exploited for bioimaging and biosensing, e. g. the detection of pyrophosphates in a nanomolar concentration range.[125]

All these metal-coordination based examples demonstrate that knowledge gained from natural dynamic systems is on the one hand used to transfer the complex forming unit (e.g. catechol, histidine, or carboxylate) into existing and well-understood polymer systems with the aim of uncovering the underlying mechanism for self-healing or toughness.[126] On the other hand, the rare and not always easily

available biogenic (protein) building blocks are replaced by sustainable and cheap synthetic polymers to target materials with desirable properties.[127]

1.3 Star-Polymer based Systems

Over the past decades, tetra-arm shaped polymer building blocks with telechelic sticker functionalities have been proven themselves as ideal candidates for the formation of model type networks.[23,128,129] Narrowly dispersed polymers in combination with simple click chemistry allow for the independent investigation of polymer-based parameters (*e.g.* molecular weight, backbone architecture, or solvent interactions) and specific crosslinker parameters (kinetics, single vs. multiple links, activation energies). Due to their inherent controllability, these networks are particularly suitable for the validation of theoretical models or simulations, and for the establishment of fundamental structure–property–relationships. Groundbreaking work has especially been done by Sakai, Shibayama and co-workers.

In 2008, they synthesized and analyzed a nearly ideal network, consisting of two types of *chemically connected* star-shaped PEG macromonomers with either amine (A-terminus) or *N*-hydroxysuccinimidyl (NHS, B-terminus) functionality.[129] Due to the mutual A-B cross-coupling, polymer back-biting was suppressed, misconnectivities could drastically be reduced, and, as time-resolved dynamic light scattering revealed, a homogeneous gel formed within 4 minutes. A remarkably high mechanical strength is achieved at gel concentrations that are even multiples of the overlap concentration c^*, and strictly equimolar concentrations of both symmetric macromonomers. These facts indicate that already slightest amounts of heterogeneities lead to a significant decrease in the mechanical gel performance, as proven later by small angle neutron scattering (SANS),[130,131] neutron spin echo (NSE),[132] and double-quantum NMR.[13] Until that approach, structure control has been challenging due to the stochastic crosslinking of polymer chains whose thermal fluctuations obey Gaussian statistics. As a result, mostly heterogeneous gels occured with dangling ends, loops, or spatial polymer concentration distributions. Due to the arbitrariness of size and localization of the heterogeneities, material property predictions by theory and simulation have been insufficient.

Since that pioneering work, a new research field based on permanently connected tetra-PEG gels has rapidly emerged.[133] Investigations including the incorporation of thermosensitive building blocks,[134] fine-tuning of the crosslinking degree,[135] control of defects,[136] or monitoring of the gelation kinetics[137,138] are only few examples that highlight the major contributions of the tetra-PEG based concept towards a better understanding of gel soft matter.

Not only the preparation and analysis of *ideal* networks have attracted attention, but also gaining control and insights into *non-ideal* gels and their properties, as these defective networks are closer to biological materials. By means of the tetra-PEG approach, Tsuji *et al.*, for example, were able to selectively induce spatial defects into the polymer network, more precisely by doping the network with nano-aggregates as well as nano-voids.[136] Noteworthy for their control of network structure is the polymer packing situation in the pre-gel solution. Inefficient packing conditions (low polymer concentration) lead to gels with local concentration shortages (negative doping), whereas a non-ideal solvent and thus pre-clustered polymer chains manifest themselves in local dense gel aggregates (positive doping).
The absence of heterogeneities qualifies tetra-PEG gels for the validation and establishment of several theoretical models, for example the rubber elasticity theory or the theory by Tanaka, Hocker, and Benedek.[139] To verify the latter, Fujiyabu *et al.*[140] used tetra-PEG gels to investigate the proposed interrelation between the osmotic bulk modulus K, the shear modulus G, the friction f, and the cooperative diffusion coefficient D (DLS) to be $D = \frac{K + \frac{4}{3} G}{f}$. Using thiol end-functionalized and maleimide end-functionalized tetra-PEGs, a simple stoichiometric imbalance (deviations from the molar ratio 1 : 1) changes the network connectivity, and therefore G, in a controlled way while the polymer volume fraction is kept constant. The expected linear interdependency of D and G was strongly supported by their experiments and a generalization for different gel concentrations and polymer molecular weights was found.

Further prominent models to describe the properties of a gel are the affine network theory[141] (1) or the phantom network theory[142] (2) that both attempt to predict the elastic modulus. Both models differ from each other in how fluctuations of the crosslinking points are treated. Crosslinking points are allowed to fluctuate in the phantom network theory, whereas these fluctuations are suppressed in the affine network theory, resulting in a twofold enhanced elastic response G_{affine} if the affine network model is used:

$$G_{\text{affine}} = \nu \, k_{\text{B}} T \tag{1}$$

$$G_{\text{phantom}} = (\nu - \mu) \, k_{\text{B}} T \tag{2}$$

Each elastically active chain ν provides an energy contribution $k_{\text{B}} T$ (Boltzmann constant k_{B} and temperature T) to the total elastic response. In the case of the phantom network model, the number of active crosslinks μ is subtracted in the calculation. Akagi and co-workers[143] used homogeneous tetra-PEG gels of different molecular weights to compare the elastic moduli with those that are predicted by

either the affine or the phantom network model. At concentrations around the polymer overlap concentration c^*, the elastic moduli are well described by the phantom network theory. Increasing the polymer volume fraction is accompanied by a transition to the affine network model. This example amongst many others emphasizes the fact that in most cases particular models are insufficient in adequately capturing the full range of gel properties.

Inspired by the advantages of the abovementioned well-known and established permanently connected tetra-PEG gels, defined star-shaped polymer building blocks also found their way into supramolecular assembling systems with all kinds of reversible crosslinks. The additional dynamic component with its complex relaxation mechanisms implies the relevance of the temporal aspect, along with the spatial one, when characterizing these networks.

The overall network rearrangement within such *transiently connected* star-shaped systems in semidilute conditions is mainly governed by the exchange kinetics of the reversible crosslinks whereas the polymer strand relaxation times are found to be faster by several orders of magnitude.[144–146] In general, the plateau modulus that quantifies the number of elastically active chains is strongly depending on the polymer concentration and additionally on the stoichiometric ratio between metal and ligand, if metallo-supramolecular systems are regarded.[43,144] A tight correlation between spatial structure characteristics and temporal properties dictates the overall network performance. To unravel these complex interdependencies, a tetra-arm polymer-based approach by Grindy *et al.* marks a breakthrough for the successful decoupling of viscoelastic relaxation modes from the spatial material structure.[147] Tetra-PEG-histidine in combination with a mixture of metal ions with distinct dissociation kinetics serves as model network to distinguish the contributions of each sort of ions to the hierarchical relaxation time spectrum. It was shown that this approach is also applicable to hydrogels consisting of mixed covalent and transient bonds as well as polymer melts.

Telechelic star-PEG networks do not only provide a platform for the investigation of fundamental physico-mechanical properties, but also help to uncover and mimic the assembling processes in supramolecular biologically relevant materials. For the latter purpose, bio-inspired sticker groups have been incorporated into tetra-PEG systems, such as peptide sequences (histidine rich domains (HRD)) or DNA.[148–152] In addition to the supramolecular motifs, hierarchical structure organization as it is often found in protein-based materials (for example pH-induced formation of β-sheet crystallites), also contributes to the stimuli-responsiveness and mechanical performance. Further control over the mechanics can be achieved by introducing pre-programmable DNA sequences that are highly selective in their assembling capabilities and responsive to salinity.

Supramolecular structures are known to provide sacrificial bonds in many hybrid networks. Under stress load, energy is first dissipated by the transient bonds, thereby preventing covalent bonds from breakage and consequent irreversible material damage.[126,153] As many metal-coordinated networks are incompatible for biomedical applications due to the toxicity of the metals, Lopez-Perez *et al.* have investigated tetra-PEG systems that are transiently crosslinked by alendronate-Ca^{2+} interactions.[154] In this work, another advantage of using defined star-shaped polymer precursors comes into effect: Narrowly dispersed PEGs that are accessible with a multitude of different molecular weights and number of arms (four-arm, six-arm, eight-arm) allow for concise comparability of hydrogels where the impact of arm length or number of arms can independently be investigated by keeping the overall sticker concentration constant. Examples that further refine the approach of using transient tetra-PEG networks are also found in nanocomposite material engineering.[155] Reversible metal-ligand interactions can also be conducted at the surface of metal ion containing nanoparticles. Li *et al.*[155] showed that despite the same type of coordination chemistry (pure Fe^{3+}-catechol interactions vs. Fe_3O_4 nanoparticle-catechol interactions), the final gel dynamics strongly depend on the number of stress-bearing chains that can easily be tuned by the size of crosslinking nanoparticles.

Star-shaped polymers have also been investigated in combination with dynamic covalent bonds as transient crosslinks.[156] As it is ubiquitous in all physically connected networks, these bonds are characterized by reversibility on accessible timescales. Representatives for these bond types are boronic acid-diol interactions[157] or products of Diels-Alder cycloadditions.[158,159] In contrast to metallo-ligand interactions where the association and dissociation is mainly dictated by their kinetic energies, the favoured forward or reverse reaction in dynamic covalent bonds is governed by the thermodynamic equilibrium and relative stabilities of the products or educts.[160] Temperature increase in dynamic covalent gels therefore leads to both, a faster relaxation and concurrent change in the number of elastically active junctions (resulting in a decreased or increased plateau modulus), whereas only the relaxation time is affected by temperature variations in model metallo-supramolecular networks. Parada *et al.*[161] used four-arm macromolecules with either 3-fluorophenylboronic acid or diol end groups to demonstrate in a joint theoretical and experimental work how the relaxation time and elastic response can adequately be simulated and tuned depending on temperature, macromonomer concentration, or macromonomer molecular weight. In addition, network dynamics are found to be strongly affected by the interplay of the boronic acid component pK_a and environmental pH. In a further step, precise controllability of network relaxation times has been achieved by Yesilyurt *et al.*[36,162] In their approach, tuning of the mechanical properties is achieved by variations in the pK_a through the use of different boronic

acid derivatives that are linked to the polymer backbone. A comprehensive study by Marco-Dufort *et al.*[41] links the macroscopic properties of dynamic boronic ester tetra-PEG gels to the underlying possible reaction pathways, thereby including several thermodynamic conditions. Quantification of equilibrium binding constants as well as kinetic reaction rates allows for a rational design and exact predictions of material properties if the chemistry of the dynamic covalent bond is thoroughly understood. In addition, the shear-thinning behavior and excellent cyto-compatibility of such dynamic covalent hydrogels can be used as injectable drug deliverers with various responsivenesses (glucose, pH) in biological material engineering.[36,163]

1.4 Light Scattering on Polymer Gels

Light scattering is a powerful non-invasive characterization technique to uncover and simultaneously investigate structural and dynamic properties of various materials, including the determination of particle size distributions in solution,[164,165] self-interactions of biologically active molecules,[166,167] or micelle formation of block copolymers.[168,169] Over the last three decades, the field of light scattering on soft matter, more specifically on polymer gels, has rapidly emerged.

In general, elastic scattering of radiation occurs due to spatio-temporal density fluctuations, that is in polymer gels provoked by the thermal motion of polymer strands (chains between two junctions) and the junctions themselves. On length scales between 1–100 nm, scattering techniques such as neutron scattering, X-ray scattering, or light scattering with their characteristic wavelengths λ determine the accessible q-range with $q = \frac{4\pi \sin(\frac{\theta}{2})}{\lambda}$ being the scattering vector. Combination of these methods covers a broad length scale including molecular size ranges of correlated single strand relaxation (1–10 nm) up to the detection of larger heterogeneities (10–100 nm).[170]

The scattered light in gels at a certain position (scattering vector q) is caused by the overall concentration fluctuations $\delta c(q,t)$ that are constituted by mainly two superimposing types: time-dependent thermodynamic concentration fluctuations $\delta c_F(q,t)$, and time-independent frozen concentration fluctuations of inhomogeneities $\delta c_C(q)$.

$$\delta c(q,t) = \delta c_F(q,t) + \delta c_C(q) \tag{3}$$

Given the fact that one component is time-depending ($\delta c_F(q,t)$) while the other one is not ($\delta c_C(q)$), there are statistically two averages feasible. Averaging a gel property (e.g. scattering intensity) over all possible gel positions yields the ensemble average $\langle \quad \rangle_E$, whereas averaging over time results in the

time average $\langle \quad \rangle_T$.[171] Since a fluctuating chain is represented by a full ensemble of spatial configurations, the time-average of these dynamic concentration fluctuations equals 0 ($\delta c_F(q,t) = 0$). By contrast, only the ensemble-average of all time-independent frozen fluctuations is zero ($\delta c_C(q) = 0$) as the Brownian motion of these scatterers is confined around an average position. The time-dependent correlation function of a given position can therefore only contain information about a configurational sub-ensemble. Consequentially, the ensemble average of the intensity does not equal the time average $\langle \quad \rangle_E \neq \langle \quad \rangle_T$, a criterion that indicates non-ergodicity. Thereby, the subscripts E and T denote the ensemble and time average, respective.

The two types of concentration fluctuations manifest themselves in two intensity contributions: the fluidic contribution $\langle I_F \rangle_T$ (blue line in the bottom graphic of **Figure 1-4**) and the static (constant) contribution $I_{C,p}$ (green line in the bottom graphic of **Figure 1-4**) that additively superimpose at each gel position.

$$\langle I \rangle_E = \langle I_F \rangle_T + I_{C\,p} \tag{4}$$

It should be noted that the lower boundary intensity $\langle I_F \rangle_T$ of a polymer gel is identical to the average intensity that is induced by an equi-concentrated but non-crosslinked solution of the same polymer building blocks ($\langle I_F \rangle_T = \langle I \rangle_T$).[8] The excess scattering is caused by structural heterogeneities or local confinement and limited diffusion of polymer segments. Hence, gel scattering is significantly enhanced compared to solution scattering.

In *static* light scattering on non-ergodic media, a typical speckle pattern is obtained if the time-average scattering intensities $\langle I \rangle_{T,p}$ of a set of randomly chosen sample positions is plotted (**Figure 1-4**). In addition, each scattering angle q provides a different specific pattern. Gel regions with large density fluctuations exhibit high intensities whereas positions with lower densities generally show lower scattering intensities. The speckle patterns are further characterized by a lower cut-off intensity $\langle I_F \rangle_T$ that contains only contributions from the fluidic concentration fluctuations and is concentration- and temperature-dependent. To calculate this cut-off intensity $\langle I_F \rangle_T$, a probability histogram of all occurring intensities $P(\langle I \rangle_{T,p})$ is fitted with the following equation (5):[171]

$$P(\langle I \rangle_{T\,p}) \approx \mathrm{H}(\langle I \rangle_{T,p} - \langle I_F \rangle_T) \cdot \exp\left(-\frac{\langle I \rangle_{T,p} - \langle I_F \rangle_T}{\langle I \rangle_E - \langle I_F \rangle_T}\right) \tag{5}$$

with the Heaviside step function $H\left(\langle I \rangle_{T,p} - \langle I_F \rangle_T\right) = 0$ if $\langle I \rangle_{T,p} - \langle I_F \rangle_T < 0$ and $H\left(\langle I \rangle_{T\,p} - \langle I_F \rangle_T\right) = 1$ if $\langle I \rangle_{T,p} - \langle I_F \rangle_T \geq 0$. The constant contribution $I_{C\,p}$ to the overall scattering intensity contains information about the static correlation length Ξ of the frozen heterogeneities. This excess scattering is calculated according to equation (4) by subtracting the fluidic contribution $\langle I_F \rangle_T$ from the

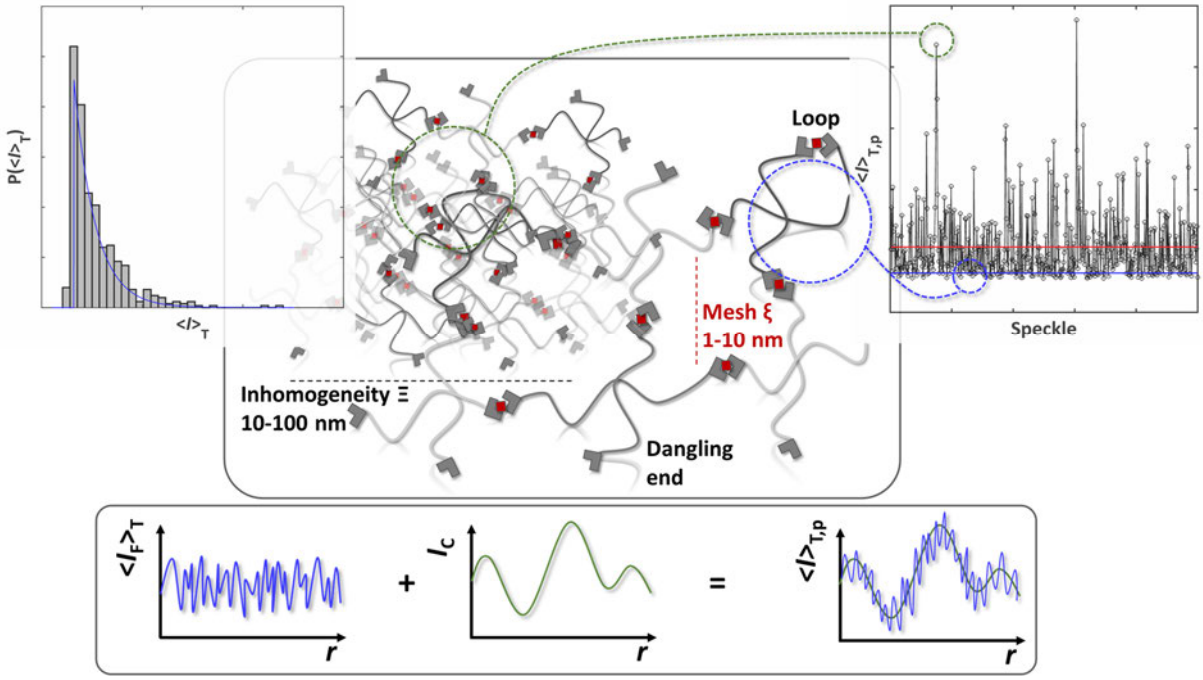

Figure 1-4. Schematic representation of a supramolecular polymer network with its specific structural characteristics such as inhomogeneities, and network defects (e. g. dangling ends end loops). A typical speckle pattern and intensity probability histogram is shown with the lower cut-off intensity (blue lines) and the ensemble-average intensity (red line). The two additive contributions to gel scattering (fluidic (blue) and static (green)) are depicted in the bottom graphs, adapted from ref. [171]

ensemble-average $\langle I \rangle_E$ at each angle separately. To calculate Ξ, an approach by Debye and Bueche can be used (6).[172] The q-dependent excess ratio R_{Excess} (that is corresponding to $I_{C,p}$) is described as

$$R_{Excess}(q) = \frac{4\pi K \Xi^3 \langle n^2 \rangle}{\left(1 + q^2 \Xi^2\right)^2} \tag{6}$$

with the optical constant K. Linearization of equation (6) yields the static correlation length Ξ and the mean-square fluctuation of the refractive index $\langle n^2 \rangle$.

A first approach to interpret *dynamic* scattering data and the concept of non-ergodicity (colloids, glasses, polymer gels)[173–175] has been published in 1989 by Pusey and van Megen.[176] It should be kept in mind that a single DLS experiment provides the time-averaged intensity correlation function $g^{(2)}(q,\tau)$:

$$g^{(2)}_{ergodic}(q,\tau) - 1 = \frac{\langle I(q,0)\, I(q,\tau) \rangle_T}{\langle I(q,0) \rangle_T^2} \tag{7}$$

that only equals the ensemble-averaged correlation function if an ergodic medium ($\langle \quad \rangle_E = \langle \quad \rangle_T$) is observed. An example for ergodic media includes a dilute or semi-dilute polymer solution with completely dissolved chains. In contrast to that, if frozen structure parts with a constant and time-independent electric scattering field become dominant, the time-average intensity $\langle I(q) \rangle_T$ is expressed by the sum of the time-average fluctuating part $\langle I_F(q) \rangle_T$ and the time-independent constant part $I_C(q)$:

$$\langle I(q)\rangle_T = \langle I_F(q)\rangle_T + I_C(q) \tag{8}$$

Equation (7) must then be extended to

$$g^{(2)}_{\text{non-ergodic}}(q,\tau) - 1 = \frac{\langle E_F(q,0)\, E_F^*(q,\tau)\rangle_T^2 + 2\, I_C(q)\langle E_F(q,0)\, E_F^*(q,\tau)\rangle_T}{\langle I(q,0)\rangle_T^2} \tag{9}$$

with the fluctuating field $E_F(q,\tau)$ and its complex conjugate $E_F^*(q,\tau)$.[175] The frozen structural heterogeneities do not exhibit all Gaussian configurations within the experimental time window thereby leading to an additional non-decaying component in the correlation function. Equation (9) can therefore be re-phrased as

$$\begin{aligned} g^{(2)}_{\text{non-ergodic}} - 1 = {} & Y^2\left[\left(f_{\text{non-ergodic}}(q,\tau)\right)^2 - \left(f_{\text{non-ergodic}}(q,\infty)\right)^2\right] \\ & + 2Y(1-Y)\left[f_{\text{non-ergodic}}(q,\tau) - f_{\text{non-ergodic}}(q,\infty)\right] \end{aligned} \tag{10}$$

with the non-ergodic correlation function $f_{\text{non-ergodic}}(q,\tau)$, and $Y = \langle I\rangle_E/\langle I\rangle_T$ being the ratio of the ensemble average and the time average intensity.[171] A comparison of all ensemble and intensity average

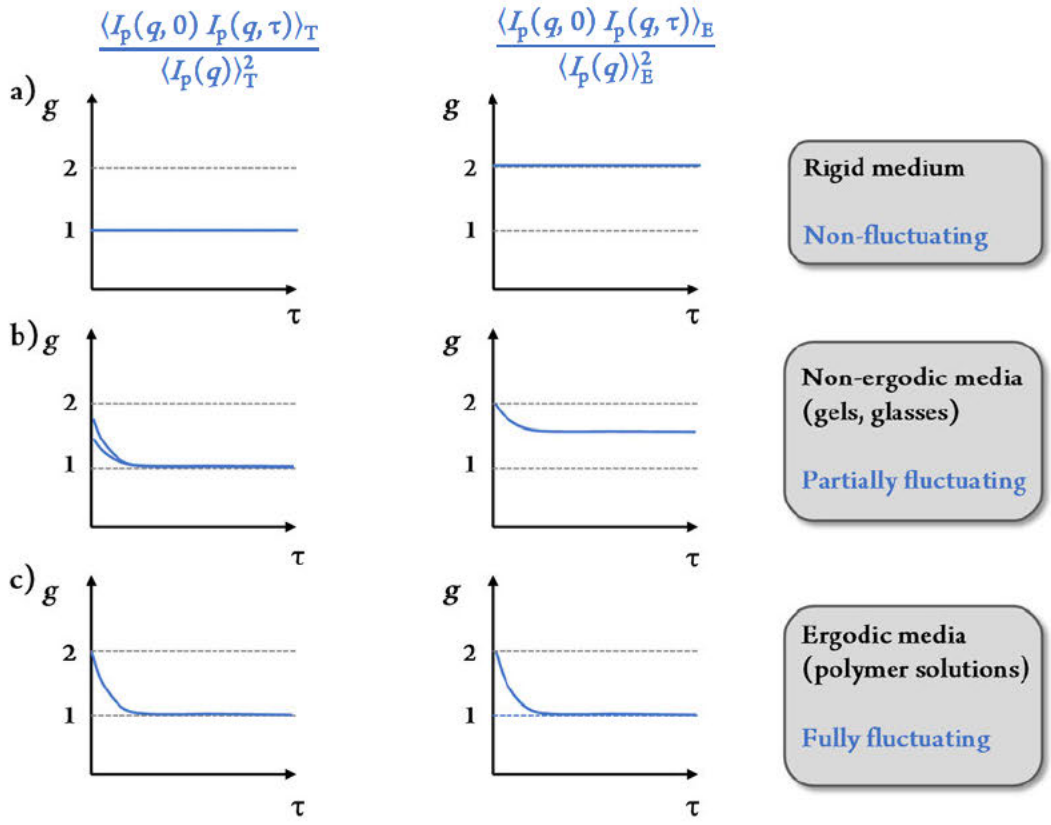

Figure 1-5. Comparison of the time average intensity correlation function and the ensemble average intensity correlation function, adapted with permission from Pusey, P. N.; van Megen, W., *Physica A: Statistical Mechanics and its Applications* **1989**, *157*, 705–741. Copyright 1989 published by Elsevier B.V. a) Rigid media do not show a decay as no time-dependent density fluctuations can be observed. b) In non-ergodic media, frozen-in components prevent a full decay of the ensemble average intensity function and further lead to an amplitude decrease in the time average function. c) A full decay and identical functions are observed in ergodic media as a full ensemble of Gaussian fluctuations is recorded during the correlation time τ.

functions is shown in **Figure 1-5**.[176] The intensity of a rigid medium with non-fluctuating components (a) does not decay as no density fluctuations occur. As $I_p(q,0) = I_p(q,\tau) = I_p(q)$ and therefore $\frac{\langle I_p(q)^2\rangle}{\langle I_p(q)\rangle^2}$, a constant value of 1 is obtained. In contrast to that, if an ergodic medium is observed (c), the time average and the ensemble average intensity correlation functions decay in an identical way. Non-ergodic media exhibit contributions from both afore-mentioned border cases (b). First, the ensemble average does not fully decay to a value of 1 due to the local confinement and restricted motion. Second, as only a sub-ensemble of possible configurations is observed in the time-averaged function, this lack of full Gaussian variable exploration results in a decreased initial amplitude but a complete decay to 1. To fully describe the configuration space, an enormous large number of position-dependent time-average functions have to be recorded and normalized.

In 1991, the partial heterodyne method was introduced by Joosten and co-workers in order to analyze the complex correlation functions coming along with such non-ergodic media.[177] In a polymer network constituted of polymer chains with segmental motion and spatially restricted crosslinks, two types of scattering contributions are present (**Figure 1-6**). First, heterodyne scattering occurs if the constant scattering field of heterogeneities or crosslinks that are assumed as local oscillators, interferes with the exponentially decaying field of a thermally activated moving chain ($\exp(-Dq^2\tau)$). Second, homodyne scattering describes the superposition of two decaying fields, induced by segmental fluctuations of two polymer chains. The field correlation function $g^{(1)}(q,\tau)$ is the product of the superimposing fields and thus becomes $\exp\left(-Dq^2\tau\right)\cdot\exp\left(-Dq^2\tau\right) = \exp(-2Dq^2\tau)$ in the case of pure homodyne scattering and $\exp(-Dq^2\tau)\cdot 1 = \exp(-Dq^2\tau)$ in the case of pure heterodyne scattering. Depending on the observed gel position, different proportions of both scattering types occur. According to Joosten *et al.*,[177] a set of intensity correlation functions $g^{(2)}(q,\tau)$ of a stochastic amount of arbitrarily chosen sample positions p contains all information to fully describe the ensemble average dynamics:

$$g^{(2)}_{T,p} - 1 = \frac{\langle I(t)I(t+\tau)\rangle_{T,p}}{\langle I(t)\rangle^2_{T,p}} = \left[X_p g^{(1)}_F(q,\tau)\right]^2 + 2X_p(1-X_p)g^{(1)}_F(q,\tau) \qquad (11)$$

with the homodyne scattering contribution X_p being the ratio of the time-average intensity $\langle I_F\rangle_T$ provoked by the *thermal fluctuating component*, and the total intensity of the chosen position $\langle I\rangle_{T,p}$. $g^{(1)}_F(q,\tau)$ denotes the corresponding field correlation function. If pure homodyne scattering is observed, X_P equals 1 and equation (11) consequentially simplifies to become the Siegert relation $g^{(1)}(q,\tau) = \sqrt{g^{(2)}(q,\tau) - 1}$ that is generally not applicable to treat data from non-ergodic media. The

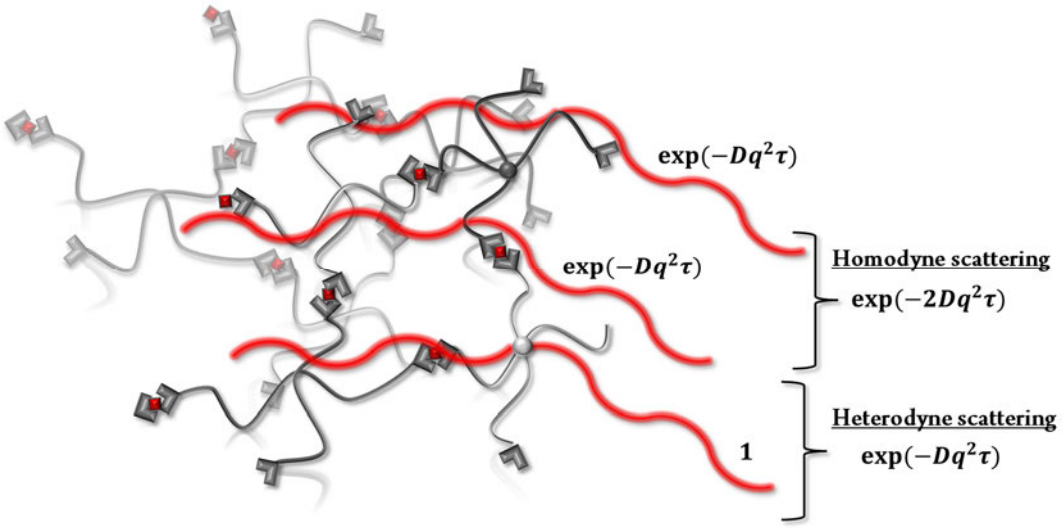

Figure 1-6. Schematic representation of the origin of homodyne and heterodyne scattering contributions in non-ergodic media, adapted from ref. [171]

amplitudes σ^2 of the correlation functions $g^{(2)}(q,\tau)$ are strongly position-dependent and can be expressed by

$$\sigma_p^2 = g_{T,p}^{(2)}(0) - 1 = X_p(2 - X_p) \tag{12}$$

Correlation functions of positions with a pronounced heterodyne scattering contribution exhibit amplitudes that are far lower than unity. Equally to

$$g_F^{(1)}(q,\tau) = \exp(-D_{HT}\, q^2\tau) \tag{13}$$

and under the assumption that the fluctuating part $g_F^{(1)}(q,\tau)$ is ergodic, a partial heterodyne diffusion coefficient D_{HT} is obtained. The contributions of homodyne and heterodyne scattering also impact D_{HT} and the following relation becomes valid:

$$D_{HT} = (2 - X_p) D_{A,p} \tag{14}$$

with the apparent collective gel diffusion coefficient D_A. It is calculated by a linearized form of equation (14):[178,179]

$$\frac{\langle I\rangle_{T,p}}{D_{A,p}} = \frac{2}{D_{HT}}\langle I\rangle_{T,p} - \frac{\langle I_F\rangle_T}{D_{HT}} \tag{15}$$

Plotting the quotient $\frac{\langle I\rangle_{T,p}}{D_{A,p}}$ vs. $\langle I\rangle_{T,p}$ provides $\langle I_F\rangle_T$ from the ordinate intercept and D_{HT} from the slope. For gels or solutions in the semi-dilute concentration regime ($c > c^*$), this diffusion coefficient describes the collective motion of polymer chains originated by internal chain modes. Via a Stokes-Einstein analogue (16), the *dynamic correlation length* ξ of the polymer blob relaxation can be estimated by

$$\xi = \frac{k_B T}{6\pi\eta D_{HT}} \tag{16}$$

with the Boltzmann constant k_B, the temperature T, and the solution viscosity η. This correlation length is commonly related to the mesh size of a polymer network. However, Tsuji *et al.*[180] used a broad library of tetra-PEG model networks by combining stars with linear chains of different molecular weights to compare a calculated network mesh size (geometric tree-like approximation) with the size of a correlation blob[181] (represented by ξ obtained from DLS, mostly also referred to as mesh size) and the size of an elastic blob[182] (obtained by rheology). They found that the correlation blobs ξ exhibit the same size regardless of the network composition (mixtures of mutual reactive linear and star precursors with different molecular weights) or end group conversion and are only depending on the total polymer concentration with a scaling law of $\xi \sim \phi^{-0.56}$. This finding strongly underlines that the mesh size obtained by DLS must be critically evaluated thereby keeping in mind that it actually displays the size of a thermally fluctuating correlation blob.

Since the implementation of these ground-breaking analysis methods, light scattering has become a valuable tool in the field of polymer gel characterization, offering both: insights in the structural as well as the dynamic properties of such soft matter materials. For example, simultaneous DLS and SLS and decomposition of the fluidic and static contributions has been applied to investigate sol–gel transitions in reversible poly(vinyl alcohol) gels.[183] Similar to their chemical counterparts, the appearance of distinct speckle patterns bespeaks the existence of frozen heterogeneities even in such highly dynamic systems. Further, analysis of ξ is used to unravel different mechanisms in the sol–gel transitions induced either by a concentration or a temperature change.

Numerous studies followed, thereby exploring structural refined and more elaborated networks, e.g. the gelation of critical tetra-arm PEG clusters[184] or incorporated thermosensitive building blocks into a regularly arranged tetra-arm PEG network.[185] The latter work investigated the change in network structure and chain dynamics of a co-network depending on the fraction of an added thermoresponsive tetra-arm copolymer that successively changes its conformation upon temperature increase above its lower critical solution temperature (LCST). Contributions of the temperature-induced formation of hydrophobic microdomains to the correlation functions and overall intensities were decomposed.

2 SCIENTIFIC GOALS

Metallo-supramolecular polymer networks provide a versatile platform for the development and engineering of new materials with various properties, as well as the exploration of fundamental structure–property–relationships and establishment of theoretical concepts. A general strategy towards engineering of new soft matter materials implies a gradual approach: comprehensive analysis of all network-forming components, establishment of methods and characterization techniques, understanding of fundamental model systems to postulate theories, and finally, incorporation of modifications into the model system to achieve desired properties. This thesis follows a similar approach and focuses on networks composed of transiently connected star-shaped macromolecules as a model system.
These highly dynamic networks are dominated by an interplay between internal structure, dynamics and mechanical response as schematically illustrated in **Figure 1-3**. All three sections (mechanics, dynamics, structure) are mainly influenced by polymeric contributions (polymer architecture, concentration, solvent interactions) as well as crosslink contributions (crosslink chemistry, thermodynamics, kinetics, type of association), thereby generating a complex and interdependent research field.
To comprehensively understand the final properties of a network resulting from the interplay of the above-mentioned characteristics (dynamics, structure, mechanical response), it is necessary to take a step back and independently unravel the influence of each structural component, even in the unconnected solution state.

In the first part of this thesis, the polymeric contributions are investigated in terms of characterizing the scattering behavior of unconnected semi-dilute polymer solutions. The unambiguous assignment of light scattering relaxation modes is of major importance and serves as a base for further understanding additional scattering contributions if, in a further step, network characterization will be focused on. Light scattering is a powerful tool to simultaneously investigate the structure and relaxation processes in soft matter. Whereas there exists a deep understanding of light scattering on permanent connected networks, the scattering characteristics of transient networks and their analysis is less explored. One aim of the thesis is to contribute to this methodical field and gain further knowledge on gel scattering thereby taking advantage of the transient star-polymer model system with independently tunable parameters such as the network strength. As the network-forming polymer backbone remains unmodified and therefore exhibits comparable scattering contributions, the impact of the varied network

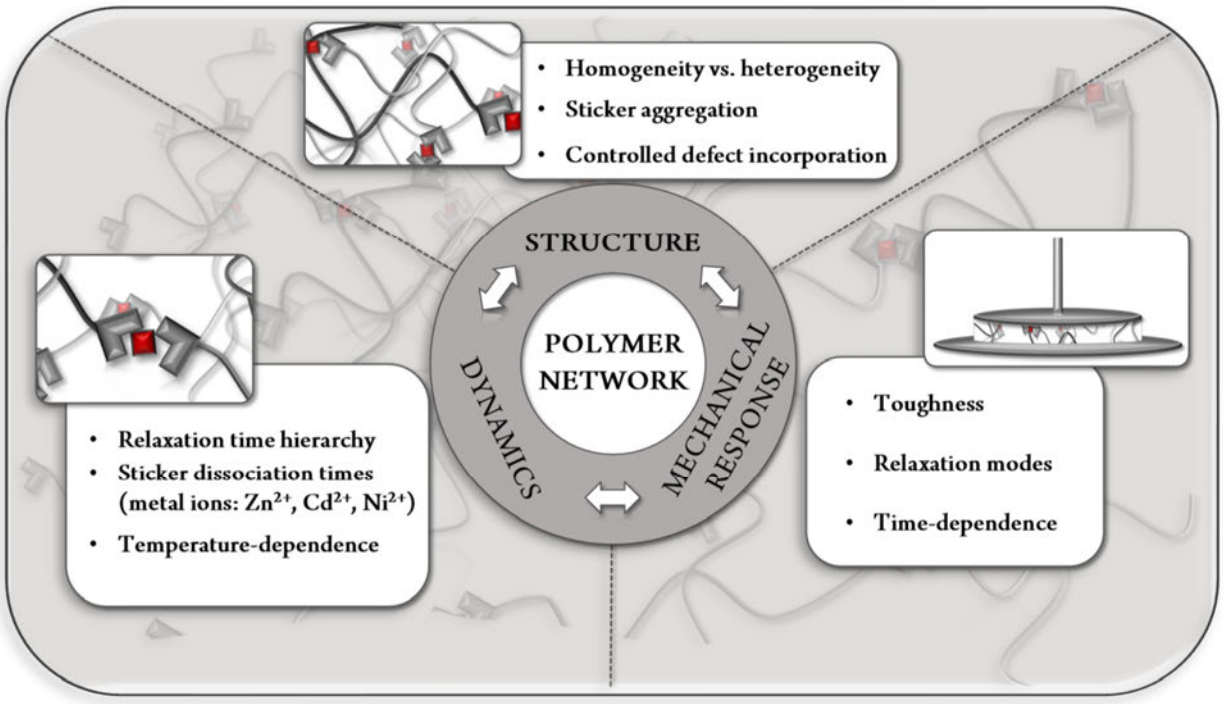

Figure 2-1. Schematic illustration of the interplay between structure, dynamics, and mechanical response in a supramolecular polymer network.

strength on the correlation functions and scattering intensities is independently explored. The dynamic relaxation modes are further related to the macroscopic viscoelasticity of the networks.

Despite many theoretical models and predictions, it remains challenging to predict final network properties starting from only knowing the properties of the isolated polymer building blocks and the chemistry of their connecting junctions. However, this interrelation is especially required in the area of smart material design if specific and complex demands such as sustainability or tailored multi-functionality are addressed. Controlling and pre-programming the network topology from a molecular perspective and therefore affecting the material properties at an early engineering stage is a main goal. Dynamic networks offer an intricated synergy of relaxation time scales, and their comprehensive understanding is essential if unravelling the molecular mechanisms is targeted.

For this purpose, a multitude of measurement techniques covering broad length and time scales to access both, temporal and structural characteristics at various temperatures is required. A further aim of this thesis addresses this challenge and interrelates the experimental results of several characterization methods, such as FRS, DLS & SLS, rheology, and UV-Vis spectroscopy. Again, a model type network consisting of monodisperse tetra-arm polymer molecules with telechelic sticker functionalities is chosen, with reversible zinc-terpyridine junctions providing distinct kinetic parameters.

Single sticker kinetics in dilute conditions are compared with relaxation times of the network in the swollen state and a complex hierarchy of viscoelastic and several diffusive motion processes is related to the elastic network response.

A thorough time- and length scale depending characterization of the structure and dynamics of transient model network opens up opportunities to systematically manipulate the chemistry of single building block macromolecules and therefore achieve an impact on the overall network properties. Many natural as well as synthetic networks exhibit structural irregularities, coming along with two main challenges: the synthesis-based complexity of controlling the generation and distribution of defects within the network and hence, the identification of tangible effects on the network properties.
As a further aim of this thesis, the influence of intentionally incorporated defects on the network dynamics and diffusive permeability is investigated by such a controlled manipulation of the network structure. The occurrence of structural defects is quantified and related to the self-diffusive properties as well as the macroscopic network response.

3 REFERENCES

(1) Staudinger, H. Über Polymerisation. *Ber. dtsch. Chem. Ges. A/B* **1920**, *53*, 1073–1085.

(2) Jenkins, A. D.; Kratochvíl, P.; Stepto, R. F. T.; Suter, U. W. Glossary of Basic Terms in Polymer Science. *Pure & Appl. Chem.* **1996**, *68*, 2287–2311.

(3) Wang, W.; Narain, R.; Zeng, H. Rational Design of Self-Healing Tough Hydrogels: A Mini Review. *Frontiers in chemistry* **2018**, *6*, 497.

(4) Mondal, S.; Das, S.; Nandi, A. K. A review on recent advances in polymer and peptide hydrogels. *Soft matter* **2020**, *16*, 1404–1454.

(5) Gennes, P.-G. de. Soft Matter (Nobel Lecture). *Angew. Chem. Int. Ed.* **1992**, *31*, 842–845.

(6) Hild, G. Model networks based on `endlinking' processes: synthesis, structure and properties. *Progress in Polymer Science* **1998**, *23*, 1019–1149.

(7) Fujiyabu, T.; Yoshikawa, Y.; Chung, U.-i.; Sakai, T. Structure-property relationship of a model network containing solvent. *Science and technology of advanced materials* **2019**, *20*, 608–621.

(8) Shibayama, M.; Norisuye, T. Gel Formation Analyses by Dynamic Light Scattering. *BCSJ* **2002**, *75*, 641–659.

(9) Ikkai, F.; Shibayama, M. Inhomogeneity control in polymer gels. *J. Polym. Sci. Part B: Polym. Phys.* **2005**, *43*, 617–628.

(10) Gu, Y.; Zhao, J.; Johnson, J. A. Polymer Networks: From Plastics and Gels to Porous Frameworks. *Angew. Chem. Int. Ed.* **2020**, *59*, 5022–5049.

(11) Jangizehi, A.; Schmid, F.; Besenius, P.; Kremer, K.; Seiffert, S. Defects and defect engineering in Soft Matter. *Soft matter* **2020**, *16*, 10809–10859.

(12) Breul, K.; Kissel, S.; Seiffert, S. Sticker Multivalency in Metallo-supramolecular Polymer Networks. *Macromolecules* **2021**, *54*, 8407–8422.

(13) Lange, F.; Schwenke, K.; Kurakazu, M.; Akagi, Y.; Chung, U.-i.; Lang, M.; Sommer, J.-U.; Sakai, T.; Saalwächter, K. Connectivity and Structural Defects in Model Hydrogels: A Combined Proton NMR and Monte Carlo Simulation Study. Macromolecules, 44(24), 9666-9674. *Macromolecules* **2011**, *44*, 9666–9674.

(14) Saalwächter, K.; Seiffert, S. Dynamics-based assessment of nanoscopic polymer-network mesh structures and their defects. *Soft matter* **2018**, *14*, 1976–1991.

(15) Zhou, H.; Woo, J.; Cok, A. M.; Wang, M.; Olsen, B. D.; Johnson, J. A. Counting primary loops in polymer gels. *Proceedings of the National Academy of Sciences of the United States of America* **2012**, *109*, 19119–19124.

(16) Gu, Y.; Kawamoto, K.; Zhong, M.; Chen, M.; Hore, M. J. A.; Jordan, A. M.; Korley, L. T. J.; Olsen, B. D.; Johnson, J. A. Semibatch monomer addition as a general method to tune and enhance the mechanics of polymer networks via loop-defect control. *Proceedings of the National Academy of Sciences of the United States of America* **2017**, *114*, 4875–4880.

(17) Kawamoto, K.; Zhong, M.; Wang, R.; Olsen, B. D.; Johnson, J. A. Loops versus Branch Functionality in Model Click Hydrogels. *Macromolecules* **2015**, *48*, 8980–8988.

(18) Zhong, M.; Wang, R.; Kawamoto, K.; Olsen, B. D.; Johnson, J. A. Quantifying the impact of molecular defects on polymer network elasticity. *Science (New York, N.Y.)* **2016**, *353*, 1264–1268.

(19) Jangizehi, A.; Ahmadi, M.; Seiffert, S. Emergence, evidence, and effect of junction clustering in supramolecular polymer materials. *Mater. Adv.* **2021**, *2*, 1425–1453.

(20) Lucca Freitas, L. de; Stadler, R. Thermoplastic elastomers by hydrogen bonding 4. Influence of hydrogen bonding on the temperature dependence of the viscoelastic properties. *Colloid Polym Sci* **1988**, *266*, 1095–1101.

(21) Wu, S.; Liu, S.; Zhang, Z.; Chen, Q. Dynamics of Telechelic Ionomers with Distribution of Number of Ionic Stickers at Chain Ends. *Macromolecules* **2019**, *52*, 2265–2276.

(22) Mahmad Rasid, I.; Do, C.; Holten-Andersen, N.; Olsen, B. D. Effect of sticker clustering on the dynamics of associative networks. *Soft matter* **2021**, *17*, 8960–8972.

(23) Rossow, T.; Seiffert, S. Supramolecular polymer gels with potential model-network structure. *Polym. Chem.* **2014**, *5*, 3018.

(24) Chen, Q.; Tudryn, G. J.; Colby, R. H. Ionomer dynamics and the sticky Rouse model. *Journal of Rheology* **2013**, *57*, 1441–1462.

(25) Tang, S.; Wang, M.; Olsen, B. D. Anomalous self-diffusion and sticky Rouse dynamics in associative protein hydrogels. *Journal of the American Chemical Society* **2015**, *137*, 3946–3957.

(26) Rubinstein, M.; Semenov, A. N. Thermoreversible Gelation in Solutions of Associating Polymers. 2. Linear Dynamics. *Macromolecules* **1998**, *31*, 1386–1397.

(27) Rubinstein, M.; Semenov, A. N. Dynamics of Entangled Solutions of Associating Polymers. *Macromolecules* **2001**, *34*, 1058–1068.

(28) Leibler, L.; Rubinstein, M.; Colby, R. H. Dynamics of reversible networks. *Macromolecules* **1991**, *24*, 4701–4707.

(29) Cates, M. E. Reptation of living polymers: dynamics of entangled polymers in the presence of reversible chain-scission reactions. *Macromolecules* **1987**, *20*, 2289–2296.

(30) Jiang, N.; Zhang, H.; Yang, Y.; Tang, P. Molecular dynamics simulation of associative polymers: Understanding linear viscoelasticity from the sticky Rouse model. *Journal of Rheology* **2021**, *65*, 527–547.

(31) Amin, D.; Likhtman, A. E.; Wang, Z. Dynamics in Supramolecular Polymer Networks Formed by Associating Telechelic Chains. *Macromolecules* **2016**, *49*, 7510–7524.

(32) Metri, V.; Louhichi, A.; Yan, J.; Baeza, G. P.; Matyjaszewski, K.; Vlassopoulos, D.; Briels, W. J. Physical Networks from Multifunctional Telechelic Star Polymers: A Rheological Study by Experiments and Simulations. *Macromolecules* **2018**, *51*, 2872–2886.

(33) Ahmadi, M.; Hawke, L. G. D.; Goldansaz, H.; van Ruymbeke, E. Dynamics of Entangled Linear Supramolecular Chains with Sticky Side Groups: Influence of Hindered Fluctuations. *Macromolecules* **2015**, *48*, 7300–7310.

(34) Semenov, A. N.; Rubinstein, M. Dynamics of Entangled Associating Polymers with Large Aggregates. *Macromolecules* **2002**, *35*, 4821–4837.

(35) Stukalin, E. B.; Cai, L.-H.; Kumar, N. A.; Leibler, L.; Rubinstein, M. Self-Healing of Unentangled Polymer Networks with Reversible Bonds. *Macromolecules* **2013**, *46*.

(36) Yesilyurt, V.; Webber, M. J.; Appel, E. A.; Godwin, C.; Langer, R.; Anderson, D. G. Injectable Self-Healing Glucose-Responsive Hydrogels with pH-Regulated Mechanical Properties. *Adv. Mater.* **2016**, *28*, 86–91.

(37) Cromwell, O. R.; Chung, J.; Guan, Z. Malleable and Self-Healing Covalent Polymer Networks through Tunable Dynamic Boronic Ester Bonds. *J. Am. Chem. Soc.* **2015**, *137*, 6492–6495.

(38) Tang, S.; Olsen, B. D. Relaxation Processes in Supramolecular Metallogels Based on Histidine–Nickel Coordination Bonds. *Macromolecules* **2016**, *49*, 9163–9175.

(39) Rao, A.; Yao, H.; Olsen, B. D. Bridging dynamic regimes of segmental relaxation and center-of-mass diffusion in associative protein hydrogels. *Phys. Rev. Research* **2020**, *2*.

(40) Danielsen, S. P. O.; Beech, H. K.; Wang, S.; El-Zaatari, B. M.; Wang, X.; Sapir, L.; Ouchi, T.; Wang, Z.; Johnson, P. N.; Hu, Y.*; et al.* Molecular Characterization of Polymer Networks. *Chemical reviews* **2021**, *121*, 5042–5092.

(41) Marco-Dufort, B.; Iten, R.; Tibbitt, M. W. Linking Molecular Behavior to Macroscopic Properties in Ideal Dynamic Covalent Networks. *J. Am. Chem. Soc.* **2020**, *142*, 15371–15385.

(42) Hackelbusch, S.; Rossow, T.; van Assenbergh, P.; Seiffert, S. Chain Dynamics in Supramolecular Polymer Networks. *Macromolecules* **2013**, *46*, 6273–6286.

(43) Rossow, T.; Habicht, A.; Seiffert, S. Relaxation and Dynamics in Transient Polymer Model Networks. *Macromolecules* **2014**, *47*, 6473–6482.

(44) Nicolella, P.; Lauxen, D.; Ahmadi, M.; Seiffert, S. Reversible Hydrogels with Switchable Diffusive Permeability. *Macromol. Chem. Phys.* **2021**, *222*, 2100076.

(45) Mahmad Rasid, I.; Holten-Andersen, N.; Olsen, B. D. Anomalous Diffusion in Associative Networks of High-Sticker-Density Polymers. *Macromolecules* **2021**, *54*, 1354–1365.

(46) Tang, S.; Habicht, A.; Li, S.; Seiffert, S.; Olsen, B. D. Self-Diffusion of Associating Star-Shaped Polymers. *Macromolecules* **2016**, *49*, 5599–5608.

(47) Ramirez, J.; Dursch, T. J.; Olsen, B. D. A Molecular Explanation for Anomalous Diffusion in Supramolecular Polymer Networks. *Macromolecules* **2018**, *51*, 2517–2525.

(48) Rao, A.; Ramírez, J.; Olsen, B. D. Mechanisms of Self-Diffusion of Linear Associative Polymers Studied by Brownian Dynamics Simulation. *Macromolecules* **2021**, *54*, 11212–11227.

(49) Rapp, P. B.; Omar, A. K.; Shen, J. J.; Buck, M. E.; Wang, Z.-G.; Tirrell, D. A. Analysis and Control of Chain Mobility in Protein Hydrogels. *J. Am. Chem. Soc.* **2017**, *139*, 3796–3804.

(50) Rapp, P. B.; Omar, A. K.; Silverman, B. R.; Wang, Z.-G.; Tirrell, D. A. Mechanisms of Diffusion in Associative Polymer Networks: Evidence for Chain Hopping. *Journal of the American Chemical Society* **2018**, *140*, 14185–14194.

(51) Li, C.-H.; Zuo, J.-L. Self-Healing Polymers Based on Coordination Bonds. *Adv. Mater.* **2020**, *32*, e1903762.

(52) Christoff-Tempesta, T.; Lew, A. J.; Ortony, J. H. Beyond Covalent Crosslinks: Applications of Supramolecular Gels. *Gels (Basel, Switzerland)* **2018**, *4*.

(53) Jangizehi, A.; Seiffert, S. Salt partitioning in ionized, thermo-responsive hydrogels: perspective to water desalination. *The Journal of Chemical Physics* **2021**, *154*, 144902.

(54) Nabeel, F.; Rasheed, T.; Bilal, M.; Li, C.; Yu, C.; Iqbal, H. M. N. Bio-Inspired Supramolecular Membranes: A Pathway to Separation and Purification of Emerging Pollutants. *Separation & Purification Reviews* **2020**, *49*, 20–36.

(55) Okesola, B. O.; Smith, D. K. Applying low-molecular weight supramolecular gelators in an environmental setting - self-assembled gels as smart materials for pollutant removal. *Chemical Society reviews* **2016**, *45*, 4226–4251.

(56) Wang, D.; Niu, J.; Wang, Z.; Jin, J. Monoglyceride-based organogelator for broad-range oil uptake with high capacity. *Langmuir* **2015**, *31*, 1670–1674.

(57) Yan, L.; Lv, M.; Su, C.; Zheng, L.; Li, J.; Ye, Z. An efficient supramolecular adsorbent for co-adsorption of dyes and metal ions from wastewater and its application in self-healing materials. *Soft matter* **2017**, *13*, 8772–8780.

(58) Lim, J. Y. C.; Goh, S. S.; Liow, S. S.; Xue, K.; Loh, X. J. Molecular gel sorbent materials for environmental remediation and wastewater treatment. *J. Mater. Chem. A* **2019**, *7*, 18759–18791.

(59) Stengelin, E.; Kuzmina, A.; Beltramo, G. L.; Koziol, M. F.; Besch, L.; Schröder, R.; Unger, R. E.; Tremel, W.; Seiffert, S. Biotherapeutics: Bone Scaffolds Based on Degradable Vaterite/PEG-Composite Microgels (Adv. Healthcare Mater. 11/2020). *Adv. Healthcare Mater.* **2020**, *9*, 2070030.

(60) Saunders, L.; Ma, P. X. Self-Healing Supramolecular Hydrogels for Tissue Engineering Applications. *Macromolecular bioscience* **2019**, *19*, e1800313.

(61) Pérez-Pedroza, R.; Ávila-Ramírez, A.; Khan, Z.; Moretti, M.; Hauser, C. A. E. Supramolecular Biopolymers for Tissue Engineering. *Advances in Polymer Technology* **2021**, *2021*, 1–23.

(62) Drury, J. L.; Mooney, D. J. Hydrogels for tissue engineering: scaffold design variables and applications. *Biomaterials* **2003**, *24*, 4337–4351.

(63) Li, L.; Zhang, K.; Wang, T.; Wang, P.; Xue, B.; Cao, Y.; Zhu, L.; Jiang, Q. Biofabrication of a biomimetic supramolecular-polymer double network hydrogel for cartilage regeneration. *Materials & Design* **2020**, *189*, 108492.

(64) Xu, W.; Song, Q.; Xu, J.-F.; Serpe, M. J.; Zhang, X. Supramolecular Hydrogels Fabricated from Supramonomers: A Novel Wound Dressing Material. *ACS applied materials & interfaces* **2017**, *9*, 11368–11372.

(65) Bernhard, S.; Tibbitt, M. W. Supramolecular engineering of hydrogels for drug delivery. *Advanced drug delivery reviews* **2021**, *171*, 240–256.

(66) Saboktakin, M. R.; Tabatabaei, R. M. Supramolecular hydrogels as drug delivery systems. *International journal of biological macromolecules* **2015**, *75*, 426–436.

(67) Skopinska-Wisniewska, J.; La Flor, S. de; Kozlowska, J. From Supramolecular Hydrogels to Multifunctional Carriers for Biologically Active Substances. *International journal of molecular sciences* **2021**, *22*.

(68) Asghari, F.; Samiei, M.; Adibkia, K.; Akbarzadeh, A.; Davaran, S. Biodegradable and biocompatible polymers for tissue engineering application: a review. *Artificial cells, nanomedicine, and biotechnology* **2017**, *45*, 185–192.

(69) Arif, U.; Haider, S.; Haider, A.; Khan, N.; Alghyamah, A. A.; Jamila, N.; Khan, M. I.; Almasry, W. A.; Kang, I.-K. Biocompatible Polymers and their Potential Biomedical Applications: A Review. *Current pharmaceutical design* **2019**, *25*, 3608–3619.

(70) Biswas, P.; Datta, H. K.; Dastidar, P. Multi-NSAID-based Zn(II) coordination complex-derived metallogelators/metallogels as plausible multi-drug self-delivery systems. *Chem. Commun.* [Online early access]. DOI: 10.1039/d1cc05334e. Published Online: Dec. 23, 2021.

(71) He, B.; Zeng, J.; Nie, Y.; Ji, L.; Wang, R.; Li, Y.; Wu, Y.; Li, L.; Wang, G.; Luo, X.*; et al.* In situ gelation of supramolecular hydrogel for anti-tumor drug delivery. *Macromolecular bioscience* **2009**, *9*, 1169–1175.

(72) Rizzo, F.; Kehr, N. S. Recent Advances in Injectable Hydrogels for Controlled and Local Drug Delivery. *Adv. Healthcare Mater.* **2021**, *10*, e2001341.

(73) Billiet, T.; Vandenhaute, M.; Schelfhout, J.; van Vlierberghe, S.; Dubruel, P. A review of trends and limitations in hydrogel-rapid prototyping for tissue engineering. *Biomaterials* **2012**, *33*, 6020–6041.

(74) Wu, H.; Zheng, J.; Kjøniksen, A.-L.; Wang, W.; Zhang, Y.; Ma, J. Metallogels: Availability, Applicability, and Advanceability. *Advanced materials (Deerfield Beach, Fla.)* **2019**, *31*, e1806204.

(75) Cametti, M.; Džolić, Z. New frontiers in hybrid materials: noble metal nanoparticles--supramolecular gel systems. *Chem. Commun.* **2014**, *50*, 8273–8286.

(76) Ossipov, D. A. Bisphosphonate-modified biomaterials for drug delivery and bone tissue engineering. *Expert opinion on drug delivery* **2015**, *12*, 1443–1458.

(77) Xu, Y.; Wu, X.; Wang, S.; Yang, C.; Li, Y.; Cao, Y. Hydroxyapatite Nanoparticle-Crosslinked Peptide Hydrogels for Three-Dimensional Culture and Differentiation of MC3T3-E1 Osteoblasts. *Journal of biomedical nanotechnology* **2019**, *15*, 2351–2362.

(78) Sang, L.; Huang, J.; Luo, D.; Chen, Z.; Li, X. Bone-like nanocomposites based on self-assembled protein-based matrices with Ca2+ capturing capability. *Journal of materials science. Materials in medicine* **2010**, *21*, 2561–2568.

(79) Eckhardt, S.; Brunetto, P. S.; Gagnon, J.; Priebe, M.; Giese, B.; Fromm, K. M. Nanobio silver: its interactions with peptides and bacteria, and its uses in medicine. *Chemical reviews* **2013**, *113*, 4708–4754.

(80) Peurifoy, S. R.; Guzman, C. X.; Braunschweig, A. B. Topology, assembly, and electronics: three pillars for designing supramolecular polymers with emergent optoelectronic behavior. *Polym. Chem.* **2015**, *6*, 5529–5539.

(81) Rogers, J. A.; Someya, T.; Huang, Y. Materials and mechanics for stretchable electronics. *Science (New York, N.Y.)* **2010**, *327*, 1603–1607.

(82) Chen, P.; Li, Q.; Grindy, S.; Holten-Andersen, N. White-Light-Emitting Lanthanide Metallogels with Tunable Luminescence and Reversible Stimuli-Responsive Properties. *J. Am. Chem. Soc.* **2015**, *137*, 11590–11593.

(83) Martínez-Calvo, M.; Kotova, O.; Möbius, M. E.; Bell, A. P.; McCabe, T.; Boland, J. J.; Gunnlaugsson, T. Healable luminescent self-assembly supramolecular metallogels possessing lanthanide (Eu/Tb) dependent rheological and morphological properties. *J. Am. Chem. Soc.* **2015**, *137*, 1983–1992.

(84) Tee, B. C.-K.; Wang, C.; Allen, R.; Bao, Z. An electrically and mechanically self-healing composite with pressure- and flexion-sensitive properties for electronic skin applications. *Nature nanotechnology* **2012**, *7*, 825–832.

(85) Zhang, W.; Yuan, C.; Guo, J.; Qiu, L.; Yan, F. Supramolecular ionic liquid gels for quasi-solid-state dye-sensitized solar cells. *ACS applied materials & interfaces* **2014**, *6*, 8723–8728.

(86) Shi, Y.; Zhou, X.; Zhang, J.; Bruck, A. M.; Bond, A. C.; Marschilok, A. C.; Takeuchi, K. J.; Takeuchi, E. S.; Yu, G. Nanostructured Conductive Polymer Gels as a General Framework Material To Improve Electrochemical Performance of Cathode Materials in Li-Ion Batteries. *Nano letters* **2017**, *17*, 1906–1914.

(87) Wang, Z.; Li, H.; Tang, Z.; Liu, Z.; Ruan, Z.; Ma, L.; Yang, Q.; Wang, D.; Zhi, C. Hydrogel Electrolytes for Flexible Aqueous Energy Storage Devices. *Adv. Funct. Mater.* **2018**, *28*, 1804560.

(88) Li, H.; Ding, Y.; Ha, H.; Shi, Y.; Peng, L.; Zhang, X.; Ellison, C. J.; Yu, G. An All-Stretchable-Component Sodium-Ion Full Battery. *Adv. Mater.* **2017**, *29*.

(89) Kim, C.-C.; Lee, H.-H.; Oh, K. H.; Sun, J.-Y. Highly stretchable, transparent ionic touch panel. *Science (New York, N.Y.)* **2016**, *353*, 682–687.

(90) Ionov, L. Hydrogel-based actuators: possibilities and limitations. *Materials Today* **2014**, *17*, 494–503.

(91) Yang, J.; Sun, X.; Kang, Q.; Zhu, L.; Qin, G.; Chen, Q. Freezing-tolerant and robust gelatin-based supramolecular conductive hydrogels with double-network structure for wearable sensors. *Polymer Testing* **2021**, *93*, 106879.

(92) Li, C.-H.; Wang, C.; Keplinger, C.; Zuo, J.-L.; Jin, L.; Sun, Y.; Zheng, P.; Cao, Y.; Lissel, F.; Linder, C.*; et al.* A highly stretchable autonomous self-healing elastomer. *Nature chemistry* **2016**, *8*, 618–624.

(93) Khare, E.; Holten-Andersen, N.; Buehler, M. J. Transition-metal coordinate bonds for bioinspired macromolecules with tunable mechanical properties. *Nat Rev Mater* **2021**, *6*, 421–436.

(94) Degtyar, E.; Harrington, M. J.; Politi, Y.; Fratzl, P. The mechanical role of metal ions in biogenic protein-based materials. *Angew. Chem. Int. Ed.* **2014**, *53*, 12026–12044.

(95) Holten-Andersen, N.; Harrington, M. J.; Birkedal, H.; Lee, B. P.; Messersmith, P. B.; Lee, K. Y. C.; Waite, J. H. pH-induced metal-ligand cross-links inspired by mussel yield self-healing polymer networks with near-covalent elastic moduli. *Proceedings of the National Academy of Sciences of the United States of America* **2011**, *108*, 2651–2655.

(96) Quan, W.-Y.; Hu, Z.; Liu, H.-Z.; Ouyang, Q.-Q.; Zhang, D.-Y.; Li, S.-D.; Li, P.-W.; Yang, Z.-M. Mussel-Inspired Catechol-Functionalized Hydrogels and Their Medical Applications. *Molecules (Basel, Switzerland)* **2019**, *24*, 2586.

(97) Waite, J. H.; Andersen, N. H.; Jewhurst, S.; Sun, C. Mussel Adhesion: Finding the Tricks Worth Mimicking. *The Journal of Adhesion* **2005**, *81*, 297–317.

(98) Waite, J.H.; Qin, X.-X.; Coyne, K. J. The peculiar collagens of mussel byssus. *Matrix Biology* **1998**, *17*, 93–106.

(99) Varshey, D. B.; Sander, J. R. G.; Friščić, T.; MacGillivray, L. R. Supramolecular Interactions. In *Supramolecular chemistry: From molecules to nanomaterials*; Gale, P. A., Steed, J. W., Eds.; Wiley: Chichester, 2012.

(100) Li, B.; Zhou, X.; Liu, X.; Ye, H.; Zhang, Y.; Zhou, Q. Metal-Organic Gels Derived from Iron(III) and Pyridine Ligands: Morphology, Self-Healing and Catalysis for Ethylene Selective Dimerization. *Chem. Asian J.* **2019**, *14*, 1582–1589.

(101) Rao, Y.-L.; Chortos, A.; Pfattner, R.; Lissel, F.; Chiu, Y.-C.; Feig, V.; Xu, J.; Kurosawa, T.; Gu, X.; Wang, C.*; et al.* Stretchable Self-Healing Polymeric Dielectrics Cross-Linked Through Metal-Ligand Coordination. *J. Am. Chem. Soc.* **2016**, *138*, 6020–6027.

(102) Balkenende, D. W. R.; Coulibaly, S.; Balog, S.; Simon, Y. C.; Fiore, G. L.; Weder, C. Mechanochemistry with metallosupramolecular polymers. *J. Am. Chem. Soc.* **2014**, *136*, 10493–10498.

(103) Burnworth, M.; Tang, L.; Kumpfer, J. R.; Duncan, A. J.; Beyer, F. L.; Fiore, G. L.; Rowan, S. J.; Weder, C. Optically healable supramolecular polymers. *Nature* **2011**, *472*, 334–337.

(104) Lin, W.; Sun, W.; Yang, J.; Shen, Z. Preparation and magnetic properties of novel supramolecular polymeric complexes containing bithiazole rings. *J Appl Polym Sci* **2008**, *110*, 1714–1722.

(105) Andersen, A.; Chen, Y.; Birkedal, H. Bioinspired Metal–Polyphenol Materials: Self-Healing and Beyond. *Biomimetics (Basel, Switzerland)* **2019**, *4*, 30.

(106) Krogsgaard, M.; Nue, V.; Birkedal, H. Mussel-Inspired Materials: Self-Healing through Coordination Chemistry. *Chemistry (Weinheim an der Bergstrasse, Germany)* **2016**, *22*, 844–857.

(107) Yan, Y.-H.; Rong, L.-H.; Ge, J.; Tiu, B. D. B.; Cao, P.-F.; Advincula, R. C. Mussel-Inspired Hydrogel Composite with Multi-Stimuli Responsive Behavior. *Macromol. Mater. Eng.* **2019**, *304*, 1800720.

(108) Zechel, S.; Hager, M. D.; Priemel, T.; Harrington, M. J. Healing through Histidine: Bioinspired Pathways to Self-Healing Polymers via Imidazole–Metal Coordination. *Biomimetics (Basel, Switzerland)* **2019**, *4*, 20.

(109) Chakrabarti, P. Geometry of interaction of metal ions with histidine residues in protein structures. *Protein engineering* **1990**, *4*, 57–63.

(110) Venkataraman, D.; Du, Y.; Wilson, S. R.; Hirsch, K. A.; Zhang, P.; Moore, J. S. A Coordination Geometry Table of the d-Block Elements and Their Ions. *J. Chem. Educ.* **1997**, *74*, 915.

(111) Mozhdehi, D.; Neal, J. A.; Grindy, S. C.; Cordeau, Y.; Ayala, S.; Holten-Andersen, N.; Guan, Z. Tuning Dynamic Mechanical Response in Metallopolymer Networks through Simultaneous Control of Structural and Temporal Properties of the Networks. *Macromolecules* **2016**, *49*, 6310–6321.

(112) Sanoja, G. E.; Schauser, N. S.; Bartels, J. M.; Evans, C. M.; Helgeson, M. E.; Seshadri, R.; Segalman, R. A. Ion Transport in Dynamic Polymer Networks Based on Metal–Ligand Coordination: Effect of Cross-Linker Concentration. *Macromolecules* **2018**, *51*, 2017–2026.

(113) Wei, C.; He, Y.; Shi, X.; Song, Z. Terpyridine-metal complexes: Applications in catalysis and supramolecular chemistry. *Coordination chemistry reviews* **2019**, *385*, 1–19.

(114) Morgan, G. T.; Burstall, F. H. 3. Dehydrogenation of pyridine by anhydrous ferric chloride. *J. Chem. Soc.* **1932**, 20.

(115) Schubert, U. *Modern terpyridine chemistry*; Wiley-VCH: Weinheim, 2006.

(116) Ludlow, J. M.; Guo, Z.; Schultz, A.; Sarkar, R.; Moorefield, C. N.; Wesdemiotis, C.; Newkome, G. R. Group 8 Metallomacrocycles – Synthesis, Characterization, and Stability. *Eur. J. Inorg. Chem.* **2015**, *2015*, 5662–5668.

(117) Holyer, R. H.; Hubbard, C. D.; Kettle, S. F. A.; Wilkins, R. G. The Kinetics of Replacement Reactions of Complexes of the Transition Metals with 2,2',2"-Terpyridine. *Inorg. Chem.* **1966**, *5*, 622–625.

(118) Heller, M.; Schubert, U. S. Syntheses of Functionalized 2,2′:6′,2″-Terpyridines. *Eur. J. Org. Chem.* **2003**, *2003*, 947–961.

(119) Schubert, U. S.; Schmatloch, S.; Precup, A. A. Access to supramolecular polymers: Large scale synthesis of 4′-chloro-2,2′ : 6′,2″-terpyridine and an application to poly(propylene oxide) telechelics. *Designed Monomers and Polymers* **2002**, *5*, 211–221.

(120) Shi, J.; Wang, M. Self-Assembly Methods for Recently Reported Discrete Supramolecular Structures Based on Terpyridine. *Chem. Asian J.* **2021**, *16*, 4037–4048.

(121) Jiang, Z.; Li, Y.; Wang, M.; Liu, D.; Yuan, J.; Chen, M.; Wang, J.; Newkome, G. R.; Sun, W.; Li, X.*; et al.* Constructing High-Generation Sierpiński Triangles by Molecular Puzzling. *Angew. Chem. Int. Ed.* **2017**, *56*, 11450–11455.

(122) Chakraborty, S.; Newkome, G. R. Terpyridine-based metallosupramolecular constructs: tailored monomers to precise 2D-motifs and 3D-metallocages. *Chemical Society reviews* **2018**, *47*, 3991–4016.

(123) Lee, J.; Moon, H. H.; Paeng, K.; Song, C. Reversible Assembly of Terpyridine Incorporated Norbornene-Based Polymer via a Ring-Opening Metathesis Polymerization and Its Self-Healing Property. *Polymers* **2018**, *10*.

(124) Sato, T.; Pandey, R. K.; Higuchi, M. Fluorescent colour modulation in Zn(II)-based metallosupramolecular polymer films by electronic-state control of the ligand. *Dalton transactions (Cambridge, England : 2003)* **2013**, *42*, 16036–16042.

(125) Bhowmik, S.; Ghosh, B. N.; Marjomäki, V.; Rissanen, K. Nanomolar pyrophosphate detection in water and in a self-assembled hydrogel of a simple terpyridine-Zn2+ complex. *J. Am. Chem. Soc.* **2014**, *136*, 5543–5546.

(126) Fullenkamp, D. E.; He, L.; Barrett, D. G.; Burghardt, W. R.; Messersmith, P. B. Mussel-inspired histidine-based transient network metal coordination hydrogels. *Macromolecules* **2013**, *46*, 1167–1174.

(127) Mozhdehi, D.; Ayala, S.; Cromwell, O. R.; Guan, Z. Self-healing multiphase polymers via dynamic metal-ligand interactions. *J. Am. Chem. Soc.* **2014**, *136*, 16128–16131.

(128) Holten-Andersen, N.; Jaishankar, A.; Harrington, M.; Fullenkamp, D. E.; DiMarco, G.; He, L.; McKinley, G. H.; Messersmith, P. B.; Lee, K. Y. C. Metal-coordination: Using one of nature's tricks to control soft material mechanics. *Journal of materials chemistry. B* **2014**, *2*, 2467–2472.

(129) Sakai, T.; Matsunaga, T.; Yamamoto, Y.; Ito, C.; Yoshida, R.; Suzuki, S.; Sasaki, N.; Shibayama, M.; Chung, U.-i. Design and Fabrication of a High-Strength Hydrogel with Ideally Homogeneous Network Structure from Tetrahedron-like Macromonomers. *Macromolecules* **2008**, *41*, 5379–5384.

(130) Matsunaga, T.; Sakai, T.; Akagi, Y.; Chung, U.-i.; Shibayama, M. Structure Characterization of Tetra-PEG Gel by Small-Angle Neutron Scattering. *Macromolecules* **2009**, *42*, 1344–1351.

(131) Matsunaga, T.; Sakai, T.; Akagi, Y.; Chung, U.-i.; Shibayama, M. SANS and SLS Studies on Tetra-Arm PEG Gels in As-Prepared and Swollen States. *Macromolecules* **2009**, *42*, 6245–6252.

(132) Hiroi, T.; Ohl, M.; Sakai, T.; Shibayama, M. Multiscale Dynamics of Inhomogeneity-Free Polymer Gels. *Macromolecules* **2014**, *47*, 763–770.

(133) Shibayama, M.; Li, X.; Sakai, T. Precision polymer network science with tetra-PEG gels—a decade history and future. *Colloid Polym Sci* **2019**, *297*, 1–12.

(134) Nakagawa, S.; Li, X.; Kamata, H.; Sakai, T.; Gilbert, E. P.; Shibayama, M. Microscopic Structure of the "Nonswellable" Thermoresponsive Amphiphilic Conetwork. *Macromolecules* **2017**, *50*, 3388–3395.

(135) Nishi, K.; Asai, H.; Fujii, K.; Han, Y.-S.; Kim, T.-H.; Sakai, T.; Shibayama, M. Small-Angle Neutron Scattering Study on Defect-Controlled Polymer Networks. *Macromolecules* **2014**, *47*, 1801–1809.

(136) Tsuji, Y.; Nakagawa, S.; Gupit, C. I.; Ohira, M.; Shibayama, M.; Li, X. Selective Doping of Positive and Negative Spatial Defects into Polymer Gels by Tuning the Pregel Packing Conditions of Star Polymers. Macromolecules. *Macromolecules* **2020**, *53*, 7537–7545.

(137) Nishi, K.; Fujii, K.; Chijiishi, M.; Katsumoto, Y.; Chung, U.-i.; Sakai, T.; Shibayama, M. Kinetic Study for AB-Type Coupling Reaction of Tetra-Arm Polymers. *Macromolecules* **2012**, *45*, 1031–1036.

(138) Nishi, K.; Fujii, K.; Katsumoto, Y.; Sakai, T.; Shibayama, M. Kinetic Aspect on Gelation Mechanism of Tetra-PEG Hydrogel. *Macromolecules* **2014**, *47*, 3274–3281.

(139) Tanaka, T.; Hocker, L. O.; Benedek, G. B. Spectrum of light scattered from a viscoelastic gel. *The Journal of Chemical Physics* **1973**, *59*, 5151–5159.

(140) Fujiyabu, T.; Yoshikawa, Y.; Kim, J.; Sakumichi, N.; Chung, U.-i.; Sakai, T. Shear Modulus Dependence of the Diffusion Coefficient of a Polymer Network. *Macromolecules* **2019**, *52*, 9613–9619.

(141) Flory, P. J. *Principles of polymer chemistry*, 19. print; Cornell Univ. Press: Ithaca, NY, 1953.

(142) James, H. M.; Guth, E. Statistical Thermodynamics of Rubber Elasticity. *The Journal of Chemical Physics* **1953**, *21*, 1039–1049.

(143) Akagi, Y.; Gong, J. P.; Chung, U.-i.; Sakai, T. Transition between Phantom and Affine Network Model Observed in Polymer Gels with Controlled Network Structure. *Macromolecules* **2013**, *46*, 1035–1040.

(144) Grindy, S. C.; Lenz, M.; Holten-Andersen, N. Engineering Elasticity and Relaxation Time in Metal-Coordinate Cross-Linked Hydrogels. *Macromolecules* **2016**, *49*, 8306–8312.

(145) Yount, W. C.; Loveless, D. M.; Craig, S. L. Strong means slow: dynamic contributions to the bulk mechanical properties of supramolecular networks. *Angew. Chem. Int. Ed.* **2005**, *44*, 2746–2748.

(146) Yount, W. C.; Loveless, D. M.; Craig, S. L. Small-molecule dynamics and mechanisms underlying the macroscopic mechanical properties of coordinatively cross-linked polymer networks. *J. Am. Chem. Soc.* **2005**, *127*, 14488–14496.

(147) Grindy, S. C.; Learsch, R.; Mozhdehi, D.; Cheng, J.; Barrett, D. G.; Guan, Z.; Messersmith, P. B.; Holten-Andersen, N. Control of hierarchical polymer mechanics with bioinspired metal-coordination dynamics. *Nature materials* **2015**, *14*, 1210–1216.

(148) Trapaidze, A.; D'Antuono, M.; Fratzl, P.; Harrington, M. J. Exploring mussel byssus fabrication with peptide-polymer hybrids: Role of pH and metal coordination in self-assembly and mechanics of histidine-rich domains. *European Polymer Journal* **2018**, *109*, 229–236.

(149) Tanaka, S.; Wakabayashi, K.; Fukushima, K.; Yukami, S.; Maezawa, R.; Takeda, Y.; Tatsumi, K.; Ohya, Y.; Kuzuya, A. Intelligent, Biodegradable, and Self-Healing Hydrogels Utilizing DNA Quadruplexes. *Chem. Asian J.* **2017**, *12*, 2388–2392.

(150) Creusen, G.; Akintayo, C. O.; Schumann, K.; Walther, A. Scalable One-Pot-Liquid-Phase Oligonucleotide Synthesis for Model Network Hydrogels. *J. Am. Chem. Soc.* **2020**, *142*, 16610–16621.

(151) Akintayo, C. O.; Creusen, G.; Straub, P.; Walther, A. Tunable and Large-Scale Model Network StarPEG-DNA Hydrogels. *Macromolecules* [Online early access]. DOI: 10.1021/acs.macromol.1c00600.

(152) Creusen, G.; Roshanasan, A.; Garcia Lopez, J.; Peneva, K.; Walther, A. Bottom-up design of model network elastomers and hydrogels from precise star polymers. *Polym. Chem.* **2019**, *10*, 3740–3750.

(153) Fantner, G. E.; Oroudjev, E.; Schitter, G.; Golde, L. S.; Thurner, P.; Finch, M. M.; Turner, P.; Gutsmann, T.; Morse, D. E.; Hansma, H.*; et al.* Sacrificial bonds and hidden length: unraveling molecular mesostructures in tough materials. *Biophysical Journal* **2006**, *90*, 1411–1418.

(154) Lopez-Perez, P. M.; da Silva, R. M. P.; Strehin, I.; Kouwer, P. H. J.; Leeuwenburgh, S. C. G.; Messersmith, P. B. Self-healing hydrogels formed by complexation between calcium ions and bisphosphonate-functionalized star-shaped polymers. *Macromolecules* **2017**, *50*, 8698–8706.

(155) Li, Q.; Barrett, D. G.; Messersmith, P. B.; Holten-Andersen, N. Controlling Hydrogel Mechanics via Bio-Inspired Polymer-Nanoparticle Bond Dynamics. *ACS nano* **2016**, *10*, 1317–1324.

(156) Marco-Dufort, B.; Tibbitt, M. W. Design of moldable hydrogels for biomedical applications using dynamic covalent boronic esters. *Materials Today Chemistry* **2019**, *12*, 16–33.

(157) Wang, Y.; Li, L.; Kotsuchibashi, Y.; Vshyvenko, S.; Liu, Y.; Hall, D.; Zeng, H.; Narain, R. Self-Healing and Injectable Shear Thinning Hydrogels Based on Dynamic Oxaborole-Diol Covalent Cross-Linking. *ACS biomaterials science & engineering* **2016**, *2*, 2315–2323.

(158) Shao, C.; Wang, M.; Chang, H.; Xu, F.; Yang, J. A Self-Healing Cellulose Nanocrystal-Poly(ethylene glycol) Nanocomposite Hydrogel via Diels–Alder Click Reaction. *ACS Sustainable Chem. Eng.* **2017**, *5*, 6167–6174.

(159) Chen, X.; Dam, M. A.; Ono, K.; Mal, A.; Shen, H.; Nutt, S. R.; Sheran, K.; Wudl, F. A thermally re-mendable cross-linked polymeric material. *Science (New York, N.Y.)* **2002**, *295*, 1698–1702.

(160) Rowan, S. J.; Cantrill, S. J.; Cousins, G. R. L.; Sanders, J. K. M.; Stoddart, J. F. Dynamic Covalent Chemistry. *Angew. Chem. Int. Ed.* **2002**, *41*, 898–952.

(161) Parada, G. A.; Zhao, X. Ideal reversible polymer networks. *Soft matter* **2018**, *14*, 5186–5196.

(162) Yesilyurt, V.; Ayoob, A. M.; Appel, E. A.; Borenstein, J. T.; Langer, R.; Anderson, D. G. Mixed Reversible Covalent Crosslink Kinetics Enable Precise, Hierarchical Mechanical Tuning of Hydrogel Networks. *Adv. Mater.* **2017**, *29*.

(163) McKinnon, D. D.; Domaille, D. W.; Cha, J. N.; Anseth, K. S. Biophysically defined and cytocompatible covalently adaptable networks as viscoelastic 3D cell culture systems. *Adv. Mater.* **2014**, *26*, 865–872.

(164) Zimbone, M.; Calcagno, L.; Messina, G.; Baeri, P.; Compagnini, G. Dynamic light scattering and UV–vis spectroscopy of gold nanoparticles solution. *Materials Letters* **2011**, *65*, 2906–2909.

(165) CHAKRABORTY, S.; SAHOO, B.; TERAOKA, I.; GROSS, R. Solution properties of starch nanoparticles in water and DMSO as studied by dynamic light scattering. *Carbohydrate Polymers* **2005**, *60*, 475–481.

(166) Beck, S.; Schultze, J.; Räder, H.-J.; Holm, R.; Schinnerer, M.; Barz, M.; Koynov, K.; Zentel, R. Site-Specific DBCO Modification of DEC205 Antibody for Polymer Conjugation. *Polymers* **2018**, *10*.

(167) Härtl, E.; Dixit, N.; Besheer, A.; Kalonia, D.; Winter, G. Weak antibody-cyclodextrin interactions determined by quartz crystal microbalance and dynamic/static light scattering. *European journal of pharmaceutics and biopharmaceutics : official journal of Arbeitsgemeinschaft fur Pharmazeutische Verfahrenstechnik e.V* **2013**, *85*, 781–789.

(168) Gohy, J.-F.; Antoun, S.; Jérôme, R. Self-aggregation of poly(methyl methacrylate)-block-poly(sulfonated glycidyl methacrylate) copolymers. *Polymer* **2001**, *42*, 8637–8645.

(169) Nakashima, K.; Bahadur, P. Aggregation of water-soluble block copolymers in aqueous solutions: recent trends. *Advances in colloid and interface science* **2006**, *123-126*, 75–96.

(170) Seiffert, S. Scattering perspectives on nanostructural inhomogeneity in polymer network gels. *Progress in Polymer Science* **2017**, *66*, 1–21.

(171) Shibayama, M. Universality and Specificity of Polymer Gels Viewed by Scattering Methods. *BCSJ* **2006**, *79*, 1799–1819.

(172) Debye, P.; Bueche, A. M. Scattering by an Inhomogeneous Solid. Journal of Applied Physics, 20(6), 518-525. *Journal of Applied Physics* **1949**, *20*, 518–525.

(173) Pham, K. N.; Egelhaaf, S. U.; Pusey, P. N.; Poon, W. C. K. Glasses in hard spheres with short-range attraction. *Physical review. E, Statistical, nonlinear, and soft matter physics* **2004**, *69*, 11503.

(174) van Megen, W.; Underwood; Pusey. Nonergodicity parameters of colloidal glasses. *Phys. Rev. Lett.* **1991**, *67*, 1586–1589.

(175) Rodd, A. B.; Dunstan, D. E.; Boger, D. V.; Schmidt, J.; Burchard, W. Heterodyne and Non-ergodic Approach to Dynamic Light Scattering of Polymer Gels: Aqueous Xanthan in the Presence of Metal Ions (Aluminum(III)). *Macromolecules* **2001**, *34*, 3339–3352.

(176) Pusey, P. N.; van Megen, W. Dynamic light scattering by non-ergodic media. *Physica A: Statistical Mechanics and its Applications* **1989**, *157*, 705–741.

(177) Joosten, J. G. H.; McCarthy, J. L.; Pusey, P. N. Dynamic and static light scattering by aqueous polyacrylamide gels. *Macromolecules* **1991**, *24*, 6690–6699.

(178) Shibayama, M.; Norisuye, T.; Nomura, S. Cross-link Density Dependence of Spatial Inhomogeneities and Dynamic Fluctuations of Poly(N -isopropylacrylamide) Gels. *Macromolecules* **1996**, *29*, 8746–8750.

(179) Shibayama, M.; Takata, S.-i.; Norisuye, T. Static inhomogeneities and dynamic fluctuations of temperature sensitive polymer gels. *Physica A: Statistical Mechanics and its Applications* **1998**, *249*, 245–252.

(180) Tsuji, Y.; Li, X.; Shibayama, M. Evaluation of Mesh Size in Model Polymer Networks Consisting of Tetra-Arm and Linear Poly(ethylene glycol)s. *Gels (Basel, Switzerland)* **2018**, *4*.

(181) Pierre-Gilles de Gennes. *Scaling Concepts in Polymer Physics*; Cornell University Press: Ithaca and London, 1979.

(182) Pincus, P. Excluded Volume Effects and Stretched Polymer Chains. *Macromolecules* **1976**, *9*, 386–388.

(183) Ikkai, F.; Shibayama, M. Static Inhomogeneities in Thermoreversible Physical Gels. *Phys. Rev. Lett.* **1999**, *82*, 4946–4949.

(184) Li, X.; Noritomi, T.; Sakai, T.; Gilbert, E. P.; Shibayama, M. Dynamics of Critical Clusters Synthesized by End-Coupling of Four-Armed Poly(ethylene glycol)s. *Macromolecules* **2019**, *52*, 5086–5094.

(185) Ohira, M.; Li, X.; Gupit, C. I.; Kamata, H.; Sakai, T.; Shibayama, M. Dynamics of thermoresponsive conetwork gels composed of poly(ethylene glycol) and poly(ethyl glycidyl ether-co-methyl glycidyl ether). *Polymer* **2018**, *155*, 75–82.

4 RESULTS AND DISCUSSION

4.1 Origin of the low-frequency plateau and the light-scattering slow mode in semidilute poly(ethylene glycol) solutions

Martha Koziol, [redacted]

Soft Matter, **2019**, *15*, 2666-2676 (DOI: 10.1039/C8SM02263A)

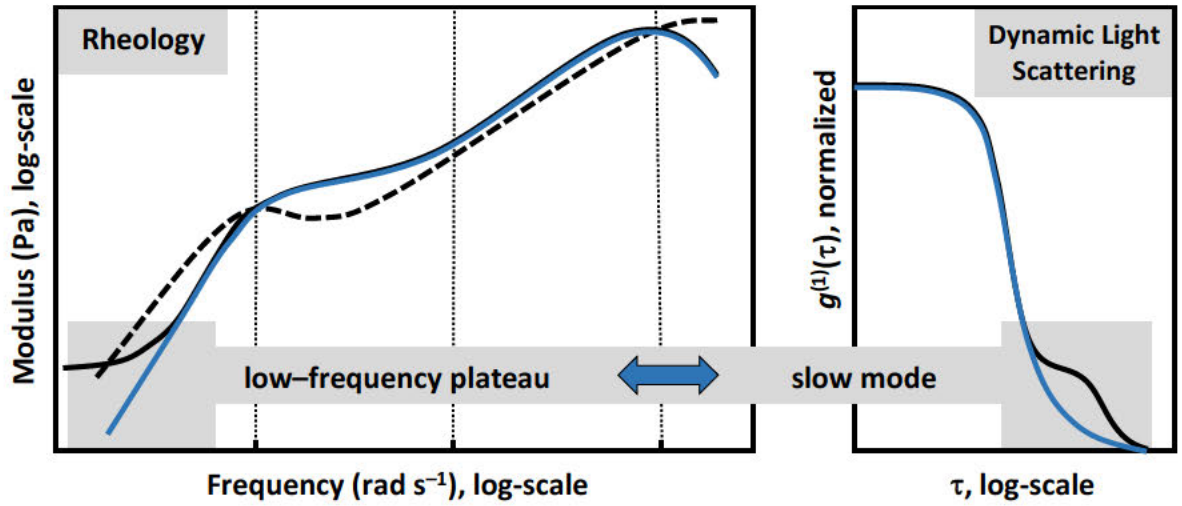

Author Contributions	
Martha Koziol	Sample purification, DLS and SLS measurements, rheology and microrheology measurements, data analysis, writing and editing of the manuscript
[redacted]	Supervision of the work, guidance for light scattering experiments, correction of the manuscript
[redacted]	Supervision and conception of the work, correction of the manuscript, acquisition of funding

With a perspective towards unravelling the interplay of structure and dynamics in supramolecular polymer networks, understanding the behavior of each single network-forming component (e. g. polymer chain contributions, sticker kinetics) in solution is mandatory. For this purpose, scattering and elastic response of semi-dilute linear poly(ethylene glycol) (PEG) solutions were investigated in this

manuscript. Although there are no associative sticker groups present, the frequently reported occurrence of a low-frequency plateau in rheology led to the hypothesis of a weak network structure that is able to store energy. Additionally, investigating the connection between such a low-frequency plateau and a slow relaxation mode that is sometimes visible in the light scattering correlation function was the main target. Complementary scattering experiments (SLS and DLS), rheology and microrheology disproved the initially stated hypothesis and no aggregates or clustering were found in the thoroughly cleaned polymer solutions. Spherical gold nanoparticles coated with short PEG chains to avoid repulsive interactions were used as probe particles to measure the elastic response and viscosity from a microscopic perspective (light scattering based microrheology). The light scattering autocorrelation functions were deconvoluted and converted via creep compliance into the elastic moduli G' and G'' thereby achieving an overlap with the macroscopic rheology data. These data showed no low-frequency plateaus even at varying temperatures such that its presence in macroscopic oscillatory shear rheology experiments was concluded as an instrument artefact.

The obtained results serve as a solid basis for further upcoming investigations of PEG chains interconnected by sticky groups thereby forming supramolecular networks. Especially the careful polymer solution sample preparation involving several filtering steps emerged as crucial if artefact-free light scattering data are matter of interpretation.

4.1.1 Abstract

A low-frequency plateau is often found in the rheological spectra of various kinds of semidilute solutions of polymers and other colloids; also, many of such solutions have been reported to show slow-modes in their dynamic light scattering autocorrelation functions. Both these observations may lead to the hypothesis of weak associative network structures built by the dissolved polymer chains or colloidal building blocks. To challenge this hypothesis, we conduct a series of comparative studies on semidilute solutions of poly(ethylene glycol) by classical rheology as well as by passive microrheology based on dynamic light scattering, along with structural studies by static light scattering. Whereas we indeed find a low-frequency plateau in classical shear rheology, even at elevated temperatures where potential polymer aggregates should be broken, no such plateau is observed in any of our microrheology experiments. Also, dynamic and static light scattering studies on the polymer solutions do not confirm the presence of larger structural entities: no slow mode can be detected in the autocorrelation function of the scattering intensity signal, and this signal is angular independent if the samples are purified by a thorough procedure of filtration. Based on these findings, we conclude that the low-frequency plateau in classical rheology results as an instrument effect caused by erroneous recording of the phase angle, although the magnitude of the torque lies well within the resolution of the rheometer. We also conclude that slow modes in dynamic light scattering on solutions of poly(ethylene glycol) are impurity-based artifacts rather than due to actual associate structures.

4.1.2 Introduction

The usual viscoelastic spectrum of homopolymer solutions in the semidilute concentration range consists of up to four regimes, as sketched in **Fig. 1A**:

(i) the terminal relaxation region at low frequencies (which is phenomenologically described by the Maxwell model)

(ii) potentially an entropy-elastic plateau where the storage modulus G' is frequency-independent and dominates over the loss modulus G'' at medium frequencies (provided that the chains are long, overlapping, and entangled)

(iii) a transition into the glassy region in the range of frequencies between the inverse entanglement time (in the case of entangled chains and presence of regime ii) or the inverse

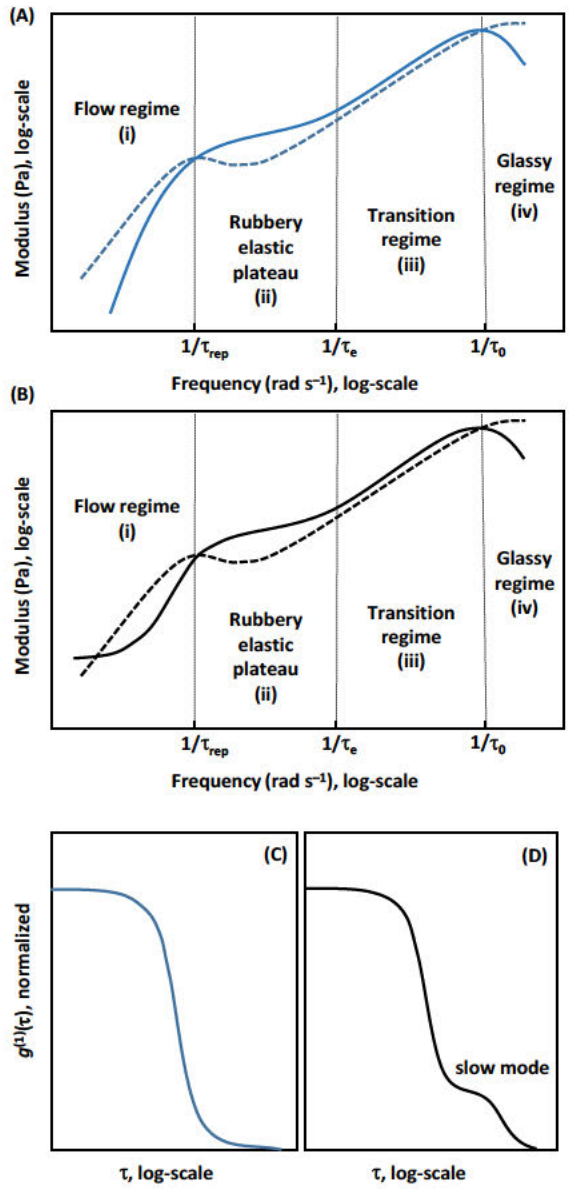

Fig. 1. Schematics of ideal and frequent actual oscillatory-shear rheological spectra (Panel A and B) and dynamic-light-scattering autocorrelation curves (Panel C and D) of semidilute polymer solutions. (A) Ideal viscoelastic spectrum of a homopolymer solution in the semidilute entangled concentration regime, with the frequency-dependent storage modulus G' (blue full line) and loss modulus G'' (blue dashed line). (B) Actual viscoelastic spectrum as often measured on many samples, displaying a bend-over of the elastic modulus G' (black full line) to a low-frequency plateau in the flow regime. (C) Ideal monomodal autocorrelation function of a semidilute polymer solution as obtained by dynamic light scattering (DLS). (D) Actual bimodal autocorrelation function with a typical slow mode as often measured on many samples.

Rouse or Zimm time (in the case of unentangled chains and absence of regime ii) and the inverse shortest relaxation time (which is phenomenologically described by the Kelvin–Voigt model)

(iv) the energy-elastic glassy region at frequencies higher than the inverse shortest relaxation time.

However, in numerous publications, a bend-over of G' to a second weak plateau in the low-frequency region has been reported, as sketched in **Fig. 1B**;[1–8] even more, this finding is not limited to polymer solutions, but has also been reported for other colloidal samples such as micellar systems.[9,10] This low-frequency plateau of the storage modulus can indicate a weak network structure to be present that is able to store elastic energy. Such a network structure may be presumed to form as a consequence of weak non-covalent association and aggregation of the polymer chains in a sample at rest, whereas at higher shear rate, as given at higher frequency if the shear amplitude is fixed, these structures might be destroyed such that normal flow and Maxwell-type scaling of the frequency-dependent storage and loss moduli is observed. Indeed, for aqueous solutions of the popular polymer poly(ethylene glycol) (PEG), formation of helical aggregates due to hydrogen bonding and due to the amphiphilic character of the polymer molecules has been reported.[11] Alternatively, a weak network structure may also be caused by embedded small air bubbles in the viscous polymer solution. Such air bubbles may even be stabilized by surface-adsorbed amphiphilic PEG chains, thereby acting as weak network nodes. In an earlier study, evidence for such

bubbles has been found in dilute PEG solutions,[12] and in the semidilute regime, these may become a cause for weak network formation.

Furthermore, the formation of large PEG chain clusters due to interactions between the hydrophobic CH_2–CH_2 units has been reported, and also the ability of the PEG chains to enclose hydrophobic impurities can be considered as an origin for aggregate formation.[13–15] All these structures can be presumed to create a weak network that may weakly store elastic energy, but that may also be destroyable by sufficiently strong shear forces, which will be present in rheology at shear oscillation frequencies higher than a certain lower limit at a given and fixed shear amplitude, thereby leading to a transition from the low-frequency weak plateau to the common Maxwellian flow regime, as sketched in **Fig. 1B**. The presumption of weak network structures and polymer aggregates may further be seen to be in agreement to findings in various dynamic light scattering studies on polymer solutions. Whereas the normalized autocorrelation function obtained from these experiments should actually just show a single-exponential decay that is addressable to the cooperative diffusive motion of overlapping PEG chain segments, as idealized in **Fig. 1C**, many measurements show an additional slow mode, as sketched in **Fig. 1D**.[16,17] In the light scattering community, the reasons for the possible existence of such slow modes have been and still are a topic of debate for more than two decades.[18] In recent publications, the slow mode has been attributed to the appearance of large aggregates,[14,19] air bubbles,[12] or impurities,[15] just as also addressed above as possible explanations for a low-frequency plateau in the rheological spectra. Alternatively, viscoelastic relaxation[20] and relaxation of correlated blobs of overlapping chain segments,[17] have been discussed as causes for a slow mode. However, a direct connection between the weak low-frequency plateau in the storage modulus G' in rheology and the appearance of a slow mode in dynamic light scattering has not been reported so far.

In this paper, we challenge the hypothesis of the presence of aggregates and clusters in semidilute PEG solutions and their presumed effects on the rheological and light scattering properties of these solutions. We do this by systematic investigation from a microscopic and a macroscopic perspective. For this purpose, we use microrheology based on dynamic light scattering (DLS) as well as classical oscillatory shear macrorheology to examine the frequency-dependent viscous and elastic contributions of the rheological properties of the polymer solutions. We choose three different temperatures (278 K, 293 K, and 323 K) to achieve variation of the external thermal energy. On top of that, we probe the dynamics and microstructure of the PEG solutions by dynamic and static light scattering (DLS and SLS) to detect potential aggregates or micro-phase separated domains larger than 10 nm.

4.1.3 Experimental Section

Materials and Sample Preparation

The material basis for our investigations are narrowly disperse PEG samples with weight-average molar masses of 1,860 g mol^{-1} (Carl Roth, denoted PEG-2k) and 23,540 g mol^{-1} (Sigma Aldrich, denoted PEG-20k); in addition, we partly use a PEG sample with a nominal molar mass of 100,000 g mol^{-1} (Alfa Aesar, denoted PEG-100k). These polymers are first purified by dissolution in dichloromethane and subsequent precipitation in cold diethylether. After drying in high vacuum, the PEG is dissolved in water, filtered through a Whatman Anotop filter (25 mm, 0.02 µm pore size) and a Millex-LG® filter (200 nm pore size), and dried again. To characterize the molar mass of the polymers and its dispersity, SEC measurements are carried out with a 1260 Infinity GPC/SEC-System (Agilent) equipped with an RI-detector and a Shodex precolumn, along with columns of type Shodex OHpak SB 804, Shodex OHpak SB 803, and Shodex OHpak SB 802.5, with an eluent mixture of water / acetonitrile (70:30) at a flow rate 1 mL min^{-1}. SEC calibration is carried out with poly(ethylene glycol) standards from PSS, Germany. We determine polydispersity indexes (PDI) of 1.03 (PEG-2k) and 1.07 (PEG 20-k). Aqueous solutions of the poly(ethylene glycol)s with different concentrations below, at, and above the overlap concentration (100, 200, 300, and 400 g L^{-1} for the PEG-2k; 35, 70, 150, and 200 g L^{-1} for the PEG-20k; 200 g L^{-1} for the PEG-100k) are prepared by dissolving the respective amount of PEG in deionized water. The solutions are gently shaken at 40 °C for three days to allow for complete dissolution of the polymer. The overlap concentration c^* is calculated as $c^* = (3M_w) / (4\pi N_A R_G^3) \approx [\eta]^{-1}$,[21] with the polymer molar mass M_w, the Avogadro number N_A, the polymer coil-radius of gyration R_G, and the intrinsic viscosity $[\eta] = 12.5 \cdot 10^{-3} \cdot M_w^{0.78}$.[22] We calculate radii of gyration of 1.62 nm for the PEG-2k, 5.13 nm for the PEG-20k, and 11.46 nm for the PEG-100k, using the formula $\langle R_G^2 \rangle^{1/2} = 6^{-1/2} \cdot 8.88 \cdot 10^{-2} \cdot M_w^{1/2}$.[23] With these values, the overlap concentrations c^* are determined to be 200 g L^{-1} (PEG-2k), 35 g L^{-1} (PEG-20k), and 11 g L^{-1} (PEG-100k). As a further characteristic quantity, the semidilute-solution correlation length ξ, which can be seen as a meshsize of the transient solution-network, is appraised as $\xi = \langle R_G^2 \rangle^{1/2} (c^*/c)^{0.75}$ with the polymer concentration c.[24] For microrheology, probe colloids with a core–shell structure are used. The cores are spherical gold nanoparticles with diameter of 15 nm purchased from NanopartzTM, whereas the shell is a PEG (M_w = 5,000 g mol^{-1}) layer. With that, the probe colloids are significantly larger than the estimated mesh size of the semidilute solution-network, so we expect comparability between the microrheology and the macrorheology results.[25] Table 1 summarises the measured and calculated molecular and structural properties of the PEG samples.

Table 1. Molecular and structural characteristics of the PEG-2k and PEG-20k samples used in this work.

Sample	M_w (g mol^{-1})	M_n (g mol^{-1})	PDI	R_G (nm)	c^* (g L^{-1})	c (g L^{-1})	ξ_{calcd} (nm)
PEG-2k	1810	1860	1.03	1.62	200	100	2.72
						200	1.62
						300	1.20
						400	0.96
PEG20-k	23540	22080	1.07	5.13	35	35	5.13
						70	3.05
						150	1.72
						200	1.39

Dynamic Light Scattering (DLS) and Microrheology

Before the actual microrheology experiments are performed, the hydrodynamic radius of the gold nanoparticles in an aqueous solution is examined by DLS, yielding a value of R_H = 23.7 nm based on an angular-independent self-diffusion coefficient of $D_s = 9.16 \cdot 10^{-8}$ cm^2 s^{-1}. DLS-based microrheology is then performed by loading the polymer solutions with the gold–PEG core–shell nanoprobes at a low gold concentration of 5 mg L^{-1} to avoid multiple scattering and interparticle interactions. The microrheology samples are prepared by dissolving the polymer in water, adding the gold, homogenization, freeze drying, and redissolution of the sample in 2 mL water to obtain a homogenous distribution of the nanoparticles in the viscous polymer solutions. All light scattering quartz glass cuvettes are thoroughly precleaned with peroxymonosulfuric acid and aqua regia, and dust particles are removed by rinsing with hot acetone. The polymer solutions are then poured into the clean cuvettes by slow filtration through syringe filters (Millex-LG®, 200 nm pore size and Whatman Anotop, 25 mm, 20 nm pore size). This filtration step is performed in a dust-free laminar flow box to obtain dust-free polymer solutions. Dynamic light scattering measurements are performed on a Multigoniometer ALV-CGS-8F SLS/DLS 5022F with a Uniphase He/Ne Laser (25 mW, λ = 632.8 nm) and a vertically polarized laser beam, with eight simultaneously working ALV-7004 multi-tau correlators at eight fiber optical ALV/High QE APD avalanche photodiodes (all components: ALV-Laservertriebsgesellschaft mbH, Langen, Germany). A constant temperature of 20 °C for all measurements is assured (± 0.1 °C) by a Lauda ultrathermostat RKS C6 (Lauda Dr. Worbser GmbH, Königshofen, Germany). A Glan–Thompson polarizer with vertical polarization (VV-mode) is installed in front of the detector to block any light depolarized by the gold nanoparticles.[26] The measured and normalized intensity autocorrelation function

$$g^{(2)}(q,\tau) = \frac{\langle I(q,t) \cdot I(q,t+\tau)\rangle}{\langle I(q,t)\rangle^2} \quad (1)$$

is converted into the amplitude autocorrelation function $F_s(q,t)$ via the Siegert relation

$$F_s(q,t) = g^{(1)}(q,\tau) = \sqrt{g^{(2)}(\tau) - 1} \quad (2)$$

with the angular- and time-dependent intensity $I(q,t)$, and the lag time τ. In these equations, the scattering vector q is defined as $q = (4\pi n_D/\lambda)\cdot\sin(\theta/2)$, with n_D, θ, and λ, the refractive index of the solvent, the scattering angle, and the laser wavelength. The amplitude autocorrelation function $F_s(q,t)$ is the Fourier transform of the van-Hove-autocorrelation function, describing the time- and space-dependent particle motion as an ensemble. The experimental autocorrelation data are fitted by an exponential function $g^{(1)}(q,\tau) = A \cdot \exp(-\tau/\tau_R)$ for ideal diluted solutions of dispersed spherical particles, with the amplitude A and the characteristic relaxation time τ_R , and the diffusion coefficient D is computed as $D = (\tau_R \cdot q^2)^{-1}$. The hydrodynamic correlation length ξ_H for polymer solutions in the semidilute concentration regime can be calculated by a Stokes–Einstein-analog relation

$$\xi_H = \frac{k_B T}{6\pi\eta D} \quad (3)$$

with the Boltzmann constant k_B, temperature T, and the viscosity η. For the microrheology conversion process, the time-dependent mean-square displacement $\langle \Delta r(t)^2 \rangle$ (MSD) of the probe colloids in the polymer solutions is extracted out of a stretched biexponential fit function using the Einstein–Smoluchowski identity $\langle \Delta r(t)^2 \rangle = 6Dt$ and

$$g^{(1)}(q,t) = g(0)\cdot\exp\left(-q^2\frac{\langle \Delta r(t)^2\rangle}{6}\right) \quad (4)$$

The MSD is then converted into the time-dependent creep compliance $J(t)$ according to $J(t) = (\pi a/k_B T)\cdot\langle \Delta r(t)^2 \rangle$, with the particle radius a.[27] To calculate the complex shear modulus $G^*(\omega)$, the numerical inversion method introduced by Evans *et al.*[28] based on

$$\frac{i\omega}{G^*(\omega)} = i\omega\cdot J(0) + (1-\exp(-i\omega t_1))\frac{\left(J_1 - J(0)\right)}{t_1} + \frac{\exp(-i\omega t_N)}{\eta} + \sum_{k=2}^{N}\left(\frac{J_k - J_{k-1}}{t_k - t_{k-1}}\right)\left(\exp(-i\omega t_{k-1}) - \exp(-i\omega t_k)\right) \quad (5)$$

is used with the free software *Compliance to Complex Moduli V3*.

Static Light Scattering

Static light scattering (SLS) is performed at an ALV-SP86 goniometer equipped with an ALV 3000 correlator, an ALV High QE APD avalanche photodiode fiber optical detection system, and a Uniphase He/Ne laser (22 mW, λ = 32.8 nm). All measurements are carried out at 293 K and at multiple

detection angles θ ranging from 30 ° to 150 ° in steps of 10 °. We use the Rayleigh ratio of toluene $R_{Tol} = 1.39 \cdot 10^{-5}$ cm^{-1} at λ = 632.8 m to calculate the Rayleigh ratio of the samples. PEG solutions without gold nanoparticles are prepared at different concentrations in the semidilute regime, all of which at or above the respective overlap concentration (200, 300, and 400 g L^{-1} for PEG-2k and 35, 70, and 200 g L^{-1} for PEG-20k). The sample and cuvette preparation is done analogous to the dynamic light scattering procedure described above. For the experimental data evaluation, we plot Kc/R against the square of the scattering vector q^2 with the contrast factor $K = 4\pi^2 n_D^2 (dn/dc)^2 / N_A \lambda^4$, using the refractive index of the solvent n_D, the refractive index increment (dn/dc), and the refractive index n of the polymer solutions. The refractive index increments for both PEG samples are experimentally determined to be 0.135 mL g^{-1} (PEG-2k) and 0.139 mL g^{-1} (PEG-20k) at λ = 632.8 nm.

Rheology

To compare the microrheology results to analogues obtained by classical macrorheology, we perform such classical shear experiments with an Anton Paar modular compact rheometer of type MCR 302 (Anton Paar, Graz, Austria) equipped with a cone–plate measuring system CP50-1/TG with a cone radius of 24.983 mm and a cone angle of 0.996 ° at 293 K. For all measurements, a solvent trap is used to suppress evaporation of the solvent. To assure comparability, the same PEG samples as in the light scattering studies are used, prepared and purified as described above. First, we investigate the linear viscoelastic regime boundaries of every sample by implementing an amplitude sweep at a constant frequency of ω = 1 rad s^{-1} and amplitudes in the range of 0.01–100% of deformation. Then, frequency sweeps are carried out in a frequency range of ω = 0.1–100 rad s^{-1}, performed from high to low frequencies, with a fixed amplitude within the linear viscoelastic regime (LVE) of the sample.

4.1.4 Results and Discussion

In this work, like in others before,[1–8] a frequency-independent plateau in the storage modulus G' is detected in oscillatory shear rheology at low frequencies, as exemplified for PEG-solutions with molar masses of 20 kg mol^{-1} and 100 kg mol^{-1}, both at c = 200 g L^{-1}, in **Fig. 2**. The value of this plateau lies up to three decades above the calculated low-torque limit of the rheometer, whose torque resolution is appraised as

$$G_{min} = \frac{F_\tau T_{min}}{\gamma_0} = \frac{3\ T_{min}}{2\pi R^3 \gamma_0}, \qquad (6)$$

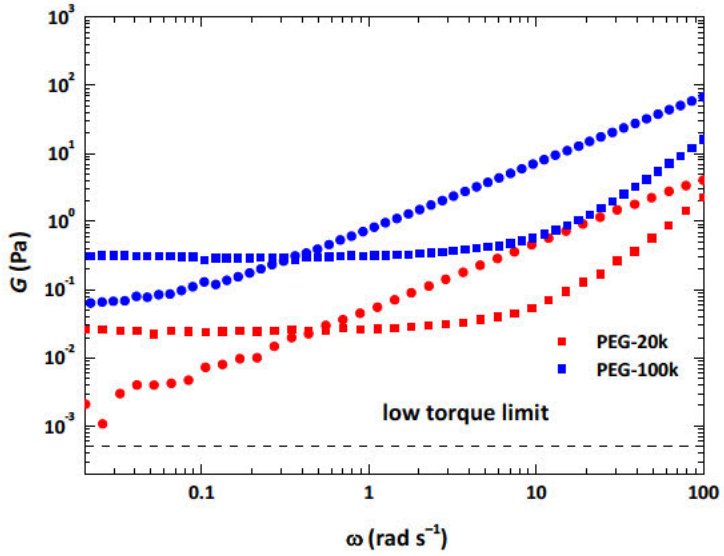

Fig. 2. Frequency-dependent storage (squares) and loss moduli (circles) of a PEG-20k solution (red) and a PEG-100k solution (blue), each at a concentration of 200 g L^{-1}, measured macroscopically with a rheometer at an amplitude well within the linear viscoelastic regime. The dashed line represents the calculated low-torque limit of the instrument.

with the minimal modulus G_{min}, the instrument minimum torque T_{min} = 0.5 nNm, the cone radius R, the deformation amplitude γ_0, and the resulting force F_τ.[29] In both solutions, the frequency-independent plateau persists up to frequencies of ω = 10 rad s^{-1}, until then the storage modulus curves bend over and approach the expected Maxwell-type terminal-flow power-law dependence with a log–log slope of 1.8.

Even with different rheometer geometries (cone–plate of different sizes, concentric cylinder, and double gap), the low-frequency plateau is obtained in every case, such that we exclude interfacial tension effects as a possible reason for its appearance. In contrast to the unusual curve shape of G', the loss modulus G'' is in accordance with the Maxwell model over the whole frequency range investigated, with a log–log slope of 1. Besides general errors in the determination of low torque values, the unexpected curve-shape of the storage modulus G' at low frequencies can be caused by phase-angle uncertainties as an effect of the instrument, as comprehensively described by Velankar and Giles.[30] According to their work, the total error in G' can be expressed as a combination of an error in the complex modulus $|G^*|$ and an error in the phase angle:

$$\frac{dG'}{G'} = \frac{d|G^*|}{|G^*|} - \tan(\delta)\, d\delta \qquad (7)$$

These errors particularly occur if the values of G' and G'' differ significantly, so even if their values lie well above the low torque limit of the rheometer, its phase angle resolution has to be taken into account. Especially fluid samples with low torque values exhibit a noisy measurement signal, thus leading to uncertainties in the correct phase-angle determination. In the words of Velankar and Giles:[30] "*as* δ

approaches 90 degrees, the fractional error in G' grows with-out bound even when the error in phase angle dδ remains finite. This is just a quantitative way of stating that it is difficult to characterize the elasticity of weakly-viscoelastic materials". The rheological spectrum of our PEG-100k solution in **Fig. 2** (blue symbols) shows that due to these errors, a low-frequency plateau can even exist at high absolute modulus-values around 0.3 Pa, despite having nearly the same ratio of G' and G'' as the pEG-20k solution (red symbols).

As an alternative interpretive approach to the latter method-inherent line of argument, the frequency-independent curve shape of G' can be seen to be not an artifact, but to actually reflect the existence of a weak network structure in the sample that is able to store external deformation energy as long as that energy is weak. At low shear frequencies, coming along with low shear rates at a given shear amplitude, this might be the case, whereas at higher shear frequencies and therefore higher shear rates, these network structures may be destroyed, leading to a transition to the normal terminal flow regime in the viscoelastic spectrum.

To examine whether the low-frequency plateau has its origin in inaccurate phase-angle values or appears as a consequence of a real underlying structural feature in the samples, and to get closer insight into this structure, we perform microrheology on the polymer solutions, thereby extending the accessible frequency range and obtaining microscopic information about the viscoelastic response of the system.

As this measurement technique does not depend on any phase-angle determination based on the quality of the initial torque and displacement signal, we may be able to identify whether inaccurate phase angles or microscopic structural irregularities are the origin of the low-frequency plateau. The second advantage of the microrheology technique for our investigation is that the effective shear forces are smaller than those in macrorheology, as there is no external load applied to the sample in microrheology, but instead, just the common thermal energy drives a diffusive motion of nanoscopic probe particles inside the polymer solutions. Therefore, we may presume that, if the hypothesis of a structural reason is correct, the low-frequency plateau in the storage modulus should be even more extended to even higher frequencies when probed by such passive microrheology.

Microrheology

Our experiments are based on dynamic light scattering, where we track the Brownian motion of spherical gold nanoparticles with a PEG corona through the polymer solutions. The PEG corona pro-

vides thermodynamic compatibility between the tracer particles and their surrounding solution-network matrixes. **Fig. 3A** exemplifies a set of the normalized autocorrelation functions of a PEG solution containing a small amount of the colloidal gold tracer particles. The experimental autocorrelation data are all well fitted by a stretched biexponential function of Kohlrausch–Williams–Watts type.

$$g^{(1)}(\tau) = A + B \cdot \exp\left(-\left(\frac{\tau}{\tau_1}\right)^C\right) + D \cdot \exp\left(-\left(\frac{\tau}{\tau_2}\right)^E\right) \quad (8)$$

From this fit, two relaxation times τ_{slow} and τ_{fast} of the diffusion processes can be computed as

$$\tau_{slow} = \frac{\tau_1}{C} \cdot \Gamma\left(\frac{1}{C}\right) \text{ and } \tau_{fast} = \frac{\tau_2}{E} \cdot \Gamma\left(\frac{1}{E}\right) \quad (9)$$

with the Gamma function Γ and the fit-function exponents C and E. Plotting the inverse relaxation times τ_{slow}^{-1} and τ_{fast}^{-1} versus the square of the scattering vector q^2 yields two straight lines through the origin, with slopes representing two different diffusion coefficients, as seen in **Fig. 3B**.

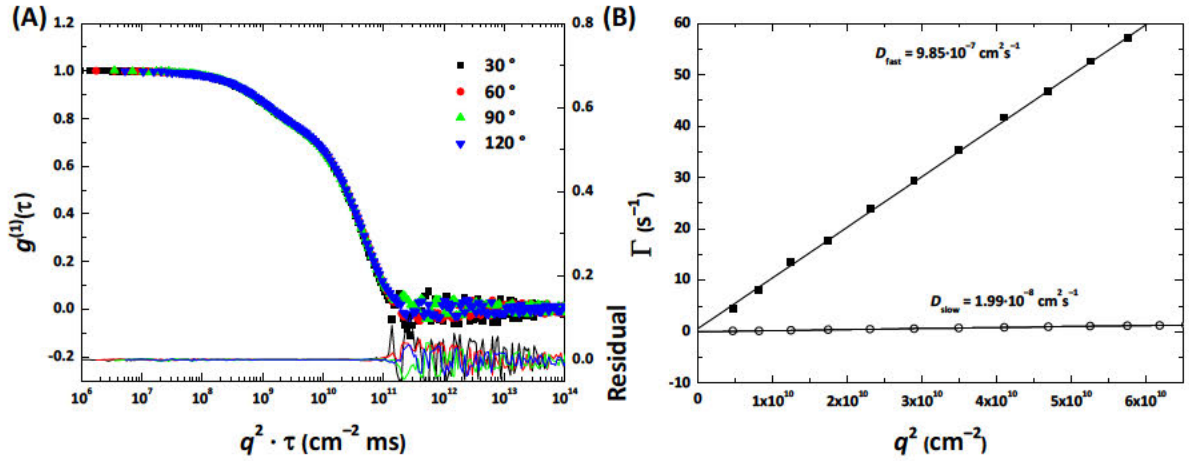

Fig. 3. (A) Normalized DLS autocorrelation function $g^{(1)}(\tau)$ of an aqueous solution of PEG-20k (c = 70 g L^{-1}), containing PEG-coated gold nanoparticles (d = 20 nm, $M_{w,PEG-corona}$ = 5000 g mol^{-1}) as probe colloids observed at scattering angles of 30 °, 60 °, 90 °, and 120 ° (black, red, green, and blue symbols), along with fits and corresponding residuals to a bi-Kohlrausch–Williams–Watts functions (bi-KWW). (B) Angular dependence of the inverse relaxation times, showing two different diffusive processes.

Fig. 4 shows the fast (filled squares) and the slow (open circles) diffusion coefficients depending on the polymer concentration for the PEG-20k samples.

We attribute the fast coefficient D_{fast} to the cooperative motion of the overlapping PEG chain segments. This cooperative diffusion coefficient increases by increase of the polymer concentration in the semidilute region (c > 35 g L^{-1} for PEG-20k, c > 200 g L^{-1} for PEG-2k), as the freely movable polymer segments between overlap points of the semidilute solution-network decrease in their length if the polymer concentration increases,[24] thereby leading to a faster relaxation, whereas in the dilute regime, the fast diffusion coefficient is nearly independent of the polymer concentration and can be described by the following equation[31]

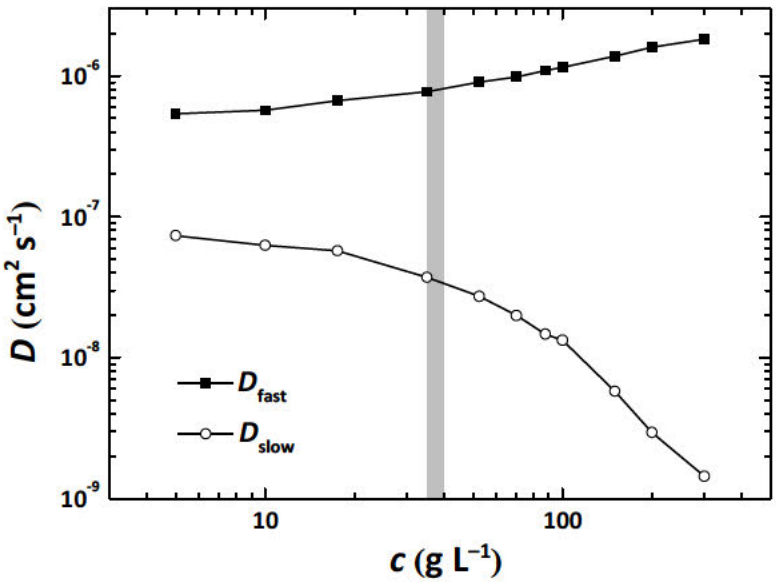

Fig. 4. Concentration dependence of the fast (filled squares) and the slow (open circles) diffusion coefficients determined by DLS on aqueous solutions of PEG-20k. The grey bar marks the polymer overlap concentration c^*.

$$D_{app} = D_s \cdot (1 + k_D c) \cdot (1 + \langle R_G^2 \rangle_z q^2) \quad (10)$$

with $k_D = 2 \cdot A_2 \cdot M_w - (R_H^3 / M_w)$, the mean-square radius of gyration $\langle R_G^2 \rangle_z$, the second virial coefficient A_2, the hydrodynamic radius R_H, and the molar mass M_w. Extrapolation of the concentration c and the scattering vector q^2 to zero results in the self-diffusion coefficient D_s of the single polymer coils.

The second observed process is slower than the fast one by two orders of magnitude and corresponds to the hindered gold tracer diffusion. With an increase in the polymer concentration and therefore the solution viscosity, the velocity of the tracer motion decreases due to greater obstruction by the surrounding medium. Based on this principle, the viscoelastic properties of that medium can be quantified from the tracer motion. As it is driven by the thermal energy $k_B T$ only, no external forces are applied, and hence, measurements in the linear viscoelastic regime are always ensured; also, the risk of measurement-induced destruction of the relevant microscopic sample structures is excluded. The tracer mean-square displacement (MSD) is extracted out of the DLS autocorrelation fit function and converted into the complex shear modulus by a numerical inversion method that works without any need for Fourier transform of the experimental data and thereby minimizes transformation errors (see experimental part).

Fig. 5 shows the resulting frequency-dependent data for the loss and storage modulus of a PEG-20k solution at $c = 150$ g L^{-1}, in comparison with the corresponding data from classical macroscopic shear rheology. We achieve good agreement of the loss modulus data from both, macro- and microrheology, in the overlapping frequency range of 10^{-1} to 60 rad s^{-1}. In contrast, the low-frequency plateau in the

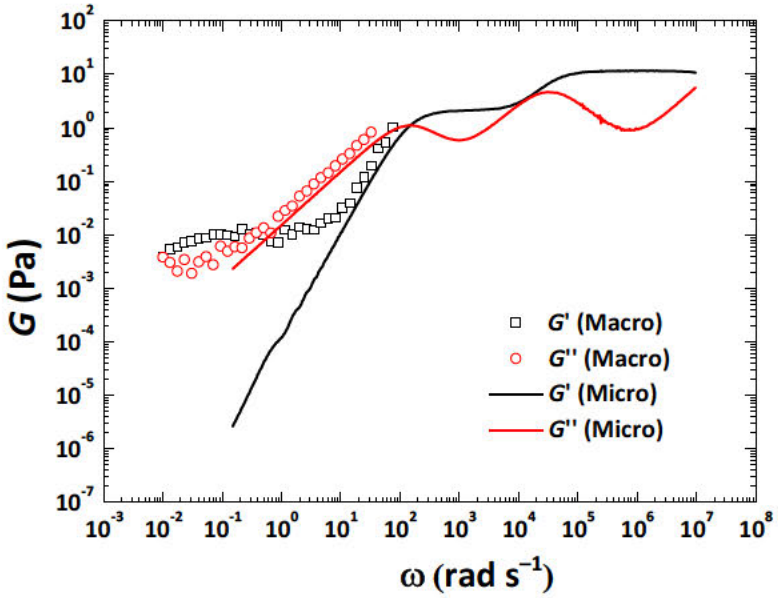

Fig. 5. Frequency dependence of storage and loss modulus (black and red) for a PEG-20k solution (c = 150 g L^{-1}), obtained by DLS-based microrheology (lines) and by classical shear rheology (open symbols).

storage modulus G' does not appear in microrheology. As the shear forces in microrheology are as weak as possible (only thermal energy $k_B T$ drives the tracer particles), according to our above hypothesis of weak network structures in the PEG solutions, these should be more likely destroyed in macrorheology than in microrheology, such that the latter method should show them even more extended than the first method. The opposite is found, though. A possible reason for the discrepancies in micro- and macrorheology could be interaction effects between the colloidal gold tracers and the polymer chains, in particular depletion effects, whereby the gold tracers are able to create their own microenvironment resulting in a layer of depleted polymer concentration surrounding the probe particle. In this case, a microscopic origin for the second plateau found in macrorheology would not be detectable. To check for that latter suspect, we design and apply a new DLS auto correlation function out of previously known experimental parameters:

$$g^{(1)}(\tau) = B \cdot \left[C \cdot \exp\left(-\frac{\tau}{\tau_{1,\text{polymer}}} \right) + D \cdot \exp\left(-\frac{\tau}{\tau_{2,\text{polymer}}} \right) \right] + E \cdot \left[F \cdot \exp\left(-\frac{\tau}{\tau_{1,\text{tracer}}} \right) + G \cdot \exp\left(-\frac{\tau}{\tau_{2,\text{tracer}}} \right) \right] \tag{11}$$

In this function, the first addend represents the matrix polymer solution; for the amplitude ratios C and D and for the two relaxation times $\tau_{1,\text{polymer}}$ and $\tau_{2,\text{polymer}}$, we plug in the estimated values from dynamic light scattering experiments of the polymer solutions without tracer particles at the same concentrations, respectively. This procedure is possible if we assume that the gold tracers show no influence on the polymer relaxation.

The second addend contains contributions of the tracer particles; for the amplitude ratios F and G, we use parameters from the fit function of the gold tracer in aqueous solution without polymer. Only the overall amplitude ratios B and E and the tracer relaxation times $\tau_{1,tracer}$ and $\tau_{2,tracer}$ are left open to fit, as the increasing viscosity of the polymer solutions compared with water leads to a decelerated tracer diffusion. The residuals in **Fig. 6** show good agreement between the designed fit function and the raw

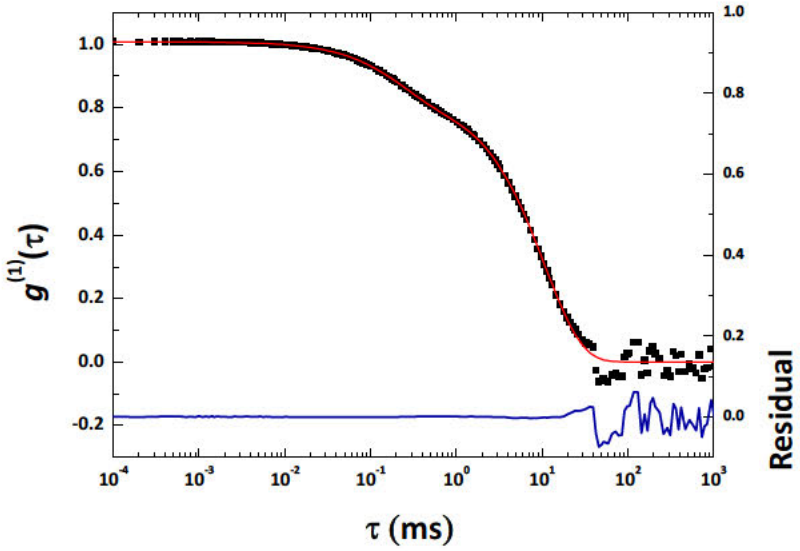

Fig. 6. DLS autocorrelation raw data (black filled squares) of an aqueous solution of PEG-20k ($c = 70$ g L^{-1}) containing PEG-coated gold nanoparticles ($d = 20$ nm, $M_{w,PEG\text{-}corona} = 5{,}000$ g mol^{-1}) along with a fit of a designed function consisting of the separate contributions of the PEG matrix and the gold tracers (red line). The residuals between the fit and the raw data are shown as blue line on the bottom.

data, confirming our first assumption that the initial polymer relaxation is not influenced by interactions with the gold nanoparticles such as depletion.

In conclusion, the former suggested weak PEG network structures could not be discovered by microrheology, leading us to the supposition that their appearance in macrorheology indeed originates by a phase-angle instrument effect. To further go into this matter, we investigate the dynamics and structure of the polymer solutions by dynamic (DLS) and static (SLS) light scattering.

Dynamic Light Scattering

DLS measurements are performed on the semidilute polymer solutions without gold nanoparticles to analyze the scattering contributions of the polymers only. Before being able to do that, we need to implement a series of multiple filtration steps to remove impurities. To explicitly illustrate the impact of that filtration sequence, **Fig. 7** shows the normalized autocorrelation functions of a freshly prepared PEG-2k solution with a concentration of $c = 100$ g L^{-1}, obtained after one to four filtration steps. Note that this concentration is below the overlap threshold of $c^* = 200$ g L^{-1}, so in this solution, we should

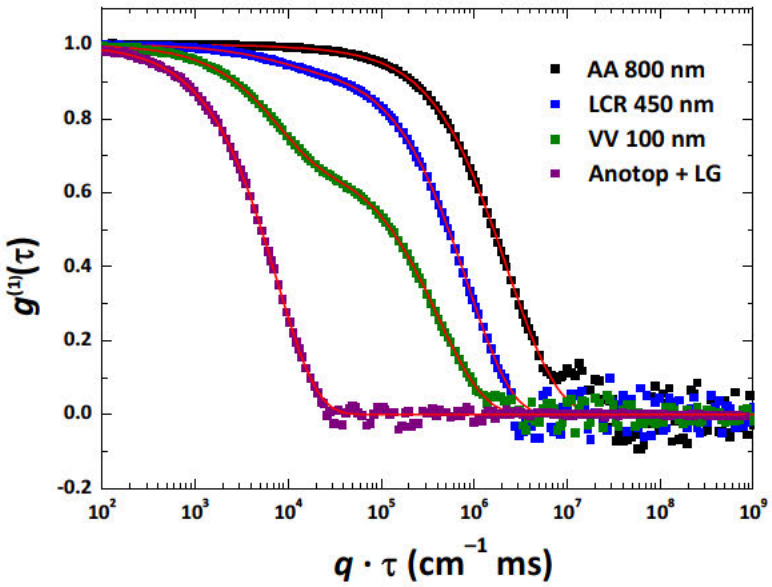

Fig. 7. Normalized autocorrelation data $g^{(1)}(\tau)$ and fit functions to them obtained from a PEG-2k sample (c = 100 g L^{-1}) after several filtration steps with a Millex-AA® filter with 800 nm pore size (black symbols), a Millex-LCR® filter with 450 nm pore size (blue symbols), a Millex-VV® filter with 100 nm pore size (green symbols), and a combination of a Whatman Anotop filter with 0.02 µm pore size and a Millex-LG® filter with 200 nm pore size (violet symbols).

definitely not expect any slow modes. Anyhow, a diffusive slow mode still appears, and only after the last filtration step with a combination of a Millex-LG® (200 nm pore size) and a Whatman Anotop filter (25 mm, 20 nm pore size), it is successfully removed and does also not reappear. Via the amplitudes of the different modes in the autocorrelation functions before that removal, we can estimate the concentration portion of impurities and its contribution to the total scattering intensity in the previous filtering steps. As an example, this is done for the PEG-2k solution after the first filtration step, where a triexponential fit function with the amplitudes B, C, and D has to be used to adequately fit the experimental data.

$$g^{(1)}(\tau) = A + B \cdot \exp\left(-\frac{\tau}{\tau_1}\right) + C \cdot \exp\left(-\frac{\tau}{\tau_2}\right) + D \cdot \exp\left(-\frac{\tau}{\tau_3}\right) \tag{12}$$

Three hydrodynamic radii are calculated to be $R_{H,1}$ = 1.4 nm, $R_{H,2}$ = 185 nm, and $R_{H,3}$ = 540 nm. In general, the total scattering intensity I_{total} consists of the sum of the scattering contributions of i species I_i, and via the normalized amplitude ratios A_i, the intensity proportion of each species can be estimated separately.

$$I_{total} = \sum_{i=1}^{N} I_i \tag{13}$$

$$\text{with } I_i = \sum_{i=1}^{N} A_i \cdot I_{total} \tag{14}$$

The amplitude ratio A_i of each relaxation process is proportional to the concentration c_i and the molar mass M_i of the species i.

$$A_i \sim c_i \cdot M_i \tag{15}$$

To estimate the molar mass M of each species i, we use the classical scaling of the radius of gyration of monodisperse Gaussian coils

$$R_g \sim M^{0.6} \tag{16}$$

and convert that radius into the hydrodynamic radius R_H through use of a relation reported by Burchard and colleagues[32]

$$R_g / R_H = 1.78 \tag{17}$$

to obtain

$$1.78 \cdot R_H \sim M^{0.6} \tag{18}$$

The concentration portion x_i of the i-th species is then obtained by

$$c_i \sim \frac{A_i}{(1.78 \cdot R_{H,i})^{0.6}} \quad \text{and} \quad x_i = \frac{c_i}{\sum_{i=1}^{N} c_i} \tag{19}$$

With the equations (13)–(19) and the three hydrodynamic radii, we estimate that only 0.79% of the sample consists of the largest species ($R_{H,3}$ = 540 nm), but this 0.79% still has a contribution to the overall scattering intensity of about 62%. This estimate shows how crucial it is to thoroughly filter samples in DLS analytics. Such filtration, however, removes material from the sample.

Table 2. Cooperative diffusion coefficients and correlation lengths of differently concentrated semidilute solutions of the polymers PEG-2k and PEG-20k, as obtained by DLS.

Polymer	c (g L^{-1})	D_{coop} (cm^2 s^{-1})	ξ_H (nm)
PEG-2k	200	$2.09 \cdot 10^{-6}$	1.03
	300	$2.21 \cdot 10^{-6}$	0.97
	400	$2.34 \cdot 10^{-6}$	0.92
PEG-20k	35	$7.57 \cdot 10^{-7}$	2.84
	70	$9.94 \cdot 10^{-7}$	2.16

To assure that a desired polymer concentration is used in DLS experiments along with assuring good sample purity, we therefore recommend to filter stock solutions, then freeze-dry them, and finally prepare the samples from the filtered and freeze-dried material. Using such purified solutions in the semidilute concentration regime, it is now possible to gain structural insight by fitting the amplitude autocorrelation function with a biexponential fit function to evaluate the cooperative diffusion coefficient, as shown in **Fig. 8A**. The second addend of the fit function is chosen to take into account polymer polydispersity, even though it is small. Using the cooperative diffusion coefficients D_{coop}, we can calculate the hydrodynamic correlation lengths ξ_H of the samples according to equation (3). Both these

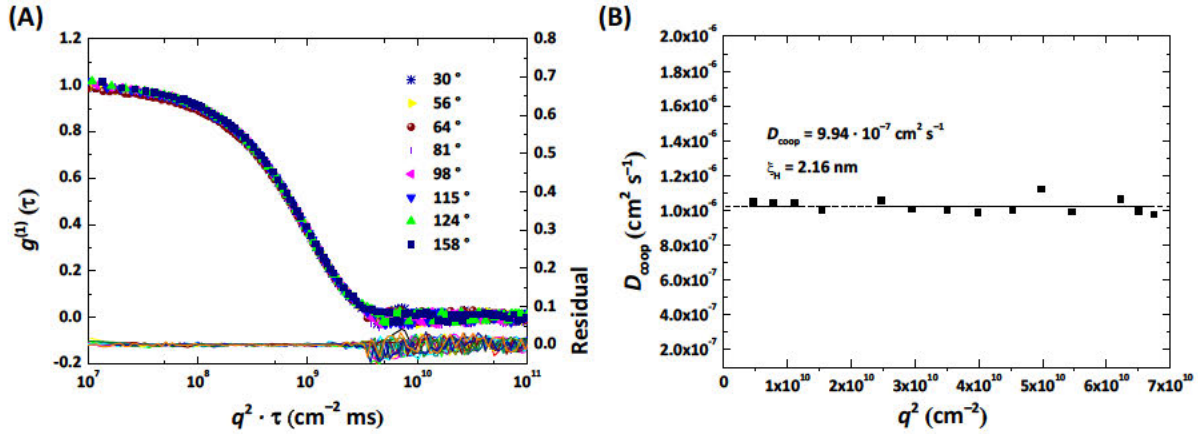

Fig. 8. (A) Experimental normalized amplitude autocorrelation function $g^{(1)}(\tau)$ of a PEG-20k solution ($c = 70$ g L^{-1}), recorded at eight different scattering angles (30 °, 56 °, 64 °, 81 °, 98 °, 115 °, 124 °, and 158 °), and residuals between a biexponential fit function and the raw data at the bottom. (B) The cooperative diffusion coefficient D_{coop} versus the square of the scattering vector q^2 shows no angular dependence and yields a hydrodynamic correlation length of $\xi_H = 2.16$ nm.

characteristic data are summarized in **Table 2** for the two classes of PEG samples investigated in our study. An increase in the polymer concentration leads to a reduction of the hydrodynamic correlation length of the chain-overlap network,[24] and as a result of this, an increase in the cooperative diffusion coefficient due to the faster wobbling of the chain strands between overlap points can be detected. After thorough purification of the polymer samples and the solutions by means of several filtration steps, we obtain no slow mode in the light scattering autocorrelation functions. From these findings, we conclude that colloidal-scale impurities, even in trace amounts only, can be the origin of a marked slow mode in PEG solutions, but if these impurities are removed by tedious but effective sample purification, no slow mode is observed. In such purified samples, the diffusion coefficient D_{coop} is independent of the square of the scattering vector q^2 (**Fig. 8B**), indicating a solution containing no particles or polymer coils with a hydrodynamic radius bigger than 10 nm. These findings are in accordance with an earlier work by Devanand and Selser[33] and lead us to the picture of homogeneous semidilute solutions without PEG aggregates, microphase separation, or crystalline PEG micro- or nanophases. Further on, the appearance of stabilized air bubbles and impurities cannot be verified.

Static Light Scattering

As a final step, we perform static light scattering experiments to detect the microstructure on scales larger than 10 nm, for example, in view of a potential presence of larger aggregates of phase-separated PEG chains. We probe the same samples as in the dynamic light scattering experiments described in the section above. Plotting the inverse Rayleigh ratio against the scattering vector shows no angular dependence of the measured scattering intensity, as seen in **Fig. 9**. No reliable slopes can be extracted

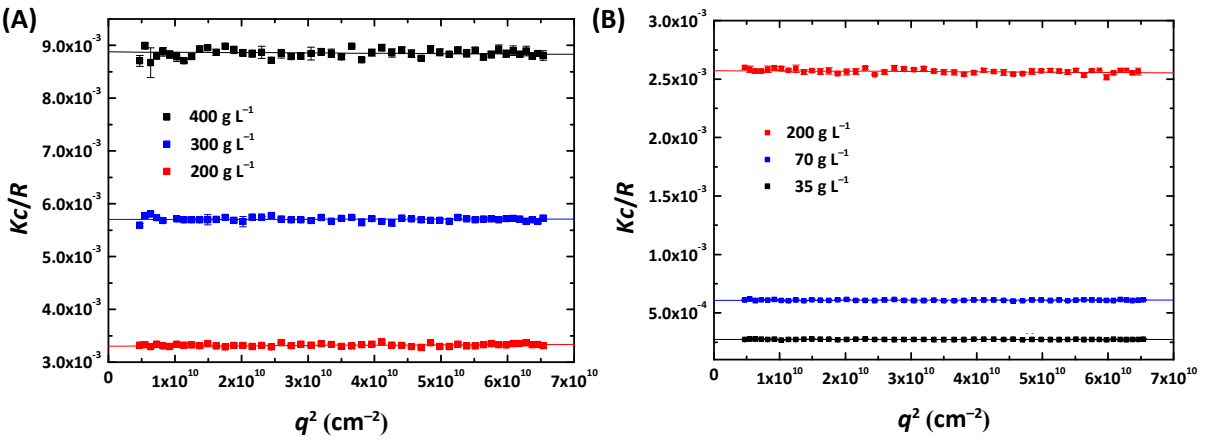

Fig. 9. Static light scattering results for PEG-2k (A) and PEG-20k (B) at three different concentrations, measured at 293 K with the experimental parameters $\lambda = 632.8$ nm, $dn/dc = 0.135$ mL g^{-1} (PEG-2k) and 0.139 mL g^{-1} (PEG-20k), and $n = 1.3288$.

out of fitted straight lines, such that we conclude all correlation lengths to be smaller than 10 nm. As a result of the static light scattering experiments, we cannot find any evidence for clusters or micro-phase separated domains of PEG in the aqueous solutions. Similar results have also been found by Borchard *et al.*[34] These findings confirm our previous DLS results. After thorough purification, the polymer solutions contain completely and homogeneously dissolved PEG chains, and we can also exclude the hypothesis of air bubbles with sizes in the range of 0.1–1 μm in the solutions.[12] As a first brief pre-conclusion, the present results intensify our above assumption that the low-frequency plateau in rheology appears to be rather an effect of the rheometer and not due to actual structural features of the PEG chains in solution. To tie up this hypothesis, we spend further investigations on the temperature dependence of the low-frequency plateau in macroscopic rheology.

Influence of Temperature

To further investigate the influence of potential weak aggregates such as hydrogen bonded or hydrophobic associations on the low-frequency plateau in rheology, we probe our samples at different temperatures. Such interactions can be broken at higher temperatures, which should lead to a distinct change in the rheological behavior of the polymer solutions.

Fig. 10 shows the frequency-dependent storage and loss moduli of the PEG-2k sample in solution at $c = 200$ g L^{-1}, measured at three different temperatures in macrorheology and at two different temperatures in microrheology. We see that the low-frequency plateau in macrorheology exists at every measured temperature, whereby the storage modulus in that plateau shows no systematic dependence on the chosen temperature. In microrheology, by contrast, again no such plateau is seen in any case. This

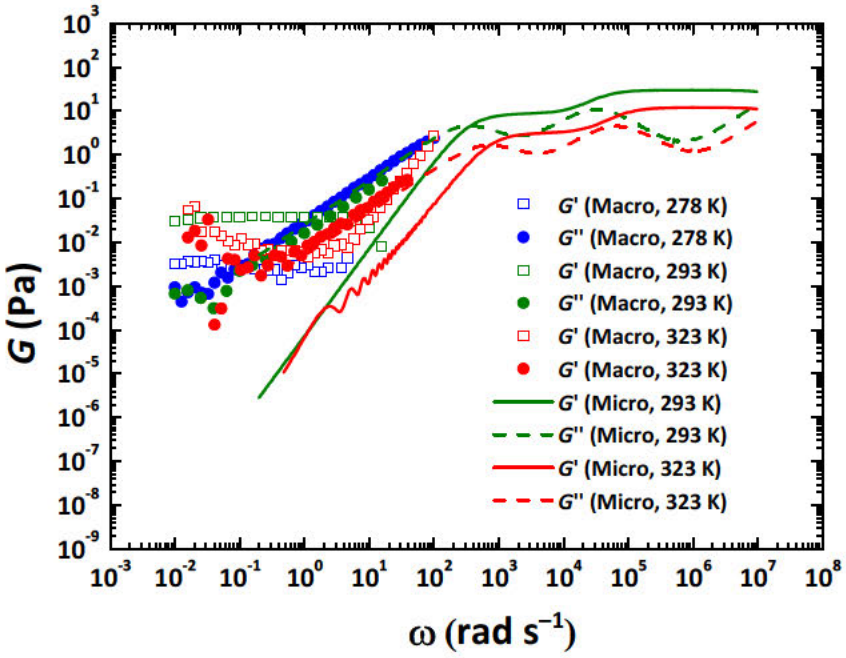

Fig. 10. Micro- and macrorheology results at different temperatures, 278 K (blue), 293 K (green), and 323 K (red), of a PEG-2k solution ($c = 200$ g L^{-1}).

finding further rules out the hypothesis of weak attractive interactions between the PEG chains to cause a weak network structure in semidilute solutions at rest.

4.1.5 Conclusions

When light scattering is performed on thoroughly purified semidilute aqueous poly(ethylene glycol) solutions, no evidence for any sort of complex structures is observed, neither slow modes in DLS nor angular dependencies in SLS. These results, though, require multiple careful purification steps of the samples before and after the preparation of the solutions. We speculate that improper purification might have been the cause of many contrary findings reported in the literature. In addition, in light-scattering-based microrheology, no low-frequency plateau of the storage modulus is observed in any case, in contrast to results of macrorheology on the same polymer solutions, in which such a low-frequency plateau is observed even at high temperatures. Hence, we consider this plateau to be an instrument effect of the classical shear rheometer, even though the data lie two decades above the low-torque limit of the instrument. In line with the work of Velankar and Giles,[30] erroneous phase-angle values appear to be the origin of this artifact. The method of microrheology overcomes this limitation and accurately probes both the high- and low-frequency regime, indicating no presence of any sort of transient or weak network structures in PEG semidilute solutions, in line with similar conclusions by Devanand and Selser[33] and Faraone *et al.*[35] These findings also appear transferrable to other types of soft-

matter systems, as a macrorheology-probed low-frequency plateau was also found, for example, in supramolecular polymer gels based on PNIPAAm[36] or even in systems with micellar components,[9,10] which may all be well explainable by our current conclusions of methodological limits in classical rheology and sample impurities in light scattering.

4.1.6 Acknowledgements

We sincerely thank [redacted] for stimulating discussions and valuable suggestions on the interpretation of macrorheology data in the low-frequency limit. This work was supported by the German Research Foundation (DFG) under grant No. SE 1888/7-1.

4.1.7 References

(1) A. W. Bosnian, L. Brunsveld, B.J.B. Folmer, R. P. Sijbesma and E. W. Meijer, *Macromol. Symp.*, **2003**, *201*, 143–154.

(2) T. Vermonden, M. J. van Steenbergen, N. A. M. Besseling, A. T. M. Marcelis, W. E. Hennink, E. J. R. Sudhölter and M. A. Cohen Stuart, *J. Am. Chem. Soc.*, **2004**, *126*, 15802–15808.

(3) F. van de Manakker, T. Vermonden, N. El Morabit, C. F. van Nostrum and W. E. Hennink, *Langmuir*, **2008**, *24*, 12559–12567.

(4) S. Hackelbusch, T. Rossow, P. van Assenbergh and S. Seiffert, *Macromolecules*, **2013**, *46*, 6273–6286.

(5) T. Rossow, A. Habicht and S. Seiffert, *Macromolecules*, **2014**, *47*, 6473–6482.

(6) H. Goldansaz, Q. Voleppe, S. Piogé, C. A. Fustin, J. F. Gohy, J. Brassinne, D. Auhl and E. van Ruymbeke, *Soft Matter*, **2015**, *11*, 762–774.

(7) M. J. Sánchez-Miranda, E. Sarmiento-Gómez and J. L. Arauz-Lara, *Eur. Phys. J. E*, **2015**, *38*, 3.

(8) A. Habicht, S. Czarnecki, T. Rossow and S. Seiffert, *J. Polym. Sci. B Polym. Phys.*, **2017**, *55*, 19–29.

(9) D. Gaudino, R. Pasquino and N. Grizzuti, *J. Rheol.*, **2015**, *59*, 1363–1375.

(10) J. E. Moore, T. M. McCoy, L. de Campo, A. V. Sokolova, C. J. Garvey, G. Pearson, B. L. Wilkinson and R. F. Tabor, *J. Colloid Interf. Sci.*, **2018**, *529*, 464–475.

(11) a) K. Tasaki, *J. Am. Chem. Soc.*, **1996**, *118*, 8459–8469; b) A. Azri, P. Giamarchi, Y. Grohens, R. Olier and M. Privat, *J. Colloid Interf. Sci.*, **2012**, *379*, 14–19; c) A. Azri, M. Privat, Y. Grohens and T. Aubry, *J. Colloid Interf. Sci.*, **2013**, *393*, 104–108;

(12) J. Wang, *Macromolecules*, **2015**, *48*, 1614–1620.

(13) a) W. F. Polik and W. Burchard, *Macromolecules*, **1983**, *16*, 978–982; b) M. Polverari and T. G. M. van de Ven, *J. Phys. Chem.*, **1996**, *100*, 13687–13695; c) M. Duval and D. Sarazin, *Polymer*, **2000**, *41*, 2711–2716; d) B. Hammouda, *Polymer*, **2009**, *50*, 5293–5297;

(14) P. Zhou and W. Brown, *Macromolecules*, **1990**, *23*, 1131–1139.

(15) B. Porsch and L.-O. Sundeloef, *Macromolecules*, **1995**, *28*, 7165–7170.

(16) a) M. Adam and M. Delsanti, *Macromolecules*, **1977**, *10*, 1229–1237; b) W. Brown and T. Nicolai, *Colloid Polym. Sci.*, **1990**, *268*, 977–990; c) D. L. Ho, B. Hammouda and S. R. Kline, *J. Polym. Sci. B Polym. Phys.*, **2003**, *41*, 135–138; d) J. Li, W. Li, H. Huo, S. Luo and C. Wu, *Macromolecules*, **2008**, *41*, 901–911; e) M. Du-val and E. Gross, *Macromolecules*, **2013**, *46*, 4972–4977;

(17) J. Wang and C. Wu, *Macromolecules*, **2016**, *49*, 3184–3191.

(18) S. Seiffert, *Prog. Polym. Sci.*, **2017**, *66*, 1–21.

(19) M. Duval, *Macromolecules*, **2000**, *33*, 7862–7867.

(20) T. Jian, D. Vlassopoulos, G. Fytas, T. Pakula and W. Brown, *Colloid Polym. Sci.*, **1996**, *274*, 1033–1043.

(21) Q. Ying and B. Chu, *Macromolecules*, **1987**, *20*, 362–366.

(22) F. E. Bailey, J. L. Kucera and L. G. Imhof, *J. Polym. Sci.*, **1958**, *32*, 517–518.

(23) P. Gregory and M. B. Huglin, *Makromol. Chem.*, **1986**, *187*, 1745–1755.

(24) M. Daoud, J. P. Cotton, B. Farnoux, G. Jannink, G. Sarma, H. Benoit, C. Duplessix, C. Picot and P. G. de Gennes, *Macromolecules*, **1975**, *8*, 804–818.

(25) E. C. Cooper, P. Johnson and A. M. Donald, *Polymer*, **1991**, *32*, 2815–2822.

(26) S. Balog, L. Rodriguez-Lorenzo, C. A. Monnier, B. Michen, M. Obiols-Rabasa, L. Casal-Dujat, B. Rothen-Rutishauser, A. Petri-Fink and P. Schurtenberger, *J. Phys. Chem. C*, **2014**, *118*, 17968–17974.

(27) J. J. Duffy, C. A. Rega, R. Jack and S. Amin, *Appl. Rheol.*, **2016**, *26*, 15130.

(28) R. M. L. Evans, M. Tassieri, D. Auhl and T. A. Waigh, *Phys. Rev. E*, **2009**, *80*, 12501.

(29) S. Spagnolie, ed., Complex Fluids in Biological Systems. Experiment, Theory, and Computation, Springer, New York, 1st edn., 2015.

(30) S. Velankar and Giles David, *Rheology Bulletin*, **2007**, *76*, 8–20.

(31) W. Schärtl, ed., Light Scattering from Polymer Solutions and Nanoparticle Dispersions, Springer-Verlag, Berlin Heidelberg, 1st edn., 2007.

(32) a) W. Burchard, M. Schmidt and W. H. Stockmayer, *Macromolecules*, **1980**, *13*, 1265–1272; b) W. Burchard and W. Richtering, *Prog. Colloid Polym. Sci.*, **1989**, *80*, 151–163;

(33) K. Devanand and J. C. Selser, *Nature*, **1990**, *343*, 739–741.

(34) H. Venohr, V. Fraaije, H. Strunk and W. Borchard, *Eur. Polym. J.*, **1998**, *34*, 723–732.

(35) A. Faraone, S. Magazù, G. Maisano, P. Migliardo, E. Tettamanti and V. Villari, *J. Chem. Phys.*, **1999**, *110*, 1801–1806.

(36) T. Rossow, S. Hackelbusch, P. van Assenbergh and S. Seiffert, *Polym. Chem.*, **2013**, *4*, 2515.

4.2 Structural and Gelation Characteristics of Metallo-Supramolecular Polymer Model-Network Hydrogels Probed by Static and Dynamic Light Scattering

Martha Franziska Koziol, [redacted]

Macromolecules **2021**, *54*, 9, 4375–4386 (DOI: 10.1021/acs.macromol.1c00036)

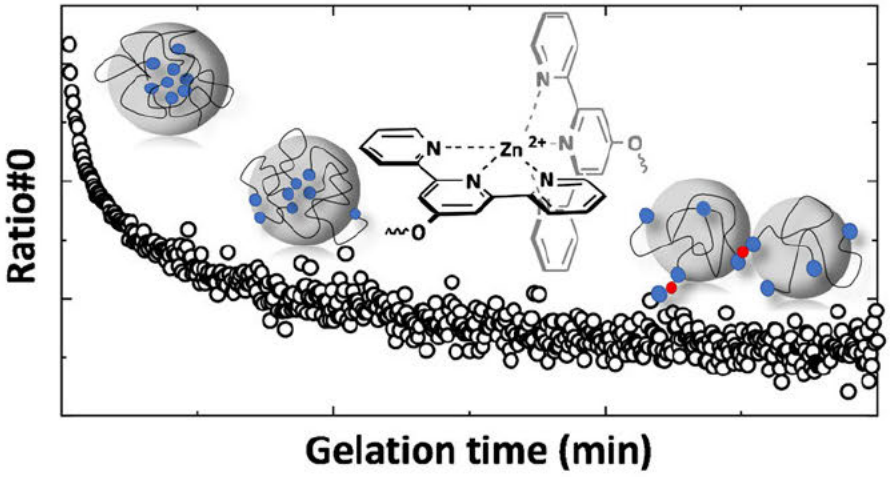

Author Contributions	
Martha Koziol	Synthesis, purification and analysis of the polymers, gelation experiments, SLS and DLS measurements, data analysis, rheology experiments, writing and editing of the manuscript
[redacted]	Guidance in data analysis, supervision of the work, correction of the manuscript
[redacted]	Supervision of the work, correction of the manuscript, acquisition of funding

In this manuscript, laser light scattering characteristics of transiently connected model networks were focus of the investigations. After synthesis and purification of the macromolecules (tetra-arm PEG-terpyridine), gels with varying network strengths were prepared by addition of either zinc, nickel or cadmium cations. The pronounced differences in the kinetic dissociation constants were found to

be reflected in the overall scattering intensities as well as the recorded autocorrelation functions and q^2-dependences of relaxation times.

A major drawback of such metal-ligand mediated networks is the instantaneous gelation once both components (metal ion solution and polymer solution) are mixed. A hindered mass transport and short equilibration times prevent the formation of homogeneous gels, and the preparation of dust-free materials for light scattering experiments remains challenging. To overcome these difficulties, a delayed gelation method was developed with externally tunable gelation times. This method additionally allows for real-time monitoring of the gelation via light scattering and consequently, a molecular network formation mechanism was proposed.

This manuscript contributes to the methodical optimization of gel preparation and light scattering experiments by implementing a simple but efficient approach towards delayed gelation of transient supramolecular systems. The results might be transferrable to other techniques, for example microfluidics. To summarize, the scattering behavior of the investigated three model networks demonstrates that amongst semi-dilute polymer solutions and permanently connected supramolecular networks, such transient networks can be classified as in-betweens.

4.2.1 Abstract

Supramolecular polymer gels are a promising class of materials whose polymer components are connected by transient bonds such as metal–ligand interactions, thereby spanning a dynamic network throughout the entire sample volume. Due to the short bond lifetimes in these networks, structural characterization on appropriate time and length scales is a challenge. To address this challenge, we vary the association strengths of telechelic poly(ethylene glycol) model networks through the use of different bivalent metal ions with the aim of conducting a systematic investigation of their scattering properties. Introduction of a preparation method that opens the opportunity to tune the gelation time allows the underlying gelation mechanism to be revealed by time-resolved light scattering. A statistical analysis of the gel scattering intensities shows major differences depending on the metal-terpyridine association strength.

4.2.2 Introduction

Laser light scattering is a powerful non-perturbative tool to study structural properties and dynamic processes of various materials, for example size distributions, nanoparticle polydispersities, or protein conformations. Since Pusey and van Megen's approach from 1989 to differentiate between the time- and ensemble-averaged intensity correlation function of a dynamic light scattering (DLS) experiment on non-ergodic media,[1] this technique rapidly evolved to further uncover the complexity of polymer network structures swollen in various solvents.[2]

Since about the early 2000s, transiently connected networks, also referred to as supramolecular polymer networks, evolved into a versatile class of soft matter with unique properties and potential for applications such as those in bio engineering[3–6] or electronics.[7,8] To rationally tune these networks and gels for such applications, structural analysis for the establishment of structure–property–relationships is essential.[9–11]

The vast majority of the existing light scattering studies and pioneering works on polymer gels is mainly focused on chemically connected polymer systems.[1,2,12–17] By contrast, there is only few studies focused on transient polymer network systems, and those samples covered in these studies are all rather specific, showing great disagreement in number, assignment, and q-dependence of the relaxation modes found. At least two relaxation modes have been found in all systems, whereby the fastest mode is always assigned to the cooperative chain dynamics of the (transient) network strands. An intermediate slower

mode is often correlated to the macroscopic viscoelastic relaxation of the entire network that can also be probed by stress relaxation tests.[18–20] If a third mode exists, then this is commonly related to the diffusion of polymer clusters or aggregates of different sizes and shapes.[21–24]

Additionally, it has been shown that the distribution and the amount of spatial inhomogeneities in gels exert a major influence on their properties.[2] Although one could expect that reversible polymer gels only exhibit a low number of spatial heterogeneities because of their short bond lifetimes, examples of inhomogeneous physical polymer gels are also known.[25,26]

In this work, we provide a systematic and comparative study on the scattering properties of metallo-supramolecular tetra-arm poly(ethylene glycol) (PEG) hydrogels, transiently connected through coordination of terpyridine termini to either zinc, nickel, or cadmium ions. By choosing these ions, we achieve a sole variation of the network strength, as assessed by the rate constant of complex dissociation ($k_{diss,Cd2+}$ = 25.11 s^{-1}, $k_{diss,Zn2+}$ = 1.25 s^{-1}, $k_{diss,Ni2+}$ = 2.5·10^{-8} s^{-1}, all at 25 °C)[27] while keeping all polymer-related parameters such as the concentration or arm length constant. We obtain liquid-like viscoelastic fluids in the case of cadmium, whereas we obtain viscoelastic gels with zinc. Due to the enormous kinetic stability of nickel–terpyridine complexes, gels formed with nickel ions can be categorized as pseudo-chemically connected networks.

In general, metal–ligand interactions incorporated into a polymer system offer a versatile platform to form supramolecular gels, as the strength of these directed interactions can easily be tuned by external stimuli (pH, temperature, solvent…) or the choice of a competing exchange partner. In combination with monodisperse star-shaped PEG macromolecular building blocks, these networks can be expected to form homogeneous structures with defined mesh sizes that can act as model systems. This is in fact a basis for our investigation, which targets at forming model-type networks of defined strength that allow scattering studies to be conducted and compared with greatest possible consistency.

A major disadvantage of these metal–ligand interactions, however, is the immediate formation of the network upon blending all components, and therefore, a homogeneous mixing is rarely possible, and structural artefacts due to incomplete mixing occur.

In this paper, we introduce a delayed preparation method based on the release of metal ions from ethylenediaminetetraacetic acid $[M(II)(EDTA)]^{2-}$ complexes by gradually protonating the EDTA with the acidity regulator D-glucono-1,5-lactone (GDL). By this method, we are able to adjust a desired gelation time and perform real-time monitoring of the gelation via light scattering. Based on our

scattering results, we propose a gelation mechanism that describes the transition from a pre-gel micellar solution structure with hydrophobic terpyridine cores to a final homogeneous gel.

Our light scattering results show the expected cooperative motion of polymer strands as a diffusive mode, and an additional *q*-independent second mode if the network relaxation time lies on similar times scales as the scattering experiment. The *q*-dependence of this slow mode is significantly affected by the differentiability of the crosslink dissociation time and the polymer-strand relaxation time.

4.2.3 Experimental Part

Materials.

All chemicals are purchased from commercial providers and, if not denoted separately, used without further purification. Tetra-arm polyethylene glycol raw material with a molar mass of 10,000 g mol^{-1} is purchased from *JenKem Technology* (Plano, TX, USA) and re-precipitated in ice cold diethyl ether before use.

Tetra-arm PEG-terpyridine. 5.31 g tetra-arm PEG-OH (2.124 mmol hydroxyl groups) and 0.599 g KOH (10.62 mmol, 5 eq. per –OH) are dried overnight in separate flaks in high vacuum. Under nitrogen atmosphere, 50 mL dry DMSO is added to the KOH, along with the dry polymer and 0.199 g Kryptofix® 222 (0.25 eq. per –OH), resulting in a yellow suspension. The reaction mixture is stirred for 1 h at 70 °C and subsequently, 1.158 g 4′-chloro-2,2′:6′,2″-terpyridine (4.328 mmol, 2 eq. per –OH) is added. The color of the solution then changes to dark red, and after 48 h at 70 °C it is cooled down to room temperature. After pouring the suspension into 250 mL of cold brine, a white precipitate is filtered, and the aqueous phase is extracted three times with 100 mL chloroform. The organic phases are dried over $MgSO_4$, the solution is concentrated in vacuum and precipitated twice in ice cold diethyl ether. 4.72 g (81%) of the yellow polymer is obtained and characterized by ^{1}H-NMR, SEC and MALDI. The degree of end group functionalization is independently determined by UV-vis and ^{1}H-NMR to be 93%. ^{1}H-NMR (DMSO-d_6, 400 MHz), δ = 8.70 (ddd, 8H), 8.61 (dt, 8H), 7.99 (m, 17H), 7.49 (ddd, 8H), 4.37 (t, 8H), 3.83 (m, 9H), 3.49 (m, 1082H, PEG backbone) ppm.

GPC (DMF with 1 g L^{-1} LiBr): M_n = 9636 g mol^{-1}, M_w = 10211 g mol^{-1}, PDI (M_w / M_n) = 1.06.

To use this polymer for light scattering experiments, it is further purified according to the following procedure: 4.72 g of tetra-arm PEG-terpyridine is dissolved in dichloromethane, 2 g activated carbon is added, and the mixture is heated to reflux for 15 minutes. After filtration, the colorless organic solution is concentrated in vacuo, and the polymer is precipitated again in ice cold diethyl ether, resulting

in a colorless fine powder. After drying in high vacuum, the polymer is re-dissolved in water, filtered through a combination of a Whatman® Anotop® syringe filter (diameter: 25 mm, pore size: 0.02 µm) and a Millex-LG syringe filter (diameter: 10 mm, pore size: 0.2 µm), and lyophilized.

Methods.

Homogeneous gel preparation. The targeted polymer concentration in all supramolecular hydrogels is set to be the overlap concentration $c^* = 56\ g\ L^{-1}$ that has been determined by capillary viscometry. A stoichiometric ratio of 2:1 of terpyridine : metal cation is used. For this purpose, an aqueous solution containing the metal ion as ethylenediaminetetraacetate complex $M(II)[EDTA]^{2-}$ (1 eq. metal ion and 1 eq. Na_4EDTA), an aqueous solution of D-glucono-1,5-lactone (2 eq.), and an aqueous solution of the tetra-arm PEG-terpyridine are vigorously mixed. All volumes and compound concentrations are chosen to result in the targeted gel concentration and matching stoichiometry once mixed. The gel solutions are transferred via syringe filters into dust-free cylindrical quartz glass cuvettes (Hellma, diameter: 20 mm), sealed with Teflon stoppers to avoid evaporation of the solvent, and left overnight to form transparent colorless gels and equilibrate.

Light scattering. All light scattering experiments are performed on a Multigoniometer ALV-CGS-8F SLS/DLS 5022F, equipped with a He/Ne Laser Uniphase (25 mW, 632.8 nm) and an ALV-7004 multi-tau correlator connected to an ALV/High QE APD Avalanche photodiode in pseudo cross correlation mode (ALV-Laservertriebs-gesellschaft mbH, Langen Germany). All measurements are carried out on an ALV rotating cuvette unit (CRTU). Temperature control (± 0.1 °C) during measurements is assured by a Lauda ultrathermostat RKS C6 (Lauda Dr. Worbser GmbH, Lauda, Königshofen, Germany). The experiments and data acquisition are controlled by an ALV software correlator ALV500/E/EPP-ALV-60X0-WIN 3.0.3.15. A wide range of scattering vectors $q = (4\pi n \sin(\theta/2)) / \lambda$ with the refractive index n, the scattering angle θ, and the incident and scattering wavelength λ is investigated. Due to non-ergodicity, the time-averaged intensity autocorrelation functions $g^{(2)}(\tau)$ of 500 different positions within the gel sample are recorded with a correlation time of 60 s and a waiting time of 5 s after each rotation.

Rheology. Rheology measurements are carried out on an Anton Paar Modular Compact Rheometer type MCR 302. A cone–plate geometry CP25-1 with a cone radius of 25 mm and an angle of 1 ° is used. The gap is set to 0.05 µm and a cooling trap prevents evaporation of the solvent. Motor adjustments and inertia calibrations are implemented prior to each measurement.

UV-Vis. Absorption spectra are measured at a Jasco V-760-ST UV/vis spectral photometer equipped with a Czerny-Turner double monochromator. Data are acquired in absorption mode with 0.2 nm data intervals in a wavelength range of 200 nm to 400 nm at 20 °C.

4.2.4 Results and Discussion

In this study, we systematically investigate the influence of junction association strengths on the structural properties of model-like tetra-arm PEG-terpyridine metallo-supramolecular hydrogels by static light scattering. Furthermore, the dynamic relaxation times obtained by dynamic light scattering experiments are related to those acquired by rheological stress–relaxation tests.

Light scattering on solutions of tetra-PEG terpyridine

To provide a solid experimental basis for our study, we first investigate aqueous and methanolic solutions of tetra-arm PEG-terpyridine without any metal ions in a dilute concentration range of 3 g L^{-1} to 40 g L^{-1}, assuming a critical overlap concentration of $c^* = 56$ g L^{-1} that has been determined by capillary viscometry.

All recorded autocorrelation functions are fitted to bi-exponential decay functions to properly account for polymer polydispersity. As already shown in a previous work on semi-dilute PEG solutions, no slow modes can be detected if proper purification of the polymers and the light scattering samples is assured (see inset **Figure 1 (B)**).[28] Upon increase of the polymer concentration in these aqueous solutions, the hydrodynamic radius R_H increases linearly by a factor of 3 from 3 nm to 9.5 nm until a critical aggregation concentration of 24.3 g L^{-1} is reached. Further increase of the concentration only leads to a slight further increase of the hydrodynamic radius.

Even at these higher concentrations, no phase-separation into a polymer-rich and a polymer-poor phase is detected. In contrast to that, no such strong concentration dependence of R_H is found in methanolic solutions of tetra-arm PEG-terpyridine, and an average R_H of 3 nm is calculated there.

The diffusion coefficients of each solution show no q-dependence, leading us to the conclusion that uniformly sized aggregates have formed in water, similar to the formation of micelles. We assume that the hydrophobic terpyridine moieties agglomerate into larger flowerlike structures with an outer hydrophilic PEG corona. The aggregation tendency of terpyridine groups in water has also been postulated for sticky block-copolymer micelles by Schubert *et al.*[29] Similar to our findings, the addition of

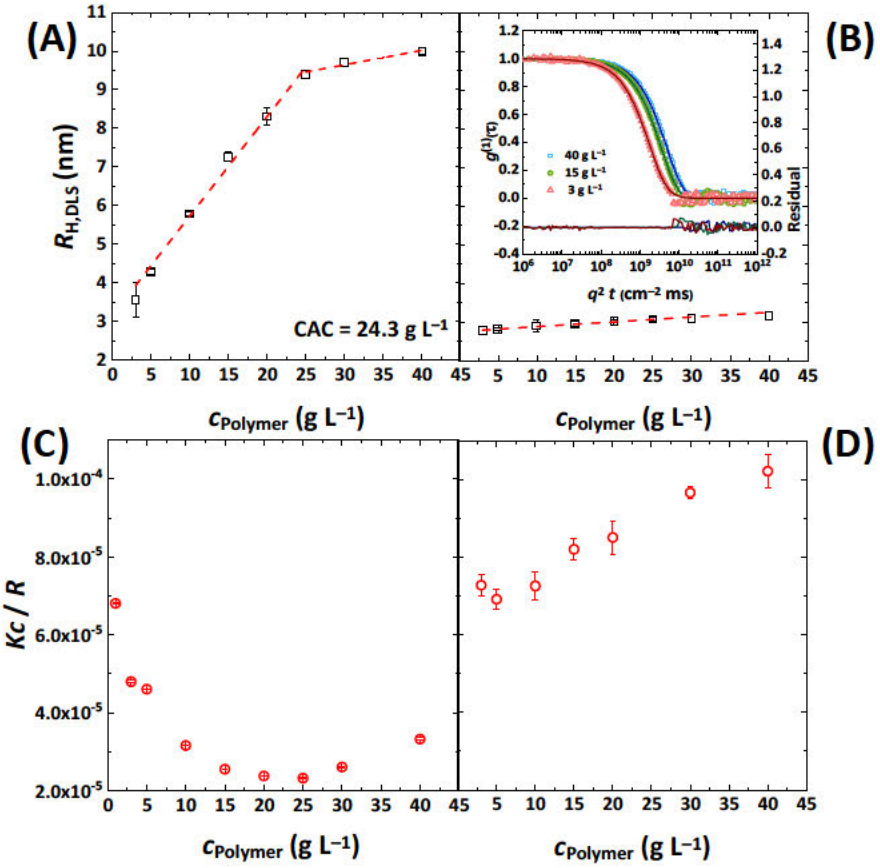

Figure 1. (A) Linear increase of the concentration-dependent hydrodynamic radius of tetra-arm PEG-terpyridine (M_w = 10,924 g mol^{-1}) in water until a critical aggregation concentration of c = 24.3 g L^{-1} is reached. (B) Hydrodynamic radius of differently concentrated tetra-arm PEG-terpyridine solutions in methanol with an average of $\overline{R_H}$ = 3 nm. All autocorrelation functions are monomodal (see inset with residuals). (C) Kc/R vs. concentration of aqueous tetra-arm PEG solutions with a minimum at the aggregation concentration. (D) Increase of Kc/R depending on the concentration in methanol.

nickel ions to their system leads to a decrease in the amount of aggregated micelles by interfering the initial hydrophobic terpyridine–terpyridine interactions.

This hypothesis is further substantiated by the static light scattering (SLS) results of aqueous solutions (**Figure 1(C)**), where a minimum of Kc/R exists at, again, a concentration of 24 g L^{-1}.

$$\frac{Kc}{R} = \frac{1}{M_w}\left(1 + \frac{1}{3}\langle R_g\rangle_z \cdot q^2\right) + A_2 c \qquad (1)$$

Considering the Zimm equation (1) with the weight average molar mass M_w, the z-average radius of gyration $\langle R_g\rangle_z$, and the second virial coefficient A_2, a decrease in Kc/R indicates a negative A_2. At a concentration of 24 g L^{-1}, however, we observe a change in the sign of A_2 followed by an increase of Kc/R (**Figure 1(C)**). Again, this finding is explainable by considering water to be a poor solvent for the tetra-arm PEG polymer that is functionalized with four hydrophobic terpyridine units per molecule. With increasing concentration, though, the macromolecules agglomerate into larger structures

with an inner hydrophobic core (consisting of terpyridine units), and an outer hydrophilic PEG corona. These aggregates exhibit much better solubility in water because the hydrophobic core is shielded by the PEG chains. This structural change results in a positive A_2. Such minima in Kc/R have also been found in other micellar systems, and their origins were partly explained by either a concentration-dependent A_2 (A_3 is then not negligible), the co-existence of micelles and un-micellized agents, or further growth of micelles/aggregates coming along with structural changes.[30–32]

Homogeneous delayed preparation method and gelation monitoring via LS

In spite of their many advantages, such as stimuli-responsiveness or the ability to self-heal, most associative macromonomer building blocks instantaneously form gels upon blending their reactive groups, and due to the drastic viscosity increase that comes along with that, a homogeneous mass transport is hindered.

Hence, compared to their chemical counterparts where specific reaction conditions are necessary and gelation times can often be tuned, the lack of homogeneous mixing in supramolecular associated network gels leads to various structural artefacts such as micro-phase separation. To address this challenge, we use a preparation method that allows the gelation time for supramolecular polymer gels crosslinked by metal ions to be tuned. In our approach, the metal (II) ions (e.g., zinc, nickel, cobalt, cadmium) are introduced into the polymeric system as 1 : 1 ethylenediaminetetraacetic acid (EDTA) pre-complexes. Upon gradual decrease of the pH and therefore protonation of the EDTA carboxylate

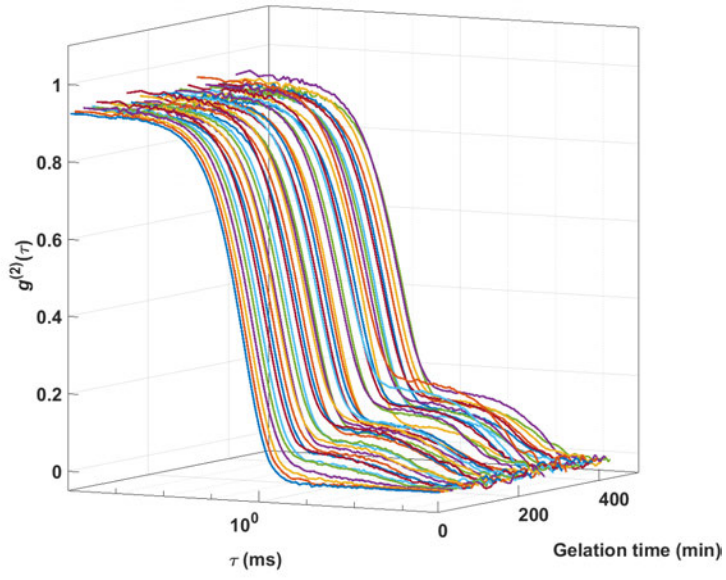

Figure 2. Time-depending intensity correlation functions $g^{(2)}(\tau)$, recorded at 30 °, monitoring the gelation process of a tetra-arm PEG-terpyridine zinc hydrogel (M_w = 10,000 g mol^{-1}, c = 56 g L^{-1}). For reasons of clarity, only every tenth run is depicted (run duration = 60 s).

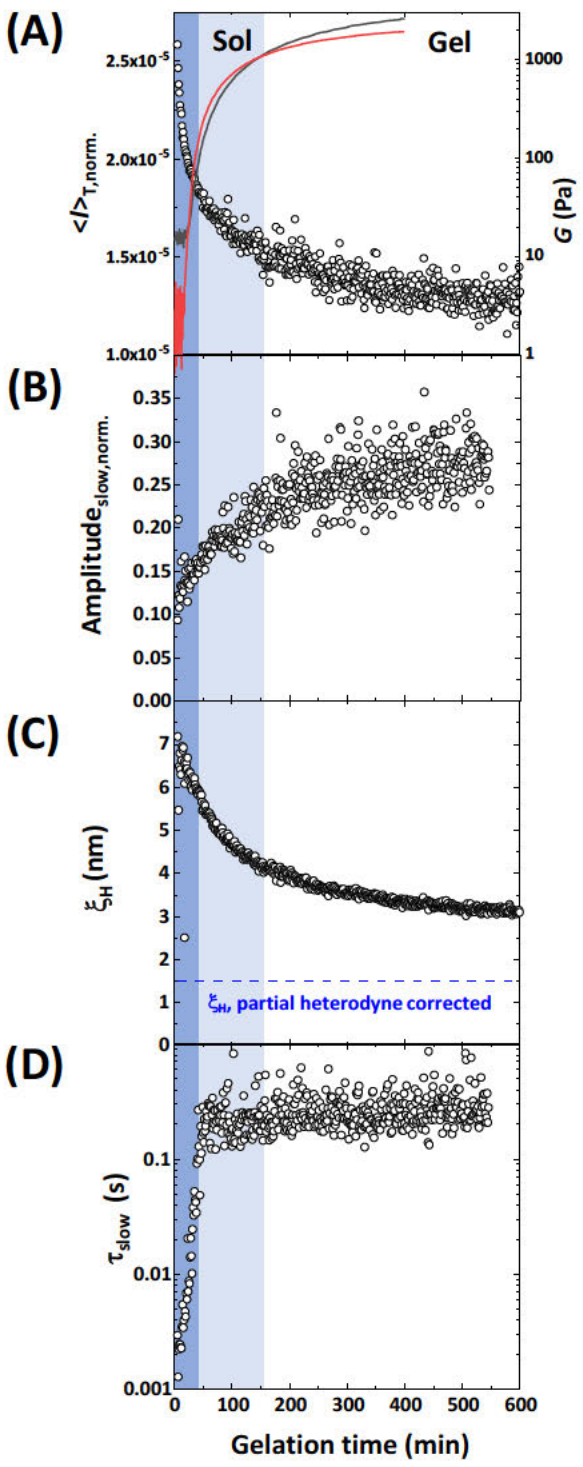

Figure 3. Gelation of a star-PEG terpyridine–zinc gel in water at a polymer concentration of 56 g L^{-1}. (A) Time-dependent normalized scattering intensity (circles), and storage (black line) and loss (red line) moduli with a gel point of 150 minutes. (B) Evolution of the intensity autocorrelation function slow mode amplitude. (C) Time-dependent decrease of the dynamic correlation length. (D) Evolution of the slow relaxation time.

groups, the metal ions are released and form a network by building the final octahedral bis-terpyridine complexes. Such a gradual decrease in pH is achieved by adding two equivalents (with respect to the metal ions) of the acidity regulator D-glucono-δ-lactone (GDL). It decomposes in water via ring-opening to form gluconic acid with a pK_a-value of 3.7 until a final pH of 4.5 is reached.[33,34] At this pH-value, the total amount of zinc cations is released from the 1 : 1 EDTA-chelate and can contribute to the network by forming complexes with terpyridine with a stability constant of $\log(K) = 6.27$.[35] Total complexation can be tracked by time-dependent UV/Vis spectroscopy where the evolution of a typical zinc-terpyridine MLCT band at 323 nm is found (figure in SI, **Figure S1**).

We employ the non-invasive light scattering method to monitor the gelation process without the application of any external shear stress. **Figure 2** shows the recorded intensity correlation functions $g^{(2)}(\tau)$ depending on the gelation time.

At the beginning of the gelation experiment, only one fast relaxation mode is present. With progressing time, a q-independent slow mode with an increasing relative amplitude evolves (**Figure 3(B)**). In addition to capturing the number and q-dependencies of the present relaxation modes, we analyze the course of the

scattering intensity during the gelation process. Instead of directly using the measured scattering intensity $\langle I \rangle_T$, we first normalize it to the intensity counts of the incident laser beam to take into account temperature-induced fluctuations of the laser beam. This normalized intensity will further be defined as $\langle I \rangle_{T,norm}$. By doing this, we find a continuous decrease until an average ratio of $1.25 \cdot 10^{-5}$ is reached (**Figure 3(A)**). This finding is in contrast to most other (chemical) gels, where the recorded intensity is remarkably enhanced during a sol–gel transition due to the excess scattering caused by spatial inhomogeneities.[13,36] Larger intensity fluctuations of partly frozen network strands are already detected after approximately 48 minutes. According to the intensity decrease and the significant reduction of the dynamic correlation length ξ_H, we presuppose that the former micellar aggregate structures of 9 nm break up during network formation. The hydrophobic terpyridine cores are pulled outwards during this process due to the enhanced hydrophilicity and repulsive interactions of a charged terpyridine–metal complex, resulting in a dynamic network with a correlation length of 1.4 nm. The proposed network formation mechanism is depicted in **Figure 4(B)**. There is no evidence for cluster formation during the gelation process, as no third diffusive mode appears during the experimental time. We conclude that the unusual larger scattering intensity of the unconnected pre-gel polymer solution compared to the gel is based on two special structural features: First, the initial presence of larger polymeric

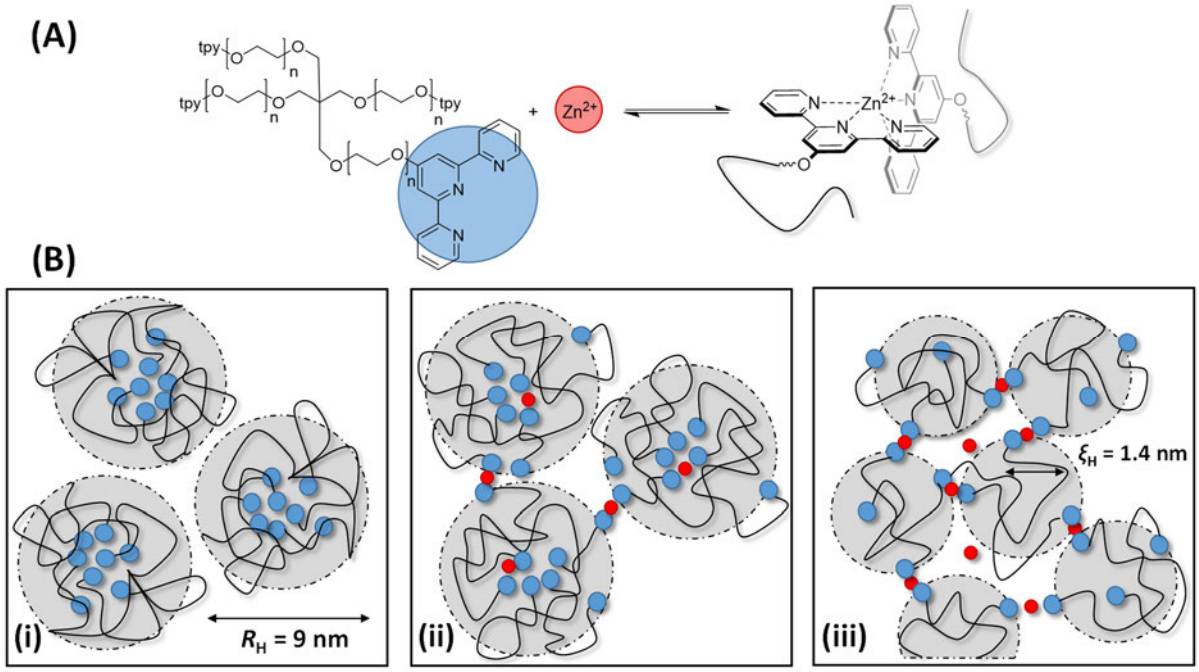

Figure 4. (A) Reaction scheme for the formation of the octahedral bis-terpyridine zinc complex. (B) Proposed gelation mechanism, starting with micellar polymer aggregates in solution with a hydrodynamic correlation length of 9 nm (i). With increasing time and zinc ion content, the hydrophobic cores start to break up to form the transient associations (ii). At completed gelation, the dynamic correlation length reaches its minimum of 1.4 nm (iii) and no more hydrophobic aggregates are present.

aggregates induces a very high scattering intensity. Second, no static inhomogeneities are found in the transiently connected gels, resulting in an unusual low scattering intensity in the gel state.

As the pH of this system is decreased and terpyridine groups are generally sensitive to protons, we further investigate the influence of a lower pH on the gelation process. For this purpose, we monitor the scattering intensity and hydrodynamic correlation length of a tetra-arm PEG-terpyridine / GDL solution without any metal ions and Na_4EDTA as a function of the pH value. These measurements reveal that the overall intensity decrease could partly be attributed to the protonation of the terpyridine heterocycles, but this process only leads to a reduction of the hydrodynamic correlation length to 5.5 nm (**Figure S4**). Due to the higher thermodynamic stability of terpyridine–zinc complexes compared to the protonated terpyridine ($\log(K_{Zn}) = 6$ vs. $\log(K_{H+}) = 4.32$),[37] we assume that the intensity decrease is nevertheless mainly governed by the formation of zinc–terpyridine complexes.

In addition to that spectroscopic assessment, we perform oscillatory shear measurements to compare the mechanical properties of gels prepared by this new method to those of gels prepared by just mixing two aqueous solutions of the polymer and the metal ions. The concentration is kept at 56 g L^{-1}. The overall curve shape can be described by the Maxwell model in all samples, but gels prepared by the delayed gelation method exhibit a slightly lower plateau modulus and higher cross-over frequencies due to the enhanced acidity of the system (rheology curves in SI, **Figure S2**). If a significant degree of terpyridine protonation occurred, this would lead to a minimized number of crosslinks in the network resulting in a significantly lower plateau modulus. As this is not the case, we conclude that protonation of terpyridine groups only plays a minor role in the gel formation process. In this context, we also emphasize that the $EDTA^{4-}$ molecules are also competing for protons. The consecutive release of zinc ions out of an Zn(II)EDTA complex can only take place if the carboxylic groups are protonated.

The gelation point is determined by rheology at the time t_{Gel}, where upon the storage modulus G' dominates over the loss modulus G''. By varying the amount of added GDL, a tailored tuning of the gelation time is possible, and we achieve gelation times in the range of 150 minutes for two equivalents of acid, 30 minutes for three equivalents, and 15 minutes for four equivalents, if we apply the same frequency of 1 Hz in all samples (figure in SI, **Figure S3**).

Following the phantom network theory approach by using the plateau modulus G_P obtained by oscillatory shear rheology, the Boltzmann constant k_B, and the absolute temperature T, it is possible to calculate the length of an elastically active chain ξ by

$$\xi = \sqrt[3]{\frac{k_B T}{G_P}} \quad (2)$$

Inserting G_P = 6166 Pa into equation (2) for the zinc gel with a polymer concentration of c = 56 g L^{-1}, we obtained ξ = 9 nm. As it has been shown,[38] neither the size of an elastic blob obtained by rheology, nor the LS dynamic correlation length can be used to appropriately calculate the real mesh size of a network.

Structure analysis of metallo-supramolecular gels by light scattering

Static light scattering

To gain further insight into the network structure and its dynamic correlations on nanoscopic length scales, simultaneous static and dynamic light scattering experiments are carried out. The three gel systems of cadmium, zinc, and nickel exhibit major differences in their intensity speckle patterns, probability distributions, and correlation functions. Gels with these metal ions are transparent and colorless and therefore suitable for light scattering experiments whereas cobalt, manganese, and iron as possible alternative ions show dark colors.

Figure 5(A) shows the averaged scattering intensities $\langle I \rangle_T$ of 500 randomly chosen points within the gels, obtained by rotating the sample cuvette prior to each measurement. Large fluctuations of $\langle I \rangle_T$ depending on the sample position are recorded in the case of nickel, whereas almost no such dependence is found for cadmium. Due to the pronounced speckle patterns, the nickel gel can be considered as a purely non-ergodic system. In contrast to that, the cadmium speckle patterns are similar to that of a solution and therefore ergodic. The zinc gel lies in between these two boundary cases, as the sticker lifetime of a zinc–terpyridine dissociation is on comparable time scales as the experimental correlation time.

As a general trend, the measured average ensemble intensity $\langle I \rangle_E$ decreases with a decrease in the metal–terpyridine dissociation constant (red line in **Figure 5(A)**). While a solution of unconnected tetra-PEG terpyridine shows an average scattering intensity of approximately 150 kHz, the scattering intensities of the networks are significantly lower; we find 72 kHz for cadmium, 69 kHz for zinc, and 47 kHz for nickel. The former micellar solution structure must change even in the case of the very weakly associating cadmium ions. We hypothesize that for the weakly associated networks with zinc and cadmium, there is a significant terpyridine fraction that is not connected to the network. As in solution, these terpyridine moieties can aggregate via π-π stacking and therefore enhance the intensity.

The nickel gel as the system with the slowest metal–ligand exchange kinetics exhibits the typical speckle pattern of a chemically connected homogeneous network where the time average $\langle \quad \rangle_T$ does not equal the ensemble average $\langle \quad \rangle_E$, thereby denoting a non-ergodic system. Its intensity population distribution $P(\langle I \rangle_T)$ in **Figure 5(B)** can be fitted by an exponential function (3) with a cutoff at the fluid intensity $\langle I_F \rangle_T$.[39]

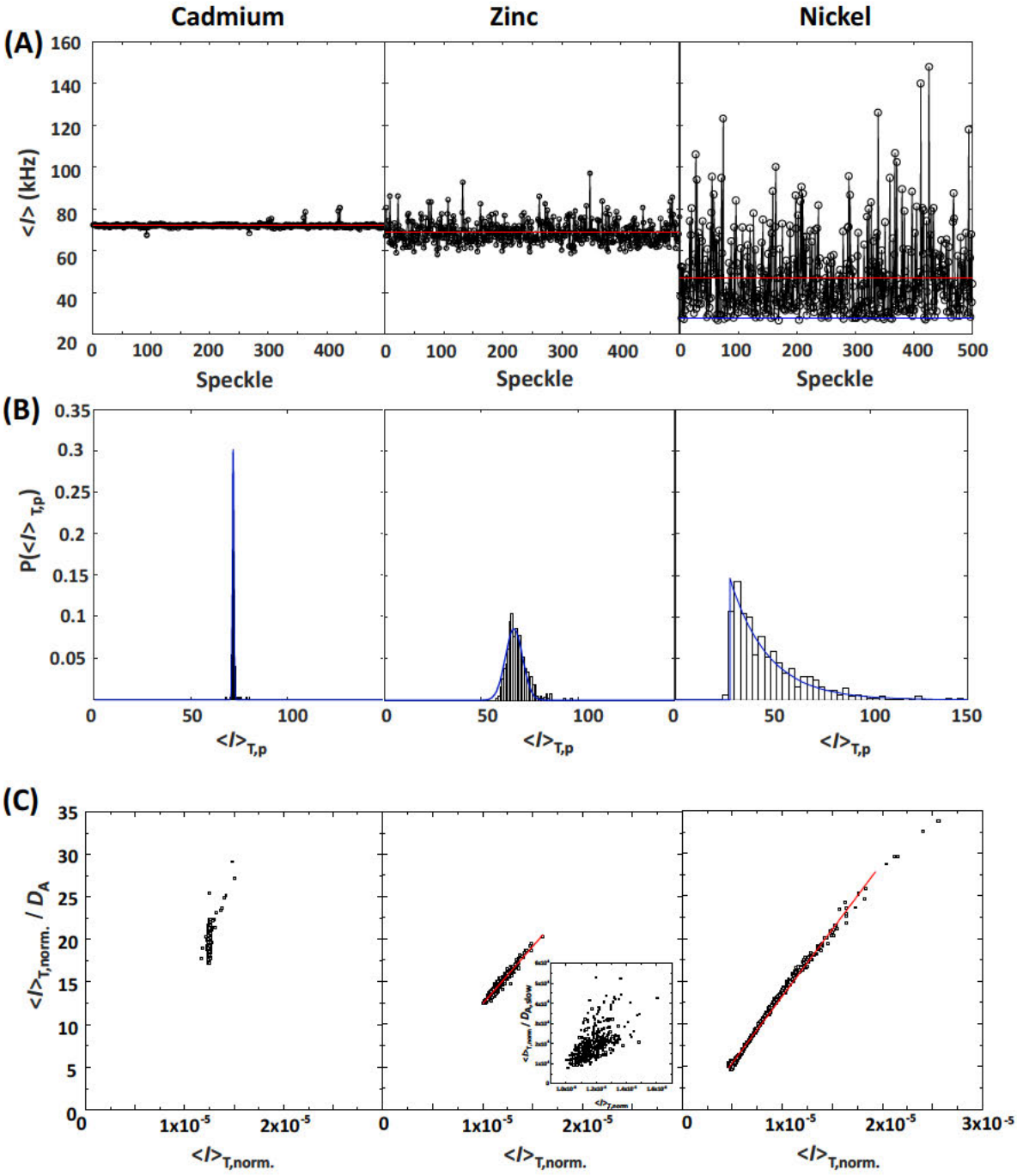

Figure 5. Comparison of the scattering properties of the metallo-supramolecular cadmium, zinc, and nickel gels. (A) Intensity speckle pattern recorded at 500 sample positions at 30 ° with $\langle I \rangle_E$ (red line) and $\langle I_T \rangle_F$ (blue line). (B) Intensity population distributions. (C) Intensity-dependent diffusion coefficients according to equation (11). Inset: The Joosten plot of the apparent slow relaxation process does not show a clear linear dependence, but instead, a dispersion of values is obtained.

$$P(\langle I\rangle_T) = a \cdot H(\langle I\rangle_T - \langle I_F\rangle_T) \cdot \exp\left(-\frac{\langle I\rangle_T - \langle I_F\rangle_T}{\langle I\rangle_E - \langle I_F\rangle_T}\right) \quad (3)$$

$H(\langle I\rangle_T - \langle I_F\rangle_T)$ denotes the Heaviside function with $H = 0$ if $(\langle I\rangle_T - \langle I_F\rangle_T) < 0$ and $H = 1$ if $\langle I\rangle_T - \langle I_F\rangle_T) \geq 0$. The function fits very well to the probability histogram, and we obtain a reasonable position-independent fluid intensity $\langle I_F\rangle_T$ = 28 kHz (see blue line in nickel speckle pattern).

In such non-ergodic media, the overall scattered intensity is composed of a fluid component $\langle I_F\rangle_T$ and a position- and angle-dependent static component $\langle I\rangle_{Excess}$. Having calculated $\langle I_F\rangle_T$, it is possible to obtain $\langle I\rangle_{Excess}$ caused by static inhomogeneities:

$$\langle I\rangle_{Excess} = \langle I\rangle_E - \langle I_F\rangle_T \quad (4)$$

$\langle I\rangle_{Excess}^{-0.5}$ is plotted against each angle q^2, and according to the Debye–Bueche approach,[40,41] which regards gels as two-phase systems with randomly distributed micro-phase separated domains, the static correlation length Ξ is obtained from the slope and ordinate intercept.[2]

$$\langle I\rangle_{Excess}^{-0.5} = \frac{1 + q^2\Xi^2}{\left(\rho_{Polymer} - \rho_{Solvent}\right) \cdot \sqrt{8\pi \cdot \Xi^3 \langle c^2\rangle}} \quad (5)$$

The Debye–Bueche plot of the nickel gel in **Figure 6** shows no significant angular dependence of the excess scattering, leading to the conclusion that no static correlation lengths larger than the instrument resolution of 10 nm are present. Therefore, we consider the nickel gel as a homogeneous network on the length scales of laser light scattering.

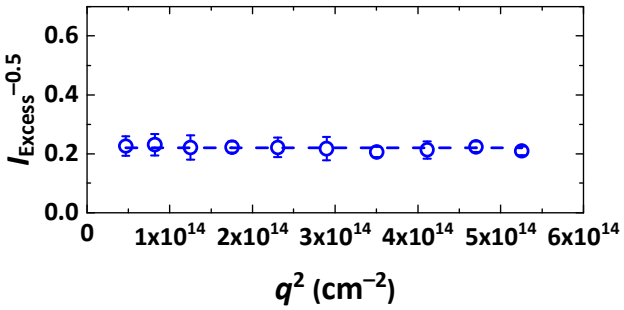

Figure 6. Debye–Bueche plot of the excess scattering intensity caused by spatial heterogeneities (open circles) vs. scattering vector q^2 for the nickel gel at a polymer concentration of 56 g L^{-1} and linear data fit (dashed line). No heterogeneities larger than the 10 nm instrument resolution are detected.

In contrast to that, the scattering properties of the weaker associated zinc and cadmium gels differ significantly from those of the nickel gel. Although the zinc gel shows the onset of typical speckle-dependent intensity fluctuations, its population distribution cannot be fitted by an exponential decay as there exists no clear lower cutoff intensity. Instead, a Gaussian distribution is used to phenomenologically fit the histogram shape (**Figure 5(B)**). Such a histogram shape might result from a superposition of several intensity distributions with multiple fluid intensities. Due to the fast ligand exchange kinetics in the cadmium and zinc gels, simultaneous detaching of one to four arms from the network is possible, thereby leading to fluctuations in the fluid intensity.

The intensity speckle pattern of the cadmium network shows no large fluctuations and is comparable to that of a semi-dilute polymer solution. We consider this system to be ergodic as $\langle I \rangle_E = \langle I \rangle_T$. Again, a narrow Gaussian distribution of scattering intensities is recorded (**Figure 5(B)**). In both networks with fast ligand exchange kinetics (cadmium and zinc), the determination of a fluidic contribution to the total scattering intensity analogous to the nickel gel is not possible.

Dynamic light scattering

The dynamic correlation length ξ_H gives further insight into the structural properties, as it can be generally related to the mesh size of a network.

Due to non-ergodicity of the zinc and nickel gels, the time-averaged autocorrelation functions $g^{(2)}(\tau)$ of 500 positions within the gels cannot be directly converted into the electric field correlation functions $g^{(1)}(\tau)$ via Siegert relation. Instead, the partial heterodyne method (PHD) introduced by Joosten *et al.*,[42] with the homodyne scattering contribution $X = \langle I_F \rangle_T / \langle I \rangle_T$ and the recorded intensity $I(t)$ is used to analyze the DLS data.

$$g^{(2)}(\tau) = \frac{\langle I(t)\, I(t+\tau) \rangle}{\langle I(t) \rangle^2} = X^2 \cdot g^{(1)}(\tau)^2 + 2X \cdot (1-X) \cdot g^{(1)}(\tau) + 1 \qquad (6)$$

Figure 7 exemplarily shows the time-averaged autocorrelation functions $g^{(2)}(\tau)$ of all three gels, measured at a temperature of 20 °C. For the zinc gel (blue symbols), two distinct relaxation modes are present with characteristic relaxation times that differ from each other by three orders of magnitude. Therefore, a sum of a stretched decay for the slow relaxation process and an unstretched decay for the fast process is used, where $b2$ and $b1$ are their respective amplitudes, τ_{fast} and τ_{slow} are the characteristic relaxation times, and α is the stretch exponent.

$$g^{(2)}(\tau) - 1 = A + \{ b1 \cdot \exp\left(-\frac{\tau}{\tau_{fast}}\right) + b2 \cdot \exp\{ \left(-\left(\frac{\tau}{\tau_{slow,KWW}} \right)^{\alpha} \right) \}^2 \qquad (7)$$

A stretch exponent α below one indicates a distribution of relaxation times and the average time $<\tau_{slow}>$ is calculated

$$\langle \tau_{slow} \rangle = \frac{\tau_{slow,KWW}}{\alpha} \cdot \Gamma\left(\frac{1}{\alpha}\right) \qquad (8)$$

with the gamma function Γ. Thus, α can be seen as a measure of heterogeneity of the dynamic processes of a system.

The fast diffusion coefficient D_{Gel} is then obtained by

$$D_{Gel,fast} = \frac{1}{q^2 \langle \tau_{fast} \rangle} \qquad (9)$$

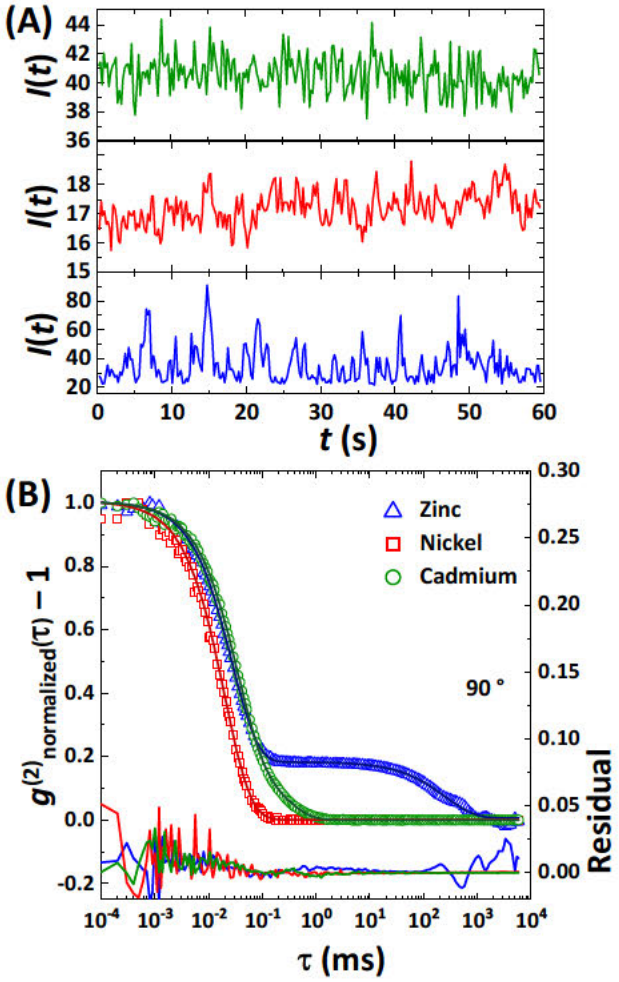

Figure 7. (A) Recorded single run intensity traces of a cadmium (green), a nickel (red), and a zinc (blue) tetra-arm PEG-terpyridine gel (M_w = 10,924 g mol^{-1}) at a polymer concentration of 56 g L^{-1}, recorded at a scattering angle of 90 ° and a temperature of 20 °C. (B) Corresponding normalized time-averaged autocorrelation functions $g^{(2)}(\tau)$ of the zinc (blue triangles), cadmium (green circles), and nickel (red squares) gels and residuals of the chosen fit functions (solid lines).

In partial heterodyne scattering processes, the obtained diffusion coefficients D_{PHD} depend on X and can be expressed by

$$D_{PHD} = (2 - X) \cdot D_{Gel} \tag{10}$$

In case of pure homodyne scattering ($X = 1$), the partial heterodyne diffusion coefficients D_{PHD} equal the collective gel diffusion coefficients D_{Gel}, whereas if $0 < X < 1$, frozen heterogeneities become dominant. A linearized form of equation (11) with the time-averaged intensity $\langle I \rangle_T$ of a position p within the sample is used to decompose the static and dynamic scattering contributions and calculate D_{PHD} as well as the fluid intensity $\langle I_F \rangle_T$:[43,44]

$$\frac{\langle I \rangle_T}{D_{Gel}} = \frac{2}{D_{PHD}} \langle I \rangle_T - \frac{\langle I_F \rangle_T}{D_{PHD}} \tag{11}$$

By plotting the ratio $\frac{\langle I\rangle_{\mathrm{T,norm.}}}{D_{\mathrm{PHD}}}$ versus the recorded normalized intensity $\langle I\rangle_{\mathrm{T,norm.}}$ in **Figure 5(C)**, the data points show a linear relation for the fast relaxation time, proving that the partial heterodyne method is not only suitable for the data evaluation of permanently crosslinked gels, but also for transiently associated ones. We obtain an angular-independent fast diffusion coefficient $D_{\mathrm{PHD,fast}} = (1.53 \pm 0.03) \cdot 10^{-6}\ \mathrm{cm^2\ s^{-1}}$. This fast mode has also been found in many other works and is assigned to the collective motion of the PEG strands between two dynamic crosslinks.[21,23,26]

The hydrodynamic correlation length ξ_{H} of these fast concentration fluctuations is further calculated with the Stokes–Einstein–equation (12), where η is the solvent viscosity, k_{B} is the Boltzmann energy, and T is the temperature, resulting in $\xi_{\mathrm{H}} = (1.49 \pm 0.02)$ nm.

$$\xi_{\mathrm{H}} = \frac{k_{\mathrm{B}} T}{6\pi\eta D_{\mathrm{PHD,fast}}} \tag{12}$$

The slower relaxation process does not show such a linear dependence on the recorded intensity, but instead, rather a broad dispersion of values is obtained (see inset of **Figure 5(C)**).

The corresponding slow relaxation times do not depend on the observed length scales q, and an average inverse relaxation time of $\tau_{\mathrm{slow}} = (2.69 \pm 1.03)\ \mathrm{s^{-1}}$ is found. This large deviation of 40% depending on the sample position might represent the dynamic heterogeneity within the zinc gel. The ability of the hydrophobic terpyridine groups to randomly agglomerate into clusters via π-π stacking leads to a broad distribution of network relaxation times. This effect is also indicated by the broad distribution of stretch exponents and even values greater than one, if we do not constrain the fit parameters (**Figure S5**). As the overall dynamics of this system is fast, these temporary small interactions are not detected by our static light scattering experiments.

In contrast to other works that attributed the existence of a third mode to the diffusion of different sized clusters within the gel,[21–24] no such slow diffusive mode is found in this study.

Unlike the zinc gel, only one relaxation mode is found in the case of nickel, and the time-averaged intensity correlation function $g^{(2)}(\tau)$ is fitted with a mono-exponential decay and the characteristic relaxation time τ_{Nickel}.

$$g^{(2)}(\tau) - 1 = A + \{b1 \cdot \exp\left(-\frac{\tau}{\tau_{\mathrm{Nickel}}}\right)\}^2 \tag{13}$$

By re-arranging the obtained intensity-dependent apparent diffusion coefficients according to equation (11), we find a linear dependency, resulting in a gel diffusion coefficient $D_{\mathrm{Nickel}} = (1.27 \pm 0.05) \cdot 10^{-6}\ \mathrm{cm^2\ s^{-1}}$ with a corresponding hydrodynamic correlation length of $\xi_{\mathrm{H}} = (1.68 \pm 0.02)$ nm. The obtained diffusion coefficients show no angular dependence.

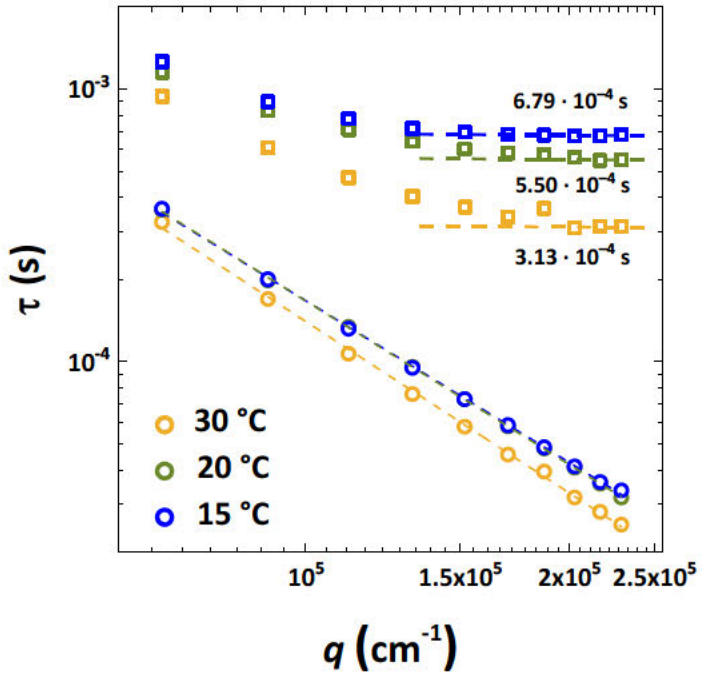

Figure 8. q-dependences of the fast (open circles) and slow (open squares) relaxation times of the tetra-arm PEG-terpyridine cadmium gel (M_w = 10,924 g mol^{-1}) at a polymer concentration of 56 g L^{-1}, measured at the temperatures of 15 °C (blue), 20 °C (green), and 30 °C (yellow). At all temperatures, the fast mode is purely diffusive with a linear q^2-dependence, whereas the slow relaxation time shows a transition from a diffusive (q^{-2}) to a viscoelastic (q^0) motion.

For the cadmium gel, all obtained apparent diffusion coefficients coincide in **Figure 5(C)**, and we consider this system to be ergodic with pure homodyne scattering and X= 1. A homodyne fitting procedure is chosen because the amplitudes of the time-averaged intensity autocorrelation functions do not depend on the recorded intensity and the baseline is reached in all functions $g^{(1)}(\tau)$.

The curve fitting with again the sum of a stretched and an unstretched exponential decay reveals a fast diffusion coefficient of $D_{fast} = (5.98 \pm 0.20) \cdot 10^{-7}$ cm^2 s^{-1} and a corresponding hydrodynamic correlation length of $\xi_H = 3.59 \pm 0.10$ nm is calculated. Even though the terpyridine-cadmium complex exhibits very fast dissociation kinetics, the pre-gel micellar solution structure changes upon addition of cadmium ions, and the obtained correlation length is much smaller than the previous 9 nm of the unconnected polymer solution. **Figure 8** shows that the slow process is non-Fickian and exhibits a transition from a diffusive to a viscoelastic relaxation depending on the observed length scale q.

The slow relaxation time at 20 °C (green symbols in **Figure 8**) decreases with an increase in q until it approaches a q-independent value of 5.5 · 10^{-4} s, that is similar to the polymer network strand relaxation at small angles. On small length scales (large q-values), the fast relaxation time is faster by a factor

of 17, whereas on larger length scales (small q-values), the difference between both relaxation times is decreased to a factor of 3.

Table 1. Comparison of $\langle I \rangle_E$, $\langle I_F \rangle_T$, D_{PHD}, and ξ_H for the equi-concentrated cadmium, zinc, and nickel gels, obtained by light scattering experiments.

	Cadmium	Zinc	Nickel
$\langle I \rangle_E$ (kHz)	72	69	47
$\langle I_F \rangle_T$ (kHz)	-	-	28
D_{PHD} (cm^2 s^{-1})	$(5.98 \pm 0.20) \cdot 10^{-7}$	$(1.53 \pm 0.03) \cdot 10^{-6}$	$(1.27 \pm 0.05) \cdot 10^{-6}$
ξ_H (nm)	3.59 ± 0.10	1.49 ± 0.02	1.68 ± 0.20

Temperature sweep

To further examine the origin of the slow mode in the zinc and cadmium gels, we conduct scattering experiments at different temperatures: 15 °C, 20 °C, 30 °C and 40 °C. **Figure 9(B)** exemplarily shows the recorded time-averaged intensity correlation functions of a zinc gel at all measured temperatures, normalized by temperature and solvent viscosity. An increase of the ensemble average scattering intensity with increasing temperature is observed from 69 kHz over 87 kHz to 117 kHz (figure in SI, **Figure S6**).

This finding can possibly be explained by the reduced solubility of PEG in water at higher temperatures due to the increased Flory-Huggins parameter χ.[17] The statistical frequencies of the stretch exponent α, the normalized amplitude of the slow process $b2n$, and the slow and fast relaxation times can be fitted according to normal distributions to obtain the characteristic mean values and standard deviations. With an increase in temperature, all distributions become narrower. The normalized amplitude of the slow mode rises linearly from 0.317 to 0.434, whereas both relaxation times decrease.

The stretch exponent α decreases from 0.970 to 0.882 (see **Figure S5**), indicating that the dynamic processes of the gel become more heterogeneous with a temperature increase. No significant q-dependence of the slow relaxation time is detected at all measured temperatures (see **Figure 9(A)**).

Assuming an Arrhenius-type behavior (equation (14)) with the temperature T, the universal gas constant R, and the dissociation constant $k = \tau^{-1}$, the activation energy E_A is calculated as

$$\frac{1}{\tau} \propto \exp\left(-\frac{E_A}{RT}\right) \tag{14}$$

We obtain $E_{A,LS\ slow,zinc} = (58 \pm 1)$ kJ mol^{-1} for the slow relaxation process and $E_{A,LS\ fast,zinc} = (12.4 \pm 0.7)$ kJ mol^{-1} for the fast one. A value in the same order of magnitude was found by Ozaki *et al.*[23] If the slow mode is assigned to the macroscopic viscoelastic network relaxation, its temperature dependence must be similar to that measured by oscillatory shear rheology as this process is mainly governed by the zinc-terpyridine junction dissociation. The inverse of the storage and loss modulus cross-over frequency is generally defined as the network relaxation time and is thus used for the determination of the activation energy according to equation (14) (**Figure S7**). The rheology-based activation energy $E_{A,Rheology} = (60 \pm 2)$ kJ mol^{-1} is (within the error) very similar to the one determined by light scattering. However, the absolute relaxation times measured by light scattering are faster by a factor of 3.5 (see inset **Figure 9(A)**). A similar difference between light scattering and rheology has been found in physical PVA-borax gels by Hébraud *et al.*[24] The temperature-dependent results for the cadmium gels are depicted in **Figure 8**. The slow mode transition from a diffusive to a viscoelastic relaxation mode is present at all three temperatures; however, the q-independent relaxation times at high angles (high q-values) do exhibit a remarkable temperature-dependence. Analogous to the slow relaxation mode in the zinc gels, we found a similar Arrhenius behavior (**Figure 9** (inset, blue symbols)) and calculated an activation energy of $E_{A,LS\ slow,cadmium} = (38 \pm 3)$ kJ mol^{-1}. As expected due to the faster dissociation constant, the obtained activation energy is lower compared to the zinc gel. These

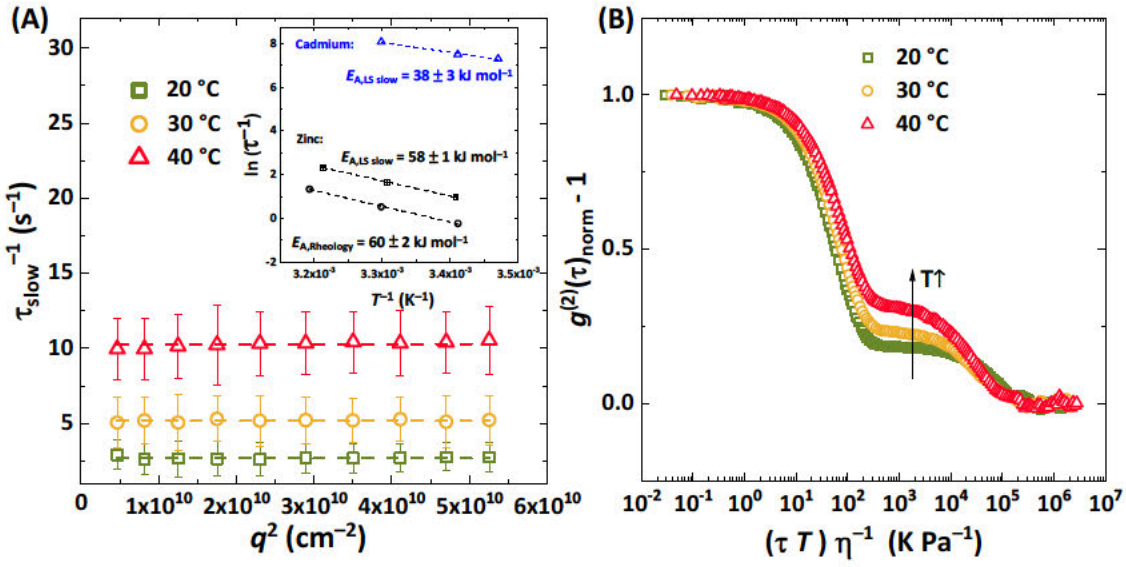

Figure 9. (A) Inverse slow relaxation time vs. scattering vector reveals no q-dependence at all chosen temperatures. Inset: Comparison of the Arrhenius-type relaxation times of the cadmium (blue symbols) and zinc gel (black symbols), obtained by light scattering (squares and triangles) and oscillatory shear rheology (circles). (B) Time-averaged autocorrelation functions of a tetra-arm PEG-terpyridine gel, connected through zinc nitrate with a polymer concentration of 56 g L^{-1}, at the temperatures 20 °C (green squares), 30 °C (yellow circles), and 40 °C (red triangles). The curves are normalized by the temperature and viscosity and show an increase in the slow mode amplitude with increasing temperature.

findings in both gels confirm the assumption that the q-independent slow mode is coupled to the macroscopic viscoelastic network relaxation on time scales of the terpyridine–metal junction dissociation.

4.2.5 Conclusion

Comparison of all network types

We have successfully characterized the scattering properties of metallo-supramolecular polymer hydrogels consisting of transiently connected tetra-arm PEG-terpyridine through ions of zinc, cadmium, and nickel. A preparation method based on a tunable delayed gelation has been implemented that opens the possibility to understand the underlying dynamic processes without creation artefacts.

On length scales of laser light scattering, we obtained networks that exhibit major differences in their scattering profiles depending on the strength of association. **Figure 10** compares all time scales of the found relaxation modes and their corresponding q-dependences. The nickel gel is comparable to chemically connected tetra-PEG networks. In addition to the fast cooperative polymer diffusion that has been found in all investigated systems (with a log–log slope of -2 in a τ vs. q plot), a q-independent slow mode is present in the zinc gel at the full investigated q-range. Its relation to the macroscopic network stress relaxation is proven in complementary temperature experiments. Although no heterogeneities could be revealed by our SLS experiments, the broad distribution of network relaxation times could be interpreted as result of microscopic terpyridine aggregation.

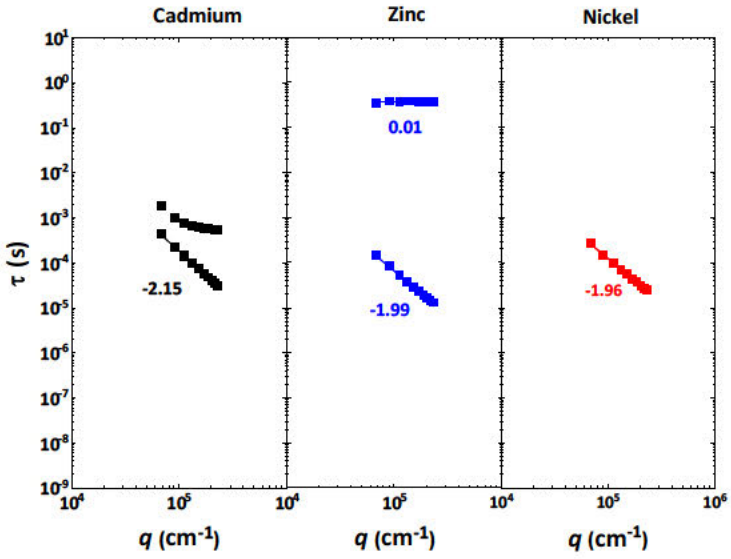

Figure 10. Comparison of the q-dependences of all relaxation modes found in the cadmium (black symbols), zinc (blue symbols), and nickel (red symbols) gels. The fast and slow relaxation times are obtained by homodyne data fitting in the case of cadmium, and partial heterodyne fitting of the nickel and zinc gel data.

The cadmium gel exhibits unique scattering properties, as the dissociation time of a terpyridine junction and the network strand fluctuation happen on comparable time scales. Therefore, the relaxation modes are discussed considering the effect of the observed length scale.

The scattering properties of transiently connected polymer gels are substantially influenced by the time scales of chain relaxation and sticker dissociation. In addition to that, a thorough sample preparation is crucial to avoid larger heterogeneities within the gel. We believe that this study provides valuable insights into the underlying network structure and resulting dynamics and can further serve as a fundament to understand more complex systems.

4.2.6 Acknowledgement

This work was supported by the German Research Foundation (DFG) under grant no. SE 1888/7-1 (Project No. 376900084).

4.2.7 References

(1) Pusey, P. N.; van Megen, W. Dynamic light scattering by non-ergodic media. *Physica A: Statistical Mechanics and its Applications* **1989**, *157*, 705–741.

(2) Seiffert, S. Scattering perspectives on nanostructural inhomogeneity in polymer network gels. *Progress in Polymer Science* **2017**, *66*, 1–21.

(3) Kopecek, J. Hydrogel biomaterials: a smart future? *Biomaterials* **2007**, *28*, 5185–5192.

(4) Singh, M. R.; Patel, S.; Singh, D. Chapter 9: Natural polymer-based hydrogels as scaffolds for tissue engineering. Nanobiomaterials in Soft Tissue Engineering 2016, 5, 231–260.

(5) Stengelin, E.; Kuzmina, A.; Beltramo, G. L.; Koziol, M. F.; Besch, L.; Schröder, R.; Unger, R. E.; Tremel, W.; Seiffert, S. Biotherapeutics: Bone Scaffolds Based on Degradable Vaterite/PEG-Composite Microgels (Adv. Healthcare Mater. 11/2020). *Adv. Healthcare Mater.* **2020**, *9*, 2070030.

(6) Holten-Andersen, N.; Harrington, M. J.; Birkedal, H.; Lee, B. P.; Messersmith, P. B.; Lee, K. Y. C.; Waite, J. H. pH-induced metal-ligand crosslinks inspired by mussel yield self-healing polymer networks with near-covalent elastic moduli. *Proceedings of the National Academy of Sciences of the United States of America* **2011**, *108*, 2651–2655.

(7) Shi, L.; Ding, P.; Wang, Y.; Zhang, Y.; Ossipov, D.; Hilborn, J. Self-Healing Polymeric Hydrogel Formed by Metal-Ligand Coordination Assembly: Design, Fabrication, and Biomedical Applications. *Macromolecular rapid communications* **2019**, *40*, e1800837.

(8) Chen, P.; Li, Q.; Grindy, S.; Holten-Andersen, N. White-Light-Emitting Lanthanide Metallogels with Tunable Luminescence and Reversible Stimuli-Responsive Properties. *J. Am. Chem. Soc.* **2015**, *137*, 11590–11593.

(9) Seiffert, S.; Sprakel, J. Physical chemistry of supramolecular polymer networks. *Chemical Society reviews* **2012**, *41*, 909–930.

(10) Voorhaar, L.; Hoogenboom, R. Supramolecular polymer networks: hydrogels and bulk materials. *Chemical Society reviews* **2016**, *45*, 4013–4031.

(11) Golkaram, M.; Loos, K. A Critical Approach to Polymer Dynamics in Supramolecular Polymers. *Macromolecules* **2019**, *52*, 9427–9444.

(12) Shibayama, M. Universality and Specificity of Polymer Gels Viewed by Scattering Methods. *BCSJ* **2006**, *79*, 1799–1819.

(13) Shibayama, M.; Norisuye, T. Gel Formation Analyses by Dynamic Light Scattering. *BCSJ* **2002**, *75*, 641–659.

(14) Ikkai, F.; Shibayama, M. Inhomogeneity control in polymer gels. *J. Polym. Sci. Part B: Polym. Phys.* **2005**, *43*, 617–628.

(15) Fujiyabu, T.; Yoshikawa, Y.; Kim, J.; Sakumichi, N.; Chung, U.-i.; Sakai, T. Shear Modulus Dependence of the Diffusion Coefficient of a Polymer Network. *Macromolecules* **2019**, *52*, 9613–9619.

(16) Tsuji, Y.; Nakagawa, S.; Gupit, C. I.; Ohira, M.; Shibayama, M.; Li, X. Selective Doping of Positive and Negative Spatial Defects into Polymer Gels by Tuning the Pregel Packing Conditions of Star Polymers. Macromolecules. *Macromolecules* **2020**, *53*, 7537–7545.

(17) Ohira, M.; Li, X.; Gupit, C. I.; Kamata, H.; Sakai, T.; Shibaya-ma, M. Dynamics of thermoresponsive conetwork gels composed of poly(ethylene glycol) and poly(ethyl glycidyl ether-co-methyl glycidyl ether). *Polymer* **2018**, *155*, 75–82.

(18) Michel, E.; Cipelletti, L.; d'Humieres, E.; Gambin, Y.; Urbach, W.; Porte, G.; Appell, J. Self-diffusion and collective diffusion in a model viscoelastic system. *Physical review. E, Statistical, nonlinear, and soft matter physics* **2002**, *66*, 31402.

(19) Michel, E.; Filali, M.; Aznar, R.; Porte, G.; Appell, J. Percolation in a Model Transient Network: Rheology and Dynamic Light Scattering †. *Langmuir* **2000**, *16*, 8702–8711.

(20) Dai, S.; Tam, K. C.; Jenkins, R. D. Dynamic Light Scattering of Semi-Dilute Hydrophobically Modified Alkali-Soluble Emulsion Solutions with Varying Length of Hydrophobic Alkyl Chains. *Macromol. Chem. Phys.* **2002**, *203*, 2312–2321.

(21) Bohdan, M.; Sprakel, J.; van der Gucht, J. Multiple relaxation modes in associative polymer networks with varying connectivity. *Physical review. E* **2016**, *94*, 32507.

(22) Blanco, M. C.; Leisner, D.; Vázquez, C.; López-Quintela, M. A. Dynamic Light Scattering in Transient Reversible Gels †. *Langmuir* **2000**, *16*, 8585–8594.

(23) Ozaki, H.; Indei, T.; Koga, T.; Narita, T. Physical gelation of supramolecular hydrogels crosslinked by metal-ligand interactions: Dynamic light scattering and microrheological studies. Polymer 2017, 128, 363–372.

(24) Narita, T.; Mayumi, K.; Ducouret, G.; Hébraud, P. Viscoelastic Properties of Poly(vinyl alcohol) Hydrogels Having Permanent and Transient Cross-Links Studied by Microrheology, Classical Rheometry, and Dynamic Light Scattering. *Macromolecules* **2013**, *46*, 4174–4183.

(25) Ikkai, F.; Shibayama, M. Static Inhomogeneities in Thermoreversible Physical Gels. *Phys. Rev. Lett.* **1999**, *82*, 4946–4949.

(26) Shibayama, M.; Tsujimoto, M.; Ikkai, F. Static Inhomogeneities in Physical Gels: Comparison of Temperature-Induced and Concentration-Induced Sol–Gel Transition. *Macromolecules* **2000**, *33*, 7868–7876.

(27) Holyer, R. H.; Hubbard, C. D.; Kettle, S. F. A.; Wilkins, R. G. The Kinetics of Replacement Reactions of Complexes of the Transition Metals with 2,2',2''-Terpyridine. *Inorg. Chem.* **1966**, *5*, 622–625.

(28) Koziol, M.; Fischer, K.; Seiffert, S. Origin of the low-frequency plateau and the light-scattering slow mode in semidilute poly(ethylene glycol) solutions. *Soft matter* **2019**, *15*, 2666–2676.

(29) Chiper, M.; Hoeppener, S.; Schubert, U. S.; Fustin, C.-A.; Go-hy, J.-F. Self-Assembly Behavior of Bis(terpyridine) and Metallo-bis(terpyridine) Pluronics in Dilute Aqueous Solutions. *Macromol. Chem. Phys.* **2010**, *211*, 2323–2330.

(30) Nolan; Phillips; Cotts; Dungan. Light Scattering Study on the Effect of Polymer Composition on the Structural Properties of PEO-PPO-PEO Micelles. *Journal of colloid and interface science* **1997**, *191*, 291–302.

(31) Schillén, K.; Jansson, J.; Löf, D.; Costa, T. Mixed micelles of a PEO-PPO-PEO triblock copolymer (P123) and a nonionic surfactant (C12EO6) in water. a dynamic and static light scattering study. *The journal of physical chemistry. B* **2008**, *112*, 5551–5562.

(32) Wanka, G.; Hoffmann, H.; Ulbricht, W. The aggregation behavior of poly-(oxyethylene)-poly-(oxypropylene)-poly-(oxyethylene)-block-copolymers in aqueous solution. *Colloid & Polymer Sci* **1990**, *268*, 101–117.

(33) Pocker, Y.; Green, E. Hydrolysis of D-glucono-delta-lactone. I. General acid-base catalysis, solvent deuterium isotope effects, and transition state characterization. *Journal of the American Chemical Society* **1973**, *95*, 113–119.

(34) Ramachandran, S.; Fontanille, P.; Pandey, A.; Larroche, C. Gluconic Acid: Properties, Applications and Microbial Production. *Food Technol. Biotechnol.* **2006**, *44*, 185–195.

(35) Catapano, M. C.; Tvrdý, V.; Karlíčková, J.; Mercolini, L.; Mladěnka, P. A simple, cheap but reliable method for evaluation of zinc chelating properties. *Bioorganic chemistry* **2018**, *77*, 287–292.

(36) Norisuye, T.; Shibayama, M.; Nomura, S. Time-resolved light scattering study on the gelation process of poly(N-isopropyl acrylamide. *Polymer* **1998**, *39*, 2769–2775.

(37) Hamilton, J. M.; Anhorn, M. J.; Oscarson, K. A.; Reibenspies, J. H.; Hancock, R. D. Complexation of metal ions, including alkali-earth and lanthanide(III) ions, in aqueous solution by the ligand 2,2',6',2''-terpyridyl. *Inorg. Chem.* **2011**, *50*, 2764–2770.

(38) Tsuji, Y.; Li, X.; Shibayama, M. Evaluation of Mesh Size in Model Polymer Networks Consisting of Tetra-Arm and Linear Poly(ethylene glycol)s. *Gels* (Basel, Switzerland) **2018**, *4*.

(39) Rodd, A. B.; Dunstan, D. E.; Boger, D. V.; Schmidt, J.; Bur-chard, W. Heterodyne and Non-ergodic Approach to Dynamic Light Scattering of Polymer Gels: Aqueous Xanthan in the Presence of Metal Ions (Aluminum(III)). *Macromolecules* **2001**, *34*, 3339–3352.

(40) Debye, P.; Bueche, A. M. Scattering by an Inhomogeneous Solid. Journal of Applied Physics, 20(6), 518-525. *Journal of Applied Physics* **1949**, *20*, 518–525.

(41) Pekeris, C. L. Note on the Scattering of Radiation in an Inhomogeneous Medium. *Physical review* **1947**, *71*, 268–269.

(42) Joosten, J. G. H.; McCarthy, J. L.; Pusey, P. N. Dynamic and static light scattering by aqueous polyacrylamide gels. *Macromolecules* **1991**, *24*, 6690–6699.

(43) Shibayama, M. Spatial inhomogeneity and dynamic fluctuations of polymer gels. *Macromol. Chem. Phys.* **1998**, *199*, 1–30.

(44) Sakai, T.; Matsunaga, T.; Yamamoto, Y.; Ito, C.; Yoshida, R.; Suzuki, S.; Sasaki, N.; Shibayama, M.; Chung, U.-i. Design and Fabrication of a High-Strength Hydrogel with Ideally Homogeneous Network Structure from Tetrahedron-like Macromonomers. *Macromolecules* **2008**, *41*, 5379–5384.

4.2.8 Supporting Information

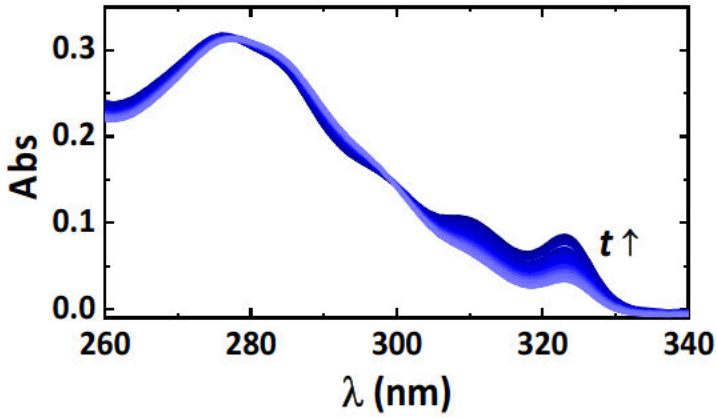

Figure S1. Time-dependent evolution of the zinc–terpyridine MLCT band, monitored via UV–vis spectroscopy during the complex formation process of zinc ions with tetra-arm PEG-terpyridine (M_w = 10,000 g mol^{-1}), in presence of the additives EDTA and GDL.

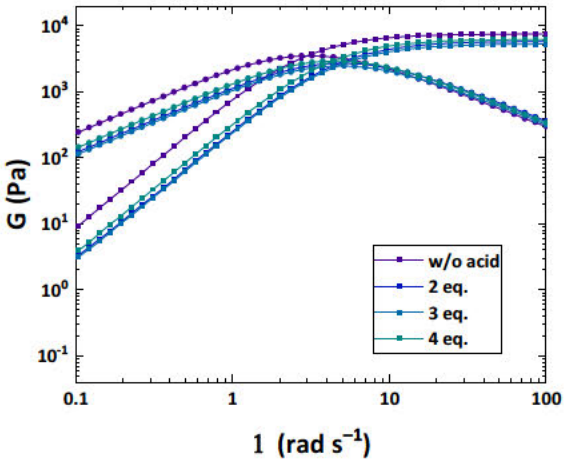

Figure S2. Comparison of the storage (filled circles) and loss (filled squares) moduli for zinc–tetra-arm PEG-terpyridine gels (c = 56 g L^{-1}) prepared by mixing two aqueous solutions of polymer and metal ions (purple) and gels prepared by a delayed gelation with the additive of 2 equivalents (dark blue), 3 equivalents (light blue), and 4 equivalents (green) of GDL.

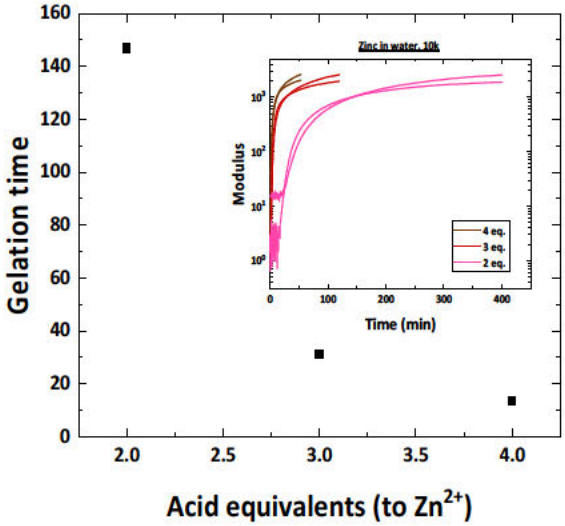

Figure S3. Gelation times depending on the amount of added GDL. Inset: Determination of the gelation time by rheology. The storage and loss moduli of three zinc tetra-arm PEG-terpyridine gels ($c = 56$ g L^{-1}) with different GDL content are plotted versus time (pink line: 2 eq. acid, red line: 3 eq. acid, and brown line: 4 eq. acid).

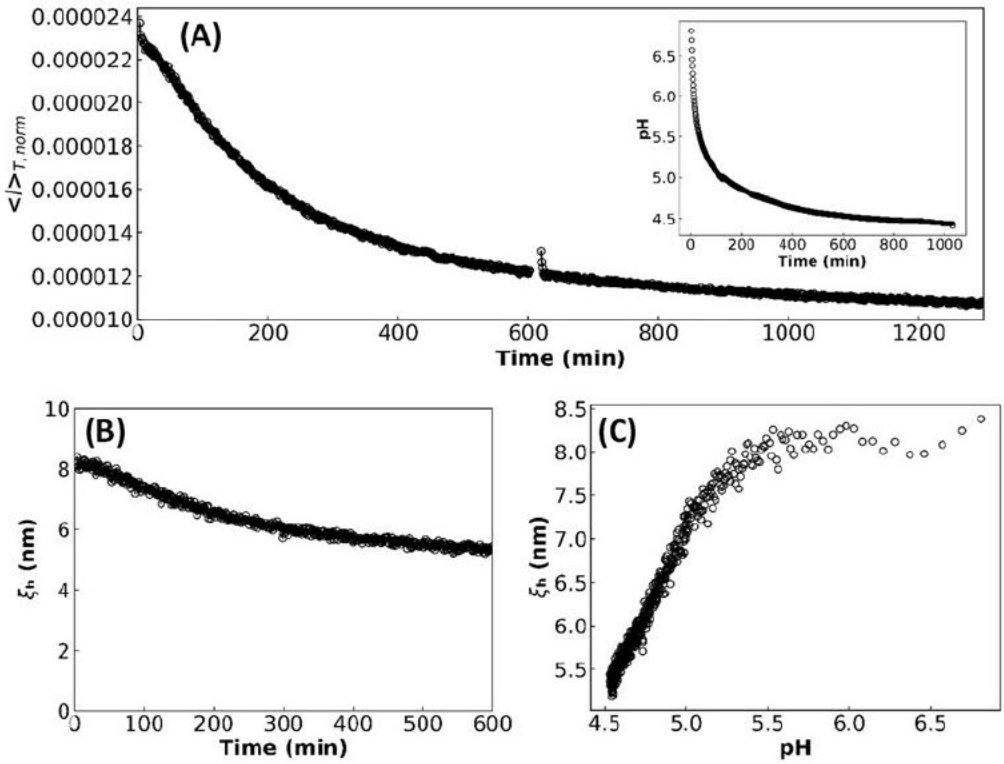

Figure S4. (A) Time-dependent normalized scattering intensity of an aqueous solution of tetra-arm PEG-terpyridine (56 g L^{-1}) and GDL (1 eq. with respect to terpyridine groups). Inset: Evolution of pH over time due to hydrolysis of GDL. (B) The calculated hydrodynamic correlation length of the polymer is decreasing from 8 nm to 5.5 nm over time. (C) Correlation between the hydrodynamic correlation length and pH.

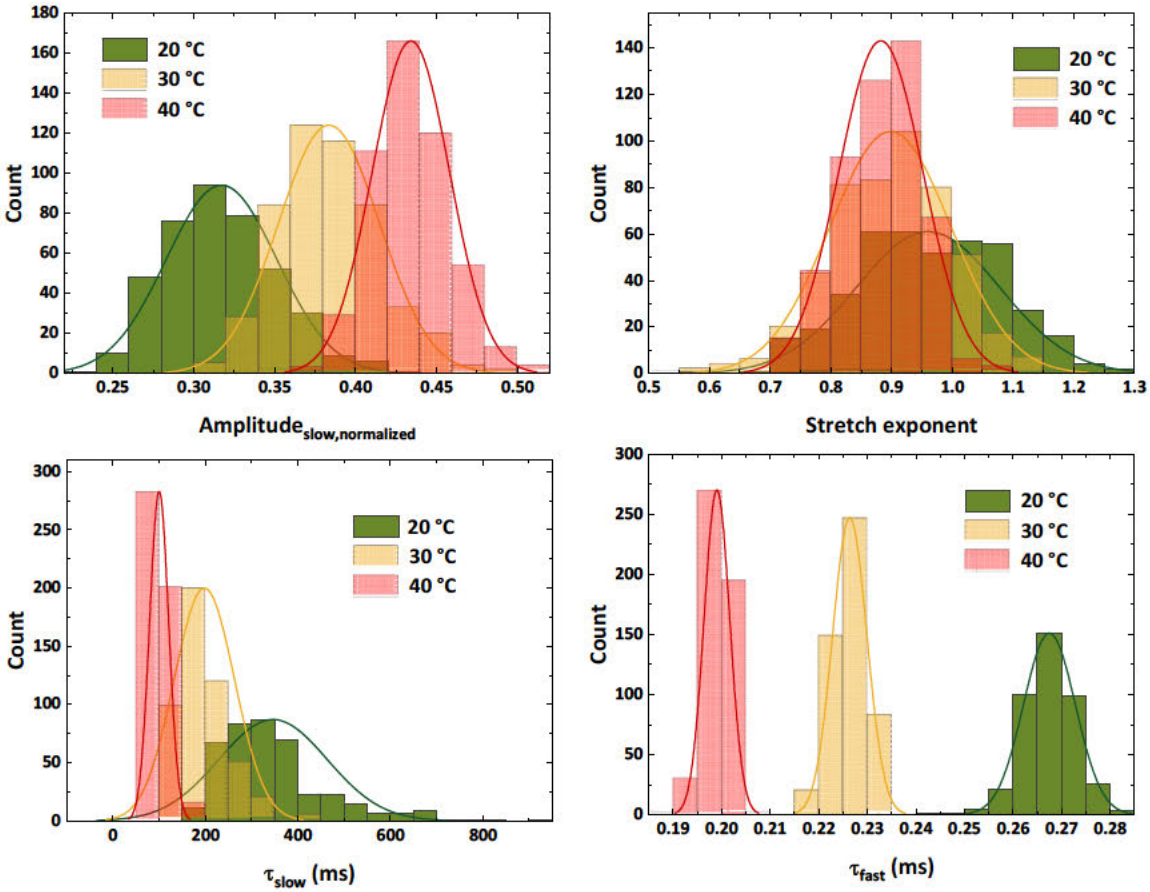

Figure S5. Intensity statistics (amplitude of the slow mode, stretch exponent α, slow and fast relaxation time) of the tetra-arm PEG-terpyridine zinc gel at 20 °C (green), 30 °C (yellow), and 40 °C (red). All fit parameters exhibit a decrease in the distribution width with increasing temperature. The fast relaxation time τ_{fast} is decreased with increasing temperature due to the enhanced thermal motion of polymer chains.

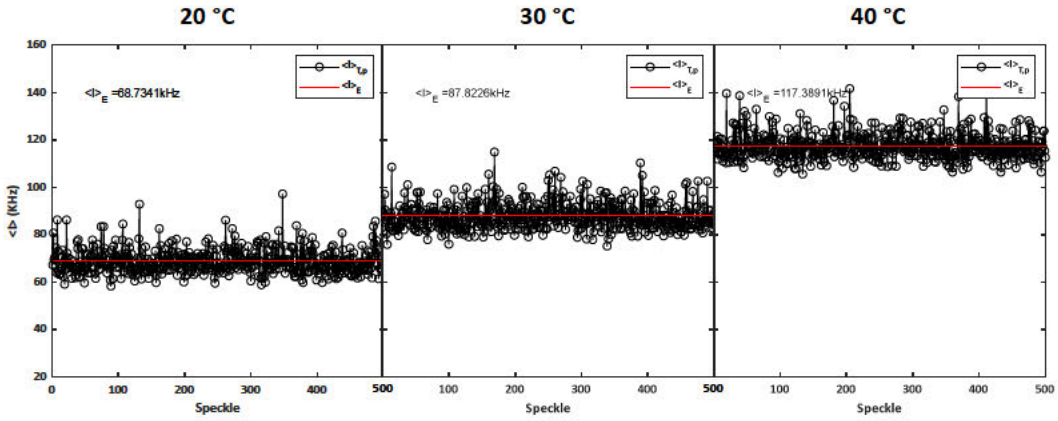

Figure S6. Recorded intensity speckles of the zinc tetra-arm PEG-terpyridine gel at temperatures of 20 °C, 30 °C, and 40 °C.

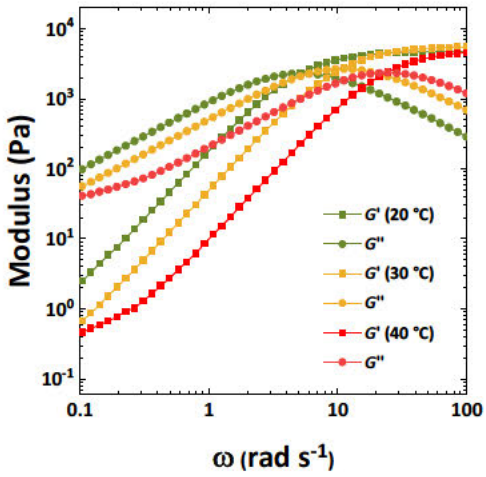

Figure S7. Frequency-dependent storage (full squares) and loss (full circles) moduli of a zinc tetra-arm PEG-terpyridine gel, probed at temperatures of 20 °C (green), 30 °C(yellow), and 40 °C(red).

4.3 Hierarchy of Relaxation Times in Supramolecular Polymer Model Networks

Martha Franziska Koziol, [redacted]

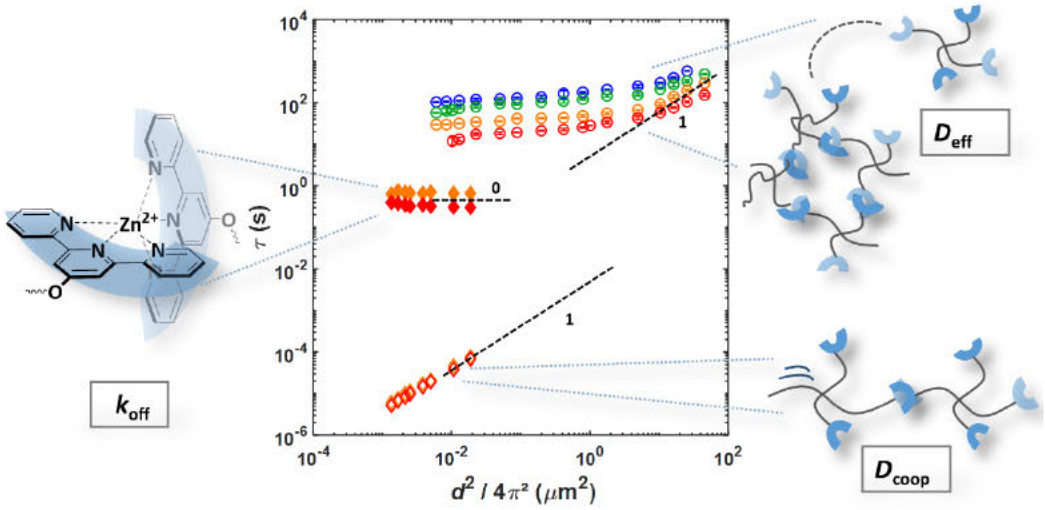

Unpublished manuscript,

submission and revised submission (21.12.2021) to *Physical Chemistry Chemical Physics*

Author Contributions	
Martha Koziol	Synthesis and analysis of the materials, rheology experiments, UV-Vis kinetic measurements, DLS and SLS experiments, FRS experiments, data analysis, writing and editing of the manuscript
[redacted]	Synthesis of the polymers
[redacted]	Synthesis of the polymers
[redacted]	Correction and discussion of the manuscript
[redacted]	Supervision and conception of the work, correction of the manuscript, acquisition of funding

The comprehensive characterization of supramolecular polymer networks often requires a synergy of several experimental techniques that cover both, a broad length and time scale. In this manuscript, the structure and dynamics of a tetra-arm PEG-terpyridine network, connected through zinc cations

in DMF, is investigated. Stress relaxation in such reversible networks is mainly influenced by the dissociation kinetics of a single sticker bond. The specific zinc–terpyridine dissociation constants and resulting activation energies were obtained in the dilute regime by UV-Vis metal exchange experiments and further related to their analogues arising in the percolated gel state.

Dynamic light scattering experiments provided a slow q–independent relaxation time with a distinct temperature-dependence comparable to the macroscopic terminal relaxation time. In addition to that, static heterogeneities were found to explicitly influence the distribution of occurring relaxation times in the autocorrelation functions, again proving a direct interplay of structure and dynamics. Heterogeneous structures therefore imply heterogeneous dynamics if a microscopic perspective is chosen. As light scattering only uncovers cooperative diffusive chain motion, the results were complemented by self-diffusion measurements of entire dye-labelled polymer building blocks (FRS). Both methods (FRS and DLS) cover a length scale range via d, respective q, that could be interconverted to yield a master curve.

The combination of all abovementioned experimental techniques unravels relaxation processes within the networks that span a time scale of 15 decades, including cooperative chain motion of short segments, viscoelastic relaxation, and center-of-mass diffusion.

4.3.1 Abstract

Supramolecular polymer gels are an evolving class of soft materials with a vast number of properties that can be tuned to desired applications. Despite continuous advances concerning polymer synthesis, sustainability or adaptability, a consistent understanding of the interplay between structure, dynamics, and diffusion processes within transient networks is lacking. In this study, the hierarchy of several relaxation processes is investigated, starting from a microscopic perspective of a single sticker dissociation event up to the center-of-mass diffusion of a star-shaped polymer building block on different length scales, as well as the resulting macroscopic mechanical response to applied external stress. In addition to that, a second focus is placed on the gel microstructure that is analyzed by light scattering. Conversion of the dynamic light scattering (DLS) inverse length scale into real space allows for a combination of relaxation times with those obtained by forced Rayleigh scattering (FRS). For these investigations, a model-type metallo-supramolecular network consisting of narrowly dispersed tetra-arm poly(ethylene glycol)-terpyridine macromolecules that are interconnected via complexation with zinc ions is chosen. Assembling the obtained activation energies reveals that all complex dissociation-governed relaxation processes exhibit similar activation energies.

4.3.2 Introduction

Polymer networks consisting of macromonomers with reversible crosslinks (also denoted as stickers) are an evolving class of materials exhibiting promising properties due to their dynamic nature. Most of these materials are considered as self-healable[1] and find applications in various fields such as biomedicine[2] or electronics.[3] The dynamic properties of such transient networks are not only influenced by the type and strength of their crosslinks (hydrogen bonds, metal–ligand–association, π-π stacking) and external stimuli (pH, temperature, or light)[4] but also by the position of the sticky groups (end-functionalization vs. sidechain sticker) and the macromonomer architecture (linear vs. stars).[5] In this regard, the approach of developing highly functional materials with tailor-made mechanical properties requires a profound understanding of the underlying dynamic processes. Although many investigations have been conducted over the past two decades, predictions of a supramolecular network's performance starting from the properties of its molecular components (e.g. macromonomers) remains challenging.[6] The complex interplay between the network topology, sticker lifetime(s), and polymer chain dynamics necessitates the use of various complementary characterization techniques to cover both a broad time window as well as an extensive spatial resolution.

Recently, Tang *et al.*[7] revealed a spectrum of several relaxation times that are involved in the total relaxation dynamics of their supramolecular system consisting of linear chains with evenly distributed sticky groups. Like many others,[8,9] they found that the sticker dissociation in the dilute limit is faster than the network exchange time measured by classical rheology. This finding can be explained by the predictions of the sticky Rouse model where a re-normalized bond lifetime τ_b^* has been introduced, showing that a sticker needs several attempts of dissociation and re-association before it can effectively liberate and find a new partner and thereby contribute to stress relaxation.[10] On top of that, an unexpected superdiffusive regime has been found in several types of associative networks including protein-based hydrogels,[11] synthetic polymer gels with extremely high sticker density,[12] or star-PEG-terpyridine gels.[13] For explanation, a two-state model has been implemented that is able to phenomenologically describe these anomalous diffusion properties. However, it does not provide a physically meaningful model framework nor meaningful assessment of microscopic variables. As a complement, a molecular model presented by Ramírez *et al.*,[14] introduces several diffusion mechanisms such as walking or hopping, with the latter being the main origin of the superdiffusive regime. By this model, real physical parameters are obtained, but the predictions overestimate several parameters such as the polymer radius of gyration by an order of magnitude. Very recently,[15] Rao and coworkers combined forced Rayleigh scattering (FRS) and neutron spin echo measurements on protein hydrogels to connect segmental polymer strand relaxations with the self-diffusion of the network components, thereby spanning a huge length scale that ranges from nanometers to several micrometers. They found at least two length-scale dependent superdiffusive regimes that reflect a multitude of relaxation mechanisms and molecular states.

In this study, we aim to further understand and compare the hierarchy of characteristic relaxation times coming along with the formation of a model type metallo-supramolecular polymer network transiently built by narrowly dispersed star-shaped poly(ethylene glycol) building blocks.
UV-Vis measurements at dilute conditions, oscillatory shear rheology, and light scattering are chosen as suitable methods to access a wide range of characteristic experimental time and length scales. Our investigations are further completed by forced Rayleigh scattering that provides valuable insights into self-diffusivities on a broad length scale. The combination of these different but yet synergistic characterization techniques allows us to transfer knowledge gained from the isolated macromonomer in solution to the whole network and connect structural as well as dynamic properties.

4.3.3 Experimental

Materials

Commercially available hydroxyl-terminated tetra-arm poly(ethylene glycol) with molar masses of 10,000 g mol^{-1} and 20,000 g mol^{-1} (further denoted as 10k and 20k) was purchased by JenKem® (TX, USA) and re-precipitated before further use. Uvasol® *N,N*-Dimethlyformamide Supelco® without further drying was used for all spectroscopic assessments.

Low molecular terpyridine-model compound. 4′-[2-(1-Methoxyethoxy)ethoxy]2,2′:6′,2′′-terpyridine (**1**) was chosen as a low-molecular model compound for the UV-Vis based determination of the complex dissociation constant in DMF.[16] The reaction route is depicted in **Scheme 1**.

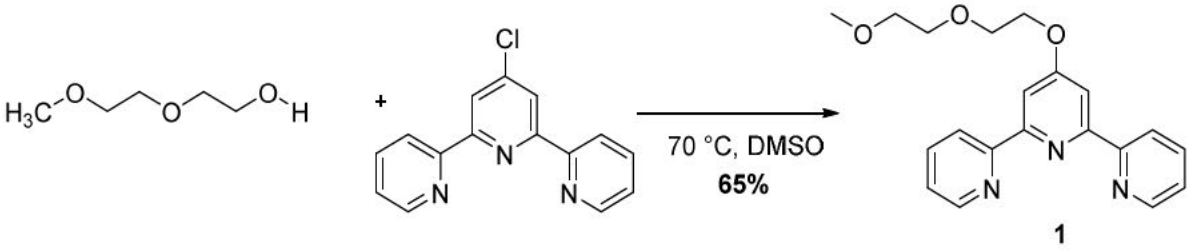

Scheme 1. Reaction scheme for the synthesis of 4′-[2-(1-Methoxyethoxy)ethoxy]2,2′:6′,2′′-terpyridine (**1**).

0.13 g mortared KOH (2.3 mmol, 2.8 eq.) was dried under vacuum overnight in a septum–sealed flask, and, after the drying procedure, 10 mL of dry DMSO was added to the flask. 1 mL of diethylene glycol monomethyl ether (5.15 mmol, 6.36 eq.) was added via syringe, and the reaction mixture was heated to 70 °C for 1 hour. 0.217 g 4′-chloro-2,2′:6′,2′′-terpyridine (0.81 mmol, 1 eq.) was added, and the reaction was stirred overnight at 70 °C. After cooling the flask to room temperature, the reaction mixture was concentrated by short-path vacuum distillation. By dropwise precipitation of the distillation bottom product into 50 mL of stirred cold water, the product (**1**) could be obtained. This slightly yellow raw product was filtered and dried, and for further purification re-dissolved in 1–2 mL DMSO, followed by re-precipitation. After drying, 0.190 g (65%) of a fine white powder was obtained. ^{1}H-NMR ($CDCl_3$) δ = 8.69 (ddd, 2H), 8.61 (dt, 2H), 8.05 (s, 2H), 7.85 (td, 2H), 7.33 (ddd, 2H), 4.42 (m, 2H), 3.94 (m, 2H), 3.76 (m, 2H), 3.59 (m, 2H), 3.40 (s, 3H, methyl-).

Tetra-arm PEG-terpyridine. Terpyridine end-group modified tetra-arm poly(ethylene glycol) (PEG) with molar masses of M_w = 10,000 g mol^{-1} and M_w = 20,000 g mol^{-1} were synthesized according to a previously published procedure.[13,17]

As summarized in **Scheme 2**, commercially available hydroxyl-terminated star-shaped PEG was reacted with mesyl chloride to yield tetra-arm PEG-mesylate that could further be converted with sodium azide to give telechelic azide functionalities. In a subsequent copper-free Huisgen click reaction, propargyl-terpyridine was added to the tetra-arm PEG-azide, and the final product was obtained.

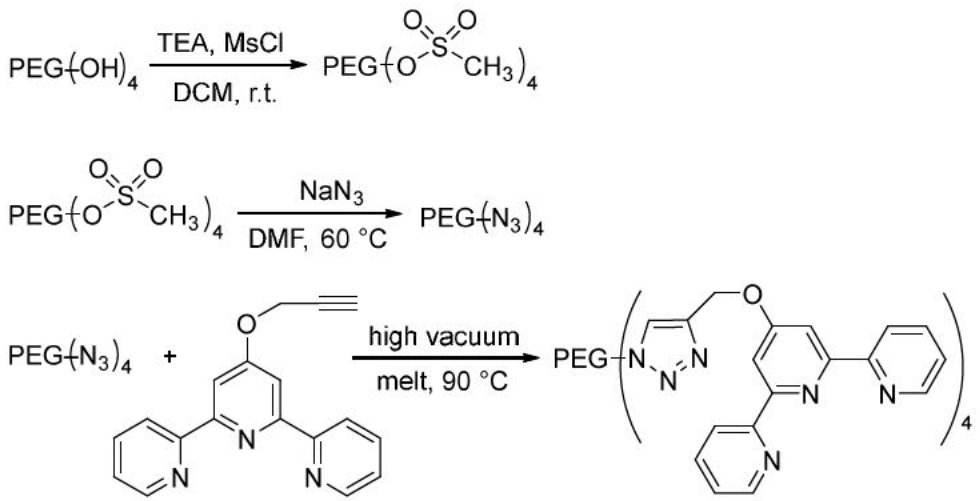

Scheme 2. Reaction scheme for the three-step synthesis of terpyridine end-functionalized tetra-arm PEG.

Fluorescence-labeled tetra-arm PEG-terpyridine. In order to obtain self-diffusivities by FRS experiments, tetra-arm polymers that carry both required functional groups, a terpyridine unit and a fluorescent dye on each arm, were synthesized as detailed elsewhere.[13] Briefly, tetra-arm PEG-OH (10,000 g mol^{-1} and 20,000 g mol^{-1}) was reacted with epichlorohydrin to give epoxy-terminated polymers. In a subsequent ring-opening reaction with sodium azide, tetra-arm PEG terminated with an azide and a hydroxyl group was obtained. Terpyridine functionalities were inserted via copper-free click reaction, and, in a following step, the remaining hydroxyl groups were activated with *p*-nitrophenylchloroformate. Further reaction with (*S*)-(+)-4-(3-amino-pyrrolidino)-7-nitrobenzofurazan (NBD) gave the final product (**Scheme 3**). Excess dye was removed via size exclusion chromatography on a Sephadex LH-20 column in methanol.

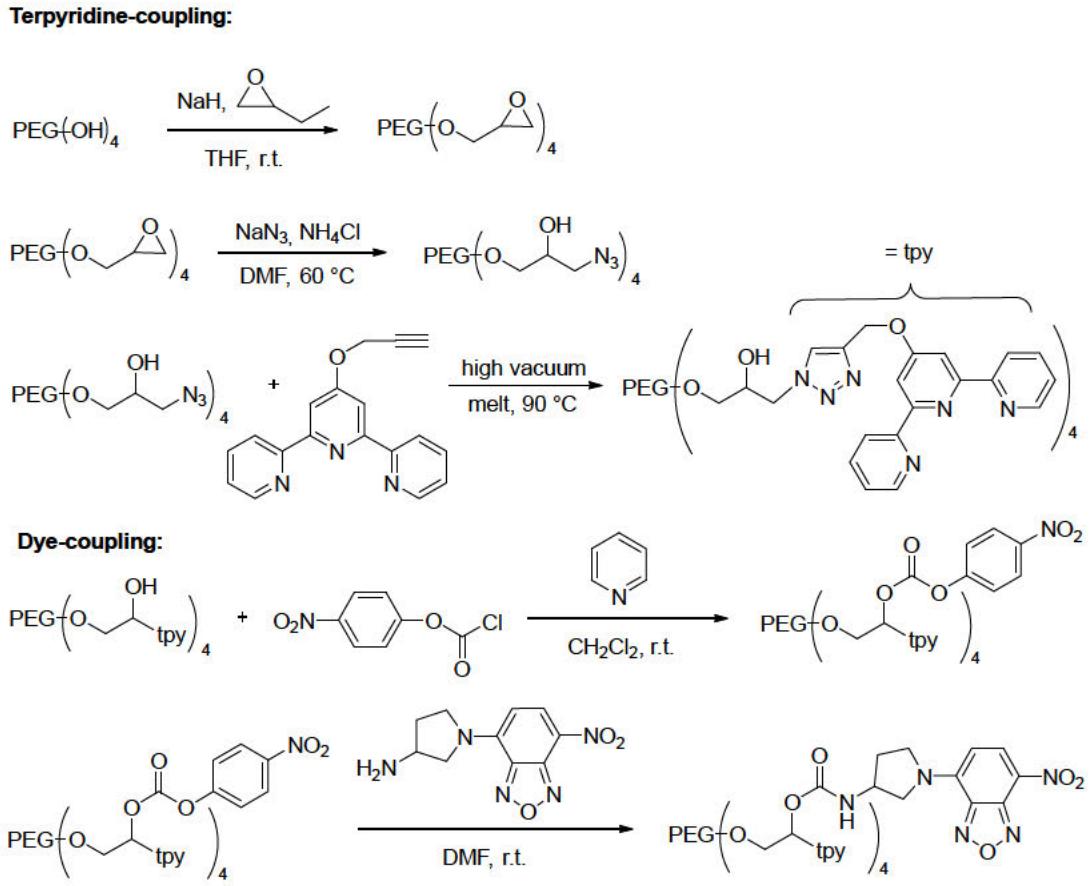

Scheme 3. Reaction route for the synthesis of terpyridine- and dye-functionalized tetra-arm PEG.

Methods

A temperature range of 10 °C–45 °C was chosen to assure good accessibility in all following characterization techniques.

Kinetic measurements based on UV-Vis spectroscopy. To study the bond dissociation kinetics of the zinc-terpyridine complexes, metal exchange experiments in the presence of a twenty-fold molar excess of copper cations were performed. Real-time monitoring of the characteristic metal ligand charge transfer (MLCT) absorption band at 336 nm was carried out on a Jasco V-760-ST spectrophotometer with steady temperatures (10 °C, 15 °C, 20 °C, and 25 °C) assured by a Haake Phoenix II thermostat (Thermo Electron Corporation). All solutions were equilibrated at the desired temperature for 15 minutes before use. 2 mL of a copper nitrate trihydrate solution ($c = 2 \cdot 10^{-4}$ mol L^{-1}) was placed into a UV-Vis cuvette and stirred rigorously. Subsequently, 10 µL of a zinc-terpyridine solution consisting of the low-molecular weight model compound (**1**) and zinc nitrate hexahydrate in a stoichiometric ratio of 2 : 1 (terpyridine : zinc) was quickly added in one shot, and the measurement was started immediately. The final terpyridine concentration was $c = 2 \cdot 10^{-5}$ mol L^{-1}. Assuming pseudo-

first order kinetics, the obtained time-dependent absorption curves were fitted to a stretched exponential function (further information in SI).

Gel preparation. Throughout this work, we use the expressions 'gel' and 'network' to identically describe the investigated material: a transiently connected supramolecular polymer network that is swollen in DMF. The stoichiometric ratio (tpy : zinc) was kept 2 : 1 in all gels. Therefore, the respective amount of a zinc nitrate hexahydrate stock solution in DMF was quickly added to a solution of tetra-arm PEG-terpyridine in DMF. For FRS experiments, 2% (w/v) of the NBD-labeled species were also added to this mixture. The immediately forming gel was vortexed for 20 s, centrifuged to remove air bubbles, and equilibrated over night at 37 °C. All gels were optically clear.

Rheology. Rheology experiments were performed on an Anton Paar modular compact rheometer type MCR 302 equipped with a cone-plate geometry CP25-1. A gap size of 0.05 μm was chosen, as well as a cone radius of 25 mm and an angle of 1 °. To prevent solvent evaporation, a cooling trap was used. Frequency sweeps were carried out in the linear viscoelastic regime (LVE), applying constant shear rates of $\gamma = 1\%$ and a logarithmic frequency range of $\omega = 0.01 - 100$ rad s^{-1}.

Forced Rayleigh Scattering. The equilibrated samples were loaded between two quartz glass disks that were separated by a Teflon spacer, sealed, and again equilibrated for another day at the desired measurement temperature. Experiments were carried out analogous to a previously detailed procedure.[12,13] In short, a laser beam (cw, 100 mW, $\lambda = 488$ nm) that was first split and subsequently focused on the sample with a certain angle θ, created a grating with the characteristic spacing *d*:

$$d = \frac{\lambda}{2 \cdot \sin(\frac{\theta}{2})} \tag{1}$$

Due to constructive interference, a short high power bleaching beam with duration of 500–1000 ms created an amplitude grating of dye concentration by irreversibly photobleaching the label on fluorescence-labeled molecules. Molecular diffusion can be monitored by a single attenuated reading beam whose diffraction intensity continuously decreases over time due to the vanishing grating. This decaying intensity $I(t)$ was fit by a slightly stretched exponential function:

$$I(t) = A + B \exp\left(-\left(\frac{t}{\tau_{FRS}}\right)^{\beta}\right)^2 \tag{2}$$

with the incoherent scattering background *A*, the amplitude *B*, the characteristic relaxation time τ_{FRS}, and the stretch exponent β. The average relaxation time $<\tau_{FRS}>$ was calculated as

$$<\tau_{FRS}> = \frac{\tau_{KWW}}{\beta} \cdot \Gamma\left(\frac{1}{\beta}\right) \tag{3}$$

with Γ being the γ function.

Light scattering. All measurements were carried out on an ALV-SP125-Goniometer, equipped with an ALV/High-QE APD-Avalanche photo diode with fiber optical detection in pseudo cross correlation mode, an ALV 5000/E/PCI correlator, and a JDSU (USA, CA) He/Ne laser (632.8 nm, 35 mW). Angular dependent measurements were performed in a range of 30 °< θ < 150 ° corresponding to wave vectors of $q = (4\pi n \sin(\theta/2)) / \lambda$ with the scattering angle θ, the wavelength λ, and the refractive index $n = 1.42083$ for dimethylformamide (DMF). To account for gel non-ergodicity, scattered light of 500 independent sample positions was recorded using an ALV cuvette rotation unit (CRTU) with a waiting time of 5 s before each measurement and an acquisition time of 30 s (45 °C), 60 s (35 °C), and 90 s (25 °C).

Static Light Scattering. To calculate absolute scattering ratios that are independent of setup parameters, the recorded sample scattering intensity is divided by the intensity of the incident laser beam. This ratio of each gel position was then normalized by the ratio of the standard toluene and multiplied with the Rayleigh ratio $RR = 1.368 \cdot 10^{-5}$ cm^{-1}. Each position-specific ratio is denoted as $\langle \text{ratio} \rangle_T$, its mean value over all 500 positions corresponds to the ensemble average $\langle \text{ratio} \rangle_E$. The scattered light of such non-ergodic systems consists of two contributions: a fluid component $\langle \text{ratio} \rangle_F$ that is mostly position- and angle-independent, and a time-independent excess ratio $\langle \text{ratio} \rangle_{Exc}$, that is caused by frozen static heterogeneities. $\langle \text{ratio} \rangle_F$ is the lower limit of occurring scattering ratios and is obtained by fitting the intensity distribution probability histogram to an exponential decaying function:

$$P(\langle \text{ratio} \rangle_T) = a \cdot H(\langle \text{ratio} \rangle_T - \langle \text{ratio} \rangle_F) \cdot \exp\left(-\frac{\langle \text{ratio} \rangle_T - \langle \text{ratio} \rangle_F}{\langle \text{ratio} \rangle_E - \langle \text{ratio} \rangle_F}\right) \quad (4)$$

with the Heaviside step function $H = 0$ for $(\langle \text{ratio} \rangle_T - \langle \text{ratio} \rangle_F) < 0$, and $H = 1$ for $(\langle \text{ratio} \rangle_T - \langle \text{ratio} \rangle_F) \geq 0$. $\langle \text{ratio} \rangle_{Exc}$ can then be calculated by applying $\langle \text{ratio} \rangle_{Exc} = \langle \text{ratio} \rangle_E - \langle \text{ratio} \rangle_F$. If the excess scattering ratio exhibits an angular dependence, it is possible to calculate the static correlation length Ξ that can be seen as a quantitative measure for gel heterogeneity. This is done using a Guinier-type function,[18] where the structure factor $S_{Guinier}$ is approximated by an exponential decay:

$$S_{Guinier} \sim \exp(-q^2 \cdot \Xi^2) \quad (5)$$

The slope of a Guinier plot ($\ln(\langle \text{ratio} \rangle_{Exc})$ vs. q^2) then equals Ξ^2.

Dynamic Light Scattering. Due to gel non-ergodicity (ensemble-averaged scattering ratio ≠ time-averaged scattering ratio), partial heterodyne data analysis is chosen to treat the recorded autocorrelation functions.[19,20] A sum of an unstretched and a stretched exponential decay captures both relaxation processes:

$$g^{(2)}(q,\tau) - 1 = X^2 \cdot (g^{(1)}(q,\tau))^2 + 2X \cdot (1 - X) \cdot g^{(1)}(q,\tau) \quad (6)$$

with

$$g^{(1)}(q,\tau) = A + b_{\text{fast}} \cdot \exp\left(-\frac{\tau}{\tau_{\text{fast}}}\right) + b_{\text{slow}} \cdot \exp(-(\frac{\tau}{\tau_{\text{KWW}}})^{\alpha}) \quad (7)$$

with the homodyne scattering contribution $X = \frac{\langle \text{ratio} \rangle_F}{\langle \text{ratio} \rangle_T}$, the baseline offset A, the amplitudes b_{fast} and b_{slow}, the characteristic relaxation times τ_{fast} and τ_{KWW} and the stretch factor α. The stretched Kohlrausch-Williams-Watts function is chosen to adequately capture the broad distribution of relaxation times ($\alpha < 1$). The average slow relaxation time τ_{slow} is calculated as

$$\tau_{\text{slow}} = \frac{\tau_{\text{KWW}}}{\alpha} \cdot \Gamma(\frac{1}{\alpha}) \quad (8)$$

with the γ function Γ.

The obtained gel diffusion coefficients $D_{\text{Gel,fast}} = (q^2 \tau_{\text{fast}})^{-1}$ exhibit a sample position dependence of the form

$$D_{\text{PHD}} = (2 - X) \cdot D_{\text{Gel,fast}} \quad (9)$$

and the collective diffusion coefficient D_{PHD} is then calculated by a linearized expression of equation (8):[20–22]

$$\frac{\langle \text{ratio} \rangle_T}{D_{\text{Gel,fast}}} = \frac{2}{D_{\text{PHD}}} \cdot \langle \text{ratio} \rangle_T - \frac{\langle \text{ratio} \rangle_F}{D_{\text{PHD}}} \quad (10)$$

with the specific speckle ratio $\langle \text{ratio} \rangle_T$ and the fluid ratio $\langle \text{ratio} \rangle_F$. As reported earlier,[21] a weighing factor $\langle \text{ratio} \rangle_T^{-1}$ is used during the linear fitting procedure. The hydrodynamic correlation length ξ_H that can be interpreted as a network mesh size, is calculated via Stokes-Einstein equation (11):

$$\xi_H = \frac{k_B T}{6\pi\eta D_{\text{PHD}}} \quad (11)$$

with the Boltzmann constant k_B, the temperature T, and the solvent viscosity η.

4.3.4 Results and Discussion

Two sets of tetra-arm PEG-terpyridine macroprecursors with different molar masses (10,000 g mol^{-1} and 20,000 g mol^{-1}, referred to as 10k and 20k gels when crosslinked in solution) that are transiently connected to percolated networks through complexation with zinc ions, are chosen as the supramolecular material base for our investigations. The samples are probed from molecular (UV spectroscopy), microscopic (light scattering and forced Rayleigh scattering), and macroscopic (rheology) perspectives.

Rheology

Rheology measurements provide insights into the macroscopic material properties manifesting themselves in time-dependent relaxation processes or elastic and viscous contributions of the mechanical response under an external applied stress. A polymer concentration of 10% (wt/v) is chosen for the 10k gels to assure a concentration well below the entanglement limit, but above the chain overlap concentration (c^* for 10k system has been determined to be 9.4% (wt/v)).[17] For the 20k gels, a concentration of 20% (wt/v) is chosen to assure an equal sticker concentration when compared to the 10k gels. **Figure 1** shows the rheological spectra of the 10k and 20k gels. As expected and also shown by several other works,[23,24] the gels exhibit one single Maxwellian relaxation due to the monodisperse polymer building blocks and the distinct dissociation rates of a zinc-terpyridine complex. The frequency-dependent storage and loss modulus (G' and G'') are fitted to a Maxwell-type model that takes into account a distribution of relaxation times.[24] The model contains a set of relaxation equations (12 – 14) that include a log-normal distribution $H(\tau)$ with its maximum at the characteristic relaxation time τ_R, the amplitude A, and the standard deviation σ^2 (Fit, Residual and exemplary distribution in SI, **Figure S2**).

$$G'(\omega) = \int_{-\infty}^{\infty} H(\tau) \frac{\omega^2\tau^2}{1+\omega^2\tau^2} \, d\ln(\tau) \tag{12}$$

$$G''(\omega) = \int_{-\infty}^{\infty} H(\tau) \frac{\omega\tau}{1+\omega^2\tau^2} \, d\ln(\tau) \tag{13}$$

$$H(\tau) = A \cdot \exp\left(-\frac{(\ln(\tau) - \ln(\tau_R))^2}{2\sigma^2}\right) \tag{14}$$

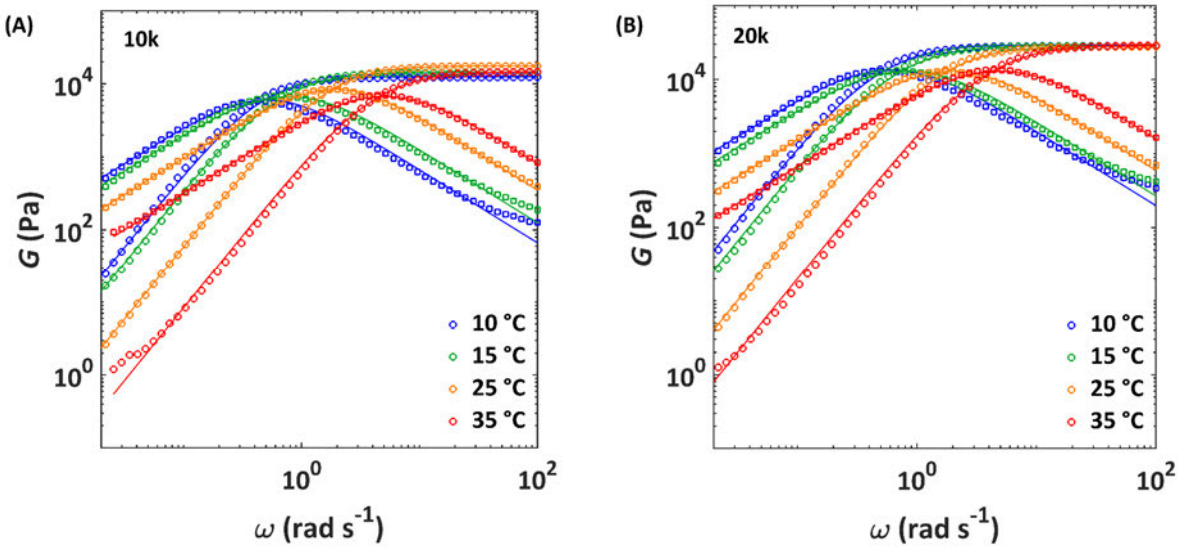

Figure 1. Frequency-dependent rheological spectra of the 10k ((A), M_w = 10,000 g mol^{-1}, 10% (wt/v)) and 20k ((B), M_w = 20,000 g mol^{-1}, 20% (wt/v)) gels at the temperatures of 10 °C, 15 °C, 25 °C, and 35 °C. Fits are shown as straight lines.

In general, all 20k gels exhibit slightly higher plateau moduli G_P than the 10k gels. A higher total polymer concentration enhances the probability of interchain bonding instead of elastically inactive intrachain bonding as it might be the case in the 10k gels. Despite different arm lengths, both gel types show nearly the same cross-over frequencies between G' and G'' at the same temperatures, and, as expected, an Arrhenius type temperature dependence if $\ln(\tau_R^{-1} = k_R)$ is plotted vs. T^{-1} (inset of **Figure 2**). From the slopes of such Arrhenius plots, activation energies are calculated to be (70.91 ± 1.30) kJ mol^{-1} (10k) and (64.44 ± 3.25) kJ mol^{-1} (20k). As expected, the activation energies for both systems (10k and 20k) are nearly identical within the margins of error. This fact is expected since the gel concentrations of both gels (10k and 20k) were chosen to be in the semi-dilute regime to avoid entanglements or other strong intramolecular interactions that could exert influence on the activation energies. In addition to the characteristic relaxation times τ_R, the model also provides the standard deviation σ^2 as a quantitative measurement for the width of the relaxation time distribution. Comparison of the gels with different arm lengths shows slightly elevated σ^2-values for the 20k gels and no significant temperature-dependence (**Figure S3**).

Dilute kinetics

The network relaxation time in transiently connected polymer systems is mainly governed by the kinetics of their single associative junctions.[7] In the tetra-arm PEG-terpyridine networks, the rate-determining step of network rearrangement is the dissociation rate of a zinc terpyridine complex, and it can be investigated by UV-Vis based metal exchange experiments. For this purpose, we synthesized a low-molecular weight model compound (**1**) consisting of a terpyridine group and only two ethylene glycol units attached to it via an oxygen atom to assure similar electronic conditions as in the polymer macromolecules. Additionally, a molecule with a distinct low molecular weight was intentionally chosen to avoid any polymer chain-related effects (e.g. chain concentration) that could lead to further interfering interactions. In our classic metal ion exchange experiment, zinc ions of the low molecular weight model compound-Zn(II)-complexes (**1**) are replaced by stronger binding Cu(II) ions that are present in a 20 fold excess. The terpyridine concentration is kept at $2 \cdot 10^{-5}$ mol L^{-1} in DMF, and the evolution of the characteristic metal ligand charge transfer (MLCT) band at 336 nm is observed. The time-dependent normalized absorbances at four different temperatures are shown in **Figure 2**.

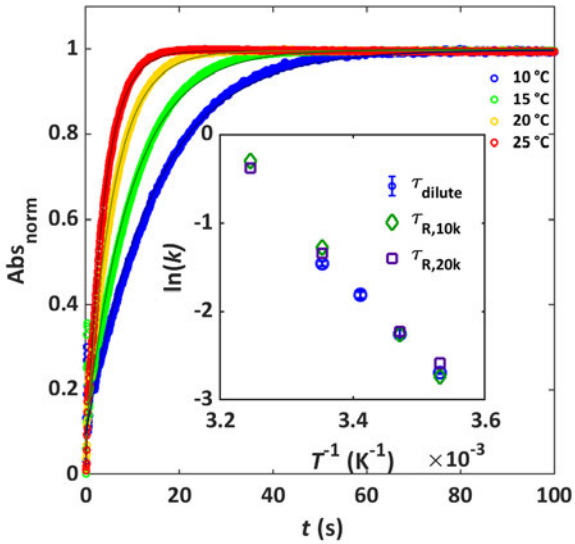

Figure 2. Normalized evolution of the Cu(II)-terpyridine complex MLCT band at 336 nm at different temperatures of 10 °C (blue), 15 °C (green), 20 ° (yellow), and 25 °C (red) in DMF. Inset: Arrhenius plot with combination of UV-Vis kinetics of the low-molecular model compound (**1**) (blue circles) and the cross-over frequencies obtained by rheology (green diamonds (10k) and purple diamonds (20k)).

Fitting these time traces to an exponential function provides the characteristic dissociation time τ_{dilute} of the zinc terpyridine complex in DMF. We obtain a lower activation energy of $E_{A,dilute} = (58.27 \pm 0.98)$ kJ mol^{-1} compared to our rheology experiments with the 10k and 20k gels ((70.91 ± 1.30) kJ mol^{-1} and (64.44 ± 3.25) kJ mol^{-1}). This finding is explainable if we consider the activation energy obtained by rheology $E_{a,Rheology}$ to consist of two additive contributions: the prior dissociation of a zinc terpyridine complex $E_{A,dilute}$ and the subsequent relaxation of the polymer chain $E_{A,polymer}$.[17,25]

By means of rheology, Rossow *et al.*[17] probed a semi-dilute solution of tetra-arm PEG-terpyridine macromolecules without addition of any metal ions to obtain the activation energy of flow $E_{a,flow}$ that is purely induced by chain relaxation. Assuming additive contributions of chain relaxation and complex dissociation, they subtracted $E_{a,flow}$ from the activation energy of gel relaxation $E_{a,Rheology}$ to calculate the activation energy for the zinc-terpyridine complex dissociation ($E_{a,break} = 57.4$ kJ mol^{-1}). Their value could experimentally be verified within the present work thereby strongly supporting the hypothesis of additive energy contributions.

The inset of **Figure 2** shows that the absolute relaxation rates $k_{dilute} = \tau_{dilute}^{-1}$ (blue open circles) are nearly the same as the macroscopic relaxation rates $k_R = \tau_R^{-1}$ measured by rheology (open green and purple diamonds). This finding stays in contrast to a study by Tang and Olsen, where the dilute relaxation time is faster by an order of magnitude compared to the macroscopic relaxation.[7] Identical τ_{dilute}

and τ_R values indicate an unexpected negligible effect of bond lifetime renormalization, and are proposed in a model introduced by Stukalin and coworkers[26] only if the associate bond strength (expressed by the activation energy $E_{A,dilute}$) is significantly higher than the restoring energy of a dangling chain (consisting of N monomers) with 2 RT ln N.[9] Our UV-Vis experiments revealed a bond strength of $E_{A,dilute}$ = (58.27 ± 0.98) kJ mol^{-1}, whereas the restoring energy of an arm ($M_{w,arm}$ = 2,500 g mol^{-1}, T = 298 K, and $N \approx 56$ for the 10k gel) can be calculated as 2 RT ln N = 19.96 kJ mol^{-1} (23.42 kJ mol^{-1} for 20k).

Amin *et. al.*[27] showed in a hybrid Monte Carlo / molecular dynamics simulation study that the fraction of unbound stickers decreases to less than 1% if the bond energy ε exceeds ε ≥ 10 $k_B T$. In our case, a bond energy of $E_{A,dilute}$ = (58.27 ± 0.98) kJ mol^{-1} corresponds to 24 $k_B T$, such that the majority of terpyridine complexes are assumed to be in the closed state. Besides the high fraction of closed complexes at these high bond energies, they also calculated a fraction of ineffective chains to be at 5% that do not contribute to network elasticity.

Light Scattering

Light scattering is a powerful non-invasive technique that is able to provide valuable insights not only into the gel microstructure (static correlation lengths), but also its dynamic processes and hydrodynamic correlation lengths. To complete the picture of hierarchical relaxation times within the supramolecular model networks, simultaneous static and dynamic light scattering experiments (SLS and DLS) on the 10k gel (10% (w/v)) at three different temperatures (25 °C, 35 °C, and 45 °C) are conducted.

Static light scattering

At each temperature, the gel exhibits a typical intensity speckle pattern (**Figure 3(A)**) with sample-position dependent intensities that compromise scattering contributions from frozen heterogeneities, as well as contributions caused by thermal fluctuations of the polymer chains that are restricted in their motion due to the crosslinks. The latter distinguish themselves by a specific lower cut-off scattering ratio that occurs with the highest probability and is referred to as the fluid ratio $\langle ratio \rangle_F$. To decompose both scattering contributions, $\langle ratio \rangle_F$ is obtained by fitting the probability histogram of all measured ratios (**Figure 3(B)**) with an exponentially decaying function (see experimental part).

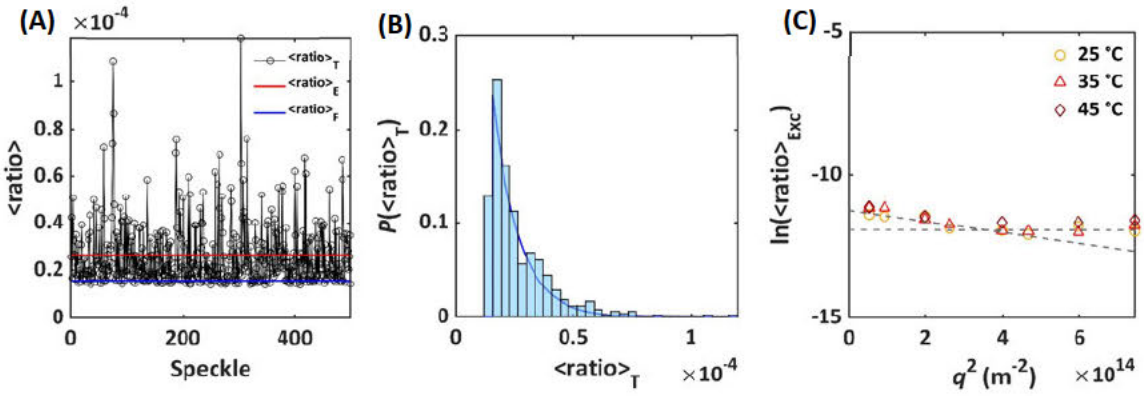

Figure 3. (A) $\langle \text{ratio} \rangle_T$ speckle pattern of 500 randomly chosen positions within the tetra-arm PEG-terpyridine zinc gel (M_w = 10,000 g mol^{-1}, 10% (w/v), DMF) at an angle of 30 ° and a temperature of T = 25 °C, with the ensemble average $\langle \text{ratio} \rangle_E$ (red line) and the fluid contribution $\langle \text{ratio} \rangle_F$ (blue line). (B) Probability distribution and Heaviside fit (blue line). (C) Guinier plot of all calculated excess ratios $\langle \text{ratio} \rangle_{Exc}$ vs. scattering vector q^2 at three different temperatures 25 °C (yellow symbols), 35 °C (red symbols), and 45 °C (maroon symbols).

Figure 4(A) shows no angular dependence of the fluid ratio (open squares) and a slight increase with increasing temperature that can be explained by the enhanced thermal motion of the polymers at

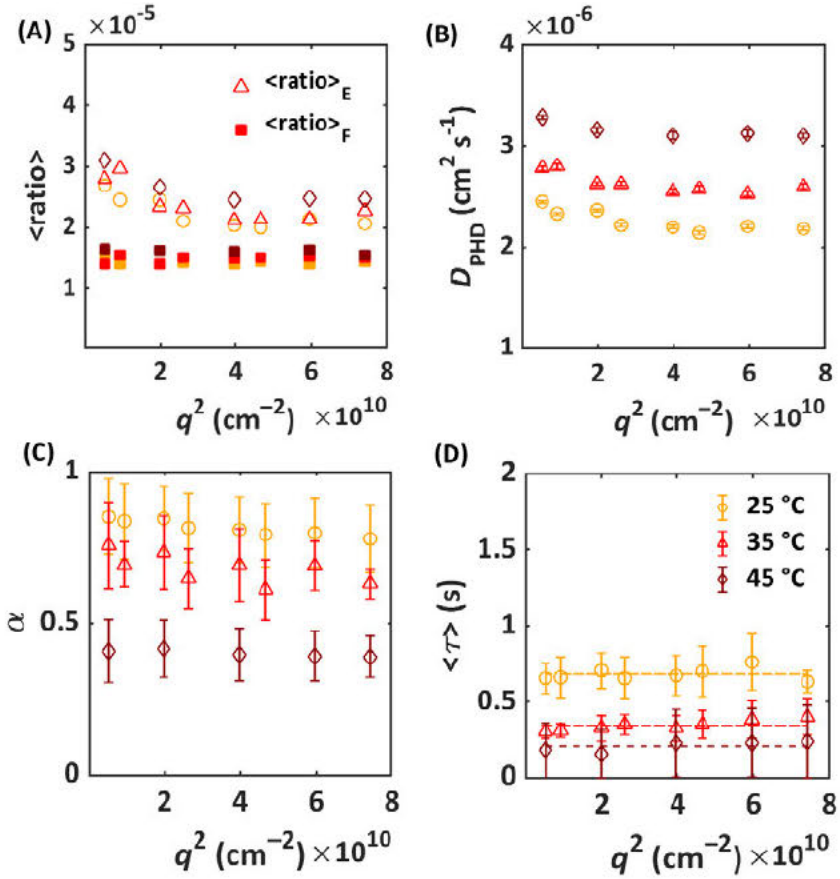

Figure 4. Results of the partial heterodyne data analysis of a zinc tetra-arm PEG-terpyridine gel (DMF, 10% (wt/v)) at three different temperatures (25 °C yellow, 35 °C red, 45 °C maroon). (A) Scattering ensemble ratio (open circles) and fluid ratio (open squares) vs. q^2. Unlike the ensemble ratio, the fluid ratio does not exhibit an angular dependency. (B) Diffusion coefficient D_{PHD} vs. scattering vector q^2. (C) The averaged stretch exponent α is decreasing with increasing temperature. Error bars depict the standard deviation of all 500 positions. (D) Angular-independent relaxation time of the slow relaxation mode occurring at the greatest frequency of all 500 measured times.

higher temperatures. In contrast to that, the overall scattering ratio $\langle \text{ratio} \rangle_E$ shows a distinct angular dependence, especially at lower angles (open circles in **Figure 4(A)**). The second scattering contributor is the additional excess scattering $\langle \text{ratio} \rangle_{Exc}$ and it is calculated by subtracting the fluid ratio from the ensemble ratio. According to the Guinier approach that treats the gel as a medium consisting of randomly distributed domains with different densities, we calculate temperature-independent static correlation lengths of $\Xi_{25°C} = (44 \pm 36)$ nm, $\Xi_{35°C} = (54 \pm 11)$ nm, and $\Xi_{45°C} = (39 \pm 22)$ nm (**Figure 3(C)**). Values in a very similar order of magnitude are also reported for non-ideal permanently connected tetra-PEG hydrogels.[28] Even though this transiently connected tetra-arm PEG-terpyridine gel is considered as a dynamic model system with its dissociating and re-associating polymer building blocks, static heterogeneities with density disparities are clearly present. The light scattering results are summarized in **Table 1**.

Dynamic light scattering

At all measured temperatures, the gel exhibits two distinct relaxation modes. The intensity correlation functions $g^{(2)}(\tau)$ of three out of five hundred randomly chosen positions within the gel are depicted in **Figure 5**. Even though the gels can be considered as non-ergodic media as they exhibit large intensity speckle pattern, the recorded autocorrelation functions fully decay to the baseline. This finding is puzzling and further systematic investigations need to be carried out in order to fully understand light scattering on reversible gels and other types of soft matter materials.

Similar to earlier studies,[29] the fast mode is assigned to the cooperative segmental relaxation of polymer blobs whereas the slow non-diffusive mode is mainly governed by the network relaxation time. On these short time scales, the diffusive fast chain motion is decoupled from the viscoelastic network relaxation. The diffusion coefficient D_{PHD} of the fast mode that can be converted into the hydrodynamic correlation length ξ_H, is obtained by partial heterodyne analysis (equations (6) – (10)). Plotting $\frac{D_{Gel,fast}}{\langle \text{ratio} \rangle_T}$ vs. $\langle \text{ratio} \rangle_T$ yields a linear dependence with D_{PHD} extracted from the resulting slope (see **Figure S5**). All calculated diffusion coefficients and hydrodynamic correlation lengths are summarized in **Table 1**. **Figure 4(B)** shows the obtained fast diffusion coefficients vs. scattering vector q^2. Only a slight dependence at low angles is visible. As expected, the diffusion coefficients increase with increasing temperature due to the faster polymer chain motion.

Table 1. ξ_H, Ξ, $\langle ratio \rangle_F$, $\langle ratio \rangle_E$, and D_{PHD} of a zinc tetra-arm PEG-terpyridine gel (10% (w/v), DMF) at three different temperatures (25 °C, 35 °C, and 45 °C).

Temperature	ξ_H (nm)	Ξ (nm)	$\langle ratio \rangle_E$ (90 °)	$\langle ratio \rangle_F$ (90 °)	D_{PHD} ($cm^2\ s^{-1}$)
25 °C	1.24	44 ± 36	$2.04 \cdot 10^{-5}$	$1.41 \cdot 10^{-5}$	$2.20 \cdot 10^{-6}$
35 °C	1.10	54 ± 11	$2.13 \cdot 10^{-5}$	$1.50 \cdot 10^{-5}$	$2.55 \cdot 10^{-6}$
45 °C	0.94	39 ± 22	$2.46 \cdot 10^{-5}$	$1.61 \cdot 10^{-5}$	$3.10 \cdot 10^{-6}$

Analysis of the q^2-independent slow mode revealed remarkable heterogeneities in the underlying dynamic processes, a fact that is qualitatively illustrated by the strong position-dependence of the correlation function amplitudes (**Figure 5(B)**). This heterogeneity is quantified by the stretch exponent α as well as the relaxation time $<\tau>$. A stretch exponent below 1 denotes a distribution of relaxation times. Comparison of the stretch exponents of all 500 sample positions of the zinc tetra-arm PEG-terpyridine gel at 25 °C and an angle of 30 ° (**Figure S6**), reveals a broad distribution ranging from 0.5 to 1. **Figure 4(C)** depicts the respective average of α depending on the scattering vector q^2 at three different temperatures. With increasing temperature, the stretch exponent decreases to an average value of 0.4. Such low values indicate a very broad distribution of relaxation times. Since these values are unusually low, we tried a fitting procedure with a tri-exponential function, but it did not provide reasonable parameters.

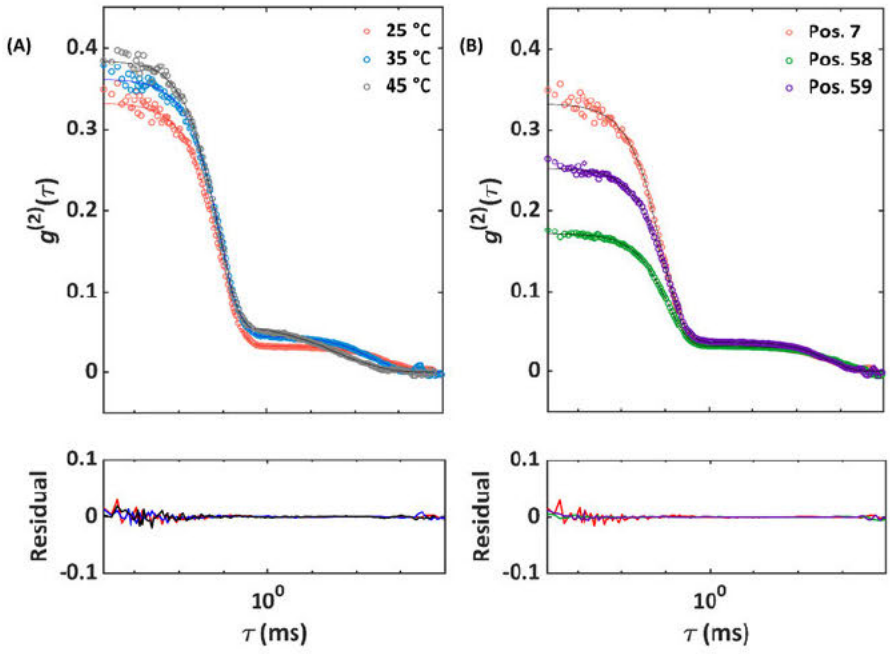

Figure 5. (A) Exemplary intensity correlation functions and fit residuals of a zinc tetra-arm PEG-terpyridine gel (DMF, 10% (w/v)) at three temperatures with fits to the sum of an exponential and a stretched exponential function (lines). (B) Exemplary intensity correlation functions and fit residuals at three randomly chosen gel positions, measured at 25 °C and an angle of 30 °, showing position-dependent variations of the initial amplitude.

An even broader distribution with relaxation times ranging from 500 ms to 2 s is also found at 25 °C (**Figure S7**). Analogous to the stretch exponent, the distribution significantly broadens with increasing temperature and as expected, the relaxation time decreases due to faster thermally activated zinc-terpyridine complex exchange. The broad relaxation time distribution that is only detectable in our light scattering experiments could originate from the former found spatial heterogeneities with their significant differences in polymer density. The position-dependent local network relaxation times are strongly affected by the micro-environment of the zinc-terpyridine complexes and the concentration of open stickers in close vicinity to bind to. Further, additional slower diffusive modes with small amplitudes that are not resolvable on the experimental time scales, might influence the slow relaxation time although fitting to a tri-exponential decay does not yield in rational results. **Figure 4(D)** summarizes the slow relaxation times depending on q^2 and the temperature. We decide to depict the relaxation times with the greatest frequency, because averaging over such a broad distribution is unsubstantiated. Due to this broad distribution, an activation energy of $E_{A,DLS} = (48.37 \pm 3.60)$ kJ mol^{-1} with a relatively large uncertainty is calculated. Combination of our static and dynamic light scattering results reveals that the spatial density distribution within the polymer gel exhibits a non-negligible impact on the network dynamics, thereby leading to an unusual broad distribution of relaxation times. To examine the reliability of our slow relaxation time determination, we introduce a second method to analyze the position-dependent intensity correlation functions. In a first step, we have grouped the recorded 500 correlation functions into five 100-packs and accordingly calculated five average correlation functions. These average functions were then fitted to equations (6) – (8) yielding five τ_{slow} values. By doing so, the statistical error of τ_{slow} could drastically be reduced and a deviant activation energy of $E_{A,group} = (66.57 \pm 3.35)$ kJ mol^{-1} is obtained. Applying the fitting of all single 500 functions at lower temperatures (25 °C and 35 °C), few very high τ_{slow}-values (that might result from incompletely resolved correlation functions due to the short experimental correlation time) shift the total average value to apparent higher values. In contrast to that, at the highest temperatures (45 °C), both analysis methods result in nearly the same $<\tau_{slow}>$ because the slow mode is well resolved in all correlation functions. This fact mainly affects the slope of the Arrhenius plot and therefore also the activation energy. This new activation energy $E_{A,group} = (66.57 \pm 3.35)$ kJ mol^{-1} is the same as the one obtained for the 10k gel by our FRS experiments.

Exemplary average correlation functions of different temperatures and a comparison of the slow-mode Arrhenius plots of both analysis methods (single vs. group) are shown in the SI (**Figure S8**).

Self-diffusion by FRS

Forced Rayleigh scattering is chosen as a method to investigate the self-diffusivities of fluorescence-labeled tetra-arm PEG-terpyridine macromolecules through the network on length scales of 0.5–24 µm. The relaxation times are obtained by monitoring the Bragg-diffracted beam intensity created by a vanishing sinusoidal dye concentration profile. Similar to previously investigated protein-based P4-coils[11,15] and linear acrylamide chains with nickel–histidine coordination bonds,[12] a phenomenological superdiffusive regime with $\langle\tau\rangle \approx d^{2\alpha}$ ($\alpha < 1$) is found in a range of d^2 = 0.3–200 µm² in the 10k gels. Beyond this range, terminal Fickian diffusion is observed in all tetra-arm PEG-terpyridine networks at various temperatures (**Figure 6(A)**).

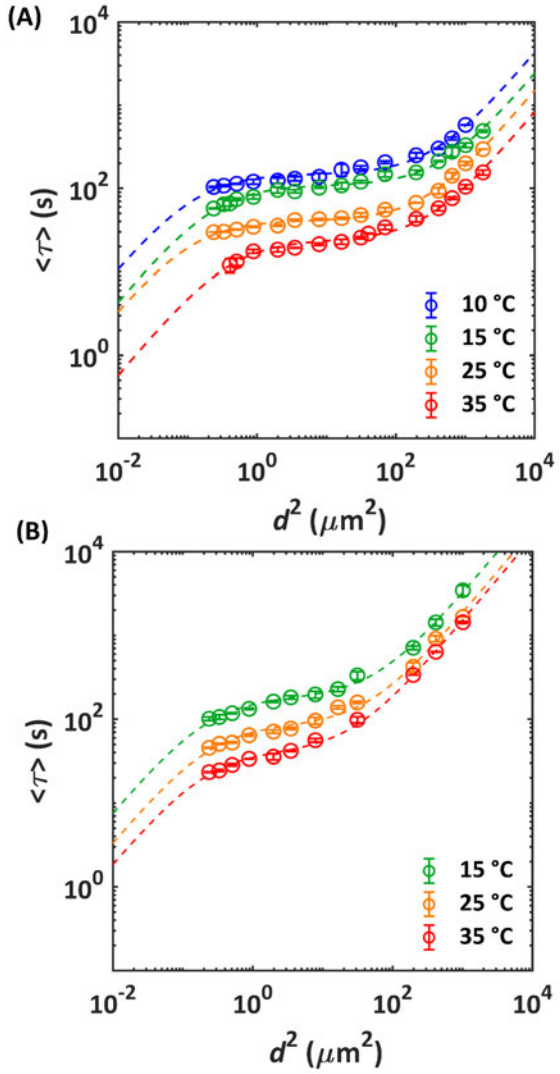

Figure 6. <τ> vs. d^2 of a zinc tetra-arm PEG-terpyridine network ((A): M_w = 10,000 g mol^{-1}, 10% (w/v) and (B): M_w = 20,000 g mol^{-1}, 20% (w/v)) at the temperatures 10 °C (blue), 15 °C (green), 25 °C (yellow), and 35 °C (red) with fits to the two-state model (dashed lines). Error bars depict standard deviations of three different gel position measurements.

As reported earlier,[11,13] the d^2-dependent relaxation times <τ> are fitted to an empirical two-state model that is based on a set of reaction-diffusion equations. The two-state model assumes the polymer to be present in two states: an immobile associated state (A, where its transient junctions are connected to the network) and a molecular state (M, where it is free to diffuse). The molecules interconvert between the two states via first-order kinetics that are characterized by the interconversion rates k_{on} and k_{off}.

$$M \underset{k_{off}}{\overset{k_{on}}{\rightleftharpoons}} A \tag{15}$$

Both states are characterized by their diffusivities D_A and D_M and the concentration changes C_M and C_A over time are described by the following equations:

$$\frac{\partial C_M}{\partial t} = D_M \frac{\partial^2 C_M}{\partial x^2} - k_{on} C_M + k_{off} C_A \tag{16}$$

$$\frac{\partial C_A}{\partial t} = D_A \frac{\partial^2 C_A}{\partial x^2} + k_{on} C_M - k_{off} C_A \quad (17)$$

By fitting the model to the data, the three parameters k_{off}, $D_{M,eff} = \frac{D_M}{(1 + K_{eq})}$ with $K_{eq} = \frac{k_{on}}{k_{off}}$, and γK_{eq} with $\gamma = \frac{D_A}{D_M}$ are obtained. γK_{eq} is anti-proportional to the width of the superdiffusive regime and can therefore be seen as a quantitative measure and is sometimes denoted as anomaly constant. $D_{M,eff}$ at large length scales denotes an effective reduced diffusivity reflecting a superposition of all relaxation modes (e. g. hopping, walking…). Despite its simplifications and the main assumption of only two existing states, the course of <τ> is captured by the two-state model throughout the whole d^2-range (**Figure 6**, dashed lines). **Figure 7** shows the obtained temperature-dependent fit parameters k_{off} (A), $D_{M,eff}$ (B), and γK_{eq} (C) for the 10k and 20k gels. It should be noted that k_{off} describes the interconversion rate from the stated phenomenological associated to the molecular state. As expected, k_{off} is decreasing with decreasing temperature whereby the 20k gel has lower absolute k_{off} values.

In terms of the model, this finding implies that the interconversion between the molecular and the associated state is faster with decreasing arm length.

Even though k_{off} cannot be directly considered to be a physical constant because it is found to have significant concentration dependencies,[11] we obtain the same activation energies of $E_{A,10k} = (62.07 \pm 4.82)$ kJ mol^{-1} and $E_{A,20k} = (58.13 \pm 1.77)$ kJ mol^{-1} as that obtained by UV-Vis measurements. The activation energy can therefore be considered as independent of arm length and total polymer concentration. The width of the superdiffusive regime is increasing with decreasing temperature and the 20k gels exhibit a less wide superdiffusive regime as expressed by the higher anomaly constant γK_{eq}. The latter fact might result as an effect of the increased total polymer concentration in the 20k gels and the consequentially decreased number of loops, as found earlier in the rheology section. Reduced loop formation would lead to fewer hopping events because more arms are attached to the

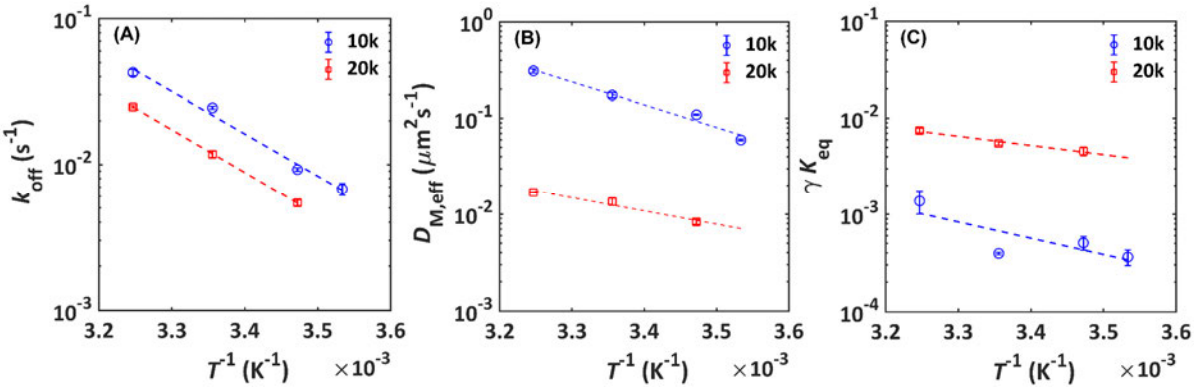

Figure 7. Temperature-dependent two-state model fit parameters k_{off} (A), $D_{M,eff}$ (B), and γK_{eq} (C) of a 10k zinc tetra-arm PEG-terpyridine (10% (w/v), blue symbols) and a 20k zinc tetra-arm PEG-terpyridine (20% (w/v), red symbols) network in DMF.

network, giving a narrower superdiffusive regime.[14] In general, hopping describes the diffusive motion when a star-polymer detaches all four arms from the network and its center-of-mass travels an unexpected large distance. Rapp *et al.*[30] showed that the equilibrium binding constant of a sticker is drastically reduced if other arms of the same molecule are already connected to the network. The chain conformation of an unattached arm is limited by the surrounding local network structure and binding is therefore entropically unfavoured. They also stated that with increasing chain length, the entropic penalty for binding generally decreases as more chain conformations are possible. We support this finding with our 20k gels where the width of the superdiffusive regime is narrowed by an order of magnitude when compared to the 10k gels.

Recent molecular simulations based on Brownian dynamics of star-shaped polymer networks predict a Fickian regime at low length scales d^2, followed by a caging regime, one (or more) apparent superdiffusive regimes and again, Fickian diffusion at large length scales with an effective diffusivity.[14] To combine our light scattering and FRS results, the reciprocal length scale q accessed by LS is converted into real space via $d = 2\pi/q$. By doing so, we obtain a length scale range between 0.23 μm and 24 μm. **Figure 8(A)** shows the jointed results. The fast mode obtained by light scattering exhibits a linear $\tau_{fast} \approx d^2$ dependency that is typical for diffusive motion (**Figure 8(A)**, open diamonds). This cooperative chain motion is faster by seven orders of magnitude than the self-diffusion of a single associating star. We achieve an overlap of our FRS and DLS data in a length scale range of $1 \cdot 10^{-2} - 2 \cdot 10^{-2}$ μm^2. At this intermediate length scale d, the center-of-mass diffusion of macromonomers, the collective segmental polymer relaxation, and the sticker dissociation is visible. The self-diffusivities probed by FRS might not be visible in our DLS experiments as the experimental time window cannot adequately capture such a slow relaxation process.

Finally, **Figure 8(B)** shows a combined Arrhenius plot of all inverse characteristic relaxation times obtained by UV-Vis, rheology, FRS and DLS. Those rate constants span a broad range of 15 orders of magnitude with the fastest rate being the relaxation of single polymer strands between the transiently connected stickers as probed by DLS. For this process, a comparably low activation energy of (11.62 ± 1.12) kJ mol^{-1} is calculated.

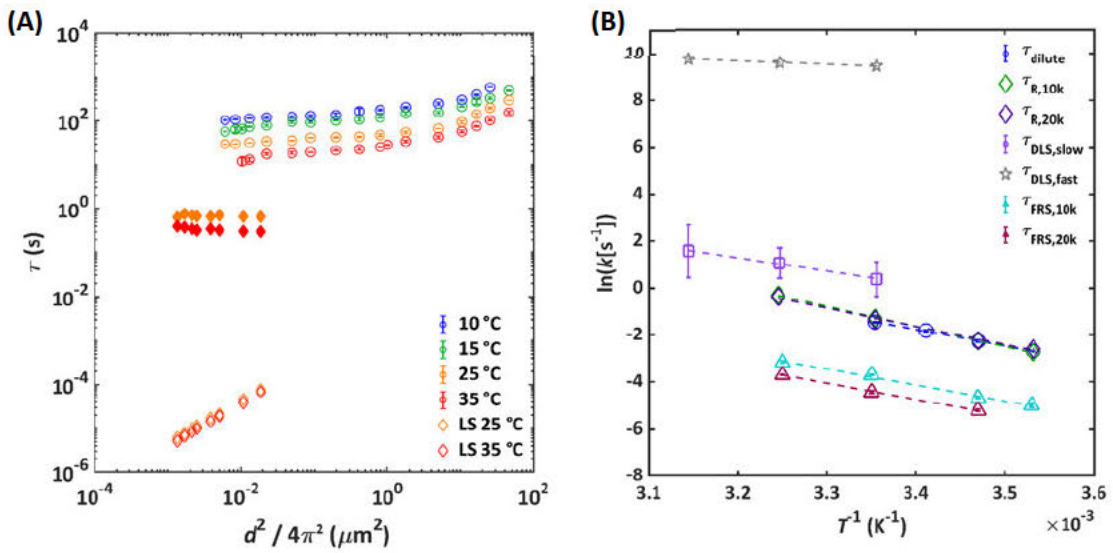

Figure 8. (A) Combination of FRS (open circles) and LS (fast mode: open diamonds, slow mode: closed diamonds) relaxation times vs. real space d^2 of a zinc tetra-arm PEG-terpyridine network (10k, 10% (w/v), in DMF) at 10 °C (blue), 15 °C (green), 25 °C (yellow), and 35 °C (red), along with fits to the two-state-model (dashed lines). (B) Comparison of the characteristic temperature-dependent relaxation times obtained in dilute conditions (blue circles), terminal relaxation times obtained by rheology measurements (green (10k) and purple (20k) diamonds), fast and slow relaxation times (single function-fitting) obtained by light scattering (grey diamonds and purple squares), and relaxation times obtained by FRS (turquoise (10k) and maroon (20k) triangles) of a zinc tetra-arm PEG-terpyridine gel in DMF.

As discussed in a previous section, the terminal relaxation times obtained by rheology coincide with the dissociation time of an isolated zinc terpyridine complex in dilute conditions (compare blue circles and green and purple diamonds in **Figure 8(B)**). Surprisingly, the slow mode that is present in all DLS intensity correlation functions exhibits a shorter relaxation time resulting in a higher relaxation rate when compared to rheology or UV-Vis. This finding is striking, as we would expect the dissociation time of the isolated zinc terpyridine complex to be the lower time limit for further emerging viscoelastic relaxation processes. As shown earlier, the unusual broad relaxation time distribution leads to large uncertainties concerning the absolute relaxation time determination. As a lower limit, the slowest times are generated by the center-of-mass diffusion of single star-shaped polymer molecules within the network. Based on our static light scattering results, we cannot exclude relaxation mechanisms through cluster/aggregate diffusion, however, such slow relaxation times are not accessible by the experimental methods used in this work. In addition to that, we have analysed all pre-exponential factors A of the linearized Arrhenius law $\ln(k) = \ln(A) - \frac{E_A}{RT}$. These factors can be interpreted as the number of attempts that a molecule needs before it finally reacts. Their absolute values and interdependencies with the corresponding activation energies are shown in the SI (**Figure S9**).

4.3.5 Conclusions

A complex hierarchy of relaxation times is studied in telechelic model-type tetra-arm PEG gels that are percolated in solution through transient zinc-terpyridine complexes. In this work, various experimental techniques such as FRS, SLS, DLS, UV-Vis, and rheology are chosen to access broad time and length scale ranges and to combine polymer self-diffusivities, single sticker dissociation times as well as mechanical stress response. In contrast to other linear polymer networks, the star-shaped polymer model network investigated in this study only exhibits a negligible effect of bond lifetime renormalization. The diffusion properties are influenced by the appearance of an anomalous superdiffusive regime that is less pronounced if the polymer arm length is increased (at constant total sticker concentration). A thorough understanding of the supramolecular network dynamics is of major importance to connect the microscopic properties with the resulting macroscopic network performance such as self-healing or permeability. In addition to that, network dynamics are often influenced by the underlying network topology and strongly depend on temperature. Combination of our FRS and LS data shows a multitude of relaxation processes, each with characteristic time and length scale dependencies. In general, these insights might be transferable to other associated polymer systems to help completing the picture of relaxation processes and mechanisms. Furthermore, we believe that this study can serve as an experimental model basis for simulation works aiming to predict the hierarchy of network relaxation times.

4.3.6 Acknowledgements

This work was supported by the German Research Foundation (DFG) under grant no. SE 1888/7-1 (Project no. 376900084). FRS experiments at MIT were supported by NSF DMR-1709315. We thank [redacted] for advice and valuable discussions concerning FRS. [redacted] acknowledges [redacted] for constant support. We thank the referees of this work for their valuable and helpful comments in the stage of peer revision.

4.3.7 References

(1) a) J. Liu, C. S. Y. Tan, Z. Yu, N. Li, C. Abell and O. A. Scherman, *Advanced materials* (Deerfield Beach, Fla.), **2017**, *29*; b) Q. Zheng, Z. Ma and S. Gong, *J. Mater. Chem. A*, **2016**, *4*, 3324–3334; c) T. Yan, K. Schröter, F. Herbst, W. H. Binder and T. Thurn-Albrecht, *Scientific reports*, **2016**, *6*, 32356; d) N. Holten-Andersen, A. Jaishankar, M. Harrington, D. E. Fullenkamp, G. DiMarco, L. He, G. H. McKinley, P. B. Messersmith and K. Y. C. Lee, *Journal of materials chemistry. B*, **2014**, *2*, 2467–2472;

e) K. Varaprasad, G. M. Raghavendra, T. Jayaramudu, M. M. Yallapu and R. Sadiku, *Materials science & engineering. C, Materials for biological applications*, **2017**, *79*, 958–971;

(2) a) M. J. Webber, E. A. Appel, E. W. Meijer and R. Langer, *Nature materials*, **2016**, *15*, 13–26; b) L. Shi, P. Ding, Y. Wang, Y. Zhang, D. Ossipov and J. Hilborn, *Macromolecular rapid communications*, **2019**, *40*, e1800837; c) C. O. Akintayo, G. Creusen, P. Straub and A. Walther, *Macromolecules*, **2021**; d) T. R. Hoare and D. S. Kohane, *Polymer*, **2008**, *49*, 1993–2007;

(3) E. W. Meijer and A. P. H. J. Schenning, Nature, 2002, 419, 353–354.

(4) J. Hoque, N. Sangaj and S. Varghese, *Macromolecular bioscience*, **2019**, *19*, e1800259.

(5) M. Golkaram and K. Loos, *Macromolecules*, **2019**, *52*, 9427–9444.

(6) S. P. O. Danielsen, H. K. Beech, S. Wang, B. M. El-Zaatari, X. Wang, L. Sapir, T. Ouchi, Z. Wang, P. N. Johnson, Y. Hu, D. J. Lundberg, G. Stoychev, S. L. Craig, J. A. Johnson, J. A. Kalow, B. D. Olsen and M. Rubinstein, *Chemical reviews*, **2021**, *121*, 5042–5092.

(7) S. Tang and B. D. Olsen, *Macromolecules*, **2016**, *49*, 9163–9175.

(8) a) A. Shabbir, I. Javakhishvili, S. Cerveny, S. Hvilsted, A. L. Skov, O. Hassager and N. J. Alvarez, *Macromolecules*, **2016**, *49*, 3899–3910; b) B. J. Gold, C. H. Hövelmann, N. Lühmann, N. K. Székely, W. Pyckhout-Hintzen, A. Wischnewski and D. Richter, *ACS Macro Lett.*, **2017**, *6*, 73–77;

(9) S. Ge, M. Tress, K. Xing, P.-F. Cao, T. Saito and A. P. Sokolov, *Soft matter*, **2020**, *16*, 390–401.

(10) M. Rubinstein and Semenov, Alexander, N., *Macromolecules*, **1998**, 1386–1397.

(11) S. Tang, M. Wang and B. D. Olsen, *Journal of the American Chemical Society*, **2015**, *137*, 3946–3957.

(12) I. Mahmad Rasid, N. Holten-Andersen and B. D. Olsen, *Macromolecules*, **2021**, *54*, 1354–1365.

(13) S. Tang, A. Habicht, S. Li, S. Seiffert and B. D. Olsen, *Macromolecules*, **2016**, *49*, 5599–5608.

(14) J. Ramirez, T. J. Dursch and B. D. Olsen, *Macromolecules*, **2018**, *51*, 2517–2525.

(15) A. Rao, H. Yao and B. D. Olsen, *Phys. Rev. Research*, **2020**, *2*.

(16) I. M. Henderson and R. C. Hayward, *Polym. Chem.*, **2012**, *3*, 1221.

(17) T. Rossow and S. Seiffert, *Polym. Chem.*, **2014**, *5*, 3018–3029.

(18) a) M. Shibayama, T. Tanaka and C. C. Han, *The Journal of Chemical Physics*, **1992**, *97*, 6829–6841; b) S. Mallam, F. Horkay, A. M. Hecht, A. R. Rennie and E. Geissler, *Macromolecules*, **1991**, *24*, 543–548; c) S. Seiffert, *Progress in Polymer Science*, **2017**, *66*, 1–21;

(19) T. Norisuye, Q. Tran-Cong-Miyata and M. Shibayama, *Macromolecules*, **2004**, *37*, 2944–2953.

(20) J. G. H. Joosten, J. L. McCarthy and P. N. Pusey, *Macromolecules*, **1991**, *24*, 6690–6699.

(21) M. Shibayama, S.-i. Takata and T. Norisuye, *Physica A: Statistical Mechanics and its Applications*, **1998**, *249*, 245–252.

(22) M. Shibayama, Y. Fujikawa and S. Nomura, *Macromolecules*, **1996**, *29*, 6535–6540.

(23) a) S. C. Grindy, M. Lenz and N. Holten-Andersen, *Macromolecules*, **2016**, *49*, 8306–8312; b) K. Breul, S. Kissel and S. Seiffert, *Macromolecules*, **2021**, *54*, 8407–8422; c) G. A. Parada and X. Zhao, *Soft matter*, **2018**, *14*, 5186–5196;

(24) S. C. Grindy, R. Learsch, D. Mozhdehi, J. Cheng, D. G. Barrett, Z. Guan, P. B. Messersmith and N. Holten-Andersen, *Nature materials*, **2015**, *14*, 1210–1216.

(25) W. Knoben, N. A. M. Besseling and M. A. Cohen Stuart, *The Journal of Chemical Physics*, **2007**, *126*, 24907.

(26) E. B. Stukalin, L.-H. Cai, N. A. Kumar, L. Leibler and M. Rubinstein, *Macromolecules*, **2013**, *46*.

(27) D. Amin, A. E. Likhtman and Z. Wang, *Macromolecules*, **2016**, *49*, 7510–7524.

(28) Y. Tsuji, S. Nakagawa, C. I. Gupit, M. Ohira, M. Shibayama and X. Li, *Macromolecules*, **2020**, *53*, 7537–7545.

(29) M. F. Koziol, K. Fischer and S. Seiffert, *Macromolecules*, **2021**, *54*, 4375–4386.

(30) P. B. Rapp, A. K. Omar, B. R. Silverman, Z.-G. Wang and D. A. Tirrell, *Journal of the American Chemical Society*, **2018**, *140*, 14185–14194.

4.3.8 Supporting Information

^{1}H-NMR

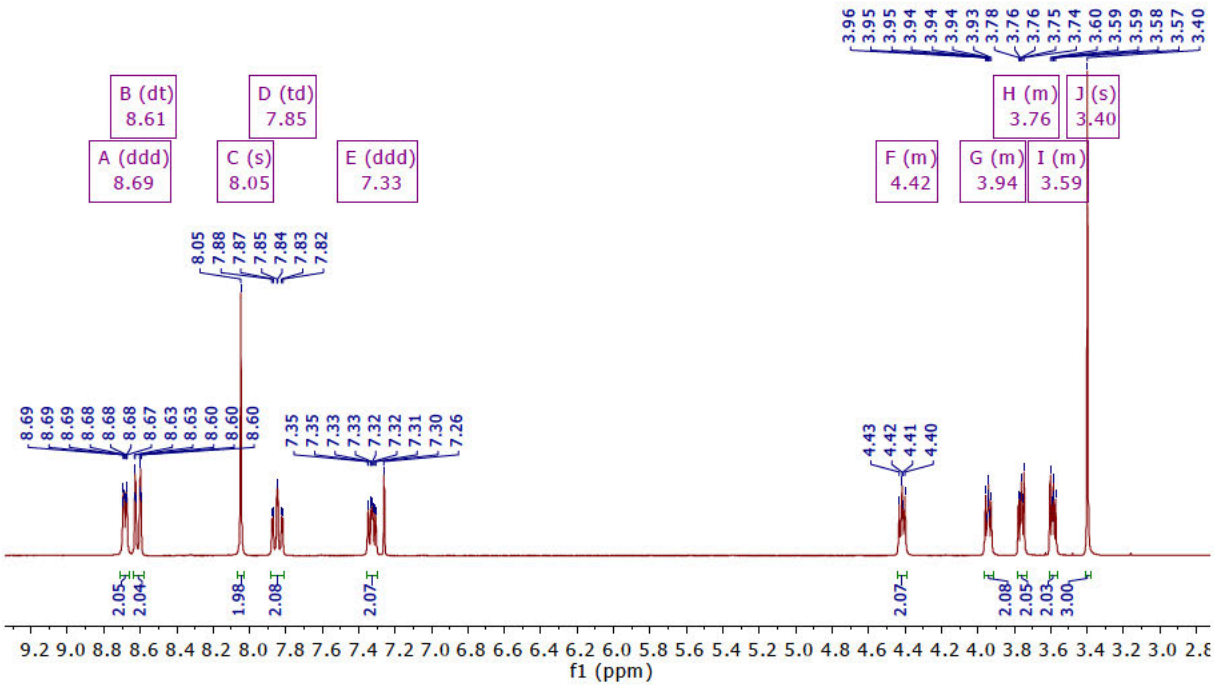

Figure S1. ^{1}H-NMR spectrum of 4′-[2-(1-Methoxyethoxy)ethoxy]2,2′:6′,2′′-terpyridine (1), 300 MHz, $CDCl_3$.

UV-Vis measurements

The zinc terpyridine bond dissociation time is determined by time-depending UV-Vis monitoring of the MLCT band at 336 nm. The time trace is fitted to an exponential function as pseudo first-order conditions are assumed:

$$\mathrm{Abs}(t) = A - B \cdot \exp\left(-\frac{t}{\tau_{\mathrm{dilute}}}\right) \qquad (1)$$

with an offset A, the maximum absorbance B, the characteristic relaxation time τ_{dilute}. Similar to Tang *et al.*,[1] several approximations are made, for example that only the forming Cu(II)-terpyridine complexes are contributing to the monitored MLCT band.

Rheology

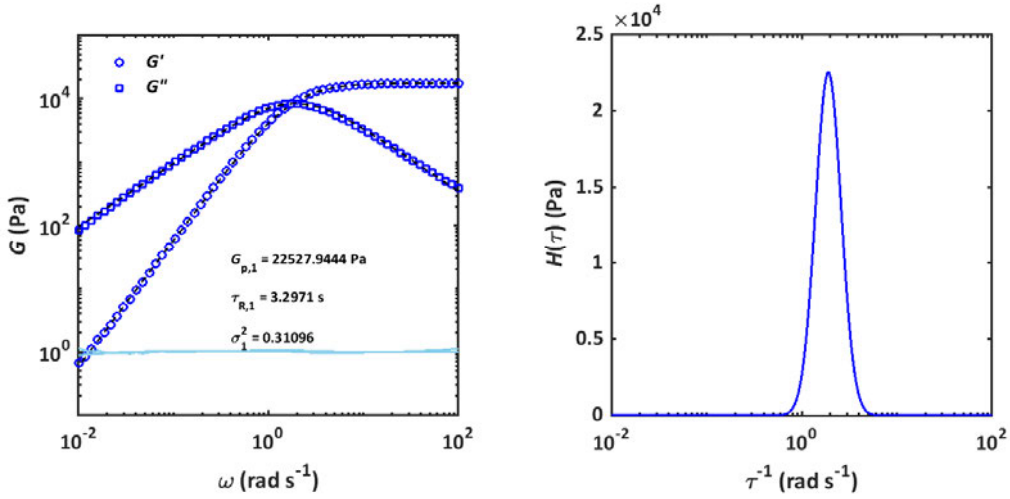

Figure S2. (A) Exemplary frequency-depending storage (open circles) and loss (open squares) modulus of a tetra-arm PEG-terpyridine gel (DMF, 10 wt%) at 25 °C and fit to a Maxwell type relaxation model (black dashed line). The residual is depicted as light blue line. (B) Resulting relaxation time distribution $H(\tau)$ of the same gel.

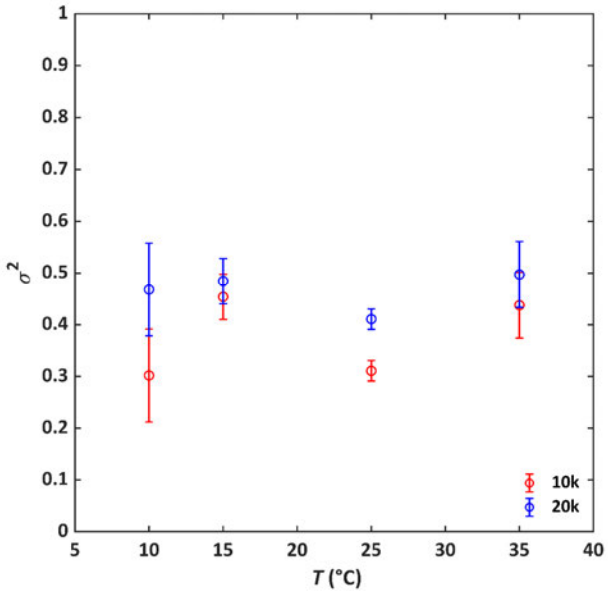

Figure S3. Standard deviation σ^2 of the relaxation time distribution of a 10k (10% (wt/v), red symbols) and a 20k (20% (wt/v), blue symbols) zinc tetra-arm PEG-terpyridine gel (DMF) depending on the temperature. Errorbars represent uncertainties within 95% confidence interval.

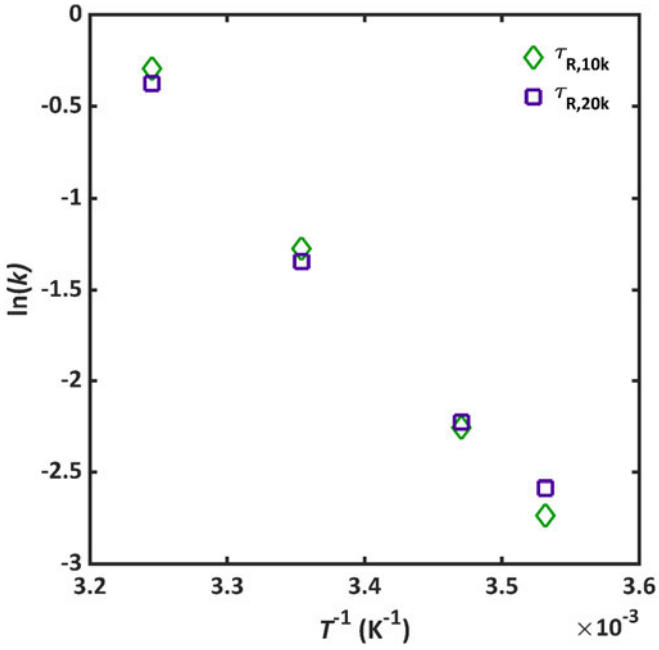

Figure S4. Arrhenius plot ($\ln(k)$ vs. T^{-1}) of the relaxation rates $k = \tau^{-1}$ obtained by oscillatory shear rheology of a 10k (green open diamonds) and a 20k (purple open squares) gel.

Light Scattering

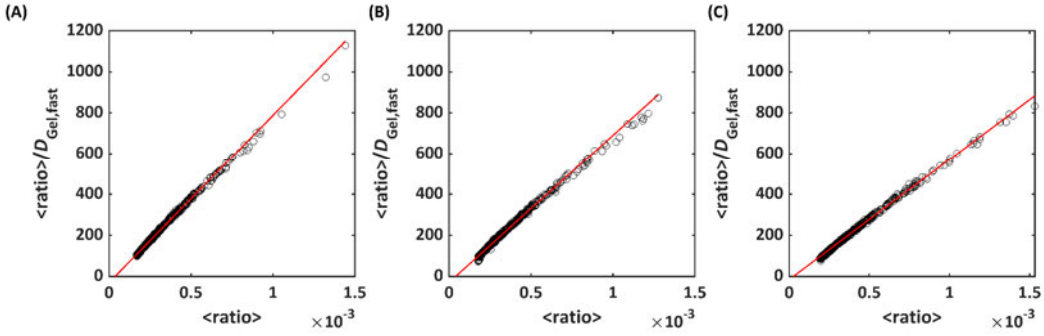

Figure S5. $\frac{\langle ratio \rangle}{D_{Gel,fast}}$ vs. <ratio> shows a linear dependence at three different temperatures 25 °C (A), 35 °C (B), and 45 °C (C). $\frac{2}{slope}$ yields the partial heterodyne diffusion coefficient D_{PHD} of the fast relaxation mode.

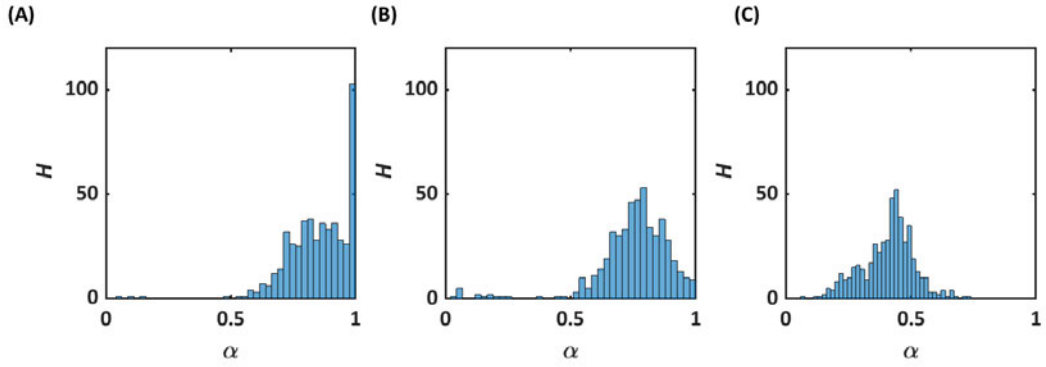

Figure S6. Distribution of stretch exponents α of a zinc tetra-arm PEG-terpyridine gel (10% (wt/v), DMF) at 25 °C (A), 35 °C (B), and 45 °C (C) at an angle of 30 °. α is decreasing with increasing temperature.

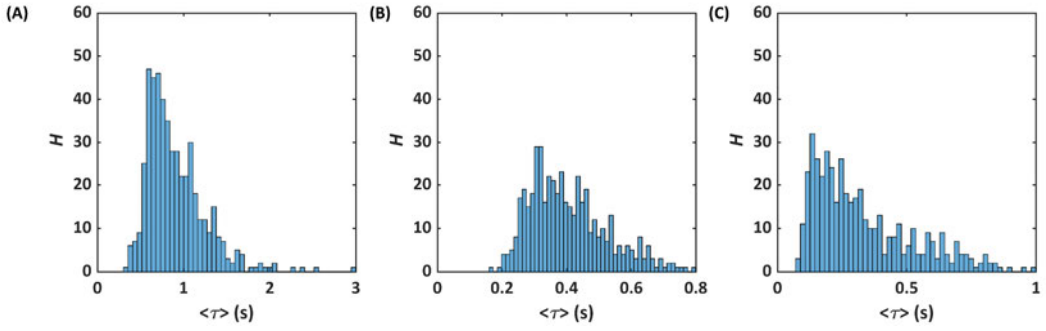

Figure S7. Frequency distribution histogram of the slow relaxation times at (A) 25 °C, (B) 35 °C, and (C) 45 °C. With increasing temperature τ shifts to lower values and the distribution broadens.

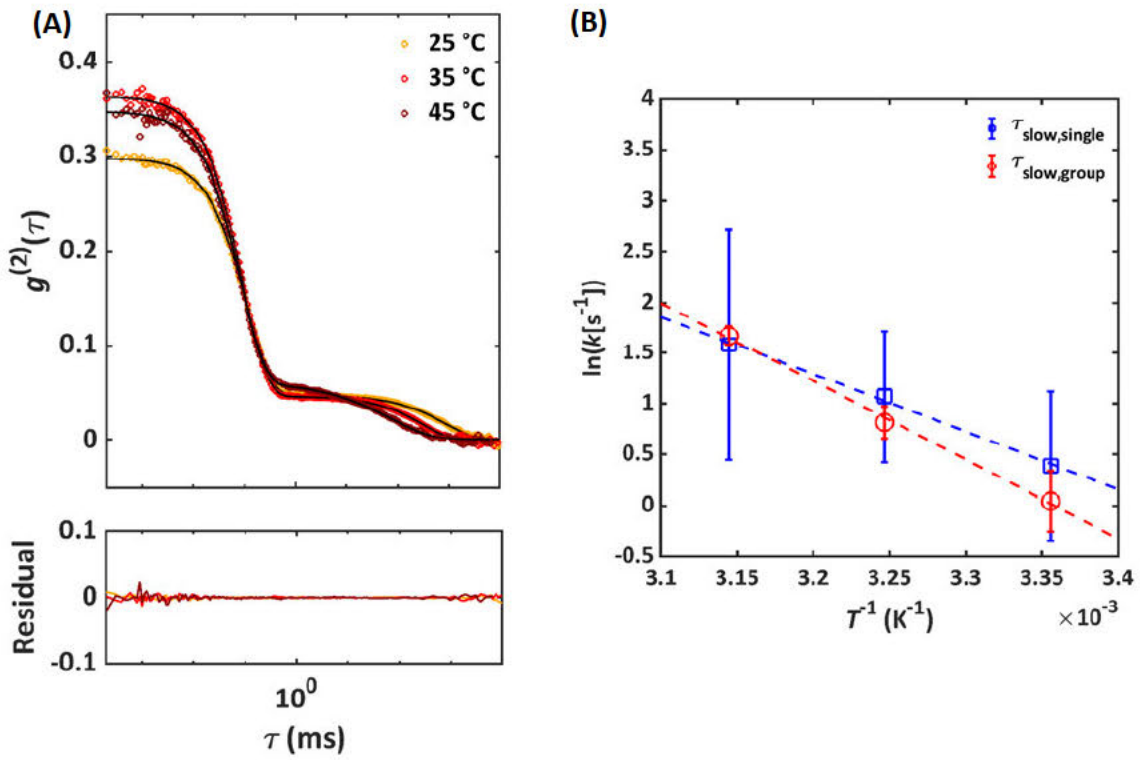

Figure S8. (A) Arrhenius plot of the temperature-dependent slow relaxation times obtained by either fitting all single 500 intensity correlation functions and subsequent averaging over the obtained 500 τ_{slow} values (blue) or fitting the average of 5 x 100 correlation functions, respective (red). (B) Exemplary average correlation function (five 100-packs) at 25 °C (yellow), 35 °C (red), and 45 °C (maroon).

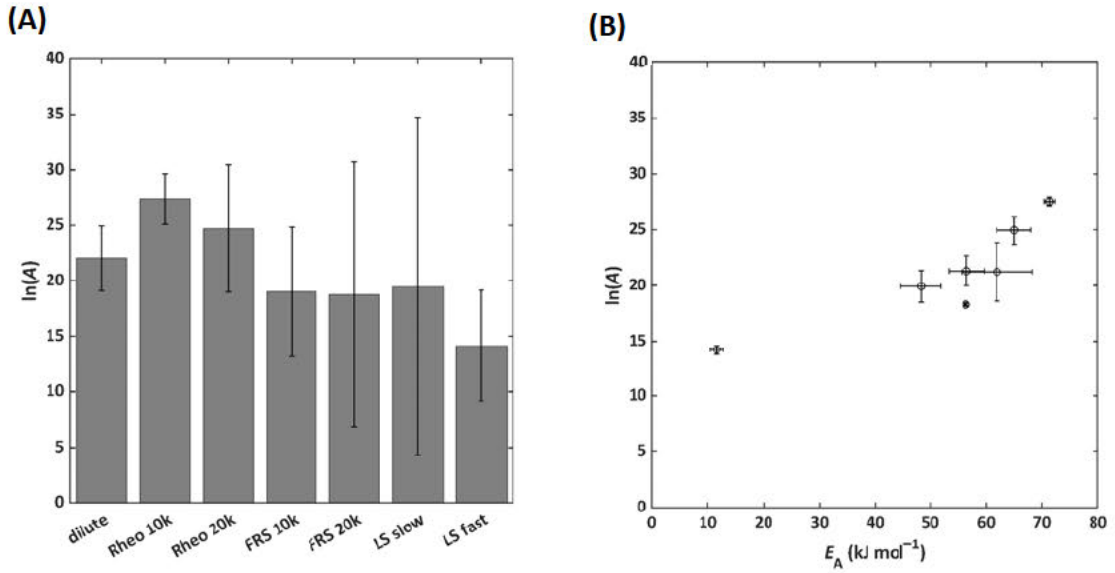

Figure S9. (A) Pre-factors of the Arrhenius law obtained by UV-Vis measurements (dilute conditions), rheology, forced Rayleigh scattering, and dynamic light scattering. Error bars depict uncertainties within a 95% confidence interval. (B) Pre-factors vs. activation energy.

Forced Rayleigh Scattering

The d^2-spacing dependence of <τ> is fitted to a previously described two-state model.[1,3–5] In summary, the model assumes the polymer to be present in two states: an immobile associated state (A, where its transient junctions are connected to the network) and a molecular state (M, where it is free to diffuse). Both states are characterized by their diffusivities D_A and D_M. Following pseudo-first order kinetics, the polymers transform between both states and the concentration changes C_M and C_A over time are described by the following equations:

$$\frac{\partial C_M}{\partial t} = D_M \frac{\partial^2 C_M}{\partial x^2} - k_{on} C_M + k_{off} C_A \quad (2)$$

$$\frac{\partial C_A}{\partial t} = D_A \frac{\partial^2 C_A}{\partial x^2} + k_{on} C_M - k_{off} C_A \quad (3)$$

k_{on} and k_{off} denote the reaction rates of the interconversion process. By fitting the model to the data, the three parameters k_{off}, $D_{M,eff} = \frac{D_M}{(1 + K_{eq})}$ with $K_{eq} = \frac{k_{on}}{k_{off}}$, and γK_{eq} with $\gamma = \frac{D_A}{D_M}$ are obtained. γK_{eq} is antiproportional to the width of the superdiffusive regime and can therefore be seen as a quantitative measure. $D_{M,eff}$ at large length scales denotes an effective reduced diffusivity reflecting a superpositon of all relaxation modes (e. g. hopping, walking …).[6]

References

[1] Tang, S.; Olsen, B. D. Relaxation Processes in Supramolecular Metallogels Based on Histidine–Nickel Coordination Bonds. *Macromolecules* **2016**, *49*, 9163–9175.

[2] Grindy, S. C.; Learsch, R.; Mozhdehi, D.; Cheng, J.; Barrett, D. G.; Guan, Z.; Messersmith, P. B.; Holten-Andersen, N. Control of hierarchical polymer mechanics with bioinspired metal-coordination dynamics. *Nature materials* **2015**, *14*, 1210–1216.

[3] Tang, S.; Wang, M.; Olsen, B. D. Anomalous self-diffusion and sticky Rouse dynamics in associative protein hydrogels. *Journal of the American Chemical Society* **2015**, *137*, 3946–3957.

[4] Tang, S.; Habicht, A.; Li, S.; Seiffert, S.; Olsen, B. D. Self-Diffusion of Associating Star-Shaped Polymers. *Macromolecules* **2016**, *49*, 5599–5608.

[5] Mahmad Rasid, I.; Holten-Andersen, N.; Olsen, B. D. Anomalous Diffusion in Associative Networks of High-Sticker-Density Polymers. *Macromolecules* **2021**, *54*, 1354–1365.

[6] Ramirez, J.; Dursch, T. J.; Olsen, B. D. A Molecular Explanation for Anomalous Diffusion in Supramolecular Polymer Networks. *Macromolecules* **2018**, *51*, 2517–2525.

4.4 Defect-controlled softness, diffusive permeability, and mesh-topology of metallo-supramolecular hydrogels

[redacted]* Martha Franziska Koziol,* [redacted]

* these authors contributed equally

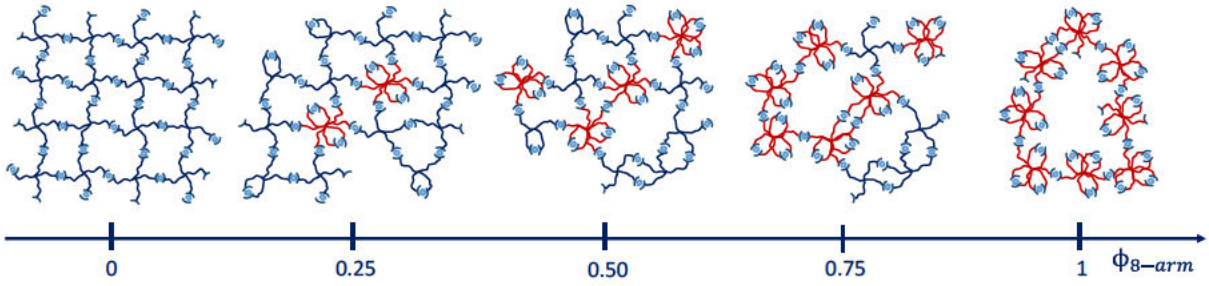

Accepted manuscript (05.12.2021),

Soft Matter, **2022**, DOI: 10.1039/D1SM01456K

Author Contributions	
[redacted]	Synthesis and analysis of the polymers, rheology experiments, sample preparation for DQ-NMR experiments, writing and editing of the manuscript
Martha Koziol	Synthesis of the dye-labelled polymers, FRAP experiments, data analysis and fitting of rheology and FRAP, writing and editing of the manuscript
[redacted]	DQ-NMR experiments and data analysis, writing of the manuscript
[redacted]	Correction and discussion of the manuscript
[redacted]	Conception of the work, discussion of the results
[redacted]	Supervision and conception of the work, correction of the manuscript, acquisition of funding

The presented manuscript contributes to the field of controlled defect engineering in soft matter. Having characterized and discussed network dynamics and structure in the previous chapters, the effects of intentionally incorporated connectivity defects into transient tetra-arm PEG-terpyridine networks were investigated herein.

As explained in detail, supramolecular polymer networks exhibit complex structures with many interwoven parameters (chemistry of polymers, kinetics of linking units, connectivity, etc.) that mutually influence the resulting mechanical properties. Creating model networks with simple variation in one single network parameter while keeping most other factors constant, remains a difficult goal if the establishment of generally applicable theories is the subject of interest.

To overcome this limitation, a series of networks consisting of four-arm macromolecules that were gradually replaced by macromolecules with eight arms of the same arm molar mass provided insights into structural changes and diffusive properties. While the sticker concentration remains equal, these networks were considered as model networks, as only one parameter (e.g. connectivity) was varied. The combined results demonstrate a direct relation between an increased defect fraction (as found in DQ-NMR measurements), the consequent decrease of the macroscopic elastic network response (plateau modulus in rheology), and a strongly increased self-diffusivity (FRAP). Here, structure and dynamics are mutually dependent. This approach directly allows for the establishment of structure–property–relationships that can further be used if material design with specific functionalities is targeted.

4.4.1 Abstract

Hydrogels are polymer networks swollen in water; they are suitable materials for biomedical applications such as tissue engineering and drug delivery. In the latter, the controlled diffusion of small diffusants inside the network is essential, as it determines the release mechanism of the drug. In general, the diffusion inside a polymer network is controlled by its mesh-size. Here, we actively control the diffusivity and also the softness of metallo-supramolecular hydrogels via the network mesh-topology by introducing connectivity defects. A model polymer network is realized based on a 4-arm poly(ethylene glycol) (pEG) where each arm is capped with terpyridine moieties that are capable to form metallo-supramolecular complexes with zinc ions. In this model network, we insert 8-arm pEG macromolecules that are functionalized with terpyridine at different ratios to create connectivity defects. With an increasing amount of 8-arm pEG, the polymer network forms more loops, as quantified by double quantum-NMR. This doped network shows an enhanced self-diffusivity of the building block molecules within the network, as examined by fluorescence recovery after photobleaching, and a higher softness, as investigated by oscillatory shear rheology. With these findings, we show that it is possible to tune the diffusivity and softness of hydrogels with defects in a rational fashion.

4.4.2 Introduction

Defect engineering in soft matter is a wide field of research that allows for tuning material properties on multiple levels.[1] In one branch of that discipline, structural inhomogeneities affect the properties of polymer-network gels, specifically the local and global elasticity,[2] fracture mechanism,[3] and the diffusive permeability of guest substances,[4] and since these properties lay the ground for the main applications of gels, the impact and ability of controlling such inhomogeneities is crucial. Prominent examples for inhomogeneities are found in hydrogels, which are three-dimensional polymer networks swollen in water.[5–7] These polymer

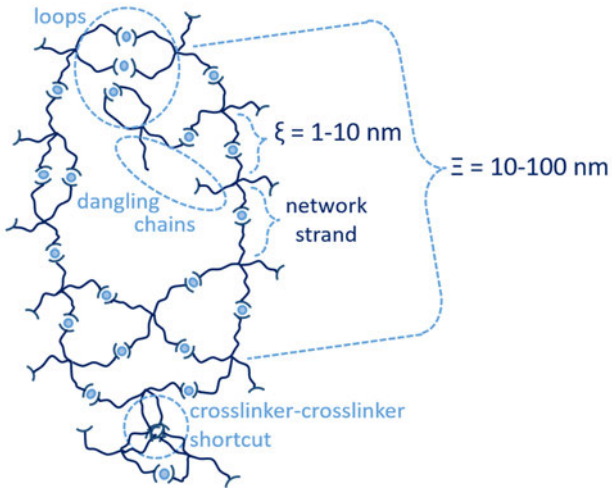

Fig. 1 Defects in polymer networks created by interconnection of four-arm star supramolecular precursors on different length scales. Local connectivity defects on the order of few nanometers form due to misconnectivities in the network. Global defects on the order of 10-100 nm result due to the inhomogeneous distribution of crosslinking density.

networks can be formed by connection of polymer strands either by supramolecular or covalent crosslinks. While covalent networks are stable in form and shape, supramolecular networks have the great advantage of being dynamic which means being responsive and recyclable. As a consequence, also the heterogeneities of covalent networks are frozen in time and space, whereas those of supramolecular networks follow spatiotemporal evolutions. The study and modelling of the extent, effect, and evolution of heterogeneities and defects in supramolecular networks require a model platform. One such platform is model transient networks formed by supramolecular crosslinking of multi-arm star-like polymer precursors. In such a network, the network strands denote the chain sections between branching points of two adjacent polymer precursors, and their length determines the network mesh-size ξ, as illustrated in **Fig. 1**. During network formation, different types of defects can form. Uneven distribution of the network crosslinks causes global spatial heterogeneities of some tens to hundreds of nanometers in space, and these defects are further pronounced when the polymer network is swollen.[8] Furthermore, irregularity in the local crosslinking-junction functionality results in local connectivity defects, which are in the magnitude of 1–10 nm, as shown **Fig. 1**.[7,9] These connectivity defects are loops, dangling chains, and crosslinker–crosslinker shortcuts. A loop is formed when several (usually two) arms of the same polymer form intra-molecular connections, or when two adjacent polymers form multiple inter-molecular connections, resulting in higher order loops.[10] A dangling chain is an arm that does not form any connections with another arm. A crosslinker-crosslinker shortcut is formed when two crosslinks interact with each other in form of uncontrolled clusters with varying number of junction functionalities. In view of this picture, we define connectivity as the number of potential intermolecular connections that a branched polymer macromolecule can form with its arms. Thus, the expected connectivity in a perfectly regular network consisting of only tetra-arm shaped telechelic polymers is four.

For rational material design, it is essential to understand how these different types of defects affect the properties of the hydrogel, such as its viscoelasticity and permeability, to optimize their use in applications. As hydrogels are constituted mainly by water, they are suitable for biomedical applications, such for example in tissue engineering or drug delivery.[11–13] However, to be used in these applications, they need to meet further requirements. In tissue engineering, for example, they need to resemble the mechanical properties of original natural tissues, and this can be challenging,[14,15] as the stiffness of living tissues can vary from a few Pascals to giga-Pascals, and it is even more challenging when considering the diverse functions of tissues.[11] In drug delivery, by contrast, not only the stiffness or softness of the

tissue is important, but also the diffusive permeability, which is governed by the mesh size of the hydrogel.[16] If the drug is smaller, similar, or larger than the network mesh-size, then the diffusion would be fast, slow, or even hindered, respectively.[16] Therefore, the control of the diffusion kinetics inside the hydrogel through engineering the mesh-size is crucial for its applications.

There are several approaches to engineer the mesh-size and its distribution in hydrogels. One way is to use precursors of different molecular weights, as suggested by Sakai *et al.*[17] These workers have systematically varied the heterogeneous distribution of the mesh-size in covalent model-network hydrogels formed by tetra-poly(ethylene glycol) (tetra-pEG), by employing precursors of two different molecular weights.[17] Despite they did not characterize the heterogeneities on the nanoscale, their macroscopic findings suggest that these bimodal networks have properties of a hydrogel having a strand size in between the arm length of the two precursors.[17]

Another approach to control the diffusion inside a hydrogel is to add dangling chains to the main network. With this strategy, Grunlan *et al.* controlled the mesh-size of a hydrogel with the introduction of thermoresponsive and charged dangling chains.[18] Their findings show that with negatively charged chains, smaller meshes are possible.[18] In an own previous work, we introduced poly(*N*-isopropylacrylamide) (pNIPAAm) dangling chains into a supramolecular polymer network and were able to similarly hinder the diffusion of small probes upon switching temperature above the lower critical solution temperature of pNIPAAm.[5] Similarly, we investigated how the network dynamics of gels, constituted by chains carrying sticky side-groups, changes with the introduction of sticky tracers having the same or lower connectivity than the network itself, thereby creating local connectivity defects.[4] Our findings show that the chain dynamics is enhanced in case of the network with connectivity defects, meaning that the probe diffuses faster than expected.[4] The effect of defects on mechanical properties has also been studied by means of simulations. For example, Shibayama *et al.* have introduced random defects in tetra-pEG networks and investigated the influence of the structural inhomogeneity on the mechanical properties.[19] Their findings show that with an increasing defect fraction, the Young modulus of the tetra-pEG networks decreased accordingly.[19]

Targeted mesh size variations or intentional incorporation of defects in polymer networks allow for a systematic investigation of their impact on the final material properties such as permeability or viscoelasticity. A recent review on defect engineering in soft matter highlights the utmost importance of structure control to implement a novel type of rational material design based on these aforementioned minor structural deviations.[1]

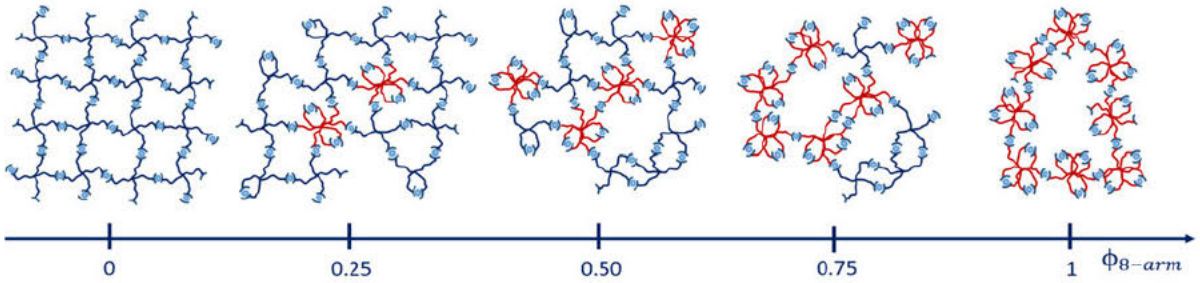

Fig. 2 Concept of this work. Metallo-supramolecular polymer-network gels composed of 4-arm pEG-terpyridine (M_w = 20 kg mol^{-1}) and 8-arm pEG-terpyridine (M_w = 40 kg mol^{-1}), combined in different ratios, thereby increasing the amount of connectivity defects in a controlled way. The impact of connectivity defects on macroscopic elastic and microscopic permeability properties are then investigated.

With this work, we aim to contribute to this emerging field of soft matter material design by presenting how to tailor supramolecular hydrogels in a systematic way via connectivity mismatches. We achieve that by systematically introducing different percentages of connectivity defects in a model supramolecular network and investigating the resulting macroscopic elastic response by oscillatory shear rheology, the microscopic self-diffusivity by fluorescence recovery after photobleaching (FRAP), and characterizing and proving the specific type of defects by double-quantum NMR (DQ-NMR).

Our material basis is composed of a supramolecular pEG hydrogel, where each arm of a star-shaped precursor is functionalized with a terpyridine unit that is capable of forming transient bis-complexes with divalent zinc ions. Starting from a regular network that only consists of 4-arm pEG-terpyridine macro-precursors (left network in **Fig. 2**), we successively replace a certain percentage of 4-arm pEG building blocks by 8-arm pEG-terpyridine polymers. To ensure a constant total terpyridine concentration, coming along with a constant number of arms, we select the molar mass of the 8-arm pEG to be a twofold of that of a 4-arm pEG. In other words, replacement of two macromolecules with four arms by one macromolecule with eight arms yields the same number of overall terpyridine units but a different degree of connectivity, keeping the same number of network strands per total volume constant (**Fig. 2**). With increasing amount of connectivity defects, the hydrogel becomes softer and the self-diffusivity inside increases, as demonstrated by complementary oscillatory shear rheology and FRAP experiments. These findings are associated with the emergence of various defect types, which are quantified by double quantum-NMR (DQ-NMR). Our results suggest a new paradigm for tuning properties of supramolecular hydrogels in a rational manner that might be transferable to other transient systems.

4.4.3 Experimental

Sample syntheses

The list of raw materials used to prepare the polymer samples of this work and the synthesis procedure can be found in the Electronic Supplementary Information.

In short, the hydroxyl termini of commercially available star-shaped pEG polymers were converted to terpyridine units by a Williamson type ether synthesis (**Figure SI1**).

Methods

Oscillatory shear rheology

To prove the effect of defects on the elastic properties of the supramolecular hydrogels, oscillatory shear rheology experiments were performed. For this purpose, stock solutions of 4-arm 20K and 8-arm 40K pEG-terpyridine with a concentration of 70 g L^{-1} were prepared by dissolving the appropriate amount of each polymer in Milli-Q water. This concentration was chosen to obtain gels in a regime well above the overlap concentration of a 4-arm 20K pEG-terpyridine (c^* = 35 g L^{-1}).[20] Another aqueous stock solution of zinc nitrate hexahydrate was prepared and a ratio of terpyridine to metal of 2 : 1 was ensured. In a glass vial, the polymer solution was inserted and then subsequently, the metal ion solution was added quickly. For hydrogels consisting of two precursor polymers (4-arm 20K and 8-arm 40K), both polymer stock solutions were mixed in a glass vial before adding the metal ion stock solution. All mixtures were then vigorously vortexed until complete gel formation. In total, five samples were prepared and characterized, with 8-arm pEG-terpyridine volume fractions $\phi_{8\text{-arm}}$ being respectively 0, 0.25, 0.5, 0.75 and 1. Finally, the gels were allowed to equilibrate overnight on a plate shaker at room temperature, to remove all air bubbles.

Oscillatory shear rheology experiments were carried out on an Anton Paar rheometer of the type MCR 302 (Anton Paar, Graz, Austria), equipped with a solvent trap to avoid dehydration and a parallel plate geometry PP-25. After equilibration, amplitude sweeps were recorded in order to determine the linear viscoelastic regime. These were done at a temperature of 25 °C, a constant shear frequency of ω = 1 rad s^{-1} and an increasing amplitude of γ = 0.1–100%. Afterwards, the sample was allowed to equilibrate again and then frequency sweeps were obtained at 25 °C, at a constant shear rate of γ = 0.1% and a frequency range of ω = 0.01–100 rad s^{-1}.

Fluorescence recovery after photobleaching

Fluorescence recovery after photobleaching was chosen as a method to microscopically investigate the self-diffusivities of 4-arm pEG-terpyridine macromolecules within the hydrogels depending on the amount of added 8-arm pEG-terpyridine. For this purpose, 3 wt% of a dye-labelled pEG moiety that contains both required functional groups on each arm, a terpyridine unit and a fluorescent NBD group, was integrated into the gels. These polymer tracers were synthesized according to a previously described procedure[21] and are visualized in **Figure SI4**.

The FRAP experiments were carried out on a Leica TCS-SP8 AOBS SMD confocal laser scanning microscope, equipped with a 20x immersion objective (HC PL APO CS2 20x/0.75 IMM, numerical aperture: 0.75) and a PMT detector. Aqueous stock solutions of the 4-arm pEG-terpyridine and the 8-arm pEG-terpyridine (c = 118.5 g L^{-1}, respectively) were prepared, as well as of the NBD-tagged fluorescent 4-arm pEG-terpyridine (c = 14.7 g L^{-1}) and the zinc nitrate hexahydrate (c = 7.28 g L^{-1}). Final gels were prepared by mixing the polymer stock solutions (40 µL total volume: 0%; 25%, 38%, 50%, 63%, 75%, and 100% 8-arm content), adding 10 µL of the dye-labelled polymer stock solution, followed by the addition of 20 µL zinc nitrate solution and subsequent vortexing. With this procedure, the desired stoichiometric ratio of terpyridine to zinc of 2 : 1 was obtained, as well as the overall polymer concentration of 70 g L^{-1}. Due to the twofold molar mass of the 8-arm pEG-terpyridine compared to the 4-arm pEG-terpyridine, the number of terpyridine stickers remains constant in all networks while a sole variation in the overall connectivity is achieved. Samples were gently shaken over night at 39 °C to reach full equilibration. After cooling to room temperature for two hours, the gels were loaded into an eight-well plate (Ibidi®) and sealed to avoid dehydration during the scans. Prior to each measurement, a set of four pre-bleach images is recorded. Permanent irradiation of the fluorophores and therefore creation of a bleached point pattern was achieved by applying a full-power laser beam (10 mW) with a duration of 1 s. A weak reading beam with a wavelength of 488 nm (maximum excitation wavelength of the NBD-dye) was used to excite the dye molecules during the scan series. For the recovery process, it is important to use a remarkable attenuated laser beam to avoid re-bleaching of the region of interest. A series of 250 images was recorded with time intervals of 0.173 s between each scan (bidirectional scan frequency: 400 Hz) to capture the re-emerging of fluorescing macromolecules into the bleached area. Analogous to previous works,[4,22] the FRAP data were analysed using a diffusion model that is based on fitting Gaussian shaped intensity profiles $I(r,t)$ to the time-depending disappearance of the initial bleached spot.[23,24] The bleached area vanishes due to the exchange and diffusive

motion of the dye-labelled supramolecular polymers throughout the system until its pre-bleached fluorescence intensity is fully recovered.

^{1}H DQ-NMR

Low-field NMR experiments were performed on a Bruker MiniSpec mq20 with a magnetic field of B_0 = 0.47 T. The pulse lengths were between 1.5 and 1.7 µs for 90 ° pulses and between 3.5 and 4.0 µs for 180 ° pulses. A BVT3000 temperature unit was used to keep the samples at a stable temperature of 30 °C ± 1 °C. Samples were synthesized in 10 mm diameter glass tubes according to the synthesis protocol presented in the rheology section and flame-sealed at about 5 cm height to prevent solvent evaporation during the experiments. For the DQ experiments, the Baum-Pines sequence[25] with incremented delays between the pulses and a constant number of two cycles was used. The recycle delay was set to 1.5 s, which is enough to filter out about 90% of the HDO signal (estimating an average longitudinal relaxation time of about $T_{1,HDO}$ = 12 s), while retaining >95% of the polymer signal (estimation $T_{1,poly}$ = 0.5 s). This was validated by the first DQ-measurement of the sample consisting of only 4-arm stars ($\phi_{8\text{-arm}} = 0$) (see DQ-NMR results), where a combined fraction of defects and solvent signal of less than 1% was measured. Therefore, we refrain from the commonly used procedure of quantifying the leftover HDO component after the T_1-filtering by exploiting the large difference in T_1 relaxation times in a saturation recovery experiment, because such a small contribution will be shown to be negligible and the introduced uncertainty significantly larger than the obtained value.

In the following, a concise overview of the obtained data using the DQ experiment and a reasoning for the data treatment is provided. For further information on the derivation and meaning of the measured quantities, the reader is referred to Ref 10. After application of the Baum–Pines sequence, two phase cycle-controlled signals are obtained: The first one is the DQ build-up function $I_{DQ}(t_{DQ})$, which contains structural information about the sample in the form of residual dipolar coupling (RDC) values and its quantitative distribution. However, it is also modulated by transverse relaxation of the total NMR signal, so the RDC is not easily accessible using only a simple fitting procedure to the $I_{DQ}(t_{DQ})$ curve. Thus, a second signal function, sometimes also called reference function $I_{ref}(t_{DQ})$ is needed for independent quantification of the relaxational contribution to the signal. Using a specific phase cycle described in Ref 26, the shape of this signal will only depend on the transverse relaxation times being present in the sample. As shown and already applied on, e.g., the tetra-pEG system of Sakai *et al.*[27] and another terpyridine-based tetra-pEG hydrogel,[28] the following fitting functions (1–3) are used for the two signals:

$$I_{DQ}(\tau_{DQ}) = \sum_{i=1}^{3} a_i \cdot I_{nDQ,i}^{A-1} \cdot \exp\left[-\left(\frac{\tau_{DQ}}{\tau_i}\right)^{\beta_i}\right] \quad (1)$$

and

$$I_{\Sigma MQ}(\tau_{DQ}) = \sum_{i=1}^{3} a_i \exp\left[-\left(\frac{\tau_{DQ}}{T_{2,i}}\right)^{\beta_i}\right] + a_{tail} \exp\left[-\frac{\tau_{DQ}}{T_{2,tail}}\right] \quad (2)$$

Here I_{nDQ} combines the Abragham-Like (A-l)-function that is defined as

$$I_{nDQ}^{A-1}(\tau_{DQ}) = 0.5\left\{1 - \exp\left[-(0.378 D_{res}\tau_{DQ})^{1.5}\right] \times \cos(0.583 D_{res}\tau_{DQ})\right\} \quad (3)$$

that was firstly derived in Ref 29. Both functions are fitted simultaneously to the $I_{\Sigma MQ}$ and I_{DQ} data, with shared parameters for the relaxation part and the respective fractions a_i. In all known cases with tetra-pEG-based systems, including this work, a minimum of 3 A-I functions is needed to sufficiently fit the curves. Each extracted component a_i corresponds to a certain species with molecular mobility and therefore to a certain type of connectivity motif in the network. A fourth, purely exponential function that is exclusive to I_{ref}, is used for characterising sample fractions with unhindered, isotropic motion (e.g., protonated solvent, sol, dangling chains), which reflects in the long tail of the relaxation function, while not contributing to the DQ function. In contrast to Ref 27, we refrain from explicitly assigning all components a_i to certain connectivities as, admittedly, the simply picture of three easily distinguishable types of connectivities is certainly a simplification in such a complex system. Instead, we only assign the component a_1 to the single link, as the single link can safely be assigned to the component with the highest RDC using the proportionality $D_{res} \sim M_c^{-1}$ and the simple argument of an increased, apparent molecular weight of the crosslinks for higher order connectivities. Analysis of the data shows that a two-component model is not sufficient, thus we still use a 3-component model as the model with the least possible parameters, and therefore, we present results in a 3-parted fashion, however, we suggest to only interpret the sum of the higher order connectivity defects a_2+a_3 or the ratio between the ideal connectivities a_1 and the sum a_2+a_3. This is especially important in the case of samples containing 8-arm stars, as here even more possible connections can be formed which, however, cannot be extracted with our approach due to the strongly increasing number of fitting parameters and the increasing fitting ambiguity.

4.4.4 Results and Discussion

Our material basis for systematically studying the effects of connectivity defects on the elastic response and diffusive permeability of supramolecular model hydrogels is composed of 4-arm and 8-arm pEG where each arm was end-capped with terpyridine units that are capable of forming bis-complexes

with zinc ions. To ensure the same number of terpyridine stickers in each sample, the 8-arm pEG was chosen with a twofold molar mass compared to the 4-arm pEG, therefore also ensuring the same arm length. To increase the amount of connectivity defects, 8-arm pEG-terpyridine was introduced into the 4-arm model pEG-terpyridine system in different volume fractions $\phi_{8\text{-arm}}$. To investigate the influence of connectivity defects on the properties of supramolecular hydrogels, the macroscopic elastic response of the gels was characterized by oscillatory shear rheology whereas the microscopical diffusive permeability was characterized by FRAP measurements. Finally, the defects were quantified nanoscopically by DQ-NMR. The combination of these three characterization techniques allows us to obtain information not only on the relaxation dynamics, but also on the structural properties of the system at multiple length scales.

Oscillatory shear rheology

The influence of connectivity defects on the macroscopic elastic response of a hydrogel was probed through oscillatory shear rheology experiments. Starting from a network purely composed of 4-arm pEG-terpyridine macromolecules, we successfully replaced different amounts of 4-arm pEG-terpyridine by 8-arm 40K polymers, thereby keeping the number of sticky terpyridine units constant, and an overall polymer concentration of 70 g L^{-1}. The volume fraction of 8-arm pEG-terpyridine $\phi_{8\text{-arm}}$ is then respectively 0, 0.25, 0.5, 0.75 and 1. Frequency-dependent dynamic moduli were investigated at 25 °C. The frequency-dependent dynamic moduli of all networks can be described by a single Maxwell element, as demonstrated in **Fig. 3 (A)** by the dashed lines. However, with increasing $\phi_{8\text{-arm}}$, a slight deviation in the moduli at high and low frequencies becomes visible. Such a deviation from the Maxwell model might be an indication of multiple relaxation times.[30] These relaxation times can derive from the relaxation of higher order loops, where two polymer stars share more than one connection or a bigger loop results by connecting several stars in circle. The measured plateau moduli depending on the volume fraction of 8-arm 40K polymers is shown in **Fig. 3 (B)**. The pure 4-arm 20K sample exhibits the highest elastic modulus corresponding to $G_{P,4\text{-arm }20K}$ = 13 kPa, whereas the lowest elastic modulus is obtained in the pure 8-arm 40K gel, corresponding to $G_{P,8\text{-arm }40K}$ = 1 kPa. The plateau storage moduli of the samples at intermediate compositions systematically decrease with increasing the volume fraction $\phi_{8\text{-arm}}$. Based on the affine network model theory, we expected all samples to show the same plateau modulus, as the number of network strands per volume (corresponding to ν) is kept constant in all gels. In this model, the plateau modulus G_N^0 is given by

$$G_N^0 = \nu RT \tag{4}$$

where ν is the number of network strands per volume, R is the universal gas constant, and T denotes the temperature. ν can be calculated from the molar concentration of pEG precursors and it corresponds to

$$\nu = \frac{f\mu}{2} \tag{5}$$

with f the functionality of the precursor and μ the density of network crosslinks.[31] Hence, the theoretical plateau modulus for both pure 8-arm 40K and 4-arm 20K networks is calculated to be roughly $G_N^0 = 17$ kPa. This value is valid for a fully percolated and defect-free theoretical polymer network. However, experimental polymer networks always show intrinsic topological defects that determine a deviation from the theoretical value.[31] In this context, the measured plateau modulus of the pure 4-arm network ($G_{P,4\text{-arm }20K} = 13$ kPa) is not significantly lower than the calculated theoretical one. Since this is the system with the highest modulus, it will be further taken as reference when compared to the other samples. If the plateau modulus is considered as a quantification of the elastically active network

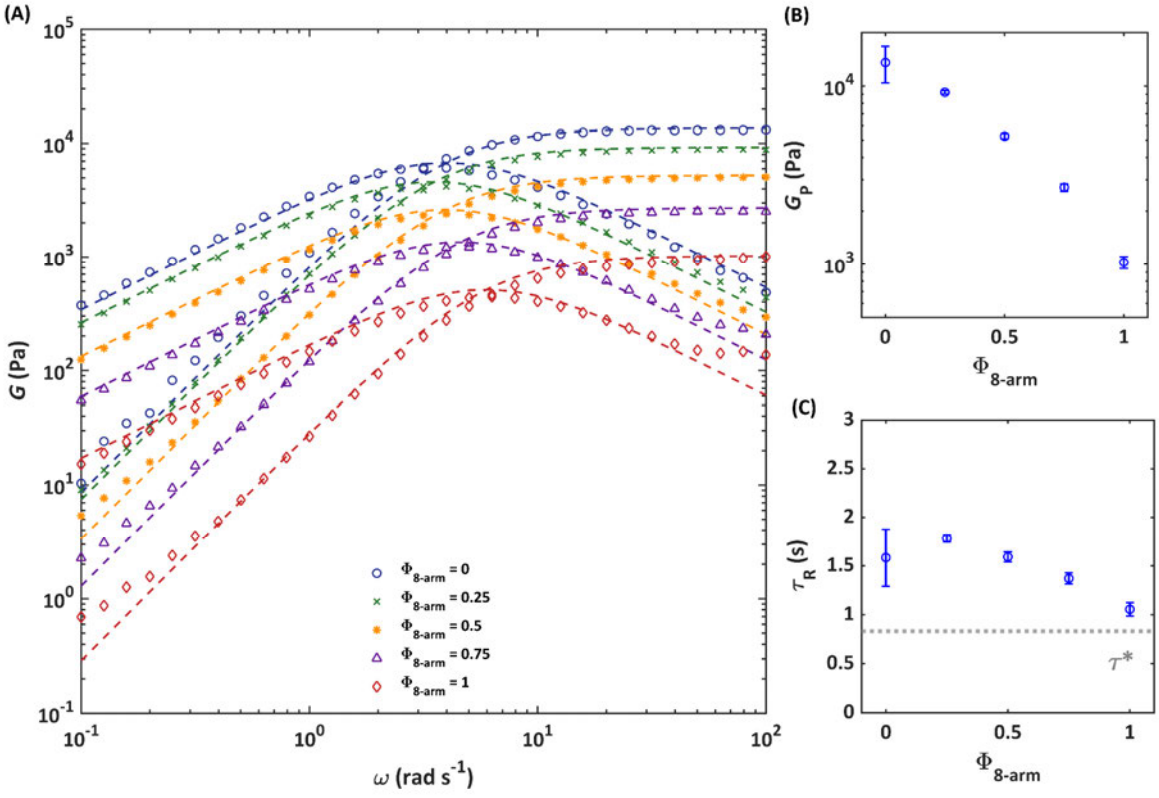

Fig. 3 Frequency-dependent elastic and loss modulus of the hydrogels composed by different ratios of 4-arm pEG-terpyridine (M_w = 20 kg mol^{-1}) and 8-arm pEG-terpyridine (M_w = 40 kg mol^{-1}) with zinc in water at a total polymer concentration of 70 g L^{-1} and a temperature of 25 °C, assuring the same terpyridine concentration in all gels. Dashed lines represent fits to the Maxwell model (A). Influence of the 8-arm pEG-terpyridine proportion on the plateau modulus G_p (B) and on the relaxation time τ_R (cross-over frequency of G' and G'') (C). The lifetime τ^* of an isolated zinc-terpyridine complex (taken from Ref. 37) in dilute aqueous conditions is depicted as dotted grey line. The error bars depict the fit parameters of the Maxwell model within a confidence interval of 95%. The pure 4-arm sample is an outlier.

strands,[5] the continuous decrease of G_p depending on an increasing amount of 8-arm in the networks, indicates a decreasing degree of network connectivity. As the matter of fact, with a higher density of arms per each molecule, the 8-arm is more likely to form intra-molecular instead of inter-molecular associations.[32] Alternative to the affine model, one could use the phantom model, which would consider the functionality of the stars instead of the total number of strands. In this case, the plateau modulus of the 8-arm pEG is predicted to be higher than that of the 4-arm pEG. In addition, the phantom model would need to define a functionality for the mixed system, which has not been taken into account so far. Up to now, it is still a matter of debate which of both models is more suitable to describe the rheological spectrum of supramolecular polymer networks, whereas a concentration-dependent transition between the two has been found for chemically crosslinked tetra-arm pEG.[33] The concentration used in this study ($2c^*$), would fall at the boundary between these two models. However, the initial hypotheses of our studies are in line with the affine model, since we designed our study such to have the same number of network strands in each sample.

The fact that the 8-arm 40K pEG network exhibits a lower plateau modulus can be explained by connectivity defects occurring due to a higher local density of arms. With such overcrowding of arms, it is more likely that two neighbouring arms of the same macromolecule find each other thereby creating loops of different orders. These loops cause a loss in modulus, because they do not actively store energy. Therefore, going from 100% 4-arm pEG-terpyridine ($\phi_{8\text{-arm}} = 0$) to 100% 8-arm pEG-terpyridine ($\phi_{8\text{-arm}} = 1$), the network becomes locally more heterogeneous.

In addition to the elastic modulus, the terminal relaxation times (inverse of the crossover frequency of G' and G'') of the networks slightly decrease with increasing $\phi_{8\text{-arm}}$ (**Fig. 3 (C)**). This can be explained by the fact that the 8-arm pEG has a higher functionality and therefore each terpyridine exchanges faster because it is easier to find another free ligand of another 8-arm polymer in close proximity. Even though, for crowded systems there is usually a prolongation of the effective lifetime of the bonds due to the constraint of other chains, this usually occurs in the melt state or at high concentrated regime, while we are still in the semi-dilute regime. In addition, it was already observed in other pEG-terpyridine telechelic systems that the dynamic of the complex in the polymer in enhanced when compared to the one of the terpyridine and metal complex alone.[34] This is in line with previous observations for associative networks with cluster forming end groups, for which it was shown that terminal flow is indeed mediated by the relaxation of single chains.[35,36] Moreover, as it can be seen from **Fig. 3 (C)**, with increasing $\phi_{8\text{-arm}}$, the dissociation times of the gels approaches the dissociation time τ^* of an isolated

zinc-terpyridine complex in dilute conditions (dotted grey line), taken from Ref. 37 as $1/k_{diss}$. The macroscopic network relaxation time measured by rheology is influenced by the complex dissociation time, as the applied shear stress is released by chain motion and subsequent breaking of the transient cross-link. However, a direct comparison between both times should be considered carefully. First, the lifetime of the isolated complex has been determined in aqueous dilute conditions whereas our network relaxation time is obtained in a semi-dilute regime of $2c^*$. An earlier work of Olsen *et al.*[38] showed by Forced Rayleigh experiments (FRS) that the complex dissociation time is also strongly influenced by the crowded environment of a network and can therefore deviate from the value obtained in dilute unpercolated conditions. Second, Wilkins *et al.*[37] used pure terpyridine (2,6-Bis(2-pyridyl)pyridine) for their metal exchange studies whereas in our case, the terpyridine unit is attached to a polymer chain via oxygen atom that influences the electronic properties of the aromatic pyridyl-ring and therefore also the complex dissociation time. With increasing 8-arm (40K) content, the macroscopic network relaxation time approaches the dissociation time in dilute conditions. In all other networks, the influence of the bond lifetime renormalization (meaning that the complex opens and closes several times before it actually releases the applied shear stress) becomes pronounced. This bond lifetime renormalization vanishes with increased defect fraction.

We further estimate the network mesh size ξ from the elastic modulus by

$$\xi = \left(\frac{RT}{G_P N_A}\right)^{1/3} \tag{6}$$

with R the universal gas constant, T the temperature, G_P the plateau modulus, and N_A the Avogadro number.[39] According to these calculations, we find an increase in the mesh size with increasing $\phi_{8\text{-arm}}$ in the network (**Fig. 4 (A)**). We suggest the 8-arm pEG molecules to significantly contribute to the formation of loops and dangling ends, leading to an increase of the average network mesh size. The

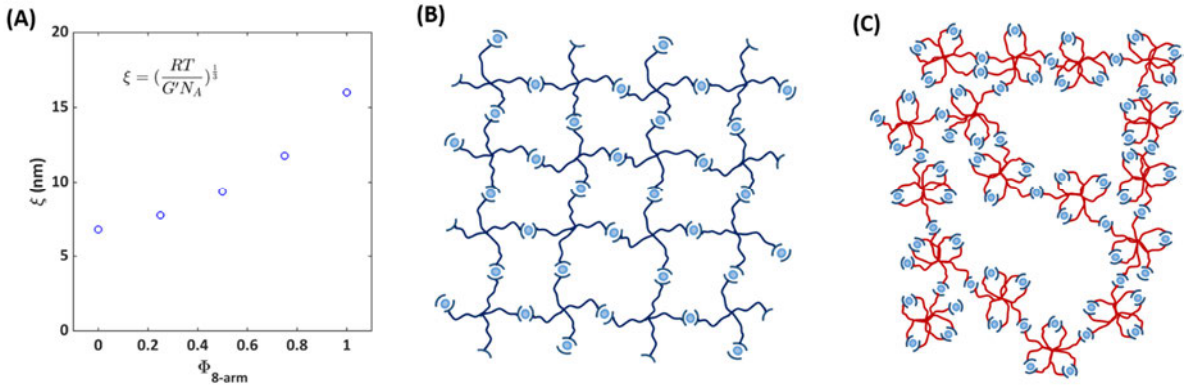

Fig. 4 Mesh-size of the network in function of the fraction of 8-arm pEG in the system (A). Ideal 4-arm 20K network with homogeneous mesh-size distribution (B) and pure 8-arm 40K network that includes connectivity defects (C). The formation of intra-molecular loops has the consequence to increase the average mesh-size of the network by forming higher order loops.

mesh-size in a pure 8-arm pEG-terpyridine network is found to be approximately three times larger than the one of the pure 4-arm pEG-terpyridine, suggesting that bigger meshes are formed as a combination of domains with a lower local density of polymers and domains with a higher local density of polymers. A schematic visualization of these higher order loops is shown in **Fig. 4**, where **Fig. 4 (B)** represents the pure 4-arm 20K network and **Fig. 4 (C)** depicts a network with included connectivity defects (pure 8-arm pEG). It is shown that with increasing number of intra-molecular connections (loop formation), the average mesh-size also increases. To prove our hypothesis on the micro- and nanoscale, we further study the diffusive permeability of the networks by FRAP, and the structural properties by DQ-NMR, as follows.

Fluorescence Recovery after Photobleaching

To microscopically investigate the influence of connectivity defects on the network structure and the resulting diffusive permeability properties, FRAP measurements were conducted.

For this purpose, a small fraction of a 4-arm polymer 20K (3 wt%) with fluorescing NBD groups attached to each arm in addition to the sticky terpyridine group was integrated into the 4-arm / 8-arm matrix gels. Based on their structural similarity, it was possible to track the intrinsic motion of the 4-arm polymer building blocks within the networks without the application of any external shear forces such as those used during rheology experiments. The self-diffusion coefficients of the investigated gels versus $\phi_{8\text{-arm}}$, are shown in **Fig. 5**.

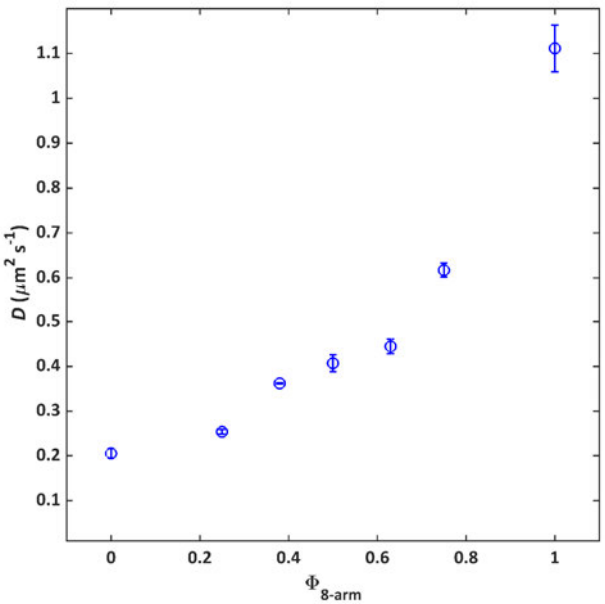

Fig. 5 Self-diffusion coefficients of a 4-arm fluorescently dye labelled pEG-terpyridine within the networks consisting of different ratios of 4-arm and 8-arm pEG-terpyridine ($c_{total} = 70\ g\ L^{-1}$), obtained by FRAP. Errorbars represent standard deviations of measurements at three randomly chosen gel positions.

As a general trend, the diffusion coefficient increases by a factor of 5 from 0.21 $\mu m^2\ s^{-1}$ to 1.1 $\mu m^2\ s^{-1}$ between the two composition extremes pure 4-arm 20K and pure 8-arm 40K. This observation is in line with the rheology results, where less elastically active

strands were formed upon increasing $\phi_{8\text{-arm}}$. Although all networks contain the same number of terpyridine stickers and therefore theoretically the same probability for a tracer molecule to attach to the network, the diffusivity in a pure 8-arm network is significantly enhanced.

The fact that the diffusion coefficient increases with $\phi_{8\text{-arm}}$, could be rationalized considering that with misconnectivities, the diffusant travels faster without actually forming transient bonds, because the next available terpyridine is farther away. This vision is coherent also with the increasing mesh-sizes calculated through rheology. The trend of the diffusion coefficient follows also the trend of the relaxation time calculated through rheology. As, a faster exchange is strictly connected to a faster diffusion.

^{1}H DQ-NMR

To directly evaluate the contribution of 8-arm stars to the formation of local defects and the overall connectivity of the polymer chains in the system, we apply static time-domain ^{1}H DQ-NMR, as described in the experimental part, on a series of networks prepared with different ratios of 4-arm pEG-terpyridine stars and 8-arm pEG-terpyridine stars (see **Fig. 6 (A)** for the normalised experimental data). Starting with a pure tetra-pEG system (4-arm 20K) transiently linked by terpyridine-zinc complexes, two different fitting approaches for the analysis of the DQ data were tried: A two-component approach assuming that two main connectivities in the network are present, being the single link and one type of connectivity defect respectively, and a three-component approach, assuming one addi-

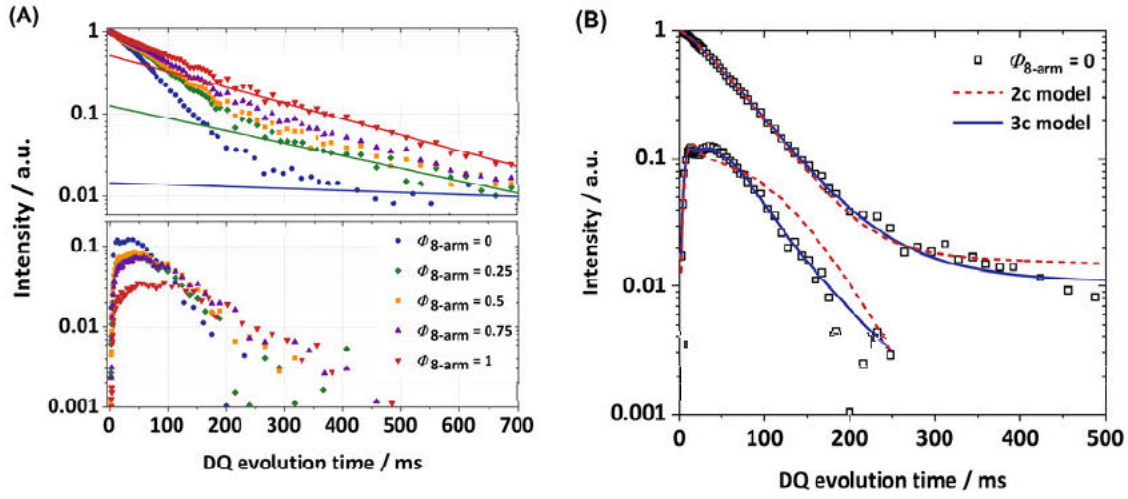

Fig. 6 (A) Overview of the measured DQ data with a shared *x*-axis but different log10-*y*-axes. Top: $I_{\Sigma QM}$ curves with exemplary tail fits (fit extrapolated to $t_{DQ} = 0$) for $\phi_{8\text{-arm}} = 0, 0.5, 1$, respectively. Bottom: Corresponding I_{DQ}. The steadily decreasing intensity is caused by the increase in the defects ('long tail') in the $I_{\Sigma MQ}$ data. (B) Exemplary data fit for $\phi_{8\text{-arm}} = 0$. The fit model with 2-components (single links + 1 connectivity defect) does not replicate the measured data, whereas the 3-component model does sufficiently fit all maxima.

tional type of misconnectivity with non-vanishing anisotropic constraints. Although previous experiments on tetra-pEG systems have already shown the necessity of three distinct components in the fitting model, the two-component approach was still tried for the sake of completeness (see **Fig. 6 (B)**). It was again shown that the two-component model (although suggested by a first glance at the data) was not sufficient and therefore one additional fit component was introduced. Again, we want to stress the ambiguity of the 3-component model that was already mentioned in the experimental section, meaning that in the final discussion one should not treat a_2 and a_3 as different components, but rather as a combined fraction of higher-order connectivities. With this in mind, we extracted three different types of connectivities, namely the single link and at least two unassigned types of connectivity defects, as well as the fraction of isotropic defects.

Firstly, we analyse the amount of isotropic material being present in a sample by quantifying the tail fraction in the relaxation signal of the DQ experiment (see **Fig. 6 (A)** for exemplary tail fits). As already mentioned, this is a quantitative sum of protonated solvent and actual isotropic polymer material (defects), where the former constitutes only a small contribution due to the choice of a rather short recycle delay of 1.5 s.

Additionally, all samples were prepared by the same preparation protocol and have the same polymer concentration and roughly the same overall volume. Therefore, we reasonably assume a comparable fraction of protonated D_2O for all samples, being at maximum 1%, as the total isotropic fraction (solvent + defects) in the DQ experiment for the pure 4-arm star system is only 1%. Across the sample series there is a trend of an increasing defect fraction from 1% to 51% with increasing number of 8-arm stars, which we mostly attribute to a steadily increasing number of loops in the 8-arm stars as it can be seen in **Fig. 7 (A).**

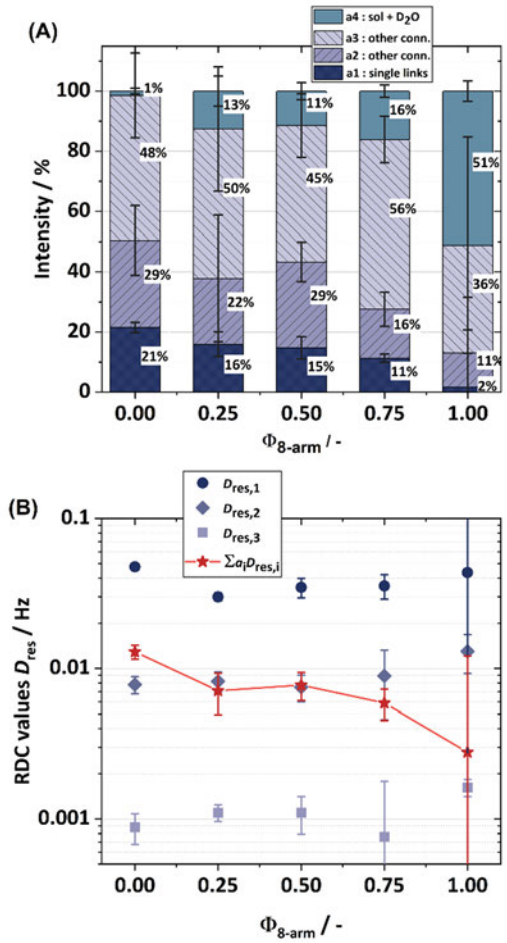

Fig. 7 (A) The fractions for each type of connectivities $a_{1\text{-}3}$ and a_{tail} as extracted from the fitting procedure are plotted vs. the respective samples. Here, $\phi_{8\text{-arm}}$ indicates the volume fraction of 40K 8-arm pEG. A clear relationship between defects and content of 40K 8-arm stars is found. (B) The corresponding residual dipolar coupling (RDC) values. Within the error bars, no significant change was observed, although the dilution effect induced by the 8-arm stars becomes visible when the weighted RDC is calculated (red star-shaped symbols; connection line as guide for the eye).

This conclusion is supported by the analysis of the corresponding RDC values. As described in the advised literature,[10] the obtained RDC values are an abstract measure of the bulk-averaged anisotropy of motion of the backbone segments under the assumption of fast orientational averaging of the segmental motion ($T \gg T_G$). Therefore, one can assume that in a network with an increasing and equally distributed number of defects, the RDC values must decrease, as these increase the effective mesh size of the network. With the introduction of the 8-arm stars, as it can be seen in **Fig. 7 (B)**, a weak but significant drop of the RDC value of the a_1 component (the single links) from 47 Hz ($\phi_{8\text{-arm}} = 0$) to 30 Hz ($\phi_{8\text{-arm}} = 0.25$) can be seen, even though in an ideal network the coupling must slightly increase given the fact that the RDCs are scaling with the phantom factor $(f-2)/f$,[40] where f is the star functionality, and we now introduced a component with $f = 8$. We attribute this effect to the increase in the defects from 1% to 13%, having, as mentioned above, a strong influence on the overall network elasticity.[41] An interesting behaviour can be found by looking now at the rest of the sample series with even more 8-arm star content. With increasing $\phi_{8\text{-arm}}$ we now assume even further decreasing RDCs for the single links, while defects increase strongly up to 51%. One would expect a vanishing RDC close to 0, as the network is now theoretically transitioning into a liquid (assuming a liquid-gel transition at 50% successful connections between the precursors).

Instead, the RDC value is not changing within the error bars, thus we necessarily must assume that not all defects are equally distributed between the network chains. Given the strong influence of loops on the RDCs, we assume that a majority of the introduced 8-arm stars are creating intra-molecular associations, therefore not or only barely contributing to the network. Thus, with increasing content of 8-

arm stars, mostly a dilution effect is observed, which is also reflected in the rheology measurements, especially in the decreasing plateau modulus and increasing network mesh size. A comparison of RDC values and plateau moduli can be made by calculating the averaged RDC of the sample (weighted by the respective fraction) without further normalisation by the respective defect fraction (because the modulus also accounts for the dilution effect of the defects), as it is proportional to the molar concentration of elastic chains.

The comparison can be found in **Fig. 8** and both curves show qualitatively the same behaviour, although the data did not overlap within the resulting error bars for the averaged RDC (under the assumption of Gaussian error propagation for a_i and $D_{res,i}$). The quantitative mismatch can mainly be attributed to the complexity of the investigated system.

The same 3-component approach was chosen for all samples, although especially samples with a mixture of 4-arm stars and 8-arm stars may show more connectivities and would therefore require a more complex model that distinguishes between them more precisely. However, an increase in the number of fit parameters would also dramatically increase the ambiguity involved in fitting, which we wanted to minimise with our decision of sticking with the model with the least possible parameters. As a final remark, it should be noted that this decision and the resulting mismatch does not influence the conclusions extracted from the experiments, as it can be seen visually, as well as from the fit optimisation, that the individual RDCs roughly stay the same, whereas the defect fraction strongly increases, therefore leading to the stated dilution effect.

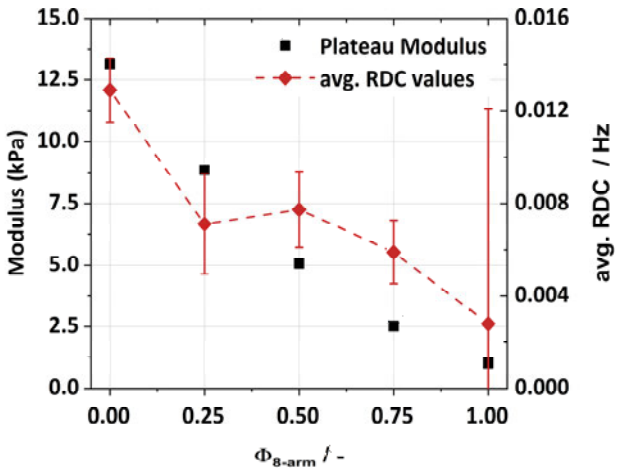

Fig. 8 On the left axis, the plateau moduli from rheology are shown and plotted against the volume fraction of 8-arm stars. On the right *y*-axis, the averaged residual dipolar coupling constant (RDC) is plotted against the same molar fractions. Both curves follow the same trend – as expected – although they do not overlap within the error, presumably due to a fit model that does not sufficiently replicate this complex system.

A similar non-linear increase of defects is reflected also in the FRAP results, where a non-linear increase in the self-diffusion coefficients is found coming along with the incorporation of 8-arm precursors, and therefore increased defect fraction (compare **Fig. 5** and **Fig. 7**). The trend of the curves is similar, but mirrored, since at high $\phi_{8\text{-arm}}$, more defects translate in a higher diffusion coefficient.
The DQ-NMR experiments revealed a dilution effect induced by an increasing fraction of 8-arm polymers that have a higher likelihood to form intra-molecular loops. Since loops do generally not contribute to the overall network elasticity, a decrease in the elastic plateau modulus is found, accompanied by an increase in the softness of the hydrogel. At the same time, the mesh size of the network increases with increasing $\phi_{8\text{-arm}}$, as the number of inter-molecular connections in the network decreases, while the number of intra-molecular connections increases. In addition to that, also the self-diffusion coefficient of a 4-arm 20K macromolecule increases with increasing $\phi_{8\text{-arm}}$, as intra-molecular loops might retard the re-attachment of diffusing dye-labelled polymers.

4.4.5 Conclusions

Hydrogels are appealing materials that, due to their high content of water, can be used for biomedical applications such as in tissue engineering and drug delivery. However, due to the amorphous structures that naturally occur in such soft matter systems, the presence of connectivity defects cannot be ignored. Their influence on the final properties of the hydrogel, such as its softness and diffusivity still remains to be further exploited. Therefore, for a rational material design, it is important to know how these defects affect the final gel properties. In this work, we have investigated the effect of connectivity defects on the softness and diffusive permeability of supramolecular pEG-terpyridine hydrogels, on multiple length scales by systematically introducing 8-arm pEG-terpyridine into a 4-arm pEG-terpyridine model network and characterizing the hydrogels with DQ-NMR, oscillatory shear rheology, and FRAP. As unravelled by DQ-NMR, the pure 8-arm pEG network is more prone to form connectivity defects such as loops. The pronounced loop formation of 8-arm pEG-terpyridine macromolecules is caused by a higher likelihood of forming intra- instead of inter-molecular connections driven by metal-ligand complexation. By increasing the fraction $\phi_{8\text{-arm}}$ of 8-arm pEG-terpyridine, these defects lead to an apparent dilution effect resulting in an increase in the mesh-size of the hydrogels and consequently an increase of the self-diffusivity and the softness of the hydrogels, as probed by oscillatory shear rheology and FRAP. These results give a first insight on the effect of controlled connectivity defects on

elastic properties of supramolecular hydrogels and bring awareness when tailoring the diffusive properties of the dynamic hydrogel is to be performed. Future perspectives might include the increase in overall polymer concentration to possibly damp the effect of the incorporated amount of 8-arm pEG (40K), and the variation of the polymer strand size to include further types of defects, as well as taking into account polydisperse building block materials.

4.4.6 Acknowledgements

This work was funded from the H2020 Programme (MARIE SKŁODOWSKA-CURIE ACTIONS) of the European Commission's Innovative Training Networks (H2020-MSCA-ITN-2017) under Do-DyNet REA Grant Agreement No.765811, as well as through the DFG Research Unit FOR 2811, SA982/14-1 (Project. No. 397384169). Parts of this work were further supported by the German Research Foundation (DFG) under Grant No. SE 1888/7-1 (Project No. 376900084). Microscopy data of this study were acquired with a confocal laser scanning microscope funded in part by the Major Research Instrumentation Program of the German Research Foundation under grant No. INST 247/878-1 FUGG. [redacted] thanks [redacted] and [redacted] for useful discussions, and [redacted] and [redacted] for support with the synthesis. [redacted] kindly thanks [redacted] for helpful methodological advices concerning FRAP. The authors would like to thank the referees of the peer-review process for their valuable and helpful comments.

4.4.7 Notes and References

(1) A. Jangizehi, F. Schmid, P. Besenius, K. Kremer and S. Seiffert, *Soft Matter*, **2020**, *16*, 10809–10859.

(2) M. Zhong, R. Wang, K. Kawamoto, B. D. Olsen and J. A. Johnson, *Science (80-.).*, **2016**, *353*, 1264–1268.

(3) S. Lin and X. Zhao, *Phys. Rev. E*, **2020**, *102*, 052503.

(4) A. Habicht, S. Czarnecki, T. Rossow and S. Seiffert, *J. Polym. Sci. Part B Polym. Phys.*, **2017**, *55*, 19–29.

(5) P. Nicolella, D. Lauxen, M. Ahmadi and S. Seiffert, *Macromol. Chem. Phys.*, **2021**, *222*, 2100076.

(6) S. Seiffert, *Polym. Chem.*, **2017**, *8*, 4472–4487.

(7) F. Di Lorenzo and S. Seiffert, *Polym. Chem.*, **2015**, *6*, 5515–5528.

(8) S. Mallam, F. Horkay, A. Hecht and E. Geissler, *Macromolecules*, **1989**, *22*, 3356–3361.

(9) Y. Gu, J. Zhao and J. A. Johnson, *Trends Chem.*, **2019**, *1*, 318–334.

(10) K. Saalwächter, in Modern Magnetic Resonance, ed. G. A. Webb, Springer International Publishing, Cham, 2017, pp. 755–781.

(11) N. Sood, A. Bhardwaj, S. Mehta and A. Mehta, *Drug Deliv.*, **2016**, *23*, 748–770.

(12) S. Mantha, S. Pillai, P. Khayambashi, A. Upadhyay, Y. Zhang, O. Tao, H. M. Pham and S. D. Tran, *Materials* (Basel)., **2019**, *12*, 3323.

(13) A. S. Hoffman, *Adv. Drug Deliv. Rev.*, **2012**, *64*, 18–23.

(14) C. F. Guimarães, L. Gasperini, A. P. Marques and R. L. Reis, *Nat. Rev. Mater.*, **2020**, *5*, 351–370.

(15) M. A. Haque, T. Kurokawa and J. P. Gong, *Polymer* (Guildf)., **2012**, *53*, 1805–1822.

(16) J. Li and D. J. Mooney, *Nat. Rev. Mater.*, **2016**, *1*, 16071.

(17) S. Kondo, H. Sakurai, U. Il Chung and T. Sakai, *Macromolecules*, **2013**, *46*, 7027–7033.

(18) P. Dong, B. J. Schott, A. K. Means and M. A. Grunlan, *ACS Appl. Polym. Mater.*, **2020**, *2*, 5269–5277.

(19) A. Sugimura, M. Asai, T. Matsunaga, Y. Akagi, T. Sakai, H. Noguchi and M. Shibayama, *Polym. J.*, **2013**, *45*, 300–306.

(20) M. Koziol, K. Fischer and S. Seiffert, *Soft Matter*, **2019**, *15*, 2666–2676.

(21) S. Tang, A. Habicht, S. Li, S. Seiffert and B. D. Olsen, *Macromolecules*, **2016**, *49*, 5599–5608.

(22) T. Rossow, A. Habicht and S. Seiffert, *Macromolecules*, **2014**, *47*, 6473–6482.

(23) S. Seiffert and W. Oppermann, *J. Microsc.*, **2005**, *220*, 20–30.

(24) G. I. Hauser, S. Seiffert and W. Oppermann, *J. Microsc.*, **2008**, *230*, 353–362.

(25) J. Baum, M. Munowitz, A. N. Garroway and A. Pines, *J. Chem. Phys.*, **1985**, *83*, 2015–2025.

(26) K. Saalwächter, P. Ziegler, O. Spyckerelle, B. Haidar, A. Vidal and J. U. Sommer, *J. Chem. Phys.*, **2003**, *119*, 3468–3482.

(27) F. Lange, K. Schwenke, M. Kurakazu, Y. Akagi, U. Chung, M. Lang, J.-U. Sommer, T. Sakai and K. Saalwächter, *Macromolecules*, **2011**, *44*, 9666–9674.

(28) M. Ahmadi, L. Löser, K. Fischer, K. Saalwächter and S. Seiffert, *Macromol. Chem. Phys.*, **2020**, *221*, 1900400.

(29) W. Chassé, J. L. Valentín, G. D. Genesky, C. Cohen and K. Saalwächter, *J. Chem. Phys.*, **2011**, *134*, 044907.

(30) A. Parker and W. Fieber, *Soft Matter*, **2013**, *9*, 1203–1213.

(31) M. Ahmadi and S. Seiffert, *Soft Matter*, **2020**, *16*, 2332–2341.

(32) R. Wang, M. Geven, P. J. Dijkstra, P. Martens and M. Karperien, *Soft Matter*, **2014**, *10*, 7328–7336.

(33) Y. Akagi, J. P. Gong, U. Chung and T. Sakai, *Macromolecules*, **2013**, *46*, 1035–1040.

(34) W. Schmolke, M. Ahmadi and S. Seiffert, *Phys. Chem. Chem. Phys.*, **2019**, *21*, 19623–19638.

(35) A. Mordvinkin, D. Döhler, W. H. Binder, R. H. Colby and K. Saalwächter, *Phys. Rev. Lett.*, **2020**, *125*, 127801.

(36) A. Mordvinkin, D. Döhler, W. H. Binder, R. H. Colby and K. Saalwächter, *Macromolecules*, **2021**, *54*, 5065–5076.

(37) R. H. Holyer, C. D. Hubbard, S. F. A. Kettle and R. G. Wilkins, *Inorg. Chem.*, **1966**, *5*, 622–625.

(38) S. Tang and B. D. Olsen, *Macromolecules*, **2016**, *49*, 9163–9175.

(39) J. Karvinen, T. O. Ihalainen, M. T. Calejo, I. Jönkkäri and M. Kellomäki, *Mater. Sci. Eng. C*, **2019**, *94*, 1056–1066.

(40) M. Rubinstein and R. H. Colby, Polymer Physics, Oxford University Press, Oxford, 2003.

(41) M. Lang, *ACS Macro Lett.*, **2018**, *7*, 536–539.

4.4.8 Supporting Information

Materials

Four-arm hydroxy-terminated poly(ethylene glycol) (pEG), M_w = 20 kg mol^{-1}, further denoted as 4-arm 20K, and 8-arm hydroxy-terminated pEG, M_w = 40 kg mol^{-1}, denoted as 8-arm 40K, were purchased from Creative PEG Works (NC, USA), and re-precipitated in cold diethyl ether before further use. Potassium hydroxide (KOH) flakes (90%) and 4'-Chloro-2,2':6',2''-terpyridine (99%) were purchased from Sigma Aldrich. Extra dry dimethyl sulfoxide (DMSO, + 99.7% over molecular sieve) is purchased from Acros Organics. Sodium chloride (NaCl, ≥ 99.5%), dichloromethane (DCM, ≥ 99.8%), and diethyl ether (≥ 99.5%) were purchased from Fisher Scientific. Zinc nitrate hexahydrate (98%) is purchased from Alfa Aesar.

Syntheses

Terpyridine-functionalized 4-arm and 8-arm polymer precursors. The hydroxyl termini of the star-shaped pEG polymers were converted to terpyridine units by the following Williamson type ether synthesis (**SI1**).

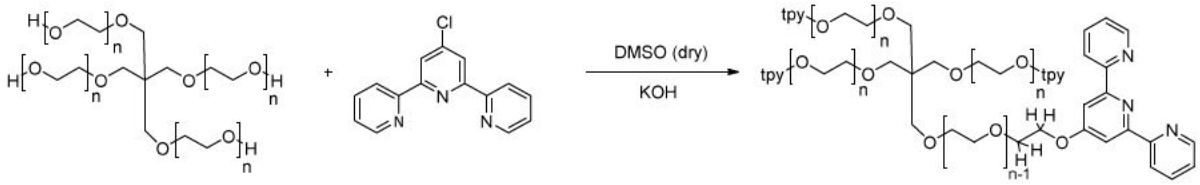

Figure SI1. Reaction route for the synthesis of tetra-arm pEG-terpyridine. The functionalization of 8-arm pEG-terpyridine is analogous.

Before use, the pEG was purified and therefore melted at 60 °C, cooled to 40 °C, dissolved in DCM, precipitated in diethyl ether, and dried under vacuum. KOH (0.056 g, 1 · 10^{-3} mol, 20 eq.) was dried in a flask for 1 h under reduced pressure, and dry DMSO (20 mL) was added in inert N_2-atmosphere. To this suspension, 4-arm pEG (M_w = 20 kg mol^{-1}, 1 g, 5 · 10^{-5} mol, 1 eq.) was added. The reaction mixture was stirred under nitrogen counter flow at 60 °C for 1 h. Afterwards, 4'-Chloro-2,2':6',2''-terpyridine (0.1340 g, 5 · 10^{-4} mol, 10 eq.) was added, and the reaction was stirred at 60 °C for another 48 h. After cooling to room temperature, the reaction mixture was added dropwise to cold water (200 mL) and a small amount of white precipitate was filtered off. To the liquid phase, brine (200 mL) was added, and the aqueous solution was washed three times with DCM (200 mL). The organic phases were collected, dried with sodium sulphate, and concentrated under vacuum. Afterwards, the polymer was precipitated in ice-cold diethyl ether (500 mL). The white powder was collected and dried under

vacuum overnight. The same reaction conditions were applied to functionalize the 8-arm 40K pEG-OH, but the reaction was performed twice to achieve a high degree of terpyridine functionalization. The degree of functionalization of terpyridine was quantified by NMR and was found to be 95% (4-arm 20K) and 90% (8-arm 40K), respectively (**SI2-SI3**).

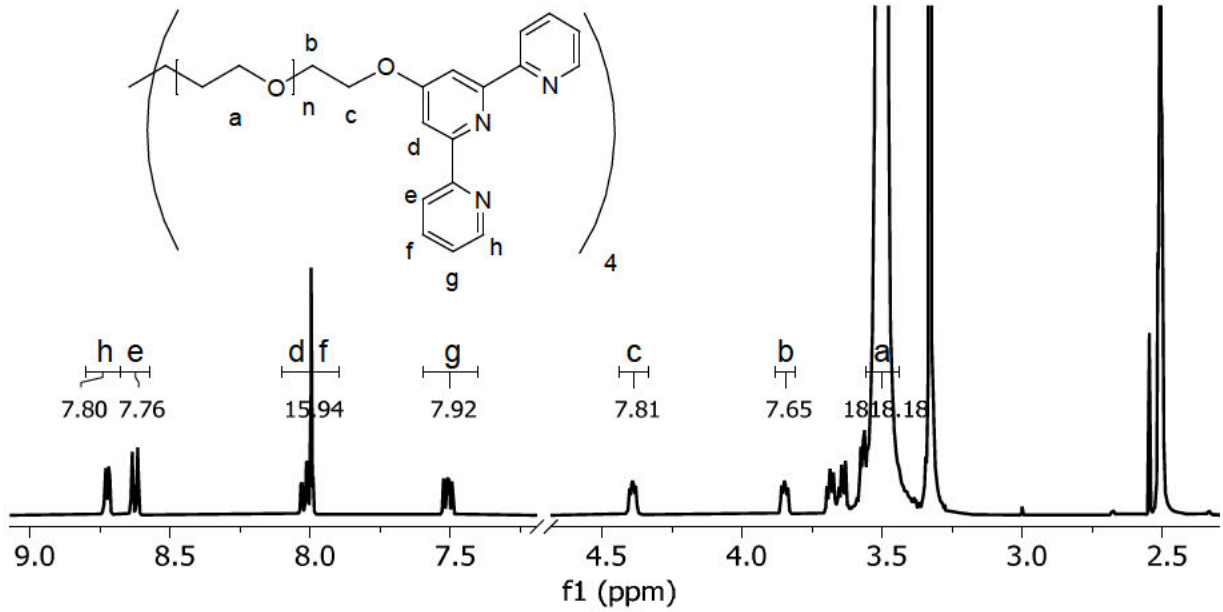

Figure SI2. [1]H-NMR of the 4-arm pEG-terpyridine (20K) in DMSO.

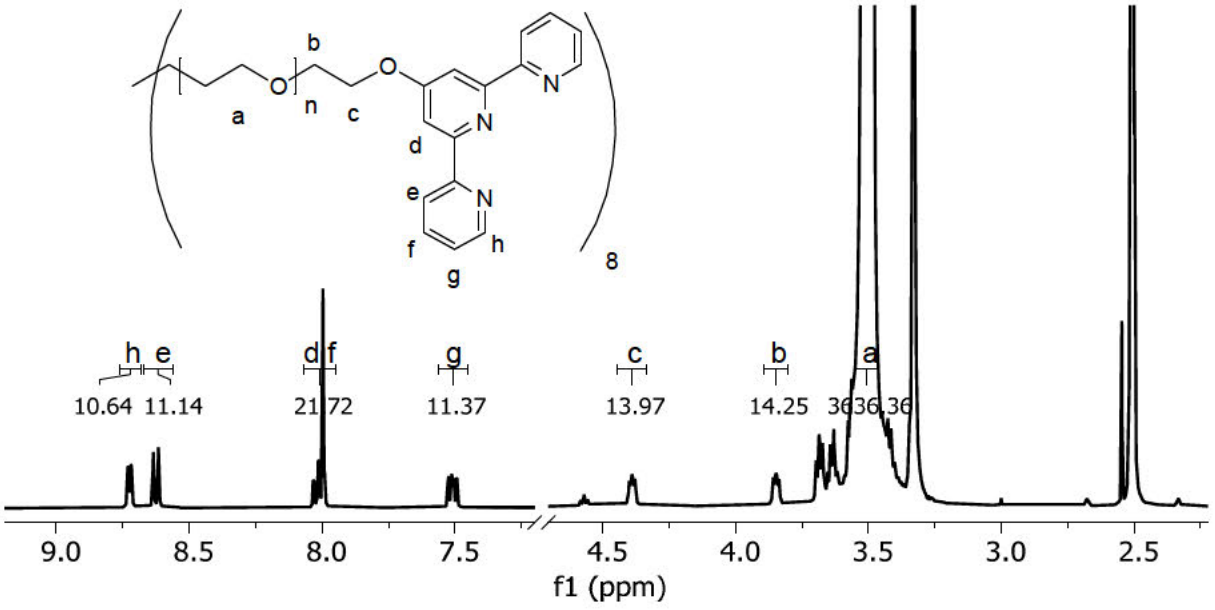

Figure SI3. [1]H-NMR of the 8-arm pEG-terpyridine (40K) in DMSO.

Fluorescence-labelled polymer tracer for FRAP measurements. To measure polymer self-diffusion coefficients by FRAP experiments, a fluorescently active dye molecule has to be attached to the polymer building blocks of interest. In addition to that, it is of major importance that the dye-labelled 4-arm polymers quantitatively contain terpyridine end-groups on each arm. These polymer tracers were synthesized according to a previously described procedure [1] and are visualized in **SI4**. In summary, hydroxy-terminated tetra-arm pEG-OH with a molar mass of 20 kg mol^{-1} was reacted with epicholorhydrin to obtain epoxy-terminated polymers. The subsequent ring-opening with sodium azide yielded in hydroxyl-azide-pEG that further reacted with propargyl-terpyridine in a copper-free Huisgen click reaction. The remaining hydroxyl groups were activated via reaction with *p*-nitrophenylchloroformate and through addition of (*S*)-(+)-4-(3-aminopyrrolidino)-7-nitrobenzofurazan (NBD), the final fluorescence-labelled tracer polymers were obtained. Unreacted excess dye was removed via size exclusion chromatography in methanol using a SephadexTM LH-20 column. The degree of terpyridine functionalization was determined by NMR to be 89% (**SI5**).

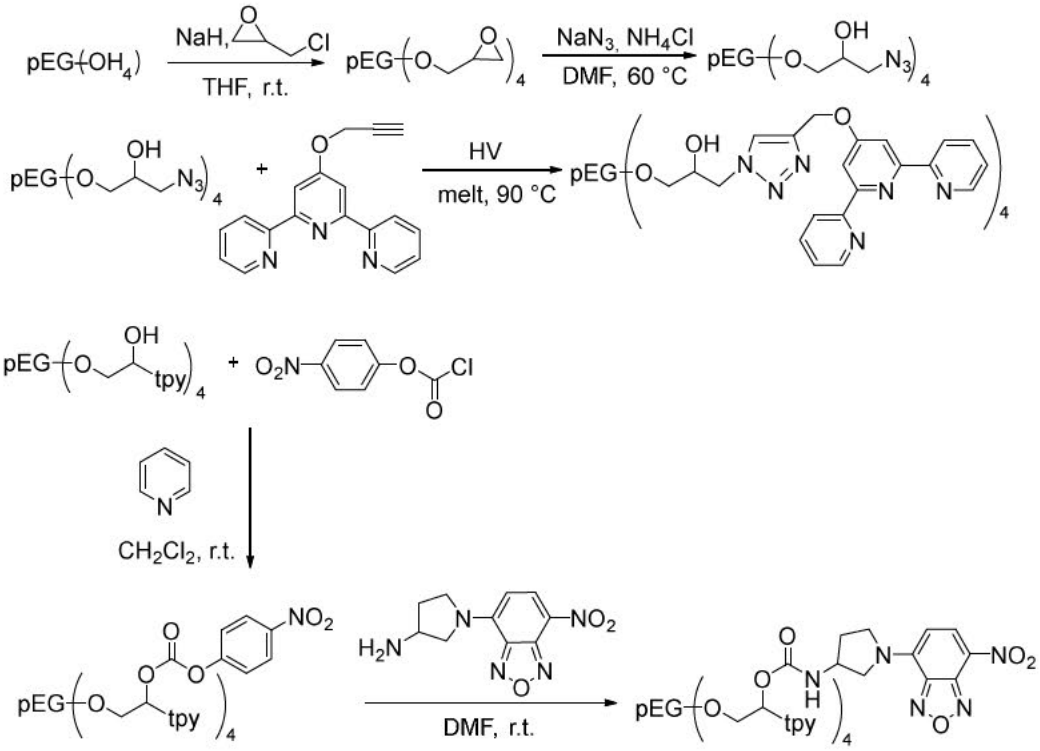

Figure SI4. Reaction route for the dye-labelled tetra-arm pEG-terpyridine (20K) tracer molecules.

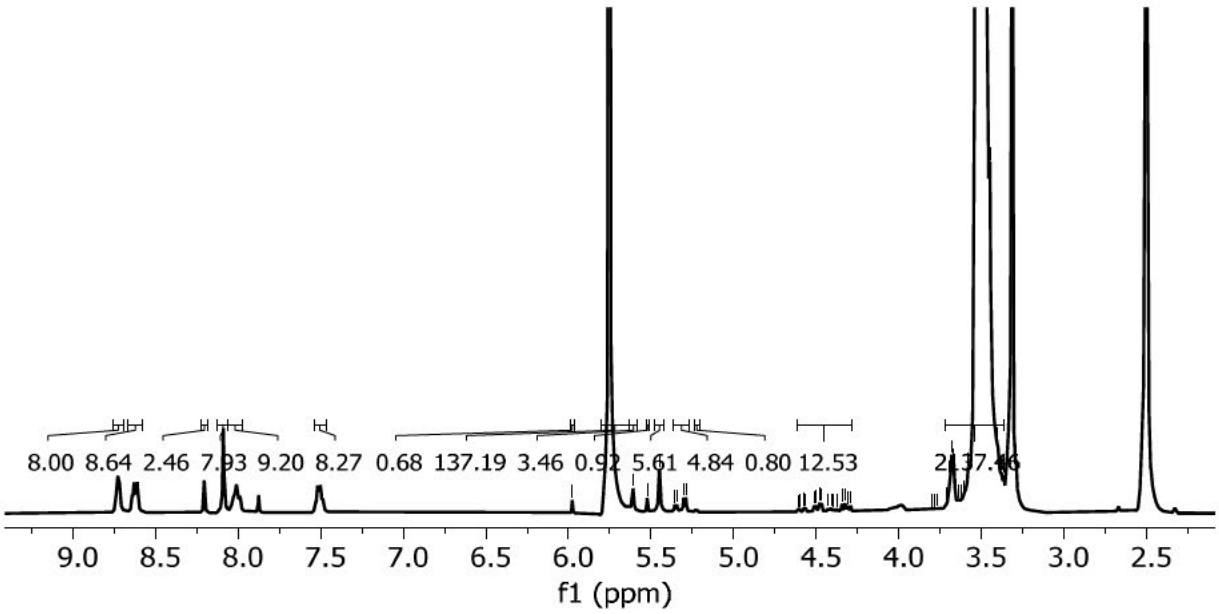

Figure SI5. ^{1}H-NMR of the 4-arm pEG-terpyridine (20K) tracer molecules in DMSO.

References

[1] S. Tang, A. Habicht, S. Li, S. Seiffert and B. D. Olsen, *Macromolecules*, **2016**, *49*, 5599–5608.

5 CONCLUSIONS AND OUTLOOK

In this thesis, the interplay of structure and dynamics in supramolecular model networks was systematically investigated. The functionalization of monodisperse tetra-arm PEG macromolecules with terpyridine ligands on each arm led to the formation of highly dynamic 3D networks once suitable transition metal cations were added. Percolated gels with many interesting properties such as self-healing were obtained by swelling of these networks in appropriate solvents. All contributions to network relaxation (e.g. segmental polymer chain relaxation or sticker kinetics, both additionally depending on the hierarchical network structure) were explored in detail using several experimental techniques, each with a characteristic time and length scale. During all investigations, a special focus was set on the network / polymer characterization by means of static and dynamic light scattering, as this technique is a powerful tool to not only obtain information on the dynamic relaxation properties, but also on the underlying structure.

In the first part, the origin of a low-frequency plateau in the storage modulus of unconnected semi-dilute aqueous PEG solutions was investigated. After thorough sample purification, no slow modes were obtained in dynamic light scattering experiments such that the existence of aggregates or clusters as possible origin for a weak energy-storing sub-network was excluded. These results were confirmed by static light scattering, where no structures larger than the instrument resolution of 10 nm were detected. DLS-microrheology with coated gold nanoparticles as probes completed the findings from a microscopic perspective. To summarize this study, the appearance of the low-frequency plateau in rheology was assigned to instrumental uncertainties that especially occur if either storage or loss modulus are dominating by several orders of magnitude.

Having investigated the scattering behavior of the abovementioned semi-dilute PEG solutions, a comprehensive light scattering study of transient tetra-arm PEG-terpyridine networks connected through transition metal ions was presented in the second part of this thesis. Semi-dilute solutions of those unconnected macromolecules showed unexpected high hydrodynamic polymer radii possibly induced by aggregation of terpyridine end groups through hydrophobic interactions and therefore formation of flower-like micelles. To avoid preparation-induced inhomogeneities due to an incomplete mass transport, a delayed gelation method was developed. This procedure allowed for real-time monitoring of the scattering intensity and evolution of a second q-independent slow mode during gelation. Impacted by the different dissociation constants coming along with the use of either zinc, nickel or

cadmium cations, the investigated non-ergodic gels obtained distinct variations in their speckle patterns, number and q-dependence of relaxation modes, and ensemble-averaged intensities. Partial heterodyne data analysis was applied for zinc and nickel gels, whereas pure homodyne scattering was obtained in case of the cadmium gels. In agreement with the fluctuation-dissipation principle, the slow relaxation mode was assigned to the total network relaxation that corresponds to the terminal relaxation time obtained by oscillatory shear rheology measurements.

The overall dynamics of transient networks are characterized by a complex interplay of sticker dissociation and re-association that are pre-programmed by their chemical composition, the relaxational polymer Rouse modes depending on the chain length or concentration, and the structural features including local defects and heterogeneities. To unravel these interdependences, the hierarchy of occurring relaxation modes on multiple length and time scales was explored by several synergistic experimental techniques such as DLS, SLS, FRS, rheology and UV-Vis. Temperature-dependent measurements provided activation energies for collective polymer motion (small length and fast time scales), viscoelastic relaxation (intermediate time and length scales), and self-diffusivities (long time limit and large length scales). Structural inhomogeneities in the range of 30–50 nm discovered by SLS were found to directly influence the emerging slow relaxation times resulting in an unusual broad position-dependent distribution.

In future soft matter engineering, the role of defects plays a crucial role to achieve smart materials with tailored properties. Controlling the incorporation of defects and their impact on resulting material properties requires a deep understanding of structure–property–relationships. For this purpose, a model system with intentionally implemented connectivity defects was investigated in the last part of this thesis. By increasing the fraction of structural irregularities as proven by MQ-NMR experiments, a decreasing elastic response and increasing self-diffusivities were obtained. These findings were assigned to an apparent dilution effect induced by an increased fraction of intramolecular inelastic loops that are invisible for further network relaxation and self-diffusion.

The wide variety of possible applications in all areas of life underlines the need for further fundamental knowledge as every transient system exhibits a unique mutual interplay between structural and dynamic properties. General approaches towards predicting the final network performance become relevant to meet the more and more complex demands on future materials.

6 PUBLICATIONS

6.1 Publications with Peer Review Process

[1] Koziol, M.; [redacted]. Origin of the low-frequency plateau and the light-scattering slow mode in semidilute poly(ethylene glycol) solutions. *Soft matter* **2019**, *15*, 2666–2676. (DOI: 10.1039/C8SM02263A)

[2] Stengelin, E.; [redacted]. Biotherapeutics: Bone Scaffolds Based on Degradable Vaterite/PEG-Composite Microgels (Adv. Healthcare Mater. 11/2020). *Adv. Healthcare Mater.* **2020**, *9*, 2070030. (DOI: 10.1002/adhm.201901820)

[3] Koziol, M. F.; [redacted] Structural and Gelation Characteristics of Metallo-Supramolecular Polymer Model-Network Hydrogels Probed by Static and Dynamic Light Scattering. *Macromolecules* **2021**, *54*, 4375–4386. (DOI: 10.1021/acs.macromol.1c00036)

[4] [redacted].;* Koziol, M., F.;* [redacted] Defect-controlled softness, diffusive permeability, and mesh-topology of metallo-supramolecular hydrogels, *Soft Matter* **2022** (accepted manuscript, DOI: 10.1039/D1SM01456K)

[5] Koziol, M. F.; [redacted]. Hierarchy of Relaxation Times in Supramolecular Polymer Model Networks (submitted and revised to *Physical Chemistry Chemical Physics*, 21.12.2021)

[6] [redacted].; Koziol, M.; [redacted] A Fast and Sustainable Route to Bassanite Nanocrystals from Gypsum. (submitted and revised to *Advanced Functional Materials*, 20.11.2021)

7 CONFERENCE CONTRIBUTIONS

7.1 Oral Contribution

Microrheology on weakly associated PEG chains in semidilute solution

Martha Koziol and [redacted], 82nd Meeting on Macromolecules and 24th Polymer Networks Group Meeting, **2018**, Prague, Czech Republic.

7.2 Poster Presentation

Impact of Clustering on the Dynamics and Relaxation Processes of Associative Metallo-Supramolecular Polymer Model Networks

Martha Koziol, [redacted], European Polymer Congress (EPF), **2019**, Crete, Greece.